MINERAL CARBONATION POTENTIAL AND TRANSITION METAL MIGRATION IN KIMBERLITE AND ULTRAMAFIC ROCKS: AN INTEGRATED STUDY OF ACID LEACHING, ENHANCED ROCK WEATHERING, AND MICROBIAL CO_2 SEQUESTRATION

by

Baolin Wang

A thesis submitted in partial fulfillment of the requirements for the degree of

Doctor of Philosophy

Department of Earth and Atmospheric Sciences
University of Alberta

Abstract

Carbonation of mafic and ultramafic rocks and mineral wastes provides a permanent way to sequester excess atmospheric CO_2. Recent research has shown that this method also offers the potential for enhanced recovery of critical metals from mine tailings. This thesis presents a comprehensive study on the potential for CO_2 sequestration through the carbonation of ultramafic rocks and mineral wastes from diamond mines. Utilizing a variety of analytical and experimental methods, this research aims to enhance our understanding of mineral carbonation processes and their application in offsetting CO_2 emissions, while also exploring the recovery of critical metals from mine tailings.

The first part of the thesis introduces an innovative application of the Partial Or No Known Crystal Structure (PONKCS) method combined with the Rietveld method and X-ray diffraction (XRD) to perform Quantitative Phase Analysis (QPA). This approach overcomes the limitations of standard methods in quantifying structurally disordered minerals like lizardite and smectites in kimberlite, which are reactive to CO_2. The study highlights the importance of instrument-specific calibration for accurate QPA and CO_2 mineralization quantification in clay-rich rocks.

The second part of the thesis evaluates the carbonation potential of processed kimberlite from the Venetia diamond mine through column acid leaching experiments. The study demonstrates the feasibility of CO_2 offset and critical metal recovery during mineral carbonation, with acid concentration significantly influencing the extraction of Mg and Ca, essential for carbon sequestration.

The third part of the thesis expands on the theme of accelerated carbon mineralization, investigating the influence of mineralogy on the weathering and carbonation potential of various ultramafic rocks and processed kimberlite. Through acid leaching experiments, the research underlines the crucial role of specific mineral compositions in determining the efficiency of CO_2 sequestration and suggests a significant potential for offsetting greenhouse gas emissions from mining operations.

Finally, a field trial conducted over a year examines the effectiveness of pH-swing and cation exchange methods combining with microbially-mediated method for carbonating serpentine-, smectite- and calcite-rich processed kimberlite. The results indicate promising strategies for enhancing weathering and carbonation, tailored to the unique mineralogy of each rock type. The study advocates for the integration of acid leaching and microbially-mediated carbonation for calcite-poor residues, and a novel cation exchange approach for calcite-rich tailings, to maximize CO_2 sequestration.

Preface

This thesis is the original work by Baolin Wang under the supervision of Dr. Sasha Wilson and Dr. Nina Zeyen. This thesis consists of four related manuscripts that have been prepared for publication in peer-reviewed international journals.

A version of Chapter 2 has been submitted to the journal *American Mineralogist* and is currently under review after the resubmission of our corrected version. I am the lead author of this manuscript and Nina Zeyen, Sasha Wilson, Rebecca Funk, and Connor C. Turvey are my coauthors. As the primary author, designed and conducted the experiments, collected, and analyzed the XRD data, developed the models and conducted Rietveld refinements, interpreted the data and wrote the manuscript. NZ contributed to data collection, interpretation and writing. SW provided the idea for the project, prepared the synthetic samples, assisted with experimental design, facilitated XRD data collection and Rietveld analysis, participated in data interpretation and writing. RF and CCT contributed to XRD data collection and interpretation. All authors contributed to the article and approved the submitted version.

A version of Chapter 3 has been published in *Applied Geochemistry*. I am the lead author of this manuscript and Nina Zeyen, Sasha Wilson, Makoto J. Honda-McNeil, Jessica L. Hamilton, Konstantin Von Gunten, Daniel S. Alessi, Thomas R. Jones, David J. Paterson, and Gordon Southam are my coauthors. As the primary author, I designed and conducted the experiments, collected, and analyzed XRD, ICP-MS, SEM-EDXS, TEM, XFM data, conducted Rietveld refinements and geochemical modelling, interpreted the data and wrote the manuscript. NZ participated in field sampling at Venetia, assisted with experimental design, contributed to XFM and TEM data collection, interpretation and writing. SW provided the idea for the project, assisted with experimental design, participated in field sampling at Venetia, facilitated XRD data collection and Rietveld analysis, participated in data interpretation and writing. MJHM facilitated XRD sample preparation and data collection. JLH and KvG assisted with geochemical modelling. JLH and DJP provided technical support and contributed to data acquisition and processing on the XFM beamline at ANSTO. GS and TRJ contributed to the data acquisition on the

XFM beamline at ANSTO. KvG and DSA facilitated ICP-MS/MS data collection and analysis. All authors contributed to the article and approved the submitted version. The reference for the manuscript follows:

Wang B., Zeyen N., Wilson S., Honda-McNeil M.J., Hamilton J.L., Von Gunten, K., Alessi D. S., Jones T., Paterson D.J., Southam G., 2024. Migration of transition metals and potential for mineral carbonation during acid leaching of processed kimberlite from Venetia diamond mine, South Africa. Applied Geochemistry, 105986, ISSN 0883-2927. https://doi.org/10.1016/j.apgeochem.2024.105986.

Chapter 4 is intended for submission to a peer-reviewed international journal. I am the lead author of this manuscript and Nina Zeyen, Maria Arizaleta, Sasha Wilson, Connor C. Turvey, Wyatt Russell, and Jessica L. Hamilton are my coauthors. As the primary author, I designed and conducted the experiments, collected, and analyzed XRD and ICP-MS data, conducted Rietveld refinements and geochemical modelling, interpreted the data and wrote the manuscript. NZ assisted with experimental design, contributed to data interpretation and writing. MA assisted with experiments and contributed to raw data collection. SW provided the idea for the project, assisted with experimental design, facilitated XRD data collection and Rietveld analysis, participated in data interpretation and writing. CCT contributed to the acquisition of CT data, data interpretation and writing. WR facilitated experimental conduct, XRD sample preparation and data collection. JLH assisted with geochemical modelling and provided technical support and contributed to data acquisition and processing on the XAS beamline at ANSTO. All authors contributed to the article and approved the submitted version.

Chapter 5 is intended for submission to a peer-reviewed international journal. I am the lead author of this manuscript and Nina Zeyen, Maria Arizaleta, Sasha Wilson, Carlos Paulo, Ian M. Power, Amanda R. Stubbs, Kwon Rausis, Khangeziwe Senzani, Senzeni Ndlovu, Andrew Vietti, Thomas Jones, and Gordon Southam are my coauthors. As the primary author, I and NZ designed and conducted the experiments, participated in field sampling at DebTech, collected, and analyzed XRD, ICP-MS, SEM-EDXS, STXM data and conducted Rietveld refinements. BW conducted geochemical modelling, interpreted the data and wrote the manuscript. NZ contributed to data interpretation and writing. MA facilitated sample preparation and contributed to raw data collection. SW provided the idea for the project, designed and conducted the experiments, participated in field sampling at DebTech, facilitated XRD data collection and Rietveld analysis, participated in data interpretation and writing. CP, IMP and ARS assisted with experimental design. CP and KR analyzed TIC data. KS, SN and AV assisted with experimental design, conducted sample collection and contributed to raw data collection. TJ and GS collected the microbial mats from the wall of the open pit of the Venetia mine, cultivated the microbial mats, conducted RNA sequence and interpreted the data. All authors contributed to the article and approved the submitted version.

Acknowledgments

This thesis is conducted by the Environmental Economic Geology Laboratory (EEGL) in the Department of Earth and Atmospheric Sciences, the University of Alberta. This project was supported by De Beers Group Services to Prof. Sasha Wilson. Further support for this project was provided by the Natural Resources Canada Clean Growth Program and the Grantham Foundation for Protection of the Environment to Prof. Sasha Wilson, Mitacs to Profs. Sasha Wilson and Nina Zeyen, the Canada Research Chairs Program to Prof. Sasha Wilson and the Natural Sciences and Engineering Research Council of Canada to Prof. Sasha Wilson.

I am profoundly grateful to have been awarded the University Graduate Fellowship from The University of Alberta. I arrived in Edmonton at the end of August 2018, and as I can recall, just two weeks later on September 12th, Edmonton experienced its first snowfall of the year. At one moment, I thought I might freeze in this place. However, having been Canada for over five years, I will always cherish the memories of the snow-covered campus, the evening rainbows following the rain outside my window, the aurora borealis over the river valley, the fruit-laden trees in front of the Tory building each early summer, and the ubiquitous, blooming dandelions. There's a saying in Chinese, "The flowers may be similar year after year, but the people change." The time has come for me to bid farewell to the University of Alberta. In the years to come, I might be forgotten, but the paths I walked on this small patch of land and the stairs I climbed will continue to be traversed by others.

I would like to acknowledge the many people who contributed to contributed to this thesis. Foremost among them is my supervisor, Sasha Wilson. Throughout these years, Sasha has provided me with invaluable support, not just academically, but also in life and in spirit. Before coming to Canada, I could not even speak English well. Thanks for taking on me as your PhD student, Sasha! Besides, the penguins in Melbourne, the beaches of Hawaii, Chicago's deep-dish pizza, the safari in South Africa, and the diamond mines of Botswana–these unforgettable memories would not have been possible without Sasha's backing. As a mentor, Sasha has always been earnestly responsible for everyone in the laboratory. I will never forget the taste of candies and coffee in our lab. When the pandemic forced the lab to close, Sasha was busier than anyone, concerned not only with the lab's adjustments but more importantly, with everyone's physical and mental well-being. From Sasha, I have learned not only what it means to be a true scientist but also how to be a better person. No matter where I go in the years ahead, even if it's halfway across the world, I will always cherish the mentor-student bond we shared.

Prof. Nina Zeyen, my co-supervisor, thanks for teaching me so much. From operating the Scanning Electron Microscopy (SEM), analyzing with the Transmission Electron Microscopy (TEM), to operating various synchrotron instruments, your guidance over these five years has been invaluable. I apologize for inadvertently passing on the flu to you after returning from Melbourne, and I'll never forget our consecutive all-nighters at the Canadian Light Source in Saskatoon with Avni Patel and Maria Arizaleta. Those days of setting up experimental apparatus together in Johannesburg, donning our rainbow-colored lab coats and moon suits, and performing autoclaving will always be cherished memories.

I am deeply thankful to every member of EEGL. Bizhou Zhu, I will always cherish our times together attending classes, studying, and preparing to meet various deadlines. Thank you, Maija Raudsepp, for teaching me how to run Phreeqc in batches and for instructing me on alkalinity measurements. My thanks also go to Connor Turvey, Jie Cheng, Maria Arizaleta, Makoto Honda-McNeil, and Wyatt Russell for their assistance with my experimental sampling and sample analysis. A special thanks to Konstantin Von Gunten and Daniel Alessi from the Department of Earth and Atmospheric Sciences! Konstantin, your guidance on operating the Inductively Coupled Plasma Mass Spectrometry (ICP-MS) and conducting digestion processes has been invaluable. And Daniel Alessi, one of my committee members, thank you for advising me on setting up column experiments and the potential impact of physical properties on the results. Additionally, thanks to Rebecca Funk and Mark Labbe from the Department of Earth and Atmospheric Sciences for their technical support throughout the five years. Jessica Hamilton, thank you for your invaluable time and effort in teaching me how to operate the MIN3P software. Your assistance in running my samples using X-ray Fluorescence Microscopy (XFM) and X-ray Absorption Spectroscopy (XAS) at the Australian Synchrotron (ANSTO) was of great importance to my research. This thesis would not have been possible without all of your help.

I would like to express my thanks to the team at Trent University. My sincere thanks go to Amanda Stubbs, Carlos Paulo, and Prof. Ian Power for their invaluable assistance in setting up my experimental apparatus in Johannesburg. Special appreciation goes to Carlos Paulo and Kwon Rausis for their dedication in analyzing over a hundred of my samples. Prof. Ian Power, I always recall our gatherings and the various contests we engaged in, and I genuinely miss those moments. Also thanks to Khangeziwe Senzani and Senzeni Ndlovu from De Beers Group Technology, as well as Andrew Vietti from Vietti Slurrytec, for their invaluable support with the sampling in my pilot experiments in Johannesburg. Additionally, I wish to express my sincere thanks to Sarah McLean, Malcolm Thurston, and Kirsten Hund from De Beers, along with Alison Shaw from Lorax Environmental, for their support and for granting us access to samples from GK. I am also grateful to Frank Marasco, Tom Jones, and Daralyn Fox of WHY Resources, who not only supported this project but also provided access to Record Ridge.

Yi Wan, my best friend in Edmonton and roommate for five years, thank you for your care throughout our time together. I am grateful for always including me on your supermarket trips throughout the last five years. I will never forget our exhilarating white-water rafting adventures, skiing in Banff at -40 °C, our New Year's travels to Vancouver and Victoria, and countless explorations of new places. These memories will remain among my most cherished treasures.

Finally, I extend my deepest gratitude to my parents, brother, sister-in-law, and nephew. During the pandemic, there was a period of over three years when I couldn't return to China to reunite with you, and I was filled with guilt when I finally did and saw how much my parents had aged. Thanks to my brother and sister-in-law, your care for our whole family during these years allowed me to pursue my studies abroad with a peaceful mind. Mom and Dad, I am immensely thankful for your patience over the past two decades, your unconditional support and respect for all my decisions. Thank you for never treating me as an extension of yourselves, but as an independent individual.

Looking forward to a smooth future. I hope this aspiration is more than just a wish. Don't stop running, and don't look back at the path taken. As much as the journey behind is cherished, there is still so much to anticipate ahead.

Table of Contents

List of Tables

List of Figures

Chapter 1

Introduction

1.1 Climate change and increasing atmospheric CO_2

In the 21st century, global warming has emerged as one of the most critical environmental challenges, significantly driven by human activities. Since the industrial revolution, the concentration of atmospheric carbon dioxide (CO_2) has surged from 280 ppm to over 420 ppm, mainly due to the extensive use of fossil fuels such as coal, petroleum, and natural gas (Lacis et al., 2010; IPCC, 2018, 2022, 2023; NOAA, 2023). This increase in greenhouse gases, coupled with deforestation and industrial processes, has led to a rise in global average surface temperature by approximately 1.1 °C above pre-industrial levels (IPCC, 2023). It is expected that the temperature will have risen by at least 1.5 °C by 2030, continuing the long-term alteration of Earth's climate (IEA, 2021; IPCC, 2023). Although improvements in energy efficiency have restrained growth in demand for electricity and fossil fuels, demand is still increasing and fossil fuels will likely remain the primary energy source until 2050 (IEA, 2021). Moreover, the greenhouse gas (GHG) emissions during 2010–2019 were higher than in any previous decade, despite a deceleration in the rate of growth of mean annual GHG emissions (IPCC, 2023). This ongoing reliance on fossil fuels and the resultant GHG emissions have accelerated global warming, leading to severe consequences such as rising sea levels, extreme weather events, biodiversity loss, and threats to food and water security (IPCC, 2023). Consequently, achieving net zero CO_2 emissions is no longer sufficient; it is urgent to actively remove between 100–1000 Gt of CO_2 from the atmosphere by the century's end to limit climate warming to below 2 °C (IPCC, 2018). Addressing these challenges requires not only a decrease in anthropogenic CO_2 emissions but also the development and implementation of effective decarbonization technologies and strategies to mitigate global warming's impacts and stabilize Earth's climate.

1.2 Carbon mineralization as a CO_2 mitigation strategy

Carbon mineralization, recognized as a secure and long-term method for storing CO_2, involves chemical reactions between CO_2 and silicate or hydroxide minerals rich in alkaline earth metals (Seifritz, 1990; Lackner et al., 1995). As a Carbon Dioxide Removal (CDR) strategy, carbon mineralization is highly regarded due to its ability to permanently and safely store large volumes of CO_2 in an environmentally friendly manner, making it a promising solution for mitigating atmospheric CO_2 levels. During carbon mineralization, atmospheric CO_2 undergoes a natural process of dissolution, forming aqueous bicarbonate (HCO_3^-) and carbonate (CO_3^{2-}) ions that react with divalent metal cations such as Mg^{2+} and Ca^{2+} to precipitate stable carbonate minerals. This reaction is thermodynamically favorable and occurs spontaneously during the weathering of mafic and ultramafic rocks, which are rich in Mg- and Ca-bearing minerals (as reviewed by Power et al., 2013a). A key focus of both experimental and field studies has been to investigate the reactivity of Mg- or Ca-bearing hydroxides and silicates including brucite [$Mg(OH)_2$], wollastonite ($CaSiO_3$), forsteritic olivine (Mg_2SiO_4), and serpentine group minerals [$Mg_3Si_2O_5(OH)_4$], as well as other minerals such as anorthite ($CaAl_2Si_2O_8$), in facilitating this process (*e.g.,* Assima et al., 2014; Harrison et al., 2013; Haug et al., 2010; Gadikota et al., 2014; Park and Fan, 2004; Hamilton et al., 2018; Munz et al., 2012).

Traditional carbon capture and storage (CCS) techniques focus on utilizing geological formations for CO_2 storage, generating economic benefits that can partially offset the costs of sequestration (Lackner, 2003). One such application involves CO_2 injection for enhanced oil recovery (EOR) in oil fields, which simultaneously leads to CO_2 sequestration in sedimentary reservoirs (Thomas, 2008). Alternatively*, in situ* carbon sequestration involves the transportation and deep subsurface injection of CO_2 (*e.g.,* into basalt formations for the Carbfix project), facilitating carbon mineralization and thus storing industrial CO_2 emissions (Gislason et al., 2010; Matter et al., 2016). Two large-scale field trials of *in situ* carbon sequestration have been conducted: Wallula in Washington State and CarbFix in Iceland, both of which have successfully mineralized CO_2 in geological formations. In the Wallula project in Washington State, USA, around 60 % of the injected CO_2 was sequestered through mineralization within two years (White et al., 2020). Meanwhile, the CarbFix project in Iceland achieved 95% mineralization in its pilot phase and has continued to mineralize over 60 % of injected CO_2 in larger-scale industrial operations, demonstrating the feasibility of safe and permanent carbon storage in basalt formations (Matter et al., 2016; Clark et al., 2020). In contrast, traditional *ex situ* carbon sequestration envisioned the use of utilize minerals such as wollastonite and ultramafic rocks containing olivine [$(Mg, Fe)_2SiO_4$] or serpentine group minerals for carbon mineralization in high-temperature and pressure reactors, with power plants near ultramafic rock deposits serving as potential CO_2 sources (Gerdemann et al., 2007).

1.3 Carbon mineralization within mine residues

Ultramafic mine residues have been studied in detail as feedstocks for a lower-energy style of *ex situ* carbon mineralization owing to their high surface area, reactivity with CO_2 and the prospect to valorize these wastes (*e.g.,* Wilson et al., 2006, 2009a, 2009b, 2010, 2014; Pronost et al., 2011; Bobicki et al., 2012; Lechat et al., 2016; Turvey et al., 2017, 2018; Hamilton et al., 2018, 2020; Mervine et al., 2018). Wilson et al. (2014) determined that passive carbonation offsets 11 % of the annual CO_2 emissions at the Mount Keith Ni mine in Western Australia. The major limitations on the rate of passive carbonation in mine tailings are dissolution of silicate minerals and the supply of CO_2 (Park and Fan, 2004; Power et al., 2013a, 2013b). The rate and amount of CO_2 sequestration can thus be increased by (1) enhancing dissolution of ultramafic mine tailings using stronger acids than the carbonic acid contained in rainwater and (2) increasing the supply of CO_2 into tailings or tailings leachates using high-CO_2 gases or bioreactors (*e.g.,* Harrison et al., 2013; McCutcheon et al., 2017; Hamilton et al., 2020; Wang et al., 2021a, 2021b).

Recently, Bullock et al. (2021) estimated ~1.1–4.5 Gt CO_2 could be captured annually by enhanced weathering of silicate mine tailings, ranging from 31–125 % of the industry's primary emissions. Globally, alkaline mineral wastes could be used to remove between 2.9 and 8.5 billion tonnes of CO_2 per year by 2100 (Renforth, 2019). Complete carbonation of the ~0.11−0.28 Mt/year of brucite [$Mg(OH)_2$] produced in tailings at the Mount Keith nickel mine, Western Australia, would sequester ~81–210 kt CO_2/year and offset ~22−57 % of the operation's CO_2 equivalent (CO_2e) emissions (Harrison et al., 2013). An average annual sequestration of 270–300 t of modern atmospheric CO_2 has been measured in kimberlite mine residues at the Diavik diamond mine, Northwest Territories, Canada (Wilson et al., 2011). Passive weathering of silicate minerals in processed kimberlite at Diavik provides a ~0.2 % offset of the mine's annual emissions of 162,000 t CO_2e. Combining carbon mineralization with biomass production utilizing a redesign of the tailings storage facilities at Diavik, could offer an estimated 2.5 % CO_2 offset of the mine's greenhouse gas emissions (Power et al., 2011). Results of more recent experimental studies of carbon mineralization at the Venetia diamond mine (South Africa) show that different carbonation strategies should be employed based on the mineralogy of processed kimberlites (*e.g.,* Mervine et al., 2018; Paulo et al., 2021; Zeyen et al., 2022; Stubbs et al., 2022).

Meanwhile, carbon mineralization has several useful co-benefits for mining operations. For instance, Power et al. (2021) demonstrated that brucite carbonation can be used to cement and stabilize serpentinite mine residues thereby protecting against dam failures. Microbially-mediated carbonation processes have also been shown to accelerate dissolution of chrysotile and to cement these asbestiform fibers in a way that minimizes windblown dust (McCutcheon et al., 2016, 2017). Concurrent carbon mineralization with enhanced recovery of critical metals, such as Ni and Co, which are needed for production and storage of renewable energy, has the potential to increase global metal production from carbon neutral or carbon negative mines (Hamilton et al., 2020; Khan et al., 2021; Wang and Dreisinger, 2022).

1.4 Motivation for this thesis

Kimberlites are well-suited for carbon mineralization due to their mineralogy and high Mg- and Ca-rich composition (Bodénan et al. 2014). However, they also represent some of the most complex, heterogeneous, and altered ultramafic rocks utilized in CO_2 sequestration, presenting unique challenges in understanding and harnessing their potential for carbon storage. Meanwhile, although carbon mineralization has been a subject of research for over three decades, the behavior and distribution of valuable transition metals such as Ni and Co during the carbonation process have only recently begun to be extensively studied (Hamilton et al., 2018). The first aim of this thesis is to develop a precise and accurate method for Quantitative Phase Analysis (QPA) in kimberlites. This development is crucial for reliably quantifying the carbonation potential and determining the actual capacity for CO_2 storage within kimberlite mine residues. By establishing a more accurate QPA approach, we can gain deeper insights into the effectiveness of kimberlite as a medium for carbon sequestration. Secondly, this thesis explores the potential to accelerate the reactivity of kimberlites for carbon mineralization, particularly through the utilization of an acid leaching method. Thirdly, this thesis aims to thoroughly investigate the behavior and mobility of transition metals, such as Ni, during enhanced weathering processes using ultramafic mine residues or rocks. This investigation applies samples from three distinct types of diamond mines or serpentinite-hosted ore deposits, providing a comprehensive understanding of how transition metals behave and migrate during the acid-leaching step of the carbonation process. This aspect of the research is particularly significant for assessing the environmental impacts and potential recovery of valuable transition metals during the carbonation of ultramafic rocks. Fourthly, the thesis presents the implementation of a large-scale, microbially-mediated carbonation trial using acid leaching and cation exchange leachates from kimberlite mine residues, offering a practical perspective on the application of these techniques in a real-world setting.

1.5 Organization of this thesis

This thesis is composed of four research manuscripts investigating the accelerated weathering and carbon mineralization of ultramafic mine residues, particularly focusing on the impact of specific mineralogy and the migration of transition metals. Additionally, it explores the implementation of carbon mineralization on a larger scale using processed kimberlite. The second chapter of this thesis (Chapter 2) establishes the foundation for this study by integrating the Partial Or No Known Crystal Structure (PONKCS) method with the Rietveld method using X-ray diffraction (XRD) patterns. This integration facilitates quantitative phase analysis and allows for the prediction of a rock's reactivity to CO_2 and the quantification of its carbon mineralization potential. This methodological approach is then applied throughout the subsequent chapters (Chapters 3, 4, and 5) of the thesis. Chapter 3 presents the migration of transition metals and potential for carbon mineralization during acid leaching of processed kimberlite from the Venetia diamond mine, South Africa. In Chapter 4, we explore the influence of specific mineralogy on the accelerated weathering and carbon mineralization potential, utilizing three distinct ultramafic materials sourced from the Gahcho Kué diamond mine (North West Territories, Canada) and the Record Ridge project (British Columbia, Canada). Chapter 5 scales up the process of microbially-mediated carbonation, employing acid leaching and cation exchange leachates derived from kimberlite mine residues at the Venetia diamond mine. This chapter aims to demonstrate the feasibility and effectiveness of this approach on a larger scale. Brief descriptions of these manuscript-style chapters are as follows.

Chapter 2 addresses the challenge of quantifying lizardite and smectites in kimberlite, which are CO_2-reactive but structurally disordered, making them difficult to analyze with standard Rietveld methods. The research employs the Partial Or No Known Crystal Structure (PONKCS) method to model the peak profiles of smectite and lizardite, considering turbostratic stacking disorder in synthetic kimberlite samples. We utilize lizardite and montmorillonite PONKCS models, tested on XRD patterns from three different diffractometers, including two similar models from one manufacturer and another from a different manufacturer. Five synthetic kimberlite samples of known composition were used to evaluate the accuracy of these PONKCS models across the three XRD instruments. We also explore the sensitivity of the PONKCS method to variations in instrument geometry. This manuscript has been submitted to the journal *American Mineralogist* and is currently under review after the resubmission of our corrected version.

Chapter 3 (published in *Applied Geochemistry*) describes the carbonation potential of ultramafic mine residues as a permanent solution for sequestering excess atmospheric CO_2, with a particular focus on processed kimberlite from the Venetia mine in South Africa. This research is also significant for its examination of the recovery of critical metals, such as nickel, during carbon mineralization of mine tailings. In the conducted experiments, processed kimberlite was subjected to daily treatment with one pore volume of either deionized water or varying concentrations of hydrochloric acid (ranging from 0.04 M to 0.16 M) over a period of 28 days and the assessment of carbonation potential and the mobility of transition metals such as nickel was carried out using a comprehensive suite of techniques. The results indicate the sources of Ca, Mg and Ni the during acid leaching process and their concentrations are used to calculate the CO_2 offset potential achievable if the technique were scaled up. Notably, while higher concentrations or volumes of acid could enhance the potential for offsetting emissions through Mg-phyllosilicates in kimberlite, it is crucial to account for and recarbonate the CO_2 released by calcite dissolution to maximize the overall effectiveness of this carbonation process.

Chapter 4 studies three distinct ultramafic materials through acid leaching in column experiments. This study assessed the impact of mineralogy on carbon mineralization potential. The materials tested included one processed kimberlite residue sample (GK) from the Gahcho

Kué diamond mine in Northwest Territories, Canada, and two serpentinite rock samples (RRP1 and RRP2) from the Record Ridge project in British Columbia, Canada. Each of these samples was treated daily with 16.6 mL of 0.12 M HCl over a period of 28 days. The GK residue sample was characterized by a variety of minerals, listed in order of abundance, including lizardite, saponite, phlogopite, albite, orthoclase, augite, a small amount of calcite (1.4 wt.%), and no brucite. In contrast, the serpentinite rock samples both exhibited high concentrations of lizardite and olivine (forsterite). RRP1 contained similar amounts of these two minerals (around 34 wt.%), while RRP2 was primarily composed of lizardite (64 wt.%) with a smaller forsterite content (less than 10 wt.%). Notably, neither RRP sample contained calcite, but both had minor amounts of brucite. This diverse mineralogical composition resulted in significantly different leachate compositions across the samples. Interestingly, a divergent pH trend was observed for the replicate RRP2 columns treated with acid. The study reaffirms the concurrent importance of chemical and physical attributes in the accurate prediction and optimization of carbon mineralization.

Chapter 5 focuses on the application of acid leaching and cation exchange for carbon mineralization at a larger scale utilizing processed kimberlites from the Venetia mine for one-year-long field trials. The processed kimberlites, characterized by their high content of Mg- and Ca-rich smectites, make them ideal for a cation exchange method. This method employs less preferred cations such as NH_4^+ to release Mg^{2+} and Ca^{2+} from the interlayer spaces of smectites during the leaching process, thereby minimizing the dissolution of primary carbonates. The field experiments were conducted using four leaching reactors, each containing approximately 850 kg of kimberlite residues. These reactors were treated weekly for six weeks with various solutions including tap water, 0.12 M HCl, 1 M ammonium acetate (NH_4OAc), and 1 M ammonium chloride (NH_4Cl). The leachates from each of these four leaching reactors were split into two 1400-L carbonation containers, and the carbonation reactions within these containers were monitored for one year. A unique aspect of this study was the employment of a microbial consortium, cultured from the Venetia mine's open pit, to facilitate microbially-mediated carbonation in one of the two carbonation containers used for each type of treatment. The other carbonation container served as an evaporative control. Comparing the results with Stubbs et al. (2022) and Paulo et al. (2023), which estimated a passive carbonation potential at Venetia of

~1.0–1.5% CO_2 offset, this microbially-mediated approach suggests the possibility of doubling these rates.

In Chapter 6, we present a comprehensive summary of the most significant findings obtained throughout this thesis. A detailed discussion regarding the implications of these results, including their relevance and potential impact is provided. Based on the conclusions drawn from this thesis, we offer insightful recommendations and perspectives for future research directions.

1.6 Chapter 1 references

Assima, G.P., Larachi, F., Molson, J., and Beaudoin, G., 2014. Impact of temperature and oxygen availability on the dynamics of ambient CO_2 mineral sequestration by nickel mining residues. Chemical Engineering Journal, 240, pp.394-403.

Bobicki, E.R., Liu, Q., Xu, Z., and Zeng, H., 2012. Carbon capture and storage using alkaline industrial wastes. Progress in Energy and Combustion Science, 38(2), pp.302-320.

Bodénan, F., Bourgeois, F., Petiot, C., Augé, T., Bonfils, B., Julcour-Lebigue, C., Guyot, F., Boukary, A., Tremosa, J., Lassin, A., and Gaucher, E.C., 2014. Ex situ mineral carbonation for CO2 mitigation: Evaluation of mining waste resources, aqueous carbonation processability and life cycle assessment (Carmex project). Minerals Engineering, 59, pp.52-63.

Bullock, L.A., James, R.H., Matter, J., Renforth, P., and Teagle, D.A., 2021. Global carbon dioxide removal potential of waste materials from metal and diamond mining. Frontiers in Climate, 3, p.694175.

Clark, D.E., Oelkers, E.H., Gunnarsson, I., Sigfússon, B., Snæbjörnsdóttir, S.Ó., Aradottir, E.S., and Gíslason, S.R., 2020. CarbFix2: CO_2 and H_2S mineralization during 3.5 years of continuous injection into basaltic rocks at more than 250 °C. Geochimica et Cosmochimica Acta, 279, pp.45-66.

Gadikota, G., Matter, J., Kelemen, P., and Park, A.H.A., 2014. Chemical and morphological changes during olivine carbonation for CO_2 storage in the presence of NaCl and $NaHCO_3$. Physical Chemistry Chemical Physics, 16(10), pp.4679-4693.

Gerdemann, S.J., O'Connor, W.K., Dahlin, D.C., Penner, L.R., and Rush, H., 2007. Ex situ aqueous mineral carbonation. Environmental Science & Technology, 41(7), pp.2587-2593.

Gislason, S.R., Wolff-Boenisch, D., Stefansson, A., Oelkers, E.H., Gunnlaugsson, E., Sigurdardottir, H., Sigfusson, B., Broecker, W.S., Matter, J.M., Stute, M., and Axelsson, G.,

2010. Mineral sequestration of carbon dioxide in basalt: A pre-injection overview of the CarbFix project. International Journal of Greenhouse Gas Control, 4(3), pp.537-545.

Hamilton, J.L., Wilson, S., Morgan, B., Turvey, C.C., Paterson, D.J., Jowitt, S.M., McCutcheon, J., and Southam, G., 2018. Fate of transition metals during passive carbonation of ultramafic mine tailings via air capture with potential for metal resource recovery. International Journal of Greenhouse Gas Control, 71, pp.155-167.

Hamilton, J.L., Wilson, S., Morgan, B., Harrison, A.L., Turvey, C.C., Paterson, D.J., Dipple, G.M., and Southam, G., 2020. Accelerating mineral carbonation in ultramafic mine tailings via direct CO_2 reaction and heap leaching with potential for base metal enrichment and recovery. Economic Geology, 115(2), pp.303-323.

Harrison, A.L., Power, I.M., and Dipple, G.M., 2013. Accelerated carbonation of brucite in mine tailings for carbon sequestration. Environmental Science & Technology, 47(1), pp.126-134.

Haug, T.A., Kleiv, R.A., and Munz, I.A., 2010. Investigating dissolution of mechanically activated olivine for carbonation purposes. Applied Geochemistry, 25(10), pp.1547-1563.

International Energy Agency., 2021. World Energy Outlook 2021: Executive Summary. VGB PowerTech, 101. (Accessed 13 March 2023).

IPCC (Intergovernmental Panel on Climate Change)., 2018. Global Warming of 1.5°C. An IPCC Special Report on the impacts of global warming of 1.5°C above preindustrial levels and related global greenhouse gas emission pathways. In: The context of strengthening the global response to the threat of climate change, sustainable development, and efforts to eradicate poverty. (Accessed 13 March 2023).

IPCC., 2022. Climate Change 2022: Impacts, Adaptation and Vulnerability. (Accessed 13 March 2023).

IPCC, 2023. Climate Change 2023: Synthesis Report. A Report of the Intergovernmental Panel on Climate Change. (Accessed 10 September 2023).

Khan, S., Wani, O.B., Shoaib, M., Forster, J., Sodhi, R.N., Boucher, D., and Bobicki, E.R., 2021. Mineral carbonation for serpentine mitigation in nickel processing: a step towards industrial carbon capture and storage. Faraday Discussions, 230, pp.172-186.

Lacis, A.A., Schmidt, G.A., Rind, D., and Ruedy, R.A., 2010. Atmospheric CO_2: Principal control knob governing Earth’s temperature. Science, 330(6002), pp.356-359.

Lackner, K.S., Wendt, C.H., Butt, D.P., Joyce Jr, E.L., and Sharp, D.H., 1995. Carbon dioxide disposal in carbonate minerals. Energy, 20(11), pp.1153-1170.

Lackner, K.S., 2003. A guide to CO_2 sequestration. Science, 300(5626), pp.1677-1678.

Lechat, K., Lemieux, J.M., Molson, J., Beaudoin, G., and Hébert, R., 2016. Field evidence of CO_2 sequestration by mineral carbonation in ultramafic milling wastes, Thetford Mines, Canada. International Journal of Greenhouse Gas Control, 47, pp.110-121.

Matter, J.M., Stute, M., Snæbjörnsdottir, S.Ó., Oelkers, E.H., Gislason, S.R., Aradottir, E.S., Sigfusson, B., Gunnarsson, I., Sigurdardottir, H., Gunnlaugsson, E., and Axelsson, G., 2016. Rapid carbon mineralization for permanent disposal of anthropogenic carbon dioxide emissions. Science, 352(6291), pp.1312-1314.

McCutcheon, J., Wilson, S., and Southam, G., 2016. Microbially accelerated carbonate mineral precipitation as a strategy for in situ carbon sequestration and rehabilitation of asbestos mine sites. Environmental Science & Technology, 50(3), pp.1419-1427.

McCutcheon, J., Turvey, C.C., Wilson, S., Hamilton, J.L., and Southam, G., 2017. Experimental deployment of microbial mineral carbonation at an asbestos mine: Potential applications to carbon storage and tailings stabilization. Minerals, 7(10), p.191.

Mervine, E.M., Wilson, S., Power, I.M., Dipple, G.M., Turvey, C.C., Hamilton, J.L., Vanderzee, S., Raudsepp, M., Southam, C., Matter, J.M., and Kelemen, P.B., 2018. Potential for offsetting diamond mine carbon emissions through mineral carbonation of processed kimberlite: an assessment of De Beers mine sites in South Africa and Canada. Mineralogy and Petrology, 112, pp.755-765.

Munz, I.A., Brandvoll, Ø., Haug, T.A., Iden, K., Smeets, R., Kihle, J., and Johansen, H., 2012. Mechanisms and rates of plagioclase carbonation reactions. Geochimica et Cosmochimica Acta, 77, pp.27-51.

NOAA (National Oceanic and Atmospheric Administration)., 2022. Global monthly mean CO_2. (Accessed 13 March 2023).

Park, A.H.A., and Fan, L.S., 2004. CO_2 mineral sequestration: physically activated dissolution of serpentine and pH swing process. Chemical Engineering Science, 59(22-23), pp.5241-5247.

Paulo, C., Power, I.M., Stubbs, A.R., Wang, B., Zeyen, N., and Wilson, S., 2021. Evaluating feedstocks for carbon dioxide removal by enhanced rock weathering and CO_2 mineralization. Applied Geochemistry, 129, p.104955.

Paulo, C., Power, I.M., Zeyen, N., Wang, B., and Wilson, S., 2023. Geochemical modeling of CO_2 sequestration in ultramafic mine wastes from Australia, Canada, and South Africa: Implications for carbon accounting and monitoring. Applied Geochemistry, 152, p.105630.

Power, I.M., Wilson, S., Small, D.P., Dipple, G.M., Wan, W., and Southam, G., 2011. Microbially mediated mineral carbonation: roles of phototrophy and heterotrophy. Environmental Science & Technology, 45(20), pp.9061-9068.

Power, I.M., Harrison, A.L., Dipple, G.M., Wilson, S., Kelemen, P.B., Hitch, M., and Southam, G., 2013a. Carbon mineralization: from natural analogues to engineered systems. Reviews in Mineralogy and Geochemistry, 77(1), pp.305-360.

Power, I.M., Wilson, S., and Dipple, G.M., 2013b. Serpentinite carbonation for CO_2 sequestration. Elements, 9(2), pp.115-121.

Power, I.M., Paulo, C., Long, H., Lockhart, J.A., Stubbs, A.R., French, D., and Caldwell, R., 2021. Carbonation, cementation, and stabilization of ultramafic mine tailings. Environmental Science & Technology, 55(14), 10056-10066.

Pronost, J., Beaudoin, G., Tremblay, J., Larachi, F., Duchesne, J., Hébert, R., and Constantin, M., 2011. Carbon sequestration kinetic and storage capacity of ultramafic mining waste. Environmental Science & Technology, 45(21), pp.9413-9420.

Renforth, P. 2019. The negative emission potential of alkaline materials. Nature communications, 10(1), 1401.

Seifritz, W., 1990. CO_2 disposal by means of silicates. Nature, 345, pp.486-486.

Stubbs, A.R., Paulo, C., Power, I.M., Wang, B., Zeyen, N., and Wilson, S., 2022. Direct measurement of CO_2 drawdown in mine wastes and rock powders: Implications for enhanced rock weathering. International Journal of Greenhouse Gas Control, 113, p.103554.

Thomas, S., 2008. Enhanced oil recovery-an overview. Oil & Gas Science and Technology-Revue de l'IFP, 63(1), pp.9-19.

Turvey, C.C., Wilson, S., Hamilton, J.L., and Southam, G., 2017. Field-based accounting of CO_2 sequestration in ultramafic mine wastes using portable X-ray diffraction. American Mineralogist: Journal of Earth and Planetary Materials, 102(6), pp.1302-1310.

Turvey, C.C., Hamilton, J.L., and Wilson, S., 2018. Comparison of Rietveld-compatible structureless fitting analysis methods for accurate quantification of carbon dioxide fixation in ultramafic mine tailings. American Mineralogist, 103(10), pp.1649-1662.

Wang, F., Dreisinger, D., Jarvis, M., Hitchins, T., and Trytten, L., 2021a. CO_2 mineralization and concurrent utilization for nickel conversion from nickel silicates to nickel sulfides. Chemical Engineering Journal, 406, p.126761.

Wang, F., Dreisinger, D., Jarvis, M., Trytten, L., and Hitchins, T., 2021b. Application and optimization of a quantified kinetic formula to mineral carbonation of natural silicate samples. Minerals Engineering, 161, p.106712.

Wang, F., and Dreisinger, D., 2022. Carbon mineralization with concurrent critical metal recovery from olivine. Proceedings of the National Academy of Sciences, 119(32), p.e2203937119.

White, S.K., Spane, F.A., Schaef, H.T., Miller, Q.R., White, M.D., Horner, J.A., and McGrail, B.P., 2020. Quantification of CO_2 mineralization at the Wallula basalt pilot project. Environmental Science & Technology, 54(22), pp.14609-14616.

Wilson, S., Raudsepp, M., and Dipple, G.M., 2006. Verifying and quantifying carbon fixation in minerals from serpentine-rich mine tailings using the Rietveld method with X-ray powder diffraction data. American Mineralogist, 91(8-9), pp.1331-1341.

Wilson, S., Dipple, G.M., Power, I.M., Thom, J.M., Anderson, R.G., Raudsepp, M., Gabites, J.E., and Southam, G., 2009a. Carbon dioxide fixation within mine wastes of ultramafic-hosted ore deposits: Examples from the Clinton Creek and Cassiar chrysotile deposits, Canada. Economic Geology, 104(1), pp.95-112.

Wilson, S., Raudsepp, M., and Dipple, G.M., 2009b. Quantifying carbon fixation in trace minerals from processed kimberlite: A comparative study of quantitative methods using X-ray powder diffraction data with applications to the Diavik Diamond Mine, Northwest Territories, Canada. Applied Geochemistry, 24(12), pp.2312-2331.

Wilson, S., Barker, S.L., Dipple, G.M., and Atudorei, V., 2010. Isotopic disequilibrium during uptake of atmospheric CO_2 into mine process waters: Implications for CO_2 sequestration. Environmental Science & Technology, 44(24), pp.9522-9529.

Wilson, S., Dipple, G.M., Power, I.M., Barker, S.L., Fallon, S.J., and Southam, G., 2011. Subarctic weathering of mineral wastes provides a sink for atmospheric CO_2. Environmental Science & Technology, 45(18), pp.7727-7736.

Wilson, S., Harrison, A.L., Dipple, G.M., Power, I.M., Barker, S.L., Mayer, K.U., Fallon, S.J., Raudsepp, M., and Southam, G., 2014. Offsetting of CO_2 emissions by air capture in mine tailings at the Mount Keith Nickel Mine, Western Australia: Rates, controls and prospects for carbon neutral mining. International Journal of Greenhouse Gas Control, 25, pp.121-140.

Zeyen, N., Wang, B., Wilson, S., Paulo, C., Stubbs, A.R., Power, I.M., Steele-Maclnnis, M., Lanzirotti, A., Newville, M., Paterson, D.J., and Hamilton, J.L., 2022. Cation exchange in smectites as a new approach to mineral carbonation. Frontiers in Climate, 4.

Chapter 2

Quantifying the potential for mineral carbonation of processed kimberlite with the Rietveld-PONKCS method

2.1 Introduction

Global average surface temperature has increased by ~1.07 °C since 1850, primarily as a result of anthropogenic carbon dioxide (CO_2) emissions, which is causing long-term changes to Earth's climate (IPCC, 2022). Decarbonization of global energy production, capture and storage of industrial CO_2 and methane emissions, and direct removal of CO_2 from the atmosphere are required to stabilize the climate (IPCC, 2018). Carbon mineralization is one approach to Carbon Dioxide Removal (CDR) that safely stores CO_2 over geologic timescales (*e.g.*, Seifritz, 1990; Lackner et al., 1995; Lackner, 2003; Power et al., 2013). Carbon mineralization is a natural process that involves dissolution of CO_2 gas to form aqueous HCO_3^- and CO_3^{2-} that react with divalent metal cations, typically Mg^{2+} and Ca^{2+}, to precipitate carbonate minerals (*e.g.,* Lackner et al., 1995; Power et al., 2013). Mineralization of CO_2 is thermodynamically favorable and occurs spontaneously during the weathering of mafic and ultramafic rocks, which contain Mg- and Ca-rich silicate and hydroxide minerals (Power et al., 2013).

Ultramafic mine tailings have been studied in detail as feedstocks for carbon mineralization (*e.g.*, Wilson et al., 2006, 2009a, 2009b, 2010, 2014; Pronost et al., 2011; Bobicki et al., 2012; Lechat et al., 2016; Turvey et al., 2017, 2018a; Hamilton et al., 2018, 2020; Mervine et al., 2018; Power et al., 2021). Mine tailings have high reactive surface area due to ore processing, which makes them more reactive to atmospheric CO_2 than unpulverized rock (Wilson et al., 2009a). For instance, complete carbonation of the ∼0.11−0.28 Mt/year of brucite [$Mg(OH)_2$] produced in tailings at the Mount Keith nickel mine, Western Australia, would sequester ∼81–210 kt CO_2/year and offset ∼22−57 % of the operation's CO_2 equivalent (CO_2e) emissions (Harrison et al., 2013). An average annual sequestration of 270–300 t of modern atmospheric CO_2 has been measured in kimberlite mine residues at the Diavik diamond mine, Northwest Territories, Canada (Wilson et al., 2011). Passive weathering of silicate minerals in processed kimberlite at Diavik provides a ~0.2 % offset of the mine's annual emissions of 162,000 t CO_2e. Bullock et al. (2021) estimated that 31–125 % of the mining industry's primary CO_2 emissions could be captured annually by enhanced weathering of silicate mine tailings. Globally, alkaline mineral wastes could be used to remove between 2.9 and 8.5 billion tonnes of CO_2 per year by 2100 (Renforth, 2019).

Carbon mineralization has several useful co-benefits for mining operations. For instance, Power et al. (2021) demonstrated that brucite carbonation can be used to cement and stabilize serpentinite mine residues thereby protecting against dam failures. Microbially-mediated carbonation processes have also been shown to accelerate dissolution of chrysotile and to cement these asbestiform fibers in a way that minimizes windblown dust (McCutcheon et al., 2016, 2017). Concurrent mineral carbonation with enhanced recovery of critical metals, such as Ni and Co, which are needed for production and storage of renewable energy, has the potential to increase global metal production from carbon neutral or carbon negative mines (Hamilton et al., 2020; Khan et al., 2021; Wang and Dreisinger, 2022).

Quantitative phase analysis (QPA) with X-ray Diffraction (XRD) data and the Rietveld method provides a measure of the weight-percent abundance of each mineral in a sample. This is very important as the mineralogy of a feedstock material is the primary control on how much carbon it has the potential to store (*i.e.*, which Ca- and Mg-bearing minerals are present and at what abundances), and it can also be used to verify and quantify the amount of carbon stored in any carbonate minerals present, both before and after reaction (Wilson et al., 2006). The original Rietveld method provides the mathematical framework for line profile fitting using neutron or X-ray diffraction patterns (Rietveld 1967, 1969). Chung's (1974) adiabatic method (also called Reference Intensity Ratios) made it possible to quantify the abundances of minerals in multiphase mixtures from XRD patterns. These two methods were later combined so that Rietveld refinements with XRD data can be used to determine accurate unit cell parameters and phase abundances as well as approximate chemical compositions for multiphase samples (Hill and Howard, 1987; Bish and Howard, 1988). QPA with the Rietveld method requires well-defined crystal structures for all phases analyzed. However, clay minerals such as smectites and the serpentine polymorphs, which are common in CO_2-reactive ultramafic rocks, generally exhibit turbostratic disorder and thus diffraction patterns of these minerals cannot easily be fitted using the traditional Rietveld method. Although clinochlore, phlogopite, and talc can exhibit structural disorder, the degree and nature of this disorder is generally less pronounced compared to minerals like montmorillonite and lizardite. The overall crystal structure of these minerals tends to be fairly well-ordered so that the standard Rietveld approach, which is less labor-intensive, is sufficient. In contrast, Pawley's (1981) framework for unit cell refinement from powder diffraction data is a structureless fitting method that does not require prior knowledge of atomic structure and thus can be applied for pattern fitting of poorly ordered phases (*e.g.*, clay minerals) in a multiphase mixture. Wilson et al. (2006) used synthetic, serpentine-rich mine tailings to test the accuracy of the combined use of the Pawley method and an internal standard (*i.e.*, the Pawley/internal standard method) to quantify serpentine minerals as "amorphous phases". Scarlett and Madsen (2006) applied structureless fitting to the quantification of disordered phases and other phases with the Partial Or No Known Crystal Structures (PONKCS) method without the addition of an internal standard.

Turvey et al. (2017, 2018a) used the PONKCS method to model the peak profiles of serpentine minerals in synthetic serpentinites and compared the accuracy and precision of the Pawley/internal standard method and the PONKCS method for quantifying serpentine mineral abundance. Although the Pawley/internal standard method can give more accurate results, it can only quantify one poorly ordered phase and is not suitable for kimberlites containing both serpentine minerals and smectite. Turvey et al. (2017, 2018a) mainly focused on quantifying the abundances of the serpentine polymorphs, all of which have similar structures and diffraction patterns. Kimberlites can also be used as feedstocks for carbon mineralization but they are more mineralogically complex than serpentinites, with multiple disordered phases including serpentine minerals and smectites (*e.g.*, Zeyen et al. 2022; Paulo et al., 2021; Stubbs et al., 2022; Mervine et al., 2018). Therefore, if we are to accurately quantify the carbonation potential as well as the amount of CO_2 storage in kimberlite mine residues, it is important to be able to measure the abundances of smectites and serpentine minerals with accuracy.

The purpose of this study is to develop an accurate approach for QPA in kimberlites. As such, lizardite and smectite PONKCS models were made using XRD patterns collected from three different X-ray diffractometers. These models were employed to assess the accuracy of the PONKCS method using synthetic samples of processed kimberlite of known mineralogical compositions to develop an accurate methodology that can be used to calculate the carbonation potential of kimberlites. We also assessed the accuracy of Rietveld refinements with PONKCS models developed for one instrument while using data collected with another XRD to assess the portability of PONKCS models between XRD instruments.

2.2 Experimental methods

2.2.1 Rietveld-PONKCS samples

Use of the PONKCS method requires that a pure sample of the disordered phase (α) be mixed with a known amount of an internal standard (*s*) to calibrate an empirical $(ZM)_\alpha$ value for the disordered phase that can then be used in the Rietveld refinement equation (Eq. 1).

$$(ZM)_\alpha = \frac{W_\alpha}{W_s} \cdot \frac{S_\alpha}{S_s} \cdot \frac{(ZMV)_s}{V_\alpha} \quad (1)$$

Where Z is the number of formula units in the unit cell, M is the mass of the formula unit, V is the unit cell volume, W is the abundance of the phase in wt.% and S is the Rietveld scale factor for both the disordered phase, α, and the internal standard, s.

PONKCS models were prepared using XRD patterns collected from 50:50 wt.% mixtures of (1) lizardite (sourced from The University of British Columbia) and NIST 676a α-Al_2O_3; (2) Ca-exchanged montmorillonite (SWy-2 obtained from the Clay Minerals Society Source Clay Repository) and NIST 676a α-Al_2O_3; and (3) Ca-exchanged montmorillonite (SWy-2) and Baikalox Ultrapure Precision α-Al_2O_3. Two montmorillonite mixtures were made, using Baikalox α-Al_2O_3 and NIST 676a α-Al_2O_3 to enable comparison between the results from the two different PONKCS models generated. Baikalox α-Al_2O_3, while not as well characterized as the NIST 676a α-Al_2O_3, was used because it is significantly less expensive. Given that both alpha-Al_2O_3 samples used in our experiments are Baikalox corundum, the difference in the results obtained using these two samples was minimal. Consequently, we did not pursue a detailed comparison of the outcomes derived from each. Montmorillonite, a dioctahedral smectite, was used because it was not possible to obtain a sufficiently large amount of high purity saponite, which is found in kimberlites, or another trioctahedral smectite. A Ca-exchange was used to stabilize the basal (001) peak position of montmorillonite to ~15 Å (after Bish et al., 2003). *ZM* values for lizardite and montmorillonite obtained from refinement of the 50:50 wt.% mixtures of lizardite or montmorillonite with corundum were fixed in refinements for the wcskim samples.

Each of these three samples was milled using agate grinding elements for 4 minutes in anhydrous ethanol with a McCrone Micronizing Mill. Samples were then air-dried at room temperature under a fume hood. The PONKCS method (Scarlett and Madsen, 2006) was applied to model the peak profiles of montmorillonite and lizardite to account for turbostratic stacking disorder. Unit-cell parameters and space groups were obtained from Mellini and Viti (1994) for lizardite and from Viani et al. (2002) for montmorillonite as a proxy for saponite, which is most commonly found in kimberlites (O'Gorman and Kitchener, 1974; Zeyen et al., 2022). The crystal structure of corundum (α-Al_2O_3) from Brown et al. (1993) was used for Rietveld refinement.

2.2.2 Synthetic processed kimberlite samples

Five samples of synthetic kimberlite mine residues of known composition were prepared by weighing and mixing different proportions of eight pure mineral constituents that are found in processed kimberlite (*e.g.*, Mervine et al., 2018): lizardite, Ca-exchanged montmorillonite (as a proxy for saponite), calcite, quartz, clinochlore, phlogopite, brucite and talc. These samples were named the "worst-case scenario kimberlites", wcskim1, wcskim2, wcskim3, wcskim4 and wcskim5, for their high abundances of structurally disordered minerals and minerals that are prone to severe preferred orientation (Table 2.1). The lizardite and Ca montmorillonite incorporated into the synthetic kimberlite samples originate from the identical source as those utilized for the construction of the PONKCS. Although brucite is rarely present in most kimberlites, it was included in weighed mixtures because it had previously been reported from South African kimberlites (Berg, 1989; Stripp et al., 2006); however, this may be the result of clinochlore peaks having been misidentified as brucite peaks in previous XRD studies (as noted by Zeyen et al., 2022). Although minerals such as forsterite, pyroxenes and dolomite are also commonly found in kimberlites (e.g., Mervine et al., 2018), they were not used to make the synthetic kimberlite mine residues. We instead chose to focus on platy and structurally disordered minerals found in much greater abundance in kimberlites as these are the most challenging to model using Rietveld refinements.

Each wcskim sample was prepared with a mass of 2 g. The mineral phases were weighed on a scale with ± 0.1 mg precision. Each mixture was milled for 6 minutes in anhydrous ethanol with a McCrone Micronizing Mill before being air-dried at room temperature within a fume hood.

The calcite, clinochlore, phlogopite and quartz standards were at least 99 wt.% pure. The remaining mineral standards contained small amounts of other phases: (1) the montmorillonite contained 6.2 wt.% quartz, (2) the lizardite contained 1.1 wt.% calcite (Wilson et al., 2009b), (3) the talc contained 5.6 wt.% clinochlore, and (4) the brucite contained 2.8 wt.% periclase and 2.6 wt.% hydromagnesite. Mineral abundances in the weighed mixtures were recalculated to reflect the refined compositions of these standards (Table 2.1). Due to their low abundances within the brucite standard, hydromagnesite and periclase were below the detection limit in the five synthetic samples using XRD. Sources of crystal structure data for detectable mineral phases in the wcskim samples are reported in Table 2.2.

Table 2.1 Mineral abundances (wt.%) in synthetic processed kimberlite samples.

Phase/Sample name	**wcskim1**	**wcskim2**	**wcskim3**	**wcskim4**	**wcskim5**
Lizardite	59.34	49.45	34.62	19.78	9.89
Ca-montmorillonite	9.38	18.76	32.83	46.91	56.29
Calcite	5.66	5.55	5.38	5.22	5.11
Quartz	5.62	6.24	7.17	8.09	8.71
Clinochlore	5.28	5.28	5.28	5.28	5.28
Phlogopite	5.00	5.00	5.00	5.00	5.00
Brucite	4.74	4.74	4.74	4.74	4.74
Talc	4.72	4.72	4.72	4.72	4.72
Periclase	0.14	0.14	0.14	0.14	0.14
Hydromagnesite	0.13	0.13	0.13	0.13	0.13
Total	100.00	100.00	100.00	100.00	100.00

Table 2.2 Sources of crystal structure data for Rietveld refinement.

Mineral	Formula	Sources of crystal structure
Lizardite	$Mg_3Si_2O_5(OH)_4$	Mellini and Viti (1994)
Ca-montmorillonite	$Ca_{x/2}(Al_{2-y}Mg_y)Si_4O_{10}(OH)_2 \bullet nH_2O$	Viani et al. (2002)
Calcite	$CaCO_3$	Maslen et al. (1995)
Quartz	SiO_2	Glinnemann et al. (1992)
Clinochlore	$Mg_5Al(AlSi_3O_{10})(OH)_8$	Smyth (1997)
Phlogopite	$KMg_3AlSi_3O_{10}(OH)_2$	Collins and Catlow (1992)
Brucite	$Mg(OH)_2$	Catti et al. (1995)
Talc	$Mg_3Si_4O_{10}(OH)_2$	Rayner and Brown (1973)

2.2.3 Data collection

Three different XRDs were used to collect patterns from the Rietveld-PONKCS samples and the synthetic processed kimberlite samples: (1) XRD A1 was equipped with a Position Sensitive Detector (PSD), no anti-scatter screen and a cobalt source ($K\alpha 1$) with a 1.78897 Å wavelength that was operated at 38 kV and 38 mA in the Department of Earth and Atmospheric Sciences, University of Alberta. (2) XRD B1 was equipped with a PSD, a stationary anti-scatter screen and a cobalt source that was operated at 40 kV and 25 mA in the Monash X-ray Platform, Monash University. (3) XRD B2 was equipped with a high-speed PSD, a motorized anti-scatter screen and a cobalt source that was operated at 35 kV and 40 mA in the Department of Earth and Atmospheric Sciences, University of Alberta. XRDs B1 and B2 are similar models made by the same manufacturer. XRD A1 was made by a different manufacturer. The makes and models of the three XRDs are not provided here, in keeping with the journal's policy on refraining from endorsement of one brand over another. Data from all three XRDs were collected from 5–80° 2θ (XRD A1) or 3–80° 2θ (XRD B1 and B2) using a step size of 0.02° 2θ at a rate of 1.2° 2θ/minute. The total counting time was 62.5 min (XRD A1) or 64.2 min (XRD B1 and B2). Detailed information concerning the goniometer radii, divergence slit sizes, calibrated zero errors, primary Soller angles and secondary Soller angles are provided in Appendix Table A1.1.

Samples were prepared for analysis in back-loading cavity mounts and loaded against frosted glass to reduce the effects of preferred orientation. The sample thickness was at least 1 mm such that the X-ray beam would be attenuated within the volume of each sample. Mineral phase identification was conducted using the DIFFRAC.EVA XRD phase analysis software (Bruker) with reference to the International Center for Diffraction Data Powder Diffraction File 4+ database (ICDD PDF4+). Rietveld refinements (Bish and Howard, 1988; Hill and Howard, 1987; Rietveld, 1969) with XRD data were used to determine mineral abundances with TOPAS 5 (Bruker). The PONKCS method (Scarlett and Madsen, 2006) was used to model the peak profiles of montmorillonite and lizardite. Unit cell parameters, crystallite size and microstrain were refined for all phases, including those whose peak profiles were fitted using PONKCS models. A third order Chebyshev polynomial and a $1/x$ function were employed to model the background curve of data collected from XRD B2. A fourth order polynomial and $1/x$ function were used to model the background curves of data obtained from XRD A1 and XRD B1. The detection limit of most mineral phases is typically no greater than 2 wt.% for the XRD patterns (Khan et al., 2020), although amorphous phases are known to have a higher detection limit (Gualtieri, 2000). Detection limits can vary amongst minerals due to differences in microabsorption contrast and peak overlap between minerals.

The goniometer zero error and the instrumental contributions to peak shape were determined for each diffractometer by refinement using XRD patterns of NIST SRM 660b LaB6 using the fundamental parameters approach (Cheary and Coehlo, 1992). Given the accuracy to which its unit cell parameter is known and owing to its generation of Bragg peaks with negligible size or strain broadening, this standard serves as a robust basis for calibration. The calibrated zero error was held constant during refinements of unknown samples while the sample displacement was refined. Although this approach allows for accurate and precise determination of unit cell parameters and peak positions for constituent minerals, these are not reported here because only phase abundances are needed to estimate carbonation potential, which is the focus of this study.

2.3 Results

XRD patterns of the Rietveld-PONKCS samples collected from XRD A1 and XRD B2 are shown in Figure 2.1. Due to different instrument parameters, such as slit sizes, goniometer radii, and the size of detector windows, the observed peak shapes and widths produced from the same sample using different XRDs can show substantial differences. Differences in the background functions can also be seen (Figure 2.1), particularly at low 2θ values, because XRD A1 does not have an air-scatter screen (leading to increased detection of Bremßtrahlung X-rays) whereas XRD B1 and B2 do. The small amount of quartz in all samples was either present in the SWy-2 standard or, in the case of the lizardite-bearing samples, introduced during McCrone milling.

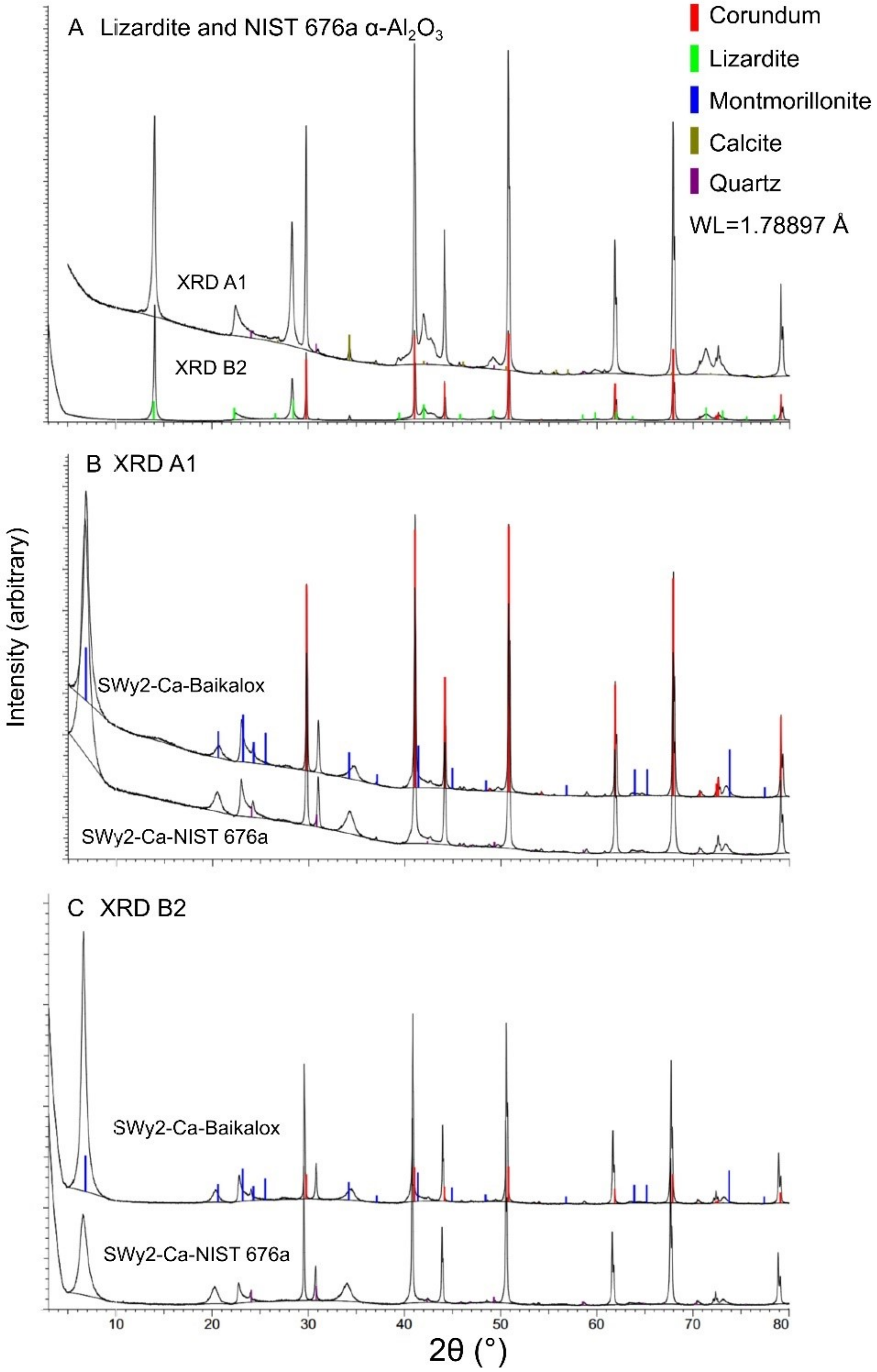

Figure 2.1 XRD patterns of Rietveld-PONKCS samples, which are 50:50 wt.% mixtures of (A) lizardite and NIST 676a α-Al_2O_3, collected using XRD A1 and XRD B2, and SWy-2 and NIST 676a α-Al_2O_3 or Baikalox α-Al_2O_3 collected using (B) XRD A1 and (C) XRD B2.

The accuracy of instrument-calibrated PONKCS models was tested using the five samples of synthetic kimberlite mine tailings. Rietveld refinement results are shown in Appendix Table A1.2. The bias between known and refined abundances for each mineral phase and the total absolute bias for all mineral phases in a sample were calculated using Eq. 2 (Omotoso et al., 2006) and are shown in Figure 2.2 and Appendix Table A1.2.

$$\text{Total absolute bias} = \sum \mathrm{abs}(W_{i,\,\text{actual}} - W_{i,\,\text{refinement}}) \qquad (2)$$

Where $W_{i,\,\text{actual}}$ is the actual weight (%) of the i^{th} mineral and $W_{i,\,\text{refinement}}$ is the refinement weight (%) of the i^{th} mineral.

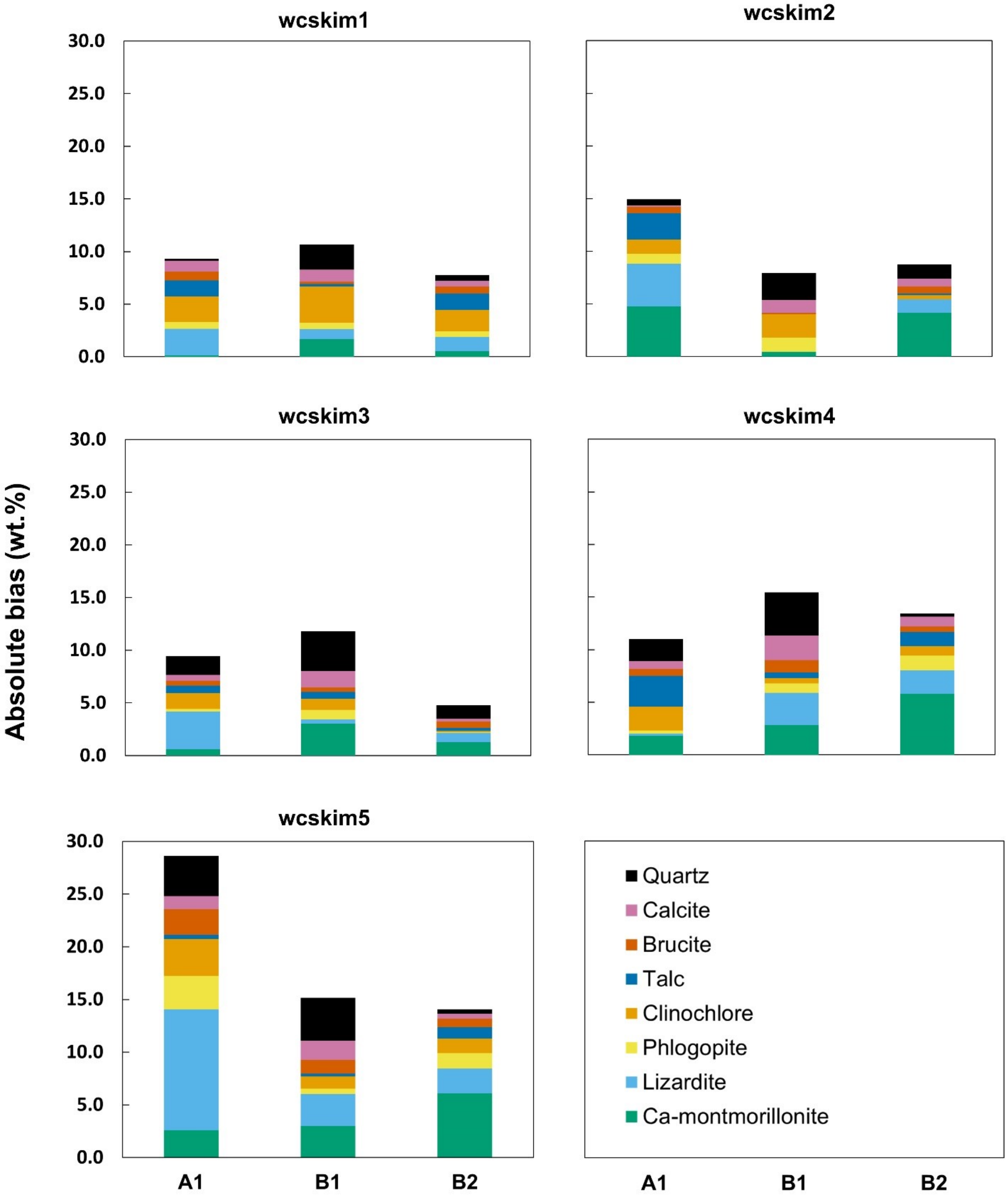

Figure 2.2 Absolute bias (wt.%) values for mineral phases in the five synthetic samples of processed kimberlite using PONKCS models that were correctly calibrated to each of the three XRDs.

Given the limitations in replicating standard samples, it was not feasible to calculate error margins for mineral abundance values presented in Figure 2.2. To address this challenge and ensure the accuracy of our findings, we instead documented the deviation between known and refined mineral quantities in Figure 2.3. This approach aligns with established best practices for quantifying accuracy in mineralogical analysis, as recommended by Bish and Howard (1988) and Hill and Howard (1987). Furthermore, by employing the absolute bias value, as defined by Omotoso et al. (2006), we provide a quantitative measure of the discrepancy between the expected and observed mineral amounts. This methodology, while not a substitute for direct error analysis, offers a transparent and methodologically sound means of assessing the precision of our mineralogical refinements within the constraints of our experimental setup.

2.3.1 XRD A1

The total absolute bias obtained from refinements using XRD data collected on XRD A1 varies from 9.3 to 28.6 wt.% (Fig. 2.2, Appendix Table A1.2) with an average of 14.6 wt.%. The amount of lizardite is consistently overestimated by 0.2–11.5 wt.% with the greatest misestimate of 11.5 wt.% occurring for the lowest abundance of lizardite (in wcskim5), a trend that has previously been observed for phases quantified using structureless pattern fitting (*e.g.,* Wilson et al., 2006). The high bias on the refined abundance of lizardite results in the high total bias in wcskim5 (28.6 wt.%). Compared with lizardite, the results for Ca-montmorillonite have a smaller range of bias values from -4.8 – +2.6 wt.% with no obvious trend relating to mineral abundance. Similarly, misestimates in the abundance of calcite show no particular trend. The abundances of clinochlore, brucite and quartz are always underestimated whereas those for talc are systematically overestimated (Fig. 2.3, Appendix Table A1.2). The abundance of phlogopite is overestimated when the abundance of montmorillonite is lowest and underestimated when it is greatest.

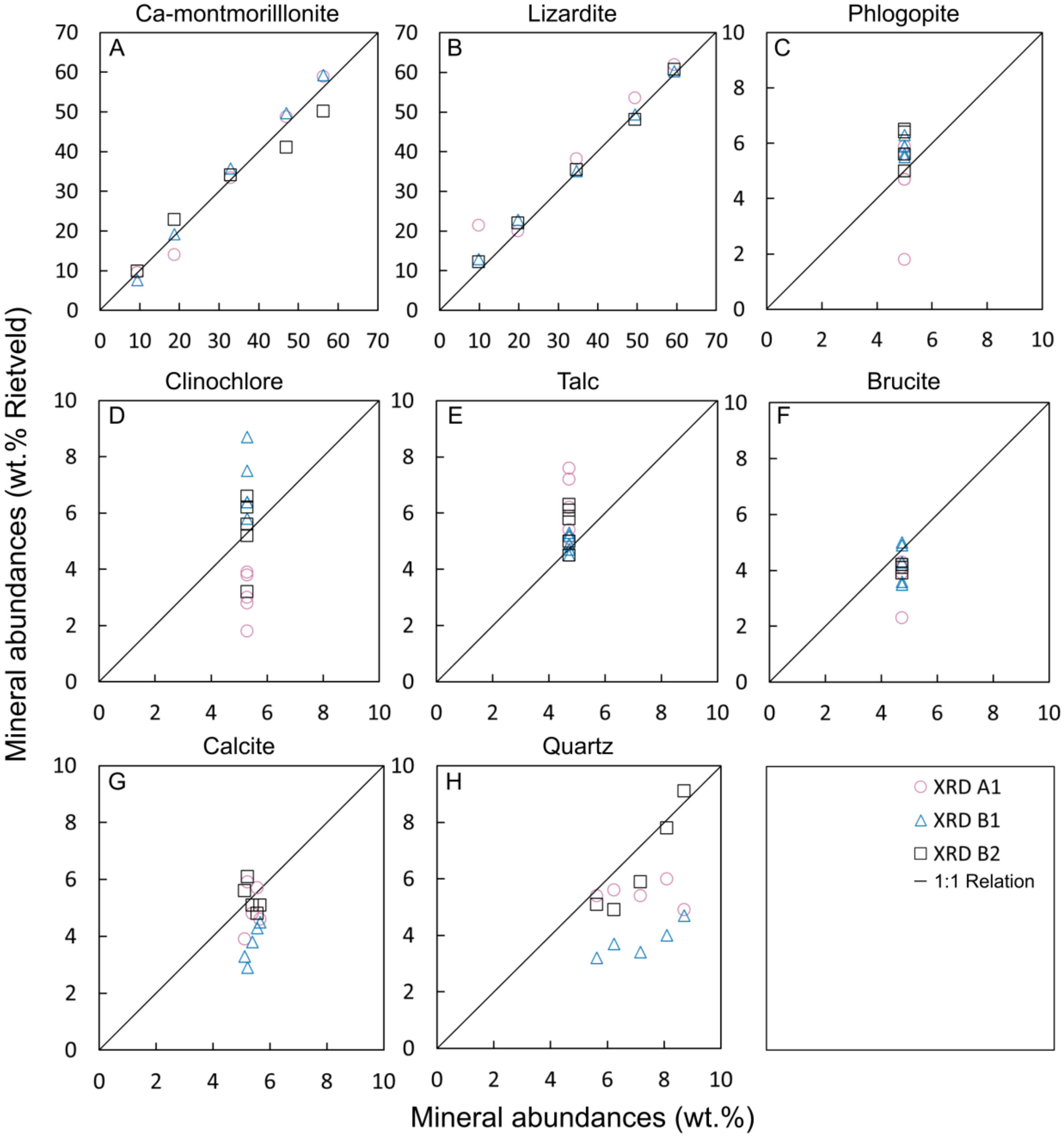

Figure 2.3 Results of Rietveld refinements for each mineral phase in the five synthetic samples of processed kimberlite using PONKCS models that were correctly calibrated to each of the three XRDs.

2.3.2 XRD B1

The total absolute bias for refinements using data from XRD B1 varies between 7.9 and 15.4 wt.% (Fig. 2.2, Appendix Table A1.2) with an average of 12.2 wt.%. As observed for XRD A1, the abundance of lizardite is systematically overestimated, with greater bias values occurring for the lowest lizardite contents; however, the range of bias values for lizardite (0–3.0 wt.%) is much smaller using XRD B1. The abundance of Ca-montmorillonite is typically overestimated (0.4–3.0 wt.%) with an underestimate of -1.7 wt.% observed only for wcskim1, which contains the least amount of this mineral. The abundances of phlogopite and clinochlore are systematically overestimated whereas those of calcite and quartz are underestimated (Fig. 2.3, Appendix Table A1.2).

2.3.3 XRD B2

Total absolute bias values for refinements with XRD B2 data vary from 4.8 to 14.1 wt.% (Fig. 2.2, Appendix Table A1.2) with an average of 9.8 wt.%. As previously observed, the abundance of lizardite is typically overestimated by 0.9 to 2.3 wt.%, with an underestimate of -1.3 wt.% occurring only for wcskim2. Refined abundances for Ca-montmorillonite are more variable, with bias results ranging from -6.1 to +4.2 wt.%, which indicates larger over- and underestimates for this phase than observed with the other two XRDs. The magnitude of misestimates for lower abundance phases is typically less than observed for the other two XRDs and there are fewer cases where the abundances of these minerals are either systematically over- or underestimated. The abundance of brucite, which is known to be 4.74 wt.%, is the exception as it is always underestimated albeit by a consistent amount of -0.8 to -0.5 wt.% (Fig. 2.3, Appendix Table A1.2).

2.3.4. Comparison of results

The Rietveld refinement results obtained using all three XRDs provide a total bias ranging from 4.2–28.6 wt.% when PONKCS models are correctly calibrated to the geometry of each instrument. Average total absolute bias values of 14.6 wt.% (XRD

A1), 12.2 wt.% (XRD B1) and 9.8 wt.% (XRD B2) are comparable with the average total absolute bias of 11.8 wt.% obtained in a previous study of 13 weighed mixtures of synthetic kimberlite mine residues (Wilson et al., 2009b) or an average of 10.3 wt.% total absolute bias value obtained using eight synthetic serpentinite mine residues (Turvey et al., 2018a). Average total absolute bias values between 10 and 15 wt.% are typically considered to be of very high accuracy for samples containing complex assemblages of clay minerals and many other low abundance phases (*e.g.*, Omotoso et al., 2006). Due to the interaction between the phlogopite (003) peak and the quartz peak, an apparent overestimation of phlogopite and underestimation of quartz were always observed in the results (Fig. 2.3, Appendix Table A1.2).

Compared with XRD A1, the peak intensities of XRD patterns are greater and resolution of the K_a and K_β peaks is better on XRD B1 and B2. This results in systematic over and underestimates in refinement residues. The relatively small difference in average bias observed amongst the three instruments is likely related in part to the absence versus presence of an air-scatter screen and differences in screen design. This becomes important owing to the large unit cells of smectites, which resultingly produce low angle peaks at ~6.8° 2θ (Co *K*α). XRD B1 is equipped with a fixed-position air-scatter screen, which allows data to be collected to lower diffraction angles than what is possible using XRD A1. Consequently, it can be seen that both lizardite and Ca-montmorillonite have visibly improved fits (Fig. 2.4B) compared to results for XRD A1 (Fig. 2.4A), which cannot be used to collect data to values <5 ° 2θ and for which it is challenging to fit the background function at low angles owing to increased detection of Bremßtrallung X-rays. The most accurate results were obtained using XRD B2 (Fig. 2.4C), which has a motorized anti-scatter screen that allows for both improved background attenuation at the lowest 2θ angles and optimized detection of diffracted X-rays at greater angles.

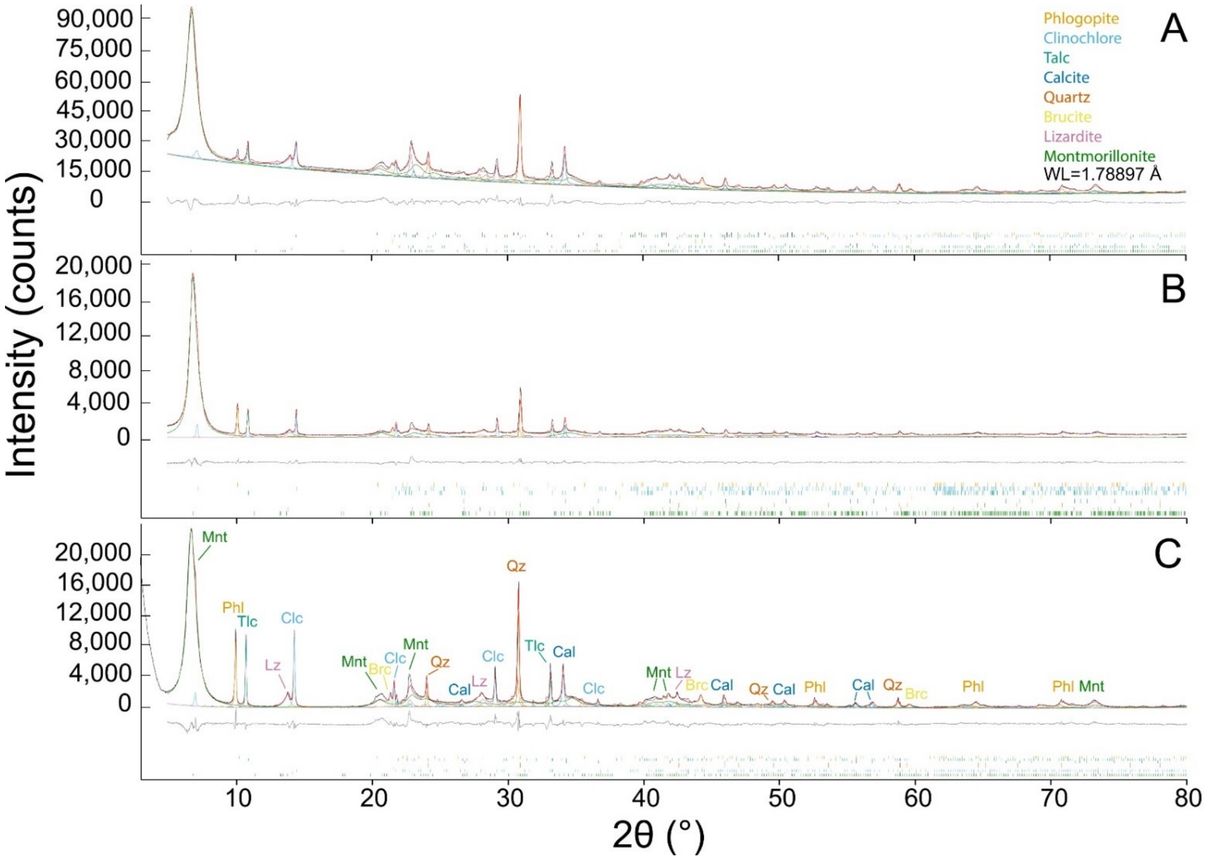

Figure 2.4 Rietveld refinement plots for wcskim5 using XRD data from, and PONKCS models that were correctly calibrated to (A) XRD A1, (B) XRD B1, and (C) XRD B2. Mineral abbreviations: Mnt = montmorillonite, Lz = lizardite, Phl = phlogopite, Clc = clinochlore, Tlc = talc, Brc = brucite, Cal = calcite, Qz = quartz.

2.3.5 Influence of instrument geometry on Rietveld-PONKCS results

PONKCS models calibrated to XRD B1 were used in refinements with XRD data collected on XRD B2 and XRD A1 to test the influence of instrument geometry on Rietveld refinement results. To do that, the lizardite and Ca-exchanged montmorillonite standard XRD patterns were collected on XRD B1 first. Then, Pawley extractions, using space group and unit cell information from Table 2.2, were used to obtain peak positions and peak intensities. *ZMV* values were then calculated for lizardite and montmorillonite using the PONKCS method to create PONKCS models for both phases. Because a Pawley extraction was used, and because the calculated *ZMV* values are empirical and unphysical, we suspected these models would be sensitive to changes in instrument parameters. Then these PONKCS models calibrated to XRD B1 were applied in refinements with XRD data collected on both XRD B2 and XRD A1. The total absolute bias obtained from refinements using data collected on XRD A1 varies from 32.1–71.6 wt.% (Fig. 2.5, Appendix Table A1.3) with an average of 48.0 wt.%. Refined abundances of lizardite are highly variable, with bias results ranging from -7.7 to +24.6 wt.% and the greatest overestimation of 24.6 wt.% is observed for wcskim5, which contains the least amount of lizardite. The abundance of Ca-montmorillonite is typically underestimated by -7.9 to -32.6 wt.%, with the greatest underestimation of -32.6 wt.% also occurring for wcskim5, which contains the greatest amount of montmorillonite. The high bias for both lizardite and Ca-montmorillonite results in the very high total bias for wcskim5 (71.6 wt.%). Due to the typical underestimation of Ca-montmorillonite abundance, the abundances of phlogopite, clinochlore, talc, brucite, calcite, and quartz are consistently overestimated. The exceptions to this trend are an underestimation of -2.3 wt.% for phlogopite in wcskim5, an underestimation of -0.7 wt.% for brucite, also observed in wcskim5, and an underestimation of -0.3 wt.% for calcite in wcskim1.

Total absolute bias values for refinements with XRD B2 data and PONKCS models calibrated to XRD B1 vary from 9.8 to 32.7 wt.% (Fig. 2.5, Appendix Table A1.3) with an average of 19.7 wt.%. Refined abundances of lizardite are variable, with bias results ranging from -5.1 to +7.9 wt.% and the greatest overestimation of 7.9 wt.% also observed for wcskim5. Similar to what was observed for XRD A1, the abundance of Ca-montmorillonite is typically underestimated by -1.9 to -15.1 wt.%, with the greatest underestimation of -15.1 wt.% also occurring for wcskim5. The high bias on the abundances of lizardite and Ca-montmorillonite results in the very high total bias for wcskim5 (32.7 wt.%). The abundances of phlogopite, clinochlore, and talc are typically overestimated whereas those for brucite, calcite, and quartz are systematically underestimated. The only exceptions to this trend are an overestimation of 0.8 wt.% for calcite and an overestimation of 0.5 wt.% for quartz, which are only observed in wcskim4.

Refined abundances of Ca-montmorillonite are underestimated using data from both XRD A1 and XRD B2. The greatest misestimations for lizardite and Ca-montmorillonite are observed for wcskim5 using both of these XRDs. This can be attributed to wcskim5 having the lowest abundance of lizardite and the highest abundance of Ca-montmorillonite, which, due to its production of a large number of peaks, has the most significant impact on the goodness of the fits. The results obtained using data from XRD B2 are more accurate because it has similar instrumental parameters to XRD B1 (*e.g.*, both instruments have an anti-scatter screen). Nonetheless, our results show that even relatively small changes in instrument parameters can lead to inconsistent and inaccurate QPA results (9.8–32.7 wt.% total bias) when using PONKCS models calibrated to another instrument. Calibrating PONKCS models to the other two XRDs used in refinements, coupled with XRD data collected from various XRDs, is expected to yield consistent results across different analytical setups.

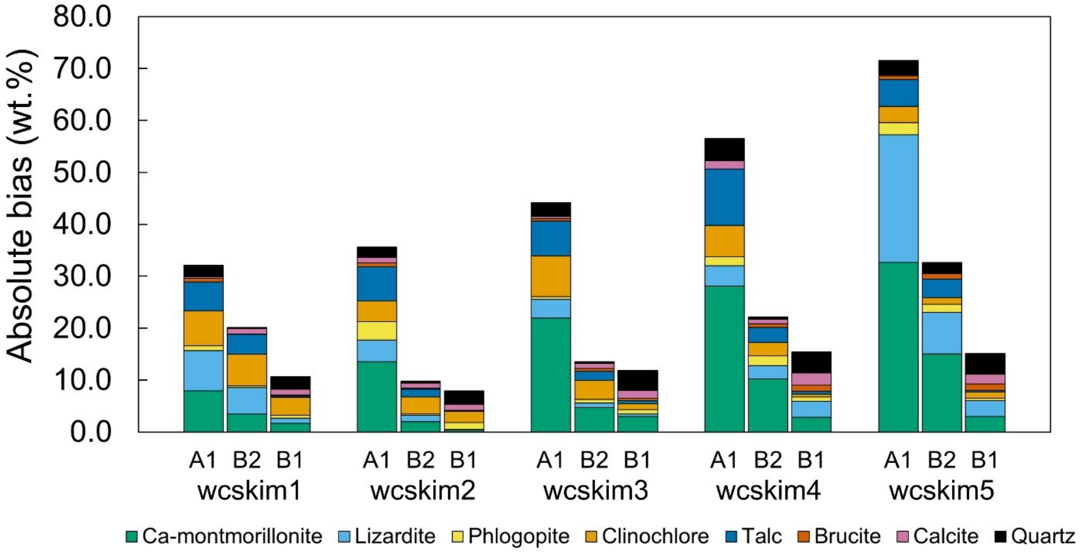

Figure 2.5 Absolute bias (wt.%) values for different phases in the five synthetic samples of processed kimberlite using PONKCS models calibrated to XRD B1.

2.4 Discussion

Three models are used during Rietveld refinement to calculate a simulated powder diffraction pattern for each phase: (1) a model for the shapes and widths of the diffraction peaks, (2) a model for any aberrations in the shapes and positions of the peaks, and (3) a model for the background (Raudseep and Pani, 2003). Both the sample preparation process and instrumental parameters influence the peak shapes observed for each phase (McCusker et al., 1999; León-Reina et al., 2016). Several factors need to be taken into account prior to data collection including: the geometry of the diffractometer, the X-ray wavelength, slit sizes, appropriate sample preparation and sample thickness and the counting time needed to obtain a useful pattern (McCusker et al., 1999). The results of the present study show that even small changes in instrument parameters (*e.g.,* between XRDs B1 and B2) can lead to inconsistent and inaccurate QPA results using PONKCS. Thus, correctly calibrated and instrument-specific PONKCS models need to be created for each X-ray diffractometer to obtain accurate QPA results.

The carbonation potentials of the five synthetic kimberlite samples were estimated by taking into account the reactivity of lizardite [$Mg_3Si_2O_5(OH)_4$], brucite [$Mg(OH)_2$] and montmorillonite [$Ca_{x/2}(Al_{2-y}Mg_y)Si_4O_{10}(OH)_2 \bullet nH_2O$]. Carbonation potential was calculated using (1) the known composition of the wcskim samples (Table 2.1), (2) Rietveld refinement results (wt.%) utilizing PONKCS models calibrated to XRD B2 (Appendix Table A1.2), which gave the most accurate results, and Rietveld refinement results (wt.%) using PONKCS models calibrated to XRD B1 with data collected on (3) XRD B2 and (4) XRD A1 (Appendix Table A1.3). Ideal stoichiometries were assumed for lizardite and brucite. Average values for Mg (1.773 wt.%) and Ca (0.841 wt.%) content in SWy-2 (Mermut and Cano, 2001) were used for montmorillonite. Assuming hydromagnesite [$Mg_5(CO_3)_4(OH)_2 \cdot 4H_2O$] forms from Mg released during complete dissolution of lizardite, brucite and montmorillonite and that calcite forms from Ca during complete cation-exchange reactions and dissolution of montmorillonite in the presence of aqueous carbonate, and a sample mass of 1 kg, the carbonation offset potential of these five synthetic samples is presented in Appendix Table A1.4 and Figure 2.6. Hydromagnesite was used in calculates because it has a 5:4 molar ratio of $Mg:CO_2$ in its crystal structure, providing a conservative estimate of carbonation offset potentials. More hydrated minerals such as lansfordite ($MgCO_3 \cdot 5H_2O$) and nesquehonite ($MgCO_3 \cdot 3H_2O$) typically decompose to hydromagnesite in mine tailings storage facilities (Wilson et al., 2006).

Owing to the comparatively low, and identical, abundance of brucite in the five wcskim samples, the carbonation potential of brucite consistently gives similar results regardless of refinement strategy. Results show that the actual carbonation offset potential of brucite in the wcskim samples is 29 g/kg. The carbonation offset potential of brucite using instrument-specific PONKCS models and data for XRD B2 gives similar results ranging from 24–26 g/kg. The carbonation offset potential of brucite varies from 22–28 g/kg using XRD B1 PONKCS models with XRD B2 data. The carbonation potential of brucite in all five synthetic kimberlite samples is systemically underestimated, and the carbonation potential of brucite is underestimated by a greater amount, ~24 % relative, when lizardite is less abundant. The carbonation offset potential of brucite varies from 24–33 g/kg using XRD B1 PONKCS models with XRD A1 data. These results overestimate the amount of CO_2 that can be sequestered by brucite when lizardite is more abundant and underestimate the carbonation potential of brucite by ~17 % relative when lizardite is less abundant (Fig. 2.6).

The actual carbonation offset potential of lizardite in the wcskim samples varies from 38–226 g/kg. The carbonation offset potential of lizardite obtained using instrument-specific PONKCS models and data for XRD B2 is similar: ranging from 47–231 g/kg. The calculated carbonation offset potential of lizardite varies from 68–207 g/kg using XRD B1 PONKCS models with XRD B2 data. The least accurate carbonation offset potentials calculated for lizardite, 90–197 g/kg, were obtained using XRD B1 PONKCS models with XRD A1 data. The latter results underestimate the amount of CO_2 that can be sequestered when lizardite is more abundant and dramatically overestimate the carbonation potential when lizardite is less abundant (Fig. 2.6).

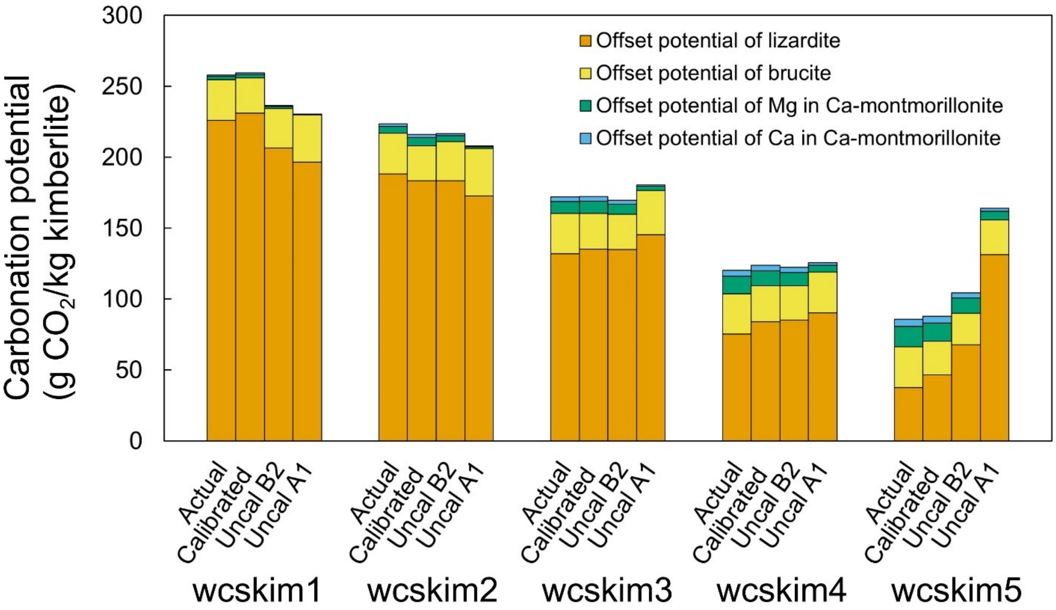

Figure 2.6 Carbonation offset potential (g/kg) of lizardite, brucite and montmorillonite calculated using the actual composition of wcskim samples (Actual), Rietveld refinement results using correctly calibrated PONKCS models and data from XRD B2 (Calibrated), and Rietveld refinement results using PONKCS models calibrated to XRD B1 with data collected on XRD B2 (Uncal B2) and XRD A1 (Uncal A1).

The actual carbonation offset potential of Mg and Ca in montmorillonite within the wcskim samples varies from 2–14 g/kg and 1–5 g/kg, respectively. The actual carbonation offset potential of montmorillonite in the wcskim samples thus varies from 3–19 g/kg, indicating a relatively low offset potential. Utilizing instrument-specific PONKCS models and data for XRD B2, the carbonation offset potential of Mg and Ca in Ca-montmorillonite shows a range of 3–13 g/kg and 1–5 g/kg, respectively. Alternatively, when employing XRD B1 PONKCS models with XRD B2 data, the carbonation offset potential of Mg and Ca in Ca-montmorillonite varies from 2–11 g/kg and 0–3 g/kg, respectively. Finally, employing XRD B1 PONKCS models with XRD A1 data, the carbonation offset potential of Mg and Ca in Ca-montmorillonite exhibits a range of 0–6 g/kg and 0–2 g/kg, respectively. The latter variations in carbonation potential result from the underestimation of montmorillonite abundance by ~56–100% relative in these particular refinements. Although montmorillonite has a low offset potential compared to brucite and lizardite, the reactivity of smectites to CO_2 using cation-exchange reactions is rapid and may be a more desirable approach to carbonation in some mining environments than acid dissolution of silicate minerals or CO_2 injection to carbonate brucite (Zeyen et al., 2022).

The mineralogy of kimberlite lends itself to mineral carbonation. A total of 4.74 Mt of ore were treated at the Venetia mine in 2016 and the mine emitted 0.21 Mt of CO_2e emissions the same year (Mervine et al., 2018). Based on Stubbs et al. (2022) and Paulo et al. (2023), it is estimated that passive carbonation at the Venetia mine could achieve a CO_2 offset potential of approximately 1.0–1.5%. Considering the average lizardite (18.8 wt.%) and smectite (27.0 wt.%) content and no brucite in the 9 fine residues deposits (FRD) samples collected (Paulo et al., 2021), the actual carbonation offset potential of lizardite in the FRD samples is 7 g/kg. Assuming the smectite in FRD samples is in the form of montmorillonite, the actual carbonation offset potential of Mg and Ca in montmorillonite within the FRD samples is 1 g/kg and 0 g/kg, respectively. The actual carbonation offset potential of lizardite and montmorillonite is 8 g/kg, accounting for an estimated CO_2 offset potential of 18 % at Venetia, which is up to around 15 times greater than the passive carbonation rate even only taking into account these two minerals. It’s noteworthy that SWy-2 is a kind of Na-montmorillonite and the carbonation offset potential of smectite at Venetia will be largely underestimated due to the high Ca content included (Zeyen et al., 2022). Meanwhile, kimberlite is amongst the most complex, heterogeneous and altered ultramafic rocks that can be used for CO_2 storage. Our results show that particular care must be taken in calibrating instrument-specific PONKCS models to estimate the carbonation potential of kimberlite using XRD data. As a supplement to the Rietveld-PONKCS method, quantitative thermogravimetric analyses (TGA) (Turvey et al., 2022) have been shown to be more accurate and precise for detection of trace amounts of brucite (as low as 0.3 wt.%) in serpentinites. The same TGA method has also been used to rule out the presence of brucite in kimberlite when there is uncertainty about its detection owing to peak overlap with chlorite (Zeyen et al., 2022). Furthermore, kimberlite samples may contain low abundances of gangue carbonate minerals, such as the calcite included in the wcskim samples, making it difficult to distinguish between previously and newly trapped CO_2 in minerals. The combination of the quantitative mineralogical approach developed in this study and those of Turvey et al. (2022) and Zeyen et al. (2022) could be used with a correction factor for CO_2 stored in gangue minerals (Paulo et al., 2021) and total carbon analysis using a LECO carbon-sulfur analyzer (Turvey et al., 2018b) to obtain a more accurate and reliable baseline estimate of carbonation potential at diamond mines.

2.5 Chapter 2 references

Berg, G.W., 1989. The significance of brucite in South African kimberlites. In Kimberlite and Related Rocks, v2: Their Mantle/Crust Setting, Diamonds and Diamond Exploration (Cambridge. England: Geological Society of Australia Special Publication 14, Blackwell Scientific), 282-296.

Bish, D.L., and Howard, S.A., 1988. Quantitative phase analysis using the Rietveld method. Journal of Applied Crystallography, 21(2), 86-91.

Bish, D.L., Carey, J.W., Vaniman, D.T., and Chipera, S.J., 2003. Stability of hydrous minerals on the martian surface. Icarus, 164, 96-103.

Brown, A.S., Spackman, M.A., and Hill, R.J., 1993. The electron distribution in corundum. A study of the utility of merging single-crystal and powder diffraction data. Acta Crystallographica Section A: Foundations of Crystallography, 49(3), 513-527.

Bullock L.A., James R.H., Matter J., Renforth P., and Teagle D.A., 2021. Global carbon dioxide removal potential of waste materials from metal and diamond mining. Frontiers in Climate, 77.

Catti, M., Ferraris, G., Hull, S., and Pavese, A., 1995. Static compression and H disorder in brucite, Mg $(OH)_2$, to 11 GPa: a powder neutron diffraction study. Physics and Chemistry of Minerals, 22(3), pp.200-206.

Cheary, R.W., and Coelho, A., 1992. A fundamental parameters approach to X-ray line-profile fitting. International Union of Crystallography, 25(2), 109-121.

Chung, F.H., 1974. Quantitative interpretation of X-ray diffraction patterns of mixtures. II. Adiabatic principle of X-ray diffraction analysis of mixtures. Journal of Applied Crystallography, 7(6), 526-531.

Collins, D.R., and Catlow, R.A., 1992. Computer simulation of structures and cohesive properties of micas. American Mineralogist, 77(11-12), 1172-1181.

Glinnemann, J., King Jr, H.E., Schulz, H., Hahn, T., La Placa, S.J., and Dacol, F., 1992. Crystal structures of the low-temperature quartz-type phases of SiO_2 and GeO_2 at elevated pressure. Zeitschrift für Kristallographie-Crystalline Materials, 198(1-4), 177-212.

Gualtieri, A.F., 2000. Accuracy of XRPD QPA using the combined Rietveld–RIR method. Journal of Applied Crystallography, 33(2), pp.267-278.

Hamilton, J.L., Wilson, S., Morgan, B., Harrison, A.L., Turvey, C.C., Paterson, D.J., Dipple, G.M., and Southam, G., 2020. Accelerating mineral carbonation in ultramafic mine tailings via direct CO_2 reaction and heap leaching with potential for base metal enrichment and recovery. Economic Geology, 115(2), 303-323.

Harrison, A.L., Power, I.M., and Dipple, G.M., 2013. Accelerated carbonation of brucite in mine tailings for carbon sequestration. Environmental Science & Technology, 47(1), 126-134.

Hill, R.J., and Howard, C.J., 1987. Quantitative phase analysis from neutron powder diffraction data using the Rietveld method. Journal of Applied Crystallography, 20(6), 467-474.

IPCC., 2018. Global warming of 1.5 °C: An IPCC Special Report on the impacts of global warming of 1.5°C above pre-industrial levels and related global greenhouse gas emission pathways. In: The context of strengthening the global response to the threat of climate change, sustainable development, and efforts to eradicate poverty. https://www.ipcc.ch/site/assets/uploads/sites/2/2019/06/SR15_Full_Report_High_Res.pdf. (Accessed 13 March 2023).

IPCC., 2022. Climate Change 2022: Impacts, Adaptation and Vulnerability. https://report.ipcc.ch/ar6/wg2/IPCC_AR6_WGII_FullReport.pdf. (Accessed 13 March 2023).

Khan, H., Yerramilli, A.S., D'Oliveira, A., Alford, T.L., Boffito, D.C. and Patience, G.S., 2020. Experimental methods in chemical engineering: X‐ray diffraction spectroscopy—XRD. The Canadian journal of chemical engineering, 98(6), pp.1255-1266.

Khan, S., Wani, O.B., Shoaib, M., Forster, J., Sodhi, R.N., Boucher, D., and Bobicki, E.R., 2021. Mineral carbonation for serpentine mitigation in nickel processing: A step towards industrial carbon capture and storage. Faraday Discussions, 230, 172-186.

Lacis, A.A., Schmidt, G.A., Rind, D., and Ruedy, R.A., 2010. Atmospheric CO_2: principal control knob governing Earth's temperature. Science, 330(6002), 356-359.

Lackner, K.S., Wendt, C.H., Butt, D.P., Joyce, E.L., and Sharp, D.H., 1995. Carbon dioxide disposal in carbonate minerals. Energy, 20, 1153–1170.

Lackner, K.S., 2003. A Guide to CO_2 Sequestration. Science.

León-Reina, L., García-Maté, M., Álvarez-Pinazo, G., Santacruz, I., Vallcorba, O., De la Torre, A.G., and Aranda, M.A.G., 2016. Accuracy in Rietveld quantitative phase analysis: a comparative study of strictly monochromatic Mo and Cu radiations. Journal of Applied Crystallography, 49(3), 722-735.

Maslen, E.N., Streltsov, V.A., Streltsova, N.R., and Ishizawa, N., 1995. Electron density and optical anisotropy in rhombohedral carbonates. III. Synchrotron X-ray studies of $CaCO_3$, $MgCO_3$ and $MnCO_3$. Acta Crystallographica Section B, 51(6).

McCusker, L.B., Von Dreele, R.B., Cox, D.E., Louër, D., and Scardi, P., 1999. Rietveld refinement guidelines. Journal of Applied Crystallography, 32(1), 36-50.

McCutcheon, J., Wilson, S., and Southam, G. 2016. Microbially accelerated carbonate mineral precipitation as a strategy for in situ carbon sequestration and rehabilitation of asbestos mine sites. Environmental Science & Technology, 50, 1419-1427.

McCutcheon, J., Turvey, C.C., Wilson, S., Hamilton, J.L., and Southam, G., 2017. Experimental deployment of microbial mineral carbonation at an asbestos mine: Potential applications to carbon storage and tailings stabilization. Minerals, 7, 191.

Mellini, M., and Viti, C., 1994. Crystal structure of lizardite-1T from Elba, Italy. American Mineralogist, 79(11), 1194-1198.

Mermut, A.R., and Cano, A.F., 2001. Baseline studies of the clay minerals society source clays: chemical analyses of major elements. Clays and Clay Minerals, 49(5), pp.381-386.

Mervine, E.M., Wilson, S., Power, I.M., Dipple, G.M., Turvey, C.C., Hamilton, J.L., Vanderzee, S., Raudsepp, M., Southam, C., Matter, J.M., and Kelemen, P.B., 2018. Potential for offsetting diamond mine carbon emissions through mineral carbonation of processed kimberlite: an assessment of De Beers mine sites in South Africa and Canada. Mineralogy and Petrology, 112, pp.755-765.

O'Gorman, J.V., and Kitchener, J.A., 1974. The flocculation and de-watering of kimberlite clay slimes. International Journal of Mineral Processing, 1(1), pp.33-49.

Omotoso, O., McCarty, D.K., Hillier, S., and Kleeberg, R., 2006. Some successful approaches to quantitative mineral analysis as revealed by the 3rd Reynolds Cup Context. Clays and Clay Minerals, 54(6), 748-760.

Paulo, C., Power, I.M., Stubbs, A.R., Wang, B., Zeyen, N., and Wilson, S., 2021. Evaluating feedstocks for carbon dioxide removal by enhanced rock weathering and CO_2 mineralization. Applied Geochemistry, 129, 104955.

Paulo, C., Power, I.M., Zeyen, N., Wang, B. and Wilson, S., 2023. Geochemical modeling of CO_2 sequestration in ultramafic mine wastes from Australia, Canada, and South Africa: Implications for carbon accounting and monitoring. Applied Geochemistry, 152, p.105630.

Pawley, G.S., 1981. Unit-cell refinement from powder diffraction scans. Journal of Applied Crystallography, 14(6), 357-361.

Power, I.M., Harrison, A.L., Dipple, G.M., Wilson, S., Kelemen, P.B., Hitch, M., and Southam, G., 2013. Carbon Mineralization: From Natural Analogues to Engineered Systems. Reviews in Mineralogy and Geochemistry, 77(1), 305-360.

Power, I.M., Paulo, C., Long, H., Lockhart, J.A., Stubbs, A.R., French, D., and Caldwell, R., 2021. Carbonation, cementation, and stabilization of ultramafic mine tailings. Environmental Science & Technology, 55(14), 10056-10066.

Raudsepp, M., and Pani, E., 2003. Application of Rietveld analysis to environmental mineralogy. Environmental aspects of mine wastes, 31, 165-180.

Rayner, J.H., and Brown, G., 1973. The crystal structure of talc. Clays and Clay Minerals, 21(2), 103-114.

Renforth, P., 2019. The negative emission potential of alkaline materials. Nature communications, 10(1), 1401.

Rietveld, H.M., 1967. Line profiles of neutron powder-diffraction peaks for structure refinement. Acta Crystallographica, 22(1), pp.151-152.

Rietveld, H.M., 1969. A profile refinement method for nuclear and magnetic structures. International Union of Crystallography, 2(2), 65-71.

Scarlett, N.V.Y., and Madsen, I.C., 2006. Quantification of Phases with Partial or No Known Crystal Structures. Powder Diffraction, 21(4), 278-284.

Seifritz, W., 1990. CO_2 disposal by means of silicates. Nature.

Smyth, J.R., 1997. Crystal Structure Refinement and Mossbauer Spectroscopy of an Ordered, Triclinic Clinochlore. Clays & Clay Minerals, 45(4), 544-550.

Stripp, G.R., Field, M., Schumacher, J.C., Sparks, R.S.J., and Cressey, G., 2006. Post-emplacement serpentinization and related hydrothermal metamorphism in a kimberlite from Venetia, South Africa. Journal of Metamorphic Geology, 24, 515-534.

Stubbs, A.R., Paulo, C., Power, I.M., Wang, B., Zeyen, N., and Wilson, S., 2022. Direct measurement of CO_2 drawdown in mine wastes and rock powders: Implications for enhanced rock weathering. International Journal of Greenhouse Gas Control, 113, 103554.

Turvey, C.C., Wilson, S., Hamilton, J.L., and Southam, G., 2017. Field-based accounting of CO_2 sequestration in ultramafic mine wastes using portable X-ray diffraction. American Mineralogist: Journal of Earth and Planetary Materials, 102(6), 1302-1310.

Turvey, C.C., Hamilton, J.L., and Wilson, S., 2018a. Comparison of Rietveld-compatible structureless fitting analysis methods for accurate quantification of carbon dioxide fixation in ultramafic mine tailings. American Mineralogist, 103(10), 1649-1662.

Turvey, C.C., Wilson, S., Hamilton, J.L., Tait, A.W., McCutcheon, J., Beinlich, A., Fallon, S.J., Dipple, G.M., and Southam, G., 2018b. Hydrotalcites and hydrated Mg-carbonates as carbon sinks in serpentinite mineral wastes from the Woodsreef chrysotile mine, New South Wales, Australia: controls on carbonate mineralogy and efficiency of CO_2 air capture in mine tailings. International Journal of Greenhouse Gas Control, 79, pp.38-60.

Turvey, C.C., Wynands, E.R., and Dipple, G.M., 2022. A new method for rapid brucite quantification using Thermogravimetric Analysis. Thermochimica Acta, 718, p.179366.

Viani, A., Gualtieri, A.F., and Artioli, G., 2002. The nature of disorder in montmorillonite by simulation of X-ray powder patterns. American Mineralogist, 87(7), 966-975.

Wang, F., and Dreisinger, D., 2022. Carbon mineralization with concurrent critical metal recovery from olivine. Proceedings of the National Academy of Sciences, 119(32), e2203937119.

Wilson, S., Raudsepp, M., and Dipple, G.M., 2006. Verifying and quantifying carbon fixation in minerals from serpentine-rich mine tailings using the Rietveld method with X-ray powder diffraction data. American Mineralogist, 91(8-9), 1331-1341.

Wilson, S., Dipple, G.M., Power, I.M., Thom, J.M., Anderson, R.G., Raudsepp, M., Gabites, J.E., and Southam, G., 2009a. Carbon dioxide fixation within mine wastes of ultramafic-hosted ore deposits: examples from the Clinton Creek and Cassiar chrysotile deposits,Canada. Economic Geology; 104 (1): 95–112.

Wilson, S., Raudsepp, M., and Dipple, G.M., 2009b. Quantifying carbon fixation in trace minerals from processed kimberlite: A comparative study of quantitative methods using X-ray powder diffraction data with applications to the Diavik Diamond Mine, Northwest Territories, Canada. Applied Geochemistry.

Wilson, S., Barker, S.L., Dipple, G.M., and Atudorei, V., 2010. Isotopic disequilibrium during uptake of atmospheric CO_2 into mine process waters: Implications for CO_2 sequestration. Environmental Science & Technology, 44(24), 9522.

Wilson, S., Dipple, G.M., Power, I.M., Barker, S.L., Fallon, S.J. and Southam, G., 2011. Subarctic weathering of mineral wastes provides a sink for atmospheric CO_2. Environmental Science & Technology, 45(18), 7727-7736.

Zeyen, N., Wang, B., Wilson, S., Paulo, C., Stubbs, A.R., Power, I.M., Steele-Maclnnis, M., Lanzirotti, A., Newville, M., Paterson, D.J., and Hamilton, J.L., 2022. Cation exchange in smectites as a new approach to mineral carbonation. Frontiers in Climate, 4.

Chapter 3

Migration of transition metals and potential for carbon mineralization during acid leaching of processed kimberlite from Venetia diamond mine, South Africa

3.1 Introduction

Earth's carbon cycle regulates climate on the timescale of millions of years by transfering carbon from surficial reservoirs, consisting of the ocean, atmosphere, biosphere and soils, into the rock record (Berner, 1998). The concentration of atmospheric CO_2 has increased exponentially from 280 ppm to over 415 ppm (NOAA, 2023) since the beginning of the industrial revolution, owing primarily to extensive use of fossil fuels such as coal, petroleum, and natural gas (Lacis et al., 2010; IPCC, 2018, 2022). Although improvements in energy efficiency have restrained growth in demand for electricity and fossil fuels, demand is still increasing and fossil fuels will likely remain the primary energy source until 2050 (IEA, 2021). Furthermore, anthropogenic emissions of greenhouse gases, aerosols, and their precursors have already increased global average surface temperature by approximately 1.1 °C above pre-industrial levels (IPCC, 2022). It is expected that temperature will have risen by at least 1.5 °C by 2030 given current trends in carbon emissions, which will cause long-term changes to Earth's climate (IEA, 2021; IPCC, 2022). As a consequence, reaching net zero CO_2 emissions is no longer enough to limit climate warming to below 2 °C — we must also actively remove on the order of 100–1000 Gt of CO_2 from the atmosphere by the end of the 21st century (IPCC, 2018).

Carbon mineralization provides safe, long-term storage of CO_2 by reaction with silicate and hydroxide minerals rich in alkaline earth metals (Seifritz, 1990; Lackner et al., 1995). Ultramafic and mafic rocks, which are rich in alkaline earth metals, are amongst the best materials to sequester CO_2 given their chemical composition and their widespread distribution (reviewed by Power et al., 2013b). Experimental and field studies have aimed to understand the reactivity of Mg- and/or Ca-bearing silicates and hydroxides such as brucite [$Mg(OH)_2$] (*e.g.,* Assima et al., 2014; Harrison et al., 2013; Hamilton et al., 2020), wollastonite ($CaSiO_3$) (*e.g.,* Huijgen et al., 2006; Min and Jun, 2018), forsteritic olivine (Mg_2SiO_4) (*e.g.,* Haug et al., 2010; Gadikota et al., 2014), serpentine group minerals [$Mg_3Si_2O_5(OH)_4$] (*e.g.,* Park and Fan, 2004; Power et al., 2013a; Hamilton et al., 2018), as well as other minerals such as the plagioclase mineral anorthite ($CaAl_2Si_2O_8$) (*e.g.,* Munz et al., 2012). In recent years, ultramafic mine tailings have been studied in detail as feedstocks for carbon mineralization owing to their high surface area, reactivity with CO_2 and the prospect to valorize these wastes (*e.g.,* Wilson et al., 2006, 2009a, 2009b, 2010, 2014; Pronost et al., 2011; Bobicki et al., 2012; Lechat et al., 2016; Turvey et al., 2017, 2018; Hamilton et al., 2018, 2020; Mervine et al., 2018). Wilson et al. (2014) determined that passive carbonation offsets 11% of the annual CO_2 emissions at the Mount Keith Ni mine in Western Australia. The major limitations on the rate of passive carbonation in mine tailings are dissolution of silicate minerals and the supply of CO_2 (Park and Fan, 2004; Power et al., 2013a, 2013b). The rate and amount of CO_2 sequestration can thus be increased by (1) enhancing dissolution of ultramafic mine tailings using stronger acids than the carbonic acid contained in rainwater and (2) increasing the supply of CO_2 into tailings or tailings leachates using high-CO_2 gases or bioreactors (*e.g.,* Harrison et al., 2013; McCutcheon et al., 2017; Hamilton et al., 2020; Wang et al., 2021a, 2021b).

Although carbon mineralization has been investigated for more than 30 years, the deportment and partitioning of transition metals during carbonation had not been extensively explored until recently (Hamilton et al., 2018). Ultramafic rocks and tailings used for carbon mineralization always contain low (<1 wt.%), but sometimes economical, concentrations of first row transition metals such as Ni, Mn, Cr, Cu, Co (*e.g.,* Zachara et al., 1991; Goff and Lackner, 1998; Margiotta et al., 2012; Wunsch et al., 2013; Sciortino et al., 2014; Hamilton et al., 2020). These transition metals can occur in minor oxides (*e.g.*, magnetite and chromite), trace alloys [*e.g.*, awaruite ($Ni_{2-3}Fe$) and wairauite (CoFe)] and sulfide minerals (Margiotta et al., 2012; Sciortino et al., 2014; Hamilton et al., 2018). They also substitute for Mg in the structures of serpentine, olivine and brucite (Goff and Lackner, 1998; Margiotta et al., 2012; Wunsch et al., 2013; Sciortino et al., 2014; Hamilton et al., 2018, 2020). Hamilton et al. (2018, 2020) proposed that carbon mineralization can be used as an ore processing, or tailings reprocessing, technology to improve recovery of critical metals such as Ni and Co, which are essential components of batteries that are needed for renewable energy storage. Carbonation of serpentine minerals, the most abundant gangue minerals in many ultramafic ores, can also be used to prevent formation of slimy coatings on ore minerals, such as pentlandite [$(Ni,Fe)_9S_8$], during froth flotation (Khan et al., 2021). The transition metals, Fe, Ni, Mn, Co, and Cr, can be released from the crystal structures of Mg-silicate minerals such as olivine and serpentine minerals during carbonation where they then become highly concentrated within secondary minerals such as ferrihydrite and sulfide minerals, making it possible to recover these previously unrecoverable metals from silicate minerals (Hamilton et al., 2020; Wang et al., 2021a; Wang and Dreisinger, 2022). These recent discoveries suggest there may be a bright future for enhanced recovery of transition metals by incorporating carbonation into mineral processing.

Here, we aim to assess the deportment and mobility of transition metals such as Ni and the potential for mineral carbonation of processed kimberlite from the Venetia mine (South Africa) using different concentrations of dilute HCl to enhance silicate mineral dissolution in laboratory column reactors. Although kimberlites contain first row transition metals at comparable abundances to other ultramafic rocks, they differ in that they are generally less basic, typically lacking brucite, and they can contain large abundances of smectites and pre-existing calcite (Zeyen et al., 2022). Thus, they may respond differently to processes that have been developed to date for coupled carbon mineralization and critical metal recovery from serpentinites. Bullock et al. (2021) estimated ~1.1–4.5 Gt CO_2 could be captured annually by enhanced weathering of silicate mine tailings, ranging from 31–125 % of the industry's primary emissions. Passive weathering of silicate minerals in processed kimberlite at the Diavik diamond mine (Canada) traps 270–300 t of modern atmospheric carbon annually (Wilson et al., 2011). Considering the 162 000 tonnes of carbon dioxide equivalent (CO_2e) emitted to process 2 Mt of mine tailings annually at Diavik, this amounts to a ~0.2 % offset of the mine's annual emissions (Wilson et al., 2011). Combining carbon mineralization with biomass production utilizing a redesign of the tailings storage facilities at Diavik, could offer an estimated 2.5 % CO_2 offset of the mine's greenhouse gas emissions (Power et al., 2011). Results of more recent experimental studies of carbon mineralization at the Venetia diamond mine (South Africa) show that different carbonation strategies should be employed based on the mineralogy of processed kimberlites (*e.g.,* Mervine et al., 2018; Paulo et al., 2021; Zeyen et al., 2022; Stubbs et al., 2022). Processed kimberlites, owing to their distinct mineralogical composition, are expected to respond differently to acid leaching and carbonation processes than other ultramafic rocks, such as serpentinites. The focus of this study is on (1) characterizing the mineralogy and elemental composition of processed kimberlite from the Venetia diamond mine within the framework of mineral carbonation, (2) accounting of leached Mg and Ca to estimate CO_2 sequestration potential, and (3) transition metal deportment, mobility and recoverability during accelerated weathering of processed kimberlites.

3.2 Geological setting

The Venetia kimberlite cluster is located in the Central Zone of the Limpopo Belt, Limpopo Province, South Africa (Fig. 3.1) and comprises 14 pipes and dykes (Kurszlaukis and Barnett, 2003; Pretorius and Barton, 2003; Stripp et al., 2006; Walters et al., 2006). These ~530 Ma pipes are the result of an ancient collision zone of the Kaapvaal and Zimbabwe Cratons (Kurszlaukis and Barnett, 2003; Walters et al., 2006). They intrude paragneisses belonging to the >2 Ga Beit Bridge Group, containing biotite gneiss, biotite schist, amphibolite biotite schist, quartzo-feldspathic gneiss, phyllite, quartzite and marble, and ~2.5 Ga to ~2.0 Ga granitic rocks (Pretorius and Barton, 2003). The Venetia kimberlites contain volcaniclastic rocks of the diatreme facies and hypabyssal rocks such as massive volcaniclastic kimberlite (MVK), layered volcaniclastic kimberlite (LVK) and dark volcaniclastic kimberlite (DVK) (Stripp et al., 2006; Walters et al., 2006). Textural descriptions note that olivine crystals can comprise up to 40 % of the MVK facies (Pretorius and Barton, 2003; Stripp et al., 2006); however, mineralogically, all of the forsterite has been replaced by lizardite [$Mg_3Si_2O_5(OH)_4$] and other clay minerals (Zeyen et al., 2022).

The Venetia mine emitted 0.21 Mt of CO_2e emissions in 2016 while mining 3.89 Mt of ore and processing 4.74 Mt of ore including freshly mined and stockpiled material (Mervine et al. 2018). Mervine et al. (2018) previously estimated that while 13.9 % of the ore treated in 2016 would need to be completely carbonated to achieve a 100 % offsetting of the mine's greenhouse gas emissions, the total CO_2 sequestration potential of the ore processed that year is on the order of 1.51 Mt.

Figure 3.7 Location of Venetia Mine, South Africa (modified from Mervine et al., 2018).

3.3 Materials and methods

3.3.1 Sample collection

Samples of processed kimberlite dominated by the massive volcaniclastic kimberlite (MVK) facies were collected from the Venetia mine in October 2017. During processing, Venetia kimberlite ore is first crushed to produce coarse ore stockpile before going through a primary scrubber. Subsequently, the ore is crushed using high pressure grinding rolls (HPGR) and passed through a secondary scrubber. Processed kimberlite with grain sizes <0.8 mm is remitted to the fine residue deposit (FRD) and coarser material (0.8–8 mm) obtained using dense media separation (DMS) is stockpiled in the coarse residue deposit (CRD) for possible future re-crushing and processing. The ratio of FRD:CRD produced at the Venetia mine is 60:40 % by mass. The FRD and CRD samples were collected from tailings storage facilities and stored in two plastic buckets for 1.3 years before the column experiments. When receiving the samples, the FRD sample was muddy while the CRD sample was dry. By the time the column experiments were begun, the water in the FRD sample had almost completely evaporated due to the dry conditions in the laboratory.

3.3.2 Experimental design

Before the experiment, a variety of FRD:CRD mass ratios, including (1) 100 % FRD, (2) 80 % FRD with 20 % CRD, (3) 70 % FRD with 30 % CRD, (4) 50 % FRD with 50 % CRD and 100 % CRD, were used to measure the flow rate of acid treatments through columns. The acid leaching experiment was ultimately conducted by mixing 70 % FRD with 30 % CRD due to the optimal flow rate for leachate recovery within 2–12 hours and the similar FRD:CRD ratio produced at the Venetia mine. In order to avoid the precipitation of salts upon drying, and to remove salts from dried materials, FRD and CRD samples were separately rinsed three times with Milli-Q water (18.2 MΩ·cm) and air-dried at room temperature in a fume hood for several days before they were mixed for experiments. A total of 910 g of dry FRD was mixed homogeneously with 390 g of dry CRD. Then, 80.5 g of mixed FRD (70 %) and CRD (30 %) was loaded into each of 15 polypropylene 60 mL syringes to a depth of 9 cm (corresponding to the 50 mL scale line of each syringe). A circular (2.67 cm diameter, 1-μm pore size) piece of nylon fabric mesh was placed at the bottom of each syringe before the addition of mixed tailings into the columns. This was done to minimize the escape of fine particles into leachates collected from the base of each syringe.

The density of bulk MVK ore and mixed, MVK-dominated processed kimberlite were measured to be 2.41 g/cm^3 and 1.61 g/cm^3 respectively. To prepare a 50 mL syringe of processed kimberlite, 80.5 g of material is required. Using the bulk density value of 2.41 g/cm^3, it was estimated that the volume of the processed kimberlite in the syringe would be 33.4 mL, leaving 16.6 mL for porosity volume. Thus a 16.6 mL volume (equivalent to 1 initial pore volume) of solution was added to each column once per day for a total of 28 days under ambient laboratory conditions from 18–22 °C. Five different treatments were applied: Milli-Q water (M0), 0.04 M (M1), 0.08 M (M2), 0.12 M (M3) and 0.16 M HCl (M4). Three replicate columns were employed for each of the five treatments for a total of three water-treated columns and 12 acid-treated columns (Fig. 3.2A). No leachate could be obtained after the first treatment (day 1), which wetted the processed kimberlite, except from the columns treated with 0.16 M HCl (less than 3 mL leachate). Leachates were collected from each of the 15 columns every day beginning on the second day of experimentation. Leachates were collected in 50 mL polypropylene tubes that were fixed with tape below each column. Sampling of leachates was done prior to addition of the next daily dose of water or dilute HCl. All the reagents used were of ACS grade.

Solid samples were collected after the 28th day of treatment. Each sample was dried in a fume hood for 60 days. The completeness of drying, which was slowed by the tendency of smectites to retain interlayer H_2O, was monitored by measuring the mass of each loaded column reactor. Once dry, each column reactor treated with HCl was separated into five parts (Fig. 3.2B): (1) the thin yellow crust that formed from 0–0.1 cm at the top surface of each column, (2) the upper 0.1–~1.9 cm of residues within each column, (3) the middle ~1.9–~5.5 cm of residues from each column, (4) the bottom ~5.5–9 cm of residues, and (5) a yellow precipitate that sometimes formed in the leachate collected from the bottom of each column. Notably, the top section constituted about 1/5 the volume of the whole column, owing to a slightly looser consistency observed post-drying. The middle and bottom sections, where no significant alteration was observed, each comprised around 2/5 the volume of the whole column.

Leachates were filtered through Basix™ 0.22 µm polyethersulfone (PES) membranes during experiments to collect the yellow precipitates on the filter membranes. Afterward, any yellow precipitates remaining in the leachates were collected using centrifugation (7200 rpm, 5 min) and rinsed three times with Milli-Q water. Similar yellow precipitates, intermixed with processed kimberlite, also formed on the interior walls of some columns just above the thin yellow crust (yellow rings on the wall of syringe in Fig. 3.2B). By contrast, the yellow precipitate did not form in the column reactors treated with H_2O and the crust of fine material at the top of each column was not yellow. For the upper, middle and bottom residues within each column treated with H_2O, each part accounted for around 1/3 the volume of the whole column. As triplicates were prepared for the experiment, one column was used for bulk chemistry and XRD analyses, one for petrographic thin sectioning and the last one was archived.

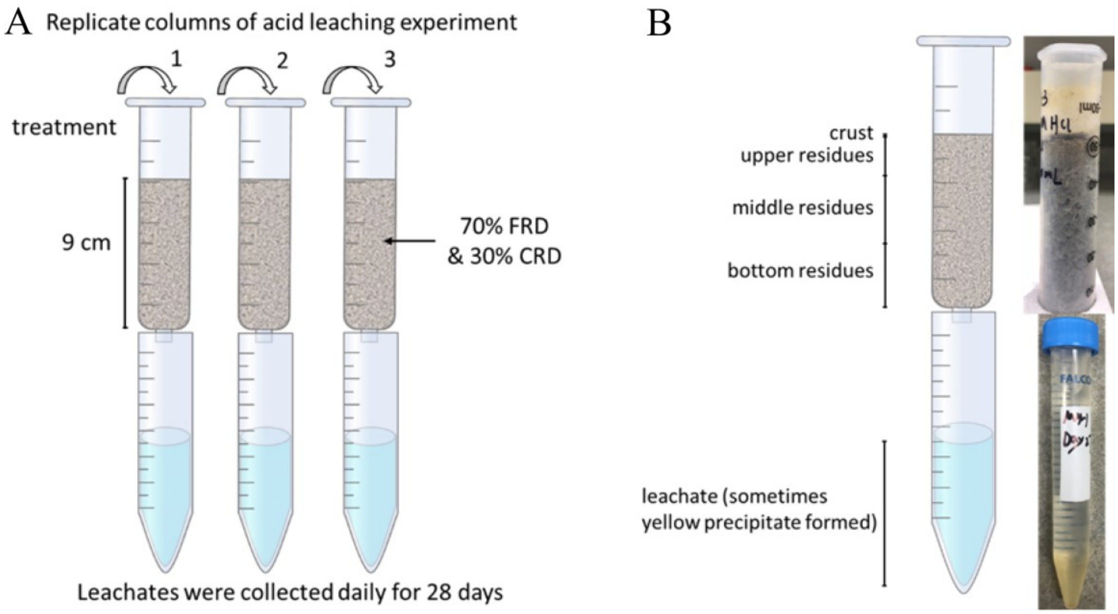

Figure 3.2 (A) Schematic illustration of the column experiment. (B) An illustration and photographs of subsamples collected from each of the HCl and Milli-Q water treated columns.

3.3.3 Analytical methods

3.3.3.1 Leachate chemistry

An Orion Star™ A329 pH/ISE/Conductivity/Dissolved Oxygen Portable Multiparameter Meter was used to measure pH, conductivity and temperature of leachates immediately after their collection. The leachates collected from days 2–8 were filtered through Basix™ 0.22 µm polyethersulfone (PES) membranes and acidified using 2–3 drops of 70 % HNO_3 immediately after collection. Leachates collected from days 9–28 were filtered and acidified on day 28 owing to a shortage of filters and supply chain disruptions during the COVID-19 pandemic. All leachate samples were stored at 4 °C in a laboratory refrigerator. Cation and anion concentrations and alkalinity of leachates were measured for days 2, 4, 6, 8, 12, 17, 20, 24 and 28 following the methods described below.

3.3.3.1.1 Cation analysis with inductively coupled plasma mass spectrometry (ICP-MS)

Leachates were analyzed using ICP-MS (Agilent 8800) in the Department of Earth and Atmospheric Sciences, University of Alberta. Details on the method are given in the Supplementary Information (Appendix Table A2.1).

3.3.3.1.2 Anion analysis with ion chromatography and alkalinity by titration

Concentrations of anions (Br^-, Cl^-, NO_2^-, NO_3^-, PO_4^{3-} and SO_4^{2-}) were determined using a Dionex DX-600 Ion Chromatography System at the Biogeochemical Analytical Service Laboratory (BASL), University of Alberta. Alkalinity was determined at BASL with the American Public Health Association (APHA) Titration Method 2320B using a Mantech PC-Titration Plus System with H_2SO_4.

3.3.3.2 Chemistry and mineralogy of solids

3.3.3.2.1 Bulk elemental chemistry

Bulk elemental chemistry of the initial FRD:CRD (70:30 %) mixture of processed kimberlite and the upper, middle and bottom samples of processed kimberlite from each column after the experiment, was determined using X-ray fluorescence (XRF), inductively coupled plasma atomic emission spectroscopy (ICP-AES) and Leco analysis at SGS Mineral Services Geochemical Laboratory in Vancouver, Canada. Details can be found in the Supplementary Information (Appendix Table A2.7).

3.3.3.2.2 Powder X-ray diffraction (XRD)

Solids subsampled from columns, including yellow leachate precipitates from two columns, five thin surface crusts, five upper residues, five middle residues and five bottom residues were prepared for analysis using powder X-ray diffraction (XRD). Solid samples were milled with an automated agate mortar and pestle. The methods by which samples were analyzed using XRD differed depending on the amount of sample available. For the two yellow precipitates, samples were hand ground with an agate mortar and pestle and mounted as slurries onto zero diffraction quartz plates using anhydrous ethanol. The five thin surface crusts and the 15 upper, middle and bottom samples were pulverized using an automated agate mortar followed by 7 minutes of milling in anhydrous ethanol with agate grinding elements in a McCrone Micronizing Mill. Samples were air-dried at room temperature within a fume hood after micronization. As these samples are rich in smectites (*i.e.*, swelling clays), the five surface crusts and 15 upper, middle and bottom samples were calcium exchanged in 30 mL (for crusts) or 150 mL (for the remaining samples) of 1 M $CaCl_2$ solution following the method described by Mervine et al. (2018). A lesser volume of 1 M $CaCl_2$ was used for crusts because of their small quantities. Samples were then stored in a NaCl slurry box at a relative humidity (RH) of 75% to stabilize the basal (001) spacing of smectites to ~15 Å (after Bish et al., 2003).

XRD patterns were collected using a Bruker D8 Advance X-ray diffractometer equipped with a high-speed energy-dispersive LYNXEYE XE-T detector and a cobalt tube that was operated at 35 kV and 40 mA in the Department of Earth and Atmospheric Sciences, University of Alberta. Data were collected from 3–80° 2θ using a step size of 0.02° 2θ at a rate of 1 s/step. Mineral phase identification was conducted using the DIFFRAC.EVA XRD phase analysis software (Bruker) with reference to the International Center for Diffraction Data Powder Diffraction File 4+ database (ICDD PDF4+). Rietveld refinements (Rietveld, 1969; Hill and Howard, 1987; Bish and Howard, 1988) with XRD data were used to determine mineral abundances using the TOPAS 5 software (Bruker). Fundamental-parameters peak fitting (Cheary and Coelho, 1992) was used for all phases. The method of Partial Or No Known Crystal Structure (PONKCS; Scarlett and Madsen, 2006) was used to model the peak profiles of smectites and lizardite to account for turbostratic stacking disorder as implemented by Mervine et al. (2018) and Wang et al. (2024). The detection limit of most minerals is generally ~0.1 wt.% for the conditions used to collect XRD data.

3.3.2.3 Electron microscopy and synchrotron X-ray fluorescence microscopy

After the experiments, three large thin sections (7 cm × 5 cm) of water- and 0.08 M and 0.16 M acid-leached columns were prepared by Vancouver Petrographics Ltd. The processed kimberlite columns were impregnated with epoxy prior to thin sectioning onto borosilicate glass slides for a final sample thickness of 30 μm. Four yellow precipitates collected from leachates after filtration, five thin surface crusts and three large thin sections were analyzed using a Zeiss Sigma 300 variable-pressure field-emission scanning electron microscope (VP-FESEM) equipped with secondary electron (SE) and backscattered electron detectors (BSD) in the Department of Earth and Atmospheric Sciences, University of Alberta. Secondary and backscattered electron images were acquired at an accelerating voltage of either 15 kV (normal mode) or 25 kV (variable pressure mode) at a working distance of ~7.6 mm and using a 30 µm aperture. The elemental compositions of mineral phases were determined using energy dispersive X-ray spectrometry (EDXS) with an EDS QUANTAX detector. EDXS data were analyzed using the ESPRIT software package (Bruker).

One subsample of a yellow precipitate collected from 0.16 M HCl leachates after filtration was analyzed using transmission electron microscopy (TEM). It was suspended in Milli-Q water and a 2-µL aliquot of the suspension was deposited on a Cu grid (ultrathin C film on a lacey carbon support film) and dried at room temperature. The sample was analyzed with a JEOL JEM-ARM200CF TEM operating at 200 kV (nanoFAB, University of Alberta). This microscope is equipped with a cold Field Emission Gun (cFEG), an ultra-high resolution pole piece, and a scanning TEM (STEM) device, which allows *Z*-contrast imaging in high angle annular dark field (HAADF) mode. Elemental mapping was done using EDXS in the STEM mode.

The trace element distributions in the three large thin sections were analyzed using X-ray fluorescence microscopy (XFM) at the Australian Synchrotron, Clayton, Australia. Overview maps were taken with an incident monochromatic X-ray beam of 18.5 keV, focused with Kirkpatrick-Baez mirrors, with 50-µm pixels and a dwell time per pixel of 2.5 ms. Selected regions of interest from the overview maps were then mapped with 3-µm pixels and a 0.15-ms dwell time. Elemental abundance data were collected using a Maia detector (Ryan et al., 2010, 2014), and the full spectrum data were processed using the GeoPIXE software program (Ryan, 2000).

3.3.3.3 Geochemical and reactive transport modeling

The activities of anions and cations as well as saturation indices (SI) of the leachates with respect to different mineral phases were calculated using PHREEQC V3.4 (Parkhurst and Appelo, 2013) and the minteq.v4 database released in 2017.

The MIN3P reactive transport code (Mayer et al., 2002; Bea et al., 2012) was used to simulate acid leaching experiments and to predict the impacts of mineral dissolution-precipitation processes (Appendix Table A2.2). Hamilton et al. (2020) previously modeled the acid leaching process of serpentinite tailings employing a similar modeling scheme. We adapted this model scheme to simulate our experiment. Hydraulic properties and mineral reactivity parameters were adapted from Bea et al. (2012). Mineral abundances used in the model (as volume fraction, Appendix Table A2.3) were based on Rietveld refinement results of the bulk processed kimberlite material used in the column experiments. Calcite ($CaCO_3$), hydroxylapatite [$Ca_5(PO_4)_3(OH)$], diopside ($MgCaSi_2O_6$), tremolite [$Ca_2Mg_5Si_8O_{22}(OH)_2$], orthoclase ($KAlSi_3O_8$), albite ($NaAlSi_3O_8$), quartz (SiO_2), phlogopite [$KMg_3AlSi_3O_{10}(OH)_2$], clinochlore [$Mg_5Al(AlSi_3O_{10})(OH)_8$], talc [$Mg_3Si_4 O_{10} (OH)_2$], lizardite (serpentine) [$Mg_3Si_2O_5(OH)_4$], and saponite (smectite) [$M^{m+}{}_{x/m}Mg_3(Al_xSi_{4-x})O_{10}(OH)_2 \cdot nH_2O$] were included with these initial abundances (Appendix Table A2.3). Chalcedony (SiO_2) and ferrihydrite (approximated as $Fe^{3+}{}_2O_3 \cdot 0.5H_2O$) were incorporated into the models as possible precipitates within the leachates using an initial volume fraction of 0 (Appendix Table A2.3). This was done in recognition that silica and iron oxides have been observed as common precipitates following acid leaching of ultramafic rocks (*e.g.,* Hamilton et al., 2020). The initial bulk density of the material was set to 1.61 g/cm^3 and porosity at 33.2 % of volume for a 28-day investigation. The length of the model column was set to be 9-cm depth and the initial chemical composition of pore water was based on the measured leachate chemistry from the second day of the leaching experiments (Appendix Table A2.4).

3.4 Results

3.4.1 Analytical results

3.4.1.1 Leachate chemistry

The pH of leachates from the columns treated with Milli-Q water, 0.04 M HCl and 0.08 M HCl remained above 7 for the entirety of the 28-day long experiments (Fig. 3.3a). The average pH of leachates collected from Milli-Q-treated experiments increased from an initial value of pH 8.88 to a final value of 9.80, while the average pH of leachates from columns treated with 0.04 M HCl and 0.08 M HCl decreased from initial values of pH 8.41 and 8.10 to final values of pH 8.02 and 7.45, respectively. By contrast, the average pH of leachates from the 0.12 M HCl and 0.16 M HCl columns decreased from initial values greater than 8 to final values of pH 6.48 and

5.97, respectively. The alkalinity of leachates from all five treatments decreased with time and increasing HCl concentration. The average alkalinity of leachates from Milli-Q-treated columns decreased slowly from 409.49 mg/L to 211.01 mg/L of $CaCO_3$ while the average alkalinity of leachates from columns treated with 0.16 M HCl decreased ultimately to the lowest measured value of 18.14 mg/L (Fig. 3.3b).

The concentrations of Mg, Ca, Si, Ni and Fe in leachates from Milli-Q-treated columns were always lower than those measured for leachates obtained from acid-treated columns (Fig. 3.3 and Appendix Table A2.5). The Mg concentration of the leachates from the acid treated columns increased with HCl concentration and time (Fig. 3.3c). For example, the concentration of Mg showed a continuous increasing trend from 109.5 ppm (day 2) to 1301 ppm (day 28) for leachates from columns treated with 0.16 M HCl. By contrast, the Ca concentration in acid-treated leachates increased rapidly in the beginning of the experiment and decreased after the 8th, 12th and 20th day for columns leached with 0.16 M, 0.12 M and 0.08 M HCl, respectively (Fig. 3.3d). The only exception was for columns treated with 0.04 M HCl, where the Ca concentration increased for the duration of the experiment. Concentrations of Si and Ni were greatest in the leachates from the 0.12 M HCl columns (Fig. 3.3g and Fig. 3.3e). The maximum Ni concentration in leachates was 27.95 ppm (day 28). Cr was detected at concentrations of 11.67 ppb or lower in all leachates (Fig. 3.3f). Given these minimal concentrations, Cr was not further considered in our detailed analysis. The concentration of Fe was initially high in the leachates obtained from 0.08 M HCl and 0.04 M HCl treated columns. The highest concentrations were measured on day 2 (2200 ppm and 1303 ppm) from the first leachates collected; thereafter, concentrations decreased until no Fe could be detected on day 17 (0.08 M HCl) and day 20 (0.04 M HCl) (Fig. 3.3h). Aqueous Fe concentrations were low (< 100 ppm) or below the detection limit of the instrument in the leachates from the Milli-Q, 0.12 M HCl and 0.16 M HCl experiments. As yellow precipitates formed in the leachates from the 0.12 M and 0.16 M HCl treated columns within a few hours after treatment, and because ICP-MS was conducted after the yellow precipitates were removed from the solutions, this could influence the evolution of leachate chemistry.

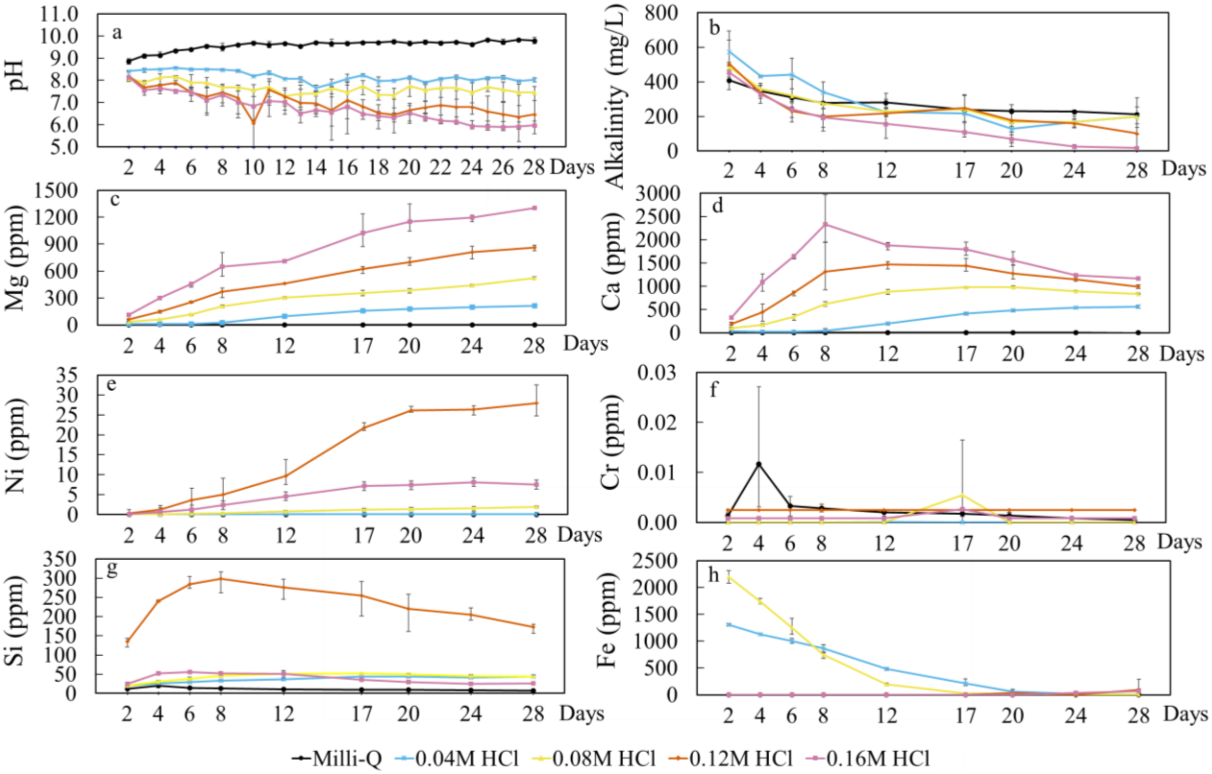

Figure 3.3 Evolution of the aqueous chemistry of daily leachate samples based on average values from triplicate column experiments which are directly proportional to acid strength.

3.4.1.2 Mineralogical changes

3.4.1.2.1 Mineralogy of the initial processed kimberlite

The initial MVK-dominated FRD, CRD and mixed FRD/CRD (Mmixed) displayed a similar mineralogical composition based on Rietveld refinement results (Fig. 3.4 and Appendix Table A2.6). Clay minerals such as lizardite $[Mg_3Si_2O_5(OH)_4]$, smectites, clinochlore $[Mg_5Al(Si_3Al)O_{10}(OH)_8]$ and talc $[Mg_3Si_4O_{10}(OH)_2]$ and other silicate minerals such as diopside ($CaMgSi_2O_6$), tremolite $[Ca_2Mg_5Si_8O_{22}(OH)_2]$, albite ($NaAlSi_3O_8$), orthoclase ($KAlSi_3O_8$), phlogopite $[KMg_3(Si_3Al)O_{10}(OH)_2]$ and quartz (SiO_2) were the main mineral phases detected. The smectite present in Venetia kimberlites has been characterized as the trioctahedral Mg- and Al-bearing mineral, saponite $[M^{m+}_{x/m}Mg_3(Al_xSi_{4-x})O_{10}(OH)_2\cdot nH_2O]$ (Zeyen et al., 2022). Calcite was present in CRD, FRD and mixed FRD/CRD with a content of 5.1 wt.%, 4.2 wt.% and 4.2 wt.%, respectively. Hydroxylapatite $[Ca_5(PO_4)_3(OH)]$ was present at abundances less than 2 wt.%.

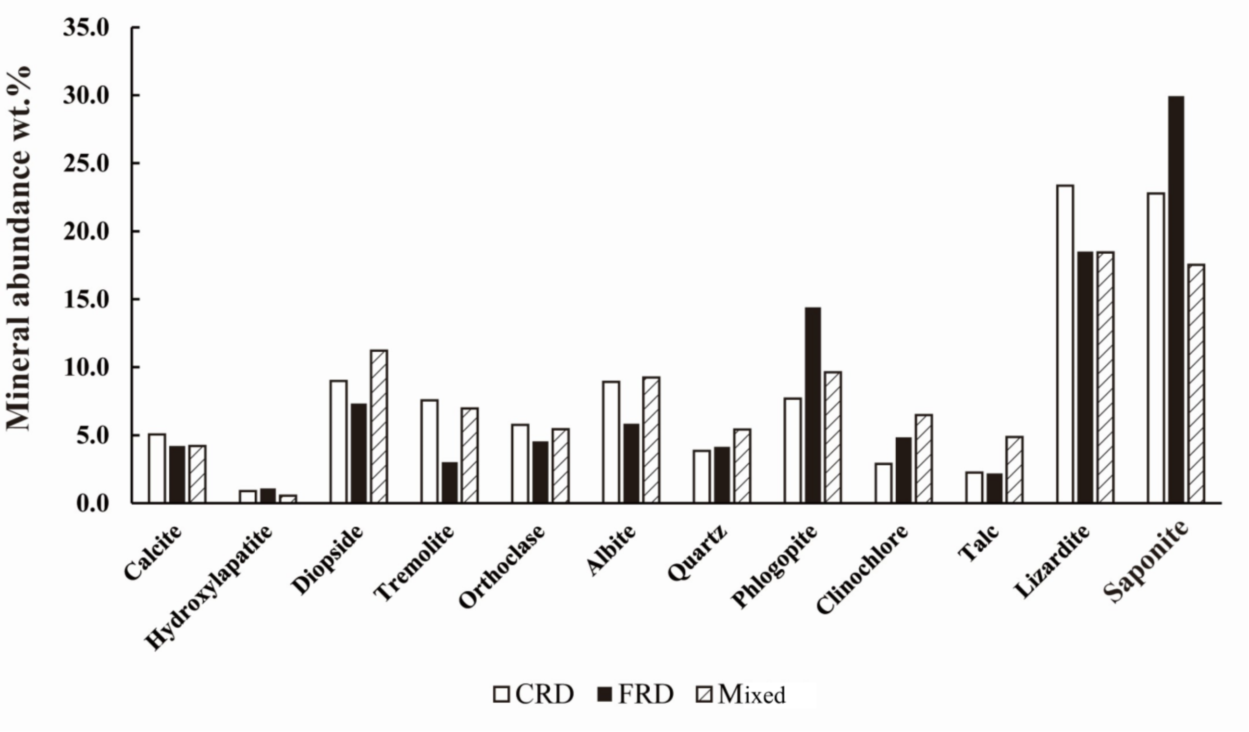

Figure 3.4 Mineralogical composition of CRD, FRD and mixed FRD/CRD (Mixed) based on Rietveld refinement results. Note the heterogeneity of kimberlite that is reflected in the comparison of the mixed values versus the FRD and CRD samples.

3.4.1.2.2 Mineralogy of the leached processed kimberlites

Rietveld refinements using XRD data were employed to assess which phases dissolved or precipitated in the column reactors during acid leaching experiments. Rietveld refinement results for solid residue samples collected from the tops (0.1–~1.9 cm), middles (~1.9–~5.5 cm) and bottoms (~5.5–9 cm) of the leached columns are shown in Fig. 3.5 and Appendix Table A2.6. No significant change in mineral abundance was observed for the Milli-Q water treated columns at any depth except for clinochlore (Fig. 3.5A). Clinochlore may have been flushed from the top of the Milli-Q water treated column to the bottom. As some minerals can react with HCl, the mineral contents of acid treated columns were expected to differ as a function of depth with dissolution occurring preferentially at the top of each column. The dissolution of calcite was observed in the top and middle samples of all acid treated columns (Fig. 3.5B–E). The calcite content was always over 4.4 wt.% in the bottom samples, which is similar to the amount of calcite in the initial mixture of FRD and CRD, indicating that calcite at the top and in the middle of columns reacted with HCl and acted as the main source for Ca in the leachates. The abundances of clay minerals (*e.g.,* lizardite, smectites) also decreased at the tops of the columns suggesting dissolution of these phases. By contrast, some minerals were more resistant to HCl, with their relative abundances decreasing with depth due to a proportion effect (*i.e.*, the dissolution of calcite and clay minerals resulted in the more resistant minerals representing a greater proportion of the samples by weight at the tops of columns). This effect was observed for diopside, orthoclase, albite and quartz in the acid treated columns. In addition to the more abundant minerals detected using XRD analyses, other minerals such as sulfides and oxides were observed in the columns with SEM-EDXS (Appendix Fig. A2.1).

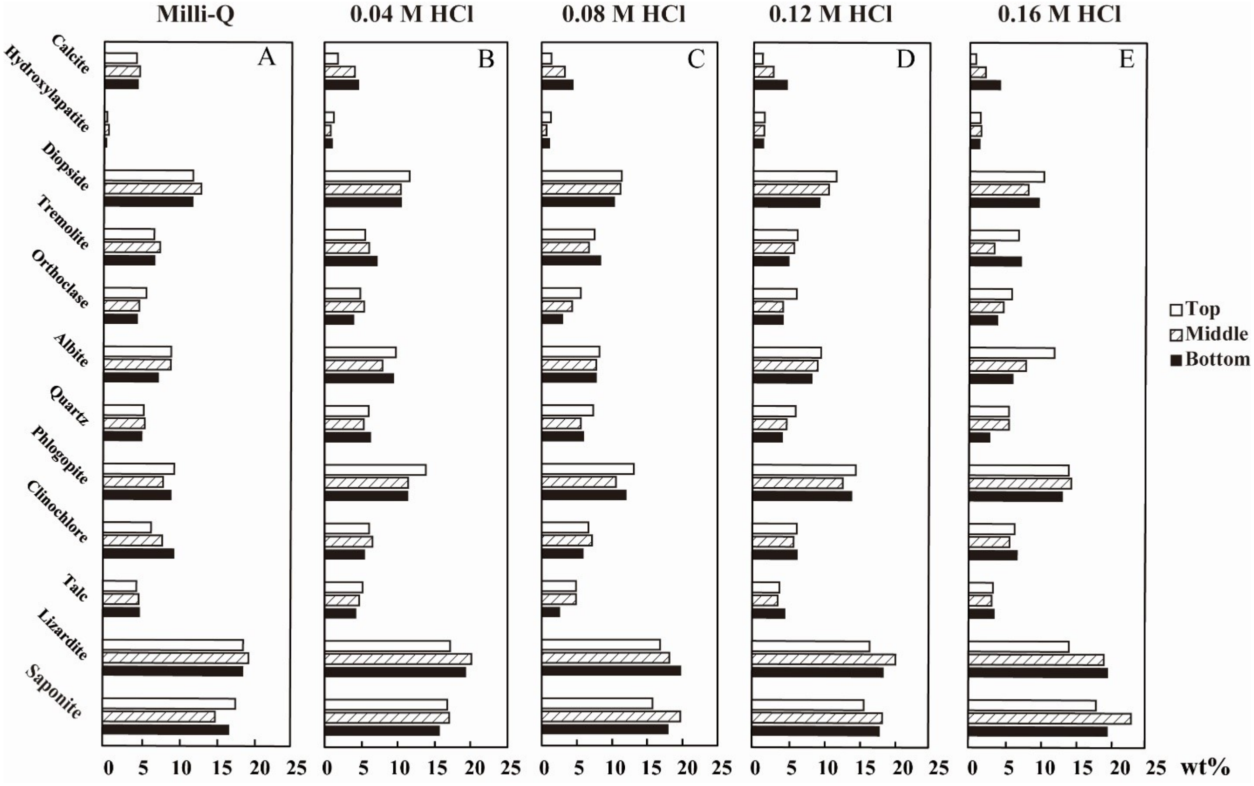

Figure 3.5 Rietveld refinement results at different depths of columns treated with (A) Milli-Q water; (B) 0.04 M HCl; (C) 0.08 M HCl; (D) 0.12 M HCl; (E) 0.16 M HCl highlighting the significant effect on calcite abundance.

3.4.1.2.3 Mineralogy of yellow precipitates

The thin yellow crusts collected at the top of the acid-leached columns (0–0.1 cm) contained similar mineral phases to those observed in the starting FRD/CRD mixture and in the leached columns based on XRD analysis. TEM-STEM-EDXS analyses showed that the yellow precipitates collected within leachates from a column treated with 0.16 M HCl on day 22 consisted of either elongated Si-rich particles (Fig. 3.6A, C, E) or Si and Fe-rich rounded grains measuring ~200–500 nm in diameter (Fig. 3.6B, D, F). TEM-SAED analyses performed on these two types of grains showed they are crystalline quartz (Fig. 3.6E) or amorphous (Fig. 3.6F). Based on SAED and XRD results, the yellow precipitates are most likely an admixture of quartz and/or amorphous silica with Fe-(hydr)oxide phase(s).

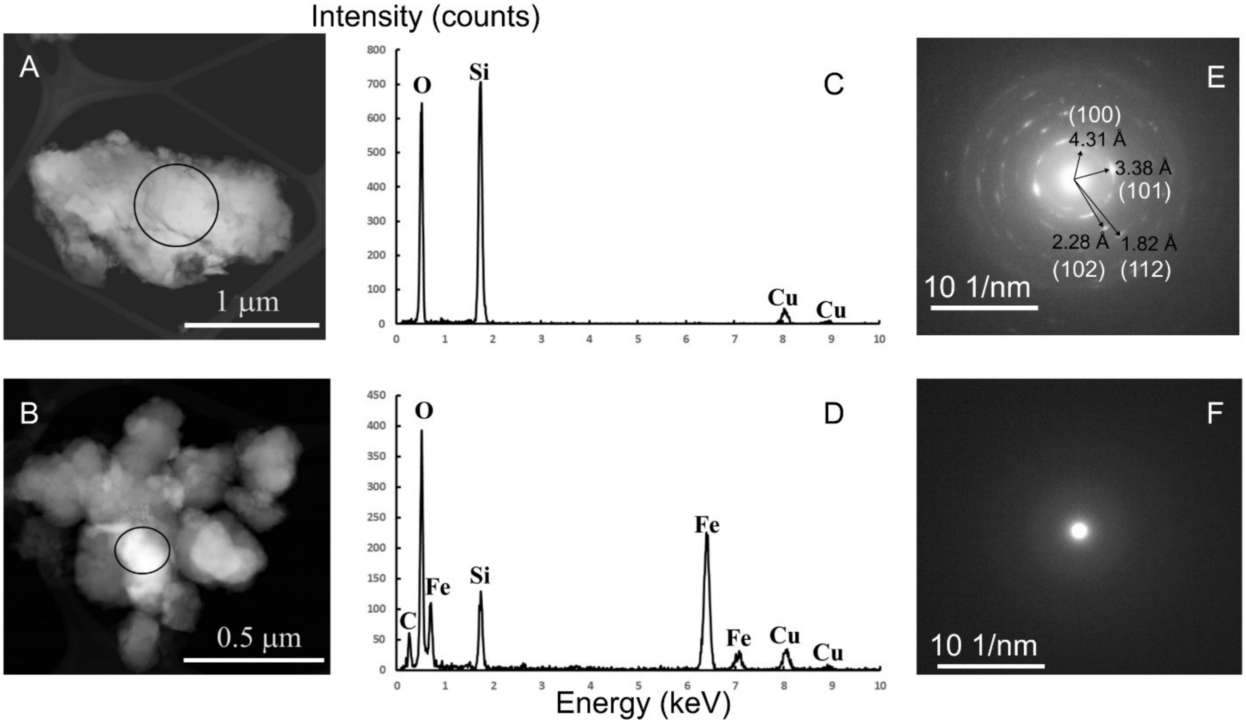

Figure 3.6 STEM micrographs of yellow precipitates collected within leachates obtained from 0.16 M HCl on day 22 consisted of (A) quartz and (B) Fe-(hydr)oxides. (C) and (D) EDXS data corresponding to the areas marked on (A) and (B). (E) and (F) Selected Area Electron Diffraction (SAED) patterns corresponding to the areas marked on (A) and (B).

3.4.1.3 Migration of metals during leaching experiments

XRF data, ICP-AES data (Appendix Table A2.7) and the isocon method (Grant, 1986) were used to analyze gains or losses of elements as a function of column depth in leaching experiments (Fig. 3.7). We considered Al_2O_3 to be immobile for ease of comparison with previous studies of enhanced weathering and mineral carbonation (Oskierski et al., 2013; Hamilton et al., 2018, 2020). Elements plotting on the isocon, which is denoted by a line, are considered to be relatively immobile. Elements plotting below the isocon are depleted relative to the initial composition of the residues used in our experiments. In contrast, elements that plot above the isocon line have become more concentrated in the columns compared to the starting composition of the residues. The elements, Cu, Zn, Co, and Cr, and major oxides, K_2O, Fe_2O_3, TiO_2, and Na_2O, in Milli-Q-treated columns consistently plot on or near the isocon line for samples from the tops, middles and bottoms of columns, indicating their limited mobility during Milli-Q water treatment. For all columns treated with HCl, Na_2O was always markedly depleted at all depths after experiments. The other elements and oxides at all depths of the 0.04 M HCl treated columns were relatively similar to the composition of the initial material. Carbon and CaO were depleted in the columns relative to the initial composition for residues at the tops and in the middle parts of columns treated with 0.08 M, 0.12 M and 0.16 M HCl. Ni was enriched in the bottom part of these three HCl-treated columns. Magnesium was depleted at the top parts of columns treated with 0.16 M HCl and became more concentrated relative to the starting composition in the bottoms of columns treated with Milli-Q, 0.08 M, 0.12 M and 0.16 M HCl. The greater concentration of magnesium in the bottom of the column treated with Milli-Q is consistent with the elevated abundance of clinochlore in this sample (Fig. 3.5A). Silica was more concentrated at the tops of columns owing to the depletion of other elements and the limited solubility of silica at low pH.

Synchrotron-based XFM analyses were performed on the thin sections to better describe the migration of transition metals such as Ni (Fig. 3.8). The distribution of Ni was homogeneous in the water-leached column (Fig. 3.8A) whereas Ni was leached from processed kimberlite at the tops of acid treated columns (Fig. 3.8B, C). This is most notable as the absence of small, Ni-rich sulfide grains at the tops of the acid-treated columns, where only large Ni-bearing grains of serpentine remain (Fig. 3.8B, C). Dissolution of serpentine was also observed (Appendix Fig. A2.2). Nickel was associated with sulfide minerals such as cobalt-bearing pentlandite

[$(Ni,Co,Fe)_9S_8$, Appendix Fig. A2.1A, C] in the processed kimberlite. Ti was associated with oxide minerals such as ilmenite ($FeTiO_3$, Appendix Fig. A2.1B,D). Aqueous Ti concentrations were usually below the detection limit (0.02279 ppb) whereas Ni concentrations were always below 27.85 ppm in leachates.

ICP-MS data for crusts and yellow precipitates on the interior walls of syringes are shown in Appendix Table A2.8 and Table A2.9. Dissolution of serpentine was observed to facilitate the migration of elements such as Si, Mg, Fe and Ni into both crusts and yellow precipitates (Appendix Fig. A2.2). The relative concentrations of elements in crusts and yellow precipitates compared with the initial mixture of FRD and CRD are shown in Fig. S3. The elements, Si, Cu, Sr, Pb P, and Mo, were depleted in crusts (Appendix Fig. A2.3A). However, Si was extremely enriched in yellow precipitates on the walls of syringes (Appendix Fig. A2.3B), showing an average enrichment factor over 13.3 times, consistent with the presence of quartz as detected using TEM. Sulfur, Zn and Ba were also concentrated in these yellow precipitates (Appendix Fig. A2.3B), with average enrichment factors of 2.94, 1.51 and 1.94, respectively. In addition, Na and S were both enriched in precipitates collected on the wall of a column treated with 0.12 M HCl.

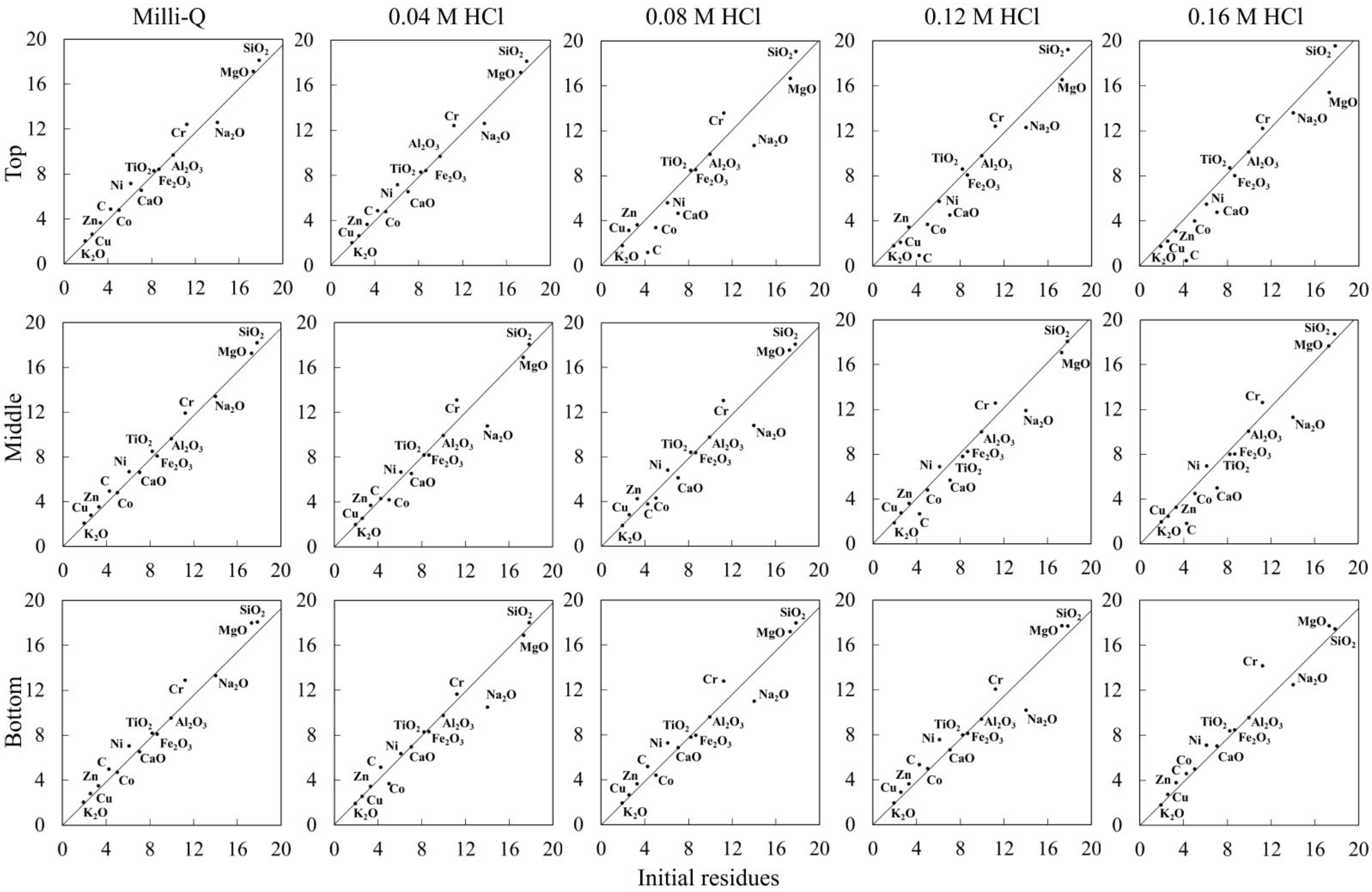

Figure 3.7 Isocon diagrams (after Grant, 1986) plotted based on conversion of XRF data, ICP-AES elemental abundance data and Leco data at different depths of columns.

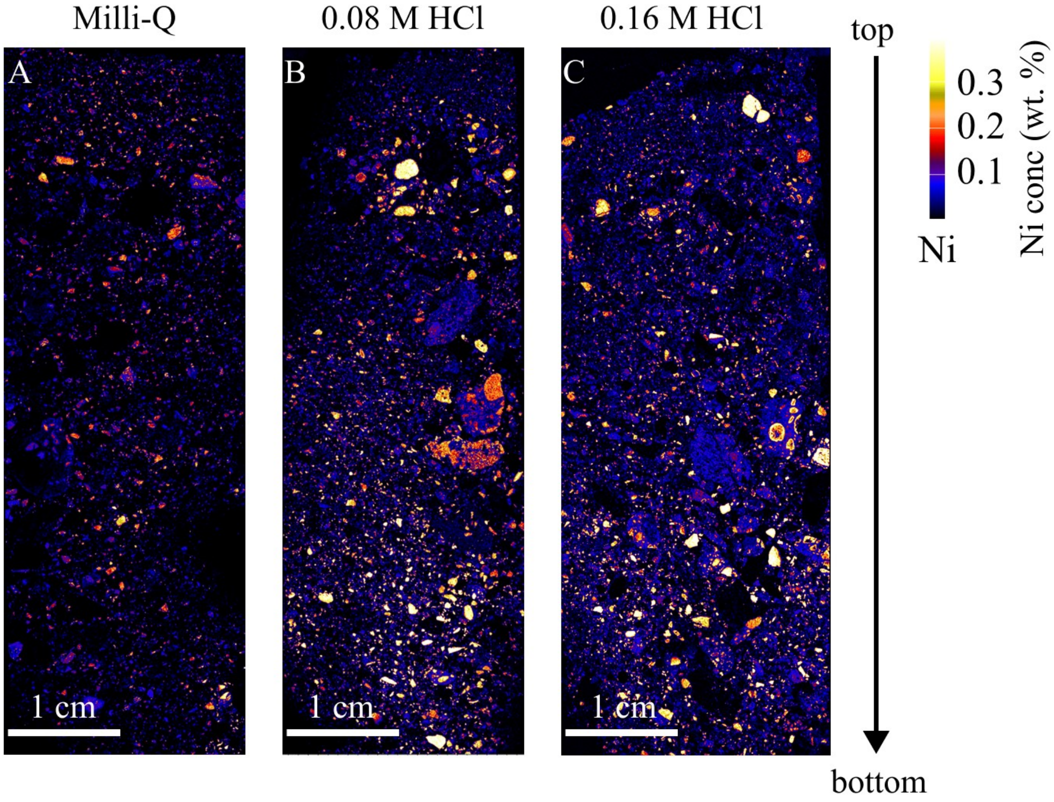

Figure 3.8 XFM maps of spatial distribution of Ni in the (A) Milli-Q, (B) 0.08 M HCl, and (C) 0.16 M HCl columns.

3.4.2 Modeling results

The saturation index (SI) values of nesquehonite ($MgCO_3 \cdot 3H_2O$), calcite, and hydromagnesite [$Mg_5(CO_3)_4(OH)_2 \cdot 4H_2O$] were calculated to assess whether carbonate minerals could precipitate from leachates. The SI values of ferrihydrite ($Fe^{3+}{}_2O_3 \cdot 0.5H_2O$) and amorphous silica were also determined since they were observed to form in the experiments (Fig. 3.9). All leachates were undersaturated with respect to nesquehonite ($MgCO_3 \cdot 3H_2O$) (Fig. 3.9A) with SI values less than 0 for all treatment types over the entire experiment. The leachates from the columns treated with 0.04 M HCl and 0.08 M HCl were undersaturated with respect to calcite ($SI<0$), and became supersaturated from day 17 and day 20, respectively. The calcite SI values (Fig. 3.9B) of leachates from the 0.12 M HCl and 0.16 M HCl columns were 0.98 and 0.30 before day 24 and day 20, respectively. All leachates were undersaturated with respect to hydromagnesite [$Mg_5(CO_3)_4(OH)_2 \cdot 4H_2O$] (Fig. 3.9C).

All leachates were supersaturated with respect to ferrihydrite ($Fe^{3+}{}_2O_3 \cdot 0.5H_2O$) (Fig. 3.9D) and amorphous silica (Fig. 3.9E). Leachates obtained from the 0.04 M and 0.08 M HCl treated columns were particularly supersaturated with respect to ferrihydrite whereas the SI values were lower for the leachates obtained from the 0.12 M and 0.16 M HCl treated columns (Fig. 3.9D). This can be explained by the observation that yellow precipitates usually formed in the leachates from the columns treated with 0.12 M and 0.16 M HCl. As such, precipitation had already occurred before the waters were filtered for cation and anion analysis.

The MIN3P model of the acid-leached columns showed the progression of acidic conditions downward through the columns at the end of the experiment (day 28) (Fig. 3.10). Modelled pH values for the column treated with Milli-Q water were always greater than 8 (Fig. 3.10A). The pH values of all columns treated with acid initially increased to approximately 2 within the first 1.5 cm of the depth, followed by a sudden increase to around 7 at varying depths, depending on the concentrations of acid employed (Fig. 3.10A). The cessation of calcite dissolution in the acid-leached columns aligned with the abrupt change of pH values, varying from 2.4 cm to 8 cm depth within the columns (Fig. 3.10B). The dissolution of calcite was limited to the upper section of the column treated with 0.04 M HCl, whereas in the column treated with 0.16 M HCl, calcite dissolution was observed to occur throughout almost the entire depth of the column. The observed increase in calcite dissolution with acid concentration was consistent with the Rietveld refinement results and the isocon plots. In columns treated with 0.04 M and 0.08 M HCl, the proportion of ferrihydrite formed was predicted to increase with depth. However, no ferrihydrite formation was observed in the columns treated with Milli-Q water or higher concentrations of acid (Fig. 3.10C). This model result could be consistent with the formation of Si- and Fe-rich yellow precipitates that were observed in the leachates, with greater amounts of precipitate having formed in leachates produced near the end of the experiment and using higher HCl concentrations. All the ferrihydrite in columns treated with 0.08 M and 0.16 M HCl fell out the bottoms of the columns due to the neutralization potential of the calcite being exceeded, and the limited buffering capacity of the other minerals.

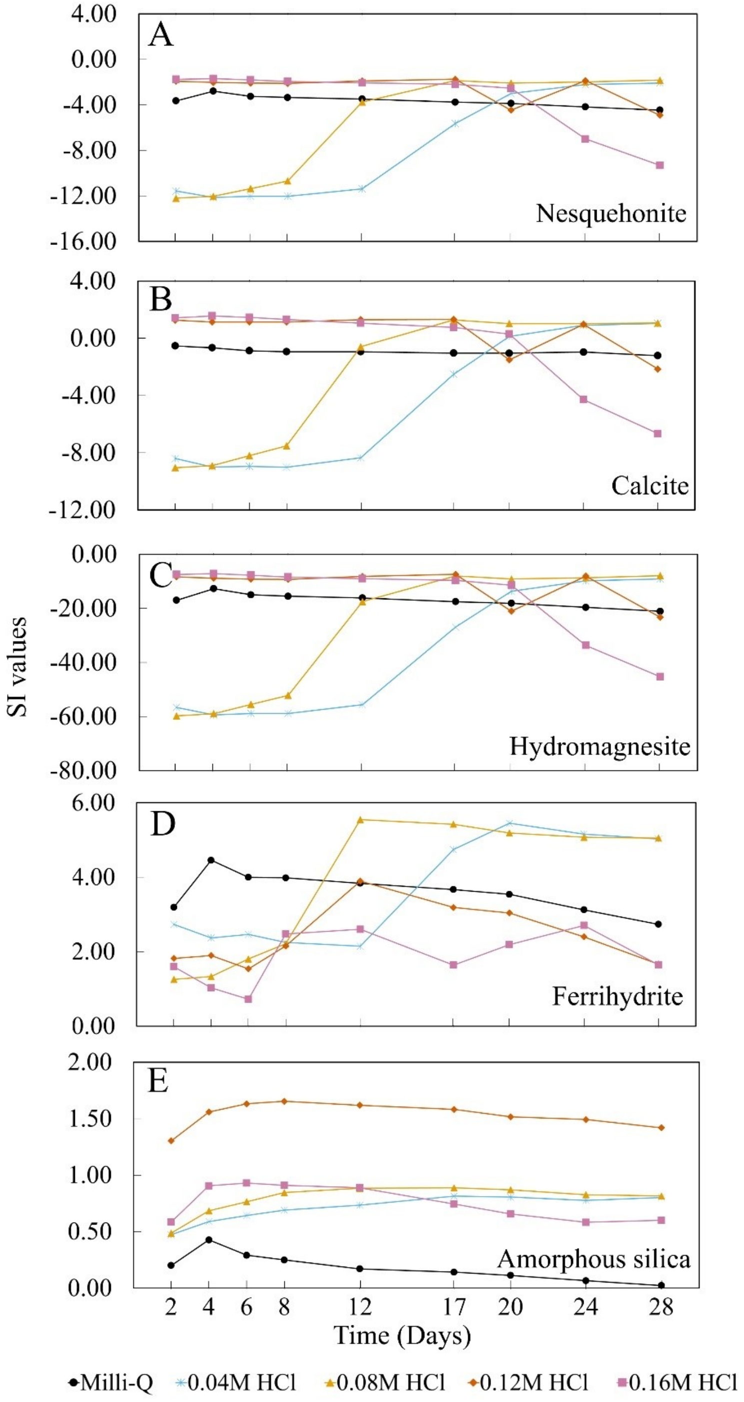

Figure 3.9 Saturation indices of the leachates with respect to different (mineral) phases *versus* time (days) as calculated using PHREEQC (Parkhurst and Appelo, 2013) from the minteq.v4 database released in 2017.

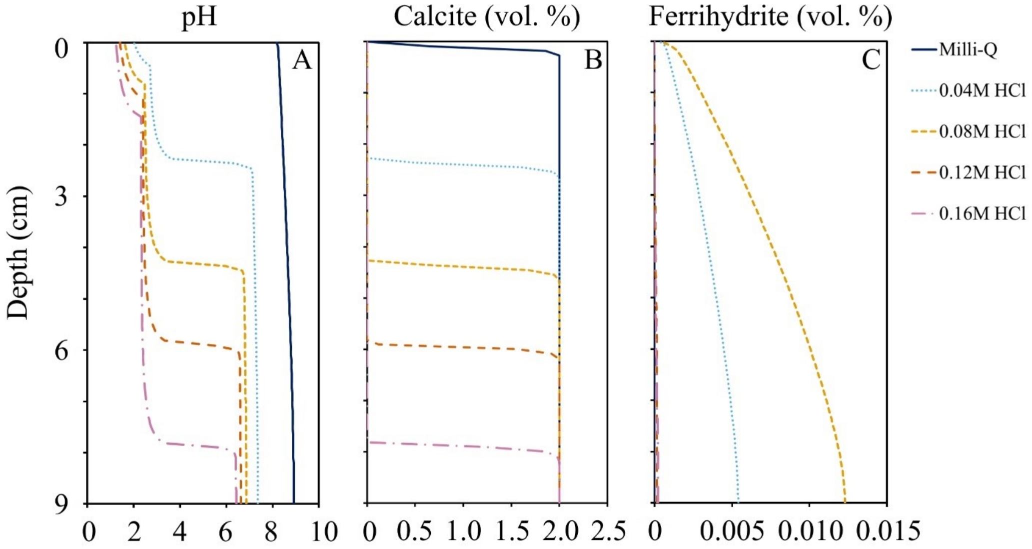

Figure 3.10 MIN3P modeled pH and mineral abundance reported as a volume fraction for calcite and ferrihydrite highlighting a pH versus calcite reaction front.

3.5 Discussion

3.5.1 Mineralogical controls on element mobility and solution chemistry

The preferential dissolution of calcite and clay minerals (*e.g.,* lizardite, smectites, talc, clinochlore) provided most of the Ca and Mg extracted from the acid-leached columns. Fe was sourced mainly from the dissolution of lizardite (Appendix Fig. A2.2). Other silicate minerals such as diopside, orthoclase, albite and quartz showed a limited degree of dissolution in the acid treated columns (Fig. 3.5B–E). Iron-rich yellow precipitates formed as an admixture of quartz and/or amorphous silica with Fe-(hydr)oxide phase(s) during the experiments.

The Ca concentrations in leachates from all acid-treated columns were much higher compared to leachates from Milli-Q-treated columns (Fig. 3.3d and Appendix Table A2.5). The dissolution of calcite is the main source for Ca (Fig. 3.5B–E). The smectite present in Venetia kimberlites is the trioctahedral Al-, Fe-, Mg- and Ca-rich mineral, saponite (Zeyen et al., 2022). The divalent cations such as Ca and Mg and transition metals such as Fe within the interlayers of saponite can be easily exchanged without modifying the T-O-T structure, *i.e.*, the octahedral layer (O) sandwiched between two tetrahedral silicate layers (T) (Zeyen et al., 2022). Thus, smectite can also act as a source for Ca and transition metals.

Based on Rietveld refinement results (Fig. 3.5B–E) and SEM-EDXS observations (Appendix Fig. A2.2), clay minerals (*i.e.,* lizardite, smectites, talc, clinochlore) were the main source for Mg. Elemental composition, crystal structure and reactive surface area control mineral dissolution rates (*e.g.,* Brantley, 2008; Power et al., 2013b). Metal-oxygen bond strength, influenced by cation size and co-ordination number, is one major control on mineral dissolution rate (Power et al., 2013b). For silicate minerals, dissolution rates tend to decrease with increasing silica polymerization, *i.e.,* the number of Si-O-Si bonds in a crystal structure (Brantley, 2008). The Si-O bond is typically the strongest and is the hardest to break in the structures of silicate minerals (Schott et al., 2009). For serpentine group minerals such as lizardite, it is a sheet silicate mineral with a 1:1 structure forming a tetrahedral silicate sheet and an octahedral brucite-like layer. The transition metals (*e.g.*, Fe, Ni) can substitute for Mg^{2+} in the brucite-like layers (*e.g.*, Park and Fan, 2004; Hamilton et al., 2018). These brucite-like layers have weaker bonding and are more easily dissolved compared to silicate layers (Park and Fan, 2004; Rozalen and Huertas, 2013). During the acid leaching process, minerals such as serpentine (Appendix Fig. A2.2) release divalent cations such as Mg^{2+} while leaving amorphous silica behind or even forming silica pseudomorphs of serpentine minerals (Wang et al., 2006; McCutcheon et al., 2015). The amorphous silica can also precipitate on the surfaces of primary phases such as serpentine grains (Hamilton et al., 2020). Furthermore, Hamilton et al. (2020) reported the observation of Fe-(hydr)oxide precipitates on the surfaces of brucite grains and within pore spaces. It is noteworthy that the processed kimberlite utilized in this study does not contain brucite. Therefore, the (hydr)oxide precipitates instead formed in the leachates and on the walls of columns treated with acid.

3.5.2. Fate of transition metals during acid-leaching of kimberlite

Transition metals (*e.g.*, Fe, Ni) were concentrated into sulfide minerals (Appendix Fig. A2.1A,C) and oxide minerals (Appendix Fig. A2.1B,D) in the processed kimberlite used in this study. They were also distributed homogeneously at low concentrations (~0.1 wt%) within grains of serpentine, likely by substitution for Mg within brucite-like layers (Figs. 3.8 and Appendix Fig. A2.2). Small grains of oxide minerals did not seem to be dissolved and thus they did not release transition metals as previously observed by Hamilton et al. (2018). As such, it is likely that dissolution of serpentine and sulfides is the primary source for Fe and other transition metals in leachates obtained in this study. After acid leaching experiments, most of the transition metals remained in serpentine and other feedstock minerals.. As a result, the formation of secondary minerals such as iron oxides was not associated with other transition metals (*e.g.*, Ni). By contrast, Hamilton et al. (2020) found that secondary Fe-(hydr)oxide minerals formed at a pH neutralization front within acid leaching columns containing brucite-bearing chrysotile mine residues. Transition metals (*e.g.*, Fe, Ni, Mn, Co, Cr) became progressively concentrated in these secondary Fe-(hydr)oxide minerals in acid-leached chrysotile mine tailings, thus providing the potential to recover these valuable metals (Hamilton et al., 2020). For acid-leached kimberlites, the Fe-(hydr)oxide minerals formed instead as a precipitate within leachates, leaving the other transition metals in solution rather than concentrating them at a discrete pH neutralization front.

The reason for this difference in migration of transition metals may be due to the specific mineralogy of these two ultramafic rock types. Jambor et al. (2007) measured and calculated different neutralization potentials (NP) for different minerals, noting that specimens of the same mineral species can show a large range of NP values as a function of different particle size distributions, reaction times and/or the temperature of acid digestion (Jambor et al., 2007). Here, the average pH of leachates from columns treated with 0.04 M HCl, 0.08 M HCl, 0.12 M HCl and 0.16 M HCl decreased to final values of 8.02, 7.45, 6.48 and 5.97, respectively (Fig. 3.3a). However, the pH of leachates produced using 0.08 M (*i.e.*, 0.16 N) H_2SO_4 to treat brucite-bearing chrysotile residues under similar experimental conditions was always greater than 9 throughout the whole experiment conducted by Hamilton et al. (2020). Within a limited pH range of approximately 1–2 pH units, there is a sharp increase in the sorption capacity of Ni cations onto hydrous iron oxide (ferrihydrite) surfaces, from near zero to nearly 100%. And this transition occurs within the pH range of approximately 6 to 8 (Bigham and Nordstrom, 2000). A different mineralogy or a smaller particle size may need to be used to form similar secondary Fe-(hydr)oxide minerals horizon in acid treated processed kimberlite columns. The neutralization potential of the Venetia kimberlite is simply too low compared to some other ultramafic rocks to create a pH swing within a column reactor. Instead, the traditional pH swing method (Park and Fan, 2004) provides a better alternative to recover transition metals by increasing the pH of leachates so these metals bind to Fe-(hydr)oxide precipitates.

Mass balance deviations (MBD) of Fe and Ni (Table 3.1) were calculated based on the ICP-MS data (for crusts, Table S8), ICP-AES data (for top, middle and bottom residues, Appendix Table A2.7), and the volume and mass fraction of the top, middle and bottom residues in each column reactor. As yellow precipitates formed within a few hours after treatment, and ICP-MS analyses were conducted after the formation of yellow precipitates, aqueous Fe was below the detection limit of less than 100 ppm in leachates from the Milli-Q, 0.12 M HCl and 0.16 M HCl experiments (Fig. 3.3h). Nickel concentrations were typically below the detection limit but occasionally had values up to 27.95 ppm in leachates (Fig. 3.3e). As such, the total mass of Fe and Ni in leachates was not included to estimate the mass balance deviation (MBD). The total masses of Fe and Ni in the initial residues were 4.65 g and 48.94 mg, respectively. Mass balance deviation (MBD) was calculated based on the equation:

$$\text{MBD}=\frac{M_R-M_O}{M_O}=\frac{M_{crust}+M_{top}+M_{middle}+M_{bottom}-M_O}{M_O} \quad (1)$$

Where M_R is the total mass of a metal in the crust and top, middle and bottom residues at the end of the experiment, M_O is the total mass of a metal in the initial residues, M_{crust} is the total mass of a metal in crust, M_{top} is the total mass of a metal in the top residues, M_{middle} is the total mass of a metal in the middle residues and M_{bottom} is the total mass of a metal in the bottom residues. A MBD value of 0 % would indicate a perfect mass balance. Deviations away from 0 % indicate either that some fraction of an element is unaccounted for in the system or that the material is highly heterogeneous in composition, which introduces error into the mass balance calculation.

The MBD values of Fe for columns treated with Milli-Q water, 0.04 M HCl, 0.08 M HCl, 0.12 M HCl and 0.16 M HCl are -4.04 %, -0.24 %, -2.49 %, -3.10 % and -3.43 %, respectively (Table 3.1). Counterintuitively, the Milli-Q-treated column shows the greatest extraction of Fe. This is almost certainly due to the heterogeneous distribution of Fe-bearing minerals in this column. For columns treated with acid, the amount of Fe extracted increases with HCl concentrations. By contrast, the MBD values of Ni for columns are greater than 0 %, indicating the inhomogeneity of the distribution of minerals in the initial residues. Additionally, measuring Ni at low abundances can be challenging and may be subject to greater uncertainty compared to Fe, which is present in relatively high abundances.

Table 3.3 The mass balance deviation (MBD) of Fe and Ni based on ICP-MS data, XRF data, ICP-AES data, volume and mass fraction in each column reactor.

Sample	Byproduct	Fe (g)	Total Fe (g)	MBD of Fe (%)	Ni (mg)	Total Ni (mg)	MBD of Ni (%)
Initial	original mixed samples	4.65	4.65	–	48.94	48.94	–
Milli-Q	crust	0.05	4.46	-4.04	0.62	56.66	15.76
	top residues	1.57			20.14		
	middle residues	1.43			17.74		
	bottom residues	1.40			18.16		
0.04 M HCl	crust	0.06	4.63	-0.24	0.70	53.08	8.45
	top residues	0.96			9.93		
	middle residues	1.85			22.29		
	bottom residues	1.76			20.16		
0.08 M HCl	crust	0.04	4.53	-2.49	0.44	54.84	12.05
	top residues	0.98			9.50		
	middle residues	1.81			21.97		
	bottom residues	1.70			22.93		
0.12 M HCl	crust	0.04	4.50	-3.10	0.48	55.52	13.44
	top residues	1.13			11.98		
	middle residues	1.68			20.47		
	bottom residues	1.65			22.59		
0.16 M HCl	crust	0.03	4.49	-3.43	0.41	54.07	10.46
	top residues	0.90			9.22		
	middle residues	1.67			21.64		
	bottom residues	1.87			22.80		

3.5.3 Mass balance for Ca and Mg

The mass balance deviations for Mg and Ca (Table 3.2) were also calculated using the compositions of solids and leachate chemistry. The total masses of Mg and Ca in the initial residues were 7.21 g and 3.70 g, respectively. The M_R for Mg and Ca in Equation (1) stands for the total mass of Mg or Ca in crust, top, middle and bottom residues and leachates. Depending on the treatment used, the MBD values for Mg ranged from 10.70 % to 17.17 % while the MBD values for Ca ranged from -0.48 % to +6.49 %.

The Mg and Ca concentrations in leachates (Fig. 3.3c and d) from three time intervals (from days 2–7, days 8–16 and days 17–28) were also used to estimate the amount of Mg and Ca extracted. Average values of the Mg and Ca concentrations were calculated for each time interval and the total concentration and extraction percentage of Mg and Ca in leachates treated with Milli-Q water, 0.04 M HCl, 0.08 M HCl, 0.12 M HCl and 0.16 M HCl were estimated (Appendix Table A2.10 and A2.11). The extraction percentage was calculated using Equation (2).

$$\text{Total extraction (\%)} = \frac{M_l}{M_o} = \frac{(Conc.1\times6+Conc.2\times9+Conc.3\times12)\times16.6\div10}{M_o} \qquad (2)$$

Where M_l is the total mass (mg) of a metal in leachates, M_O is the total mass (mg) of a metal in the initial residues, Conc.1 is the average concentration (ppm) of a metal in leachates from days [2, 8), Conc.2 is the average concentration (ppm) of a metal in leachates from days [8, 17), and Conc.3 is the average concentration (ppm) of a metal in leachates from days [17, 28]. The numbers 6, 9, and 12 refer to the number of days over which the experiment was conducted. The 16.6 represents the volume (in mL) of Milli-Q water or acid that was added daily. The use of the number 10 is a mathematical adjustment to convert our results into percentage terms.

The percentage of calcite dissolved by each type of acid treatment was assessed using Rietveld refinement results (Table 3.3). This led to the sudden increases in pH observed in Fig. 3.10A due to the consumption of protons during the dissolution process. The initial mixed bulk samples contained 4.2 wt.% calcite, which corresponds to a mass of approximately 3.4 g in each of the column reactors. The percentage of calcite dissolution is estimated to be 5.9 %, 20.6 %, 26.5 % and 35.3 % in the column reactors treated with 0.04 M, 0.08 M, 0.12 M and 0.16 M HCl, respectively. For the column reactor treated with Milli-Q water, the final estimated mass of calcite was 3.6 g (based on refined abundances of 4.3 wt.%, 4.7 wt.% and 4.6 wt.% in the top, middle and bottom of the column, respectively) and thus no calcite dissolution was detected. The accuracy in Rietveld quantitative phase analysis can be close to ±0.10 wt.% in stable fits with good precision (León-Reina et al., 2016); however, the relative error is likely to be greater due to the low abundance of calcite present. The amount of calcite dissolved increased with greater HCl concentration as expected. The proportion of Ca in the leachates obtained from calcite dissolution was also calculated (Table 3.4). Calcite dissolution is estimated to provide 50.00 %, 76.47 %, 65.38 % and 63.89 % of total Ca in the leachates treated with 0.04 M, 0.08 M, 0.12 M and 0.16 M HCl, respectively. Calcite dissolution was thus the main source for Ca in leachates.

A total of 4.74 Mt of ore were treated at the Venetia mine in 2016 and the mine emitted 0.21 Mt of CO_2e emissions the same year. Assuming all Mg^{2+} in leachates could precipitate as hydromagnesite, the most stable of the hydrated Mg-carbonate phases, the CO_2 offset potential of leached Mg was calculated and compared with the amount of CO_2 emitted by calcite dissolution (Fig. 3.11, Appendix Table A2.12 and A2.13). As all leachates were undersaturated with respect to hydromagnesite and the less soluble phase, nesquehonite (Fig. 3.9A, C), more CO_2 may need to be supplied into leachates to form carbonate minerals while adding base to increase the pH. The dissolution of clay minerals provides Mg, accounting for an estimated CO_2 offset potential of 2.1 %, 5.6 %, 9.8 % and 15.8 % for the column reactors treated with 0.04 M, 0.08 M, 0.12 M and 0.16 M HCl, respectively at Venetia. By contrast, calcite dissolution in the columns would correspond to an increase of 2.1 %, 8.1 %, 10.4 % and 14.3 % in annual CO_2 emissions at Venetia, which means CO_2 released by calcite dissolution would largely negate the CO_2 offset potential provided by Mg unless all the leached calcium is also recarbonated. However, the leached Ca from silicate dissolution could also provide an estimated CO_2 offset potential of 2.1 %, 2.5 %, 5.5 % and 8.1 % (Appendix Table A2.14). If no effort was made to reprecipitate the dissolved calcite, the net estimated CO_2 offset potentials are 2.1 %, 0.0 %, 4.9 % and 9.6 %. Moreover, if all calcite can be dissolved and all Mg in the processed kimberlite can be extracted with a higher concentration of HCl or another acid, the maximum CO_2 offset potential by Mg and Ca from silicate dissolution will be 292.9 % and 72.5 % (365.4 % total) of the mine's annual emissions, while the maximum CO_2 release from calcite will only be -41.7 % (Fig. 3.11). There is of course the possibility of recarbonating the Ca leached from calcite, but this would not constitute CO_2 sequestration since it was sourced from a pre-existing carbonate mineral. If all of the calcite were reprecipitated, dissolution of Mg- and Ca-bearing silicate minerals would sequester 4.2 %, 8.1 %, 15.3 % and 23.9 % of the Venetia mine's annual emissions, with greater offsets attainable using higher concentrations of HCl. Detailed Life Cycle Assessment (LCA) and Techno-Economic Analysis (TEA) are needed to optimize this leaching process and to ensure it is carbon negative, but this work is beyond the scope of the current study.

Table 3.2 Mass balance for Mg and Ca based on ICP-MS, and ICP-AES data.

Sample	Byproduct	Mg (g)	Total Mg (g)	MBD of Mg (%)	Ca (g)	Total Ca (g)	MBD of Ca (%)
Initial	original mixed samples	7.21	7.21	–	3.70	3.70	–
Milli-Q	crust	0.10	8.30	15.01	0.04	3.69	-0.48
	top residues	2.85			1.29		
	middle residues	2.64			1.19		
	bottom residues	2.71			1.16		
	leachates	0.00			0.00		
0.04 M HCl	crust	0.13	7.98	10.70	0.02	3.77	1.74
	top residues	1.58			0.55		
	middle residues	3.23			1.53		
	bottom residues	3.00			1.52		
	leachates	0.05			0.14		
0.08 M HCl	crust	0.09	8.17	13.31	0.02	3.79	2.32
	top residues	1.61			0.56		
	middle residues	3.20			1.36		
	bottom residues	3.14			1.51		
	leachates	0.14			0.34		
0.12 M HCl	crust	0.09	8.45	17.17	0.02	3.78	2.01
	top residues	2.00			0.65		
	middle residues	3.01			1.19		
	bottom residues	3.11			1.40		
	leachates	0.24			0.52		
0.16 M HCl	crust	0.07	8.44	16.97	0.02	3.94	6.49
	top residues	1.49			0.55		
	middle residues	3.14			1.06		
	bottom residues	3.34			1.60		
	leachates	0.39			0.72		

Table 3.3 Percentage of calcite dissolution for each column reactor.

Sample	Byproduct	Calcite (%)	Mass (g)	Calcite (g)	Total calcite (g)	Calcite dissolution (%)
Initial residues	/	4.2	80.5	3.4	3.4	/
Milli-Q	top residues	4.3	28.13	1.2	3.6	-5.9
	middle residues	4.7	26.52	1.2		
	bottom residues	4.6	25.72	1.2		
0.04 M HCl	top residues	1.8	16.26	0.3	3.2	5.9
	middle residues	4.2	33.32	1.4		
	bottom residues	4.8	31.70	1.5		
0.08 M HCl	top residues	1.4	16.96	0.2	2.7	20.6
	middle residues	3.3	32.31	1.1		
	bottom residues	4.5	31.50	1.4		
0.12 M HCl	top residues	1.3	20.91	0.3	2.5	26.5
	middle residues	2.8	29.76	0.8		
	bottom residues	4.8	29.76	1.4		
0.16 M HCl	top residues	0.8	16.76	0.1	2.2	35.3
	middle residues	2.2	31.13	0.7		
	bottom residues	4.4	31.93	1.4		

Table 3.4 Proportions of Ca from calcite and silicate dissolution in leachates.

Sample	Ca from calcite dissolution (g)	Total Ca in leachates (g)	Proportion of Ca from calcite dissolution in leachates (%)	Proportion of Ca from silicates dissolution in leachates (%)
M0-1	-0.10	0.00	/	/
M1-1	0.07	0.14	50.00	50.00
M2-1	0.26	0.34	76.47	23.53
M3-1	0.34	0.52	65.38	34.62
M4-1	0.46	0.72	63.89	36.11

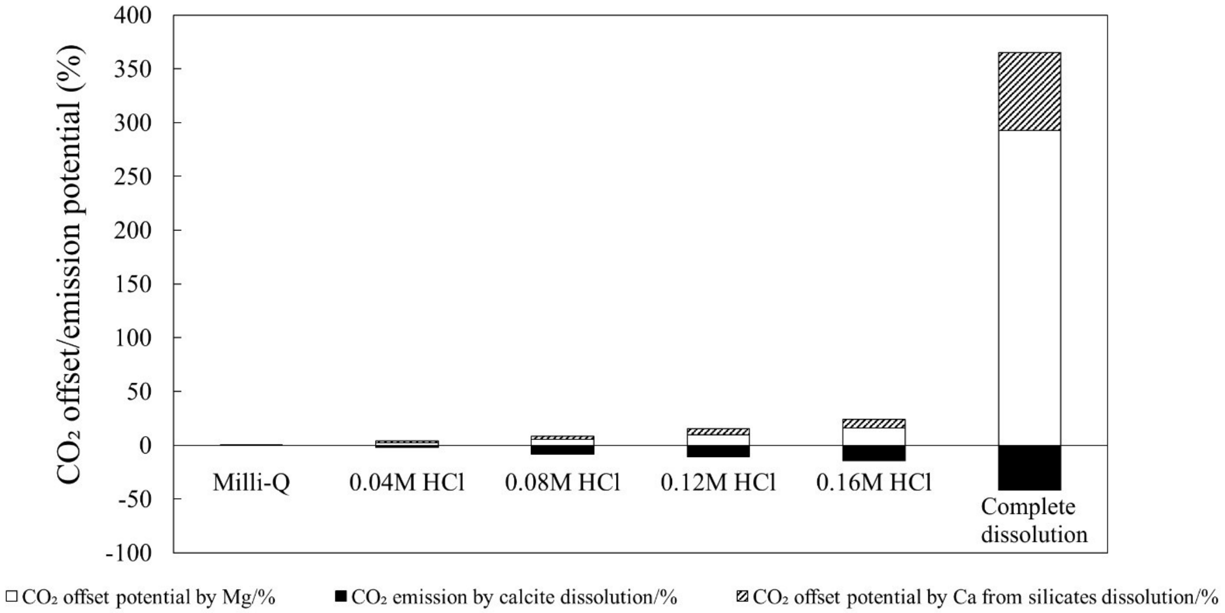

Figure 3.11 CO_2 offset potential of Mg and Ca silicate minerals and CO_2 emissions from calcite at the Venetia Mine.

3.6 Implications

This study proposed an acid-leaching method to enhance weathering of kimberlite for mineral carbonation. Silicate minerals provide Mg and Ca leached from columns, accounting for an estimated CO_2 offset potential ranging from 4.2–23.9 % of total emissions at Venetia. However, this acid-leaching method may not be suitable for calcite-rich processed kimberlite. The initial bulk samples contained 4.2 wt.% calcite and CO_2 released by calcite dissolution decreases the net CO_2 offset potential. Greater concentrations and/or amounts of acid could be used to access more of the full offset potential of Mg and Ca silicates while the CO_2 released by calcite dissolution must also be won back by recarbonating the leached Ca. Based on this study and the results of Hamilton et al. (2020), the very specific mineralogy of each ultramafic rock type and even each kimberlite facies will play a dramatic role in controlling mineral carbonation potential. For ultramafic residues rich in smectites and also carbonates, Zeyen et al. (2022) proposed the cation exchange method as a more suitable strategy for mineral carbonation because this process extracts labile Mg and Ca from smecites while minimizing calcite dissolution. However, this acid leaching method holds more promise for serpentine-rich and carbonate-poor residues such as processed kimberlite from the Gahcho Kué diamond mine in Canada.

A second carbonation step is necessary to form carbonate minerals from the leachates produced in this study. An increase in pH values of leachates treated with acid is needed. The use of a base such as NaOH to increase pH will increase the cost of carbonation and may also lead to CO_2 emissions during the production of the base. Although increasing the pH is an effective method for precipitating calcium and magnesium hydroxides, it is important to note that the introduction of CO_2 can decrease pH such that solutions are saturated with respect to calcite but undersaturated relative to brucite and Mg-carbonate minerals (Zhu et al., 2022a, 2022b). Zhu et al. (2022a, 2022b) found that when slurries of brucite and portlandite were reacted with 10% CO_2 in N_2, the portlandite reacted to form calcite whereas all of the brucite dissolved and no Mg-carbonate minerals formed. Alternatively, some microorganisms play a fundamental role in mineral dissolution and weathering of silicate minerals (also called bioleaching, *e.g.*, Power et al., 2010) and in modifying the DIC (dissolved inorganic carbon) and solution pH (*e.g.,* Dupraz et al., 2009). Power et al. (2011) demonstrated that heterotrophy increases DIC concentrations while phototrophy leads to alkalinization of leachates from acid-treated processed kimberlite to promote precipitation of carbonate minerals. Previous studies also showed that leachates inoculated with a microbial consortium dominated by cyanobacteria can accelerate carbonate mineral precipitation in both ultramafic mine residues and leachates derived from them (McCutcheon et al., 2014, 2016, 2017).

3.7 Conclusions

This study shows that the CO_2 sequestration potential of abundant, Mg-rich clay minerals and other Mg- and Ca-bearing silicates in kimberlites can only be accessed by first dissolving pre-existing Ca-carbonate minerals, which releases CO_2. Although Mg and Ca sourced from silicate minerals accounts for an estimated CO_2 offset potential ranging from 4.2–23.9 % at the Venetia diamond mine, the CO_2 emission potential of pre-existing calcite ranges from 2.1–14.3 %. After acid leaching experiments, most of the transition metals remained in feedstock minerals such as serpentine or oxides. Moreover, the formation of secondary minerals such as iron (hydr)oxides was not associated with other transition metals (*e.g.,* Ni) due to the low pH in leachates. The very specific mineralogy of each ultramafic rock type is a dramatic control on carbonation potential as well as how critical metals might be recovered during CO_2 mineralization. This must dictate which treatment pathways should be used for enhanced weathering and carbonation. Nowadays, large-scale field experiments and industrial applications related to carbon mineralization are still rare. Hence, ways to improve the efficiency of carbon mineralization in mine sites are of great importance. Based on the results of this study, dilute acid leaching holds the greatest potential for serpentine-rich and carbonate-poor mine residues. For carbonate-rich mine residues, dissolution of carbonate minerals during the acid leaching process will decrease the potential offset and recarbonating the leached Ca would be necessary while not constituting CO_2 sequestration.

3.8 Chapter 3 references

Assima, G.P., Larachi, F., Molson, J., and Beaudoin, G., 2014. Impact of temperature and oxygen availability on the dynamics of ambient CO_2 mineral sequestration by nickel mining residues. Chemical Engineering Journal, 240, pp.394-403.

Bea, S.A., Wilson, S., Mayer, K.U., Dipple, G.M., Power, I.M., and Gamazo, P., 2012. Reactive transport modeling of natural carbon sequestration in ultramafic mine tailings. Vadose Zone Journal, 11(2).

Berner, R.A., 1998. The carbon cycle and carbon dioxide over Phanerozoic time: the role of land plants. Philosophical Transactions of the Royal Society of London. Series B: Biological Sciences, 353(1365), pp.75-82.

Bigham, J.M., and Nordstrom, D.K., 2000. Iron and aluminum hydroxysulfates from acid sulfate waters. Reviews in mineralogy and geochemistry, 40(1), pp.351-403.

Bish, D.L., and Howard, S.A., 1988. Quantitative phase analysis using the Rietveld method. Journal of Applied Crystallography, 21(2), pp.86-91.

Bish, D.L., Carey, J.W., Vaniman, D.T., and Chipera, S.J., 2003. Stability of hydrous minerals on the martian surface. Icarus, 164(1), pp.96-103.

Bobicki, E.R., Liu, Q., Xu, Z., and Zeng, H., 2012. Carbon capture and storage using alkaline industrial wastes. Progress in Energy and Combustion Science, 38(2), pp.302-320.

Brantley, S.L., 2008. Kinetics of mineral dissolution. Kinetics of water-rock interaction, pp.151-210.

Bullock, L.A., James, R.H., Matter, J., Renforth, P., and Teagle, D.A., 2021. Global carbon dioxide removal potential of waste materials from metal and diamond mining. Frontiers in Climate, 3, p.694175.

Cheary, R.W., and Coelho, A., 1992. A fundamental parameters approach to X-ray line-profile fitting. Journal of Applied Crystallography, 25(2), pp.109-121.

Dupraz, C., Reid, R.P., Braissant, O., Decho, A.W., Norman, R.S., and Visscher, P.T., 2009. Processes of carbonate precipitation in modern microbial mats. Earth-Science Reviews, 96(3), pp.141-162.

Gadikota, G., Matter, J., Kelemen, P., and Park, A.H.A., 2014. Chemical and morphological changes during olivine carbonation for CO_2 storage in the presence of NaCl and $NaHCO_3$. Physical Chemistry Chemical Physics, 16(10), pp.4679-4693.

Goff, F., and Lackner, K.S., 1998. Carbon dioxide sequestering using ultramafic rocks. Environmental Geosciences, 5(3), pp.89-101.

Grant, J.A., 1986. The isocon diagram: a simple solution to Gresens' equation for metasomatic alteration. Economic Geology, 81(8), pp.1976-1982.

Hamilton, J.L., Wilson, S., Morgan, B., Turvey, C.C., Paterson, D.J., Jowitt, S.M., McCutcheon, J., and Southam, G., 2018. Fate of transition metals during passive carbonation of ultramafic mine tailings via air capture with potential for metal resource recovery. International Journal of Greenhouse Gas Control, 71, pp.155-167.

Hamilton, J.L., Wilson, S., Morgan, B., Harrison, A.L., Turvey, C.C., Paterson, D.J., Dipple, G.M. and Southam, G., 2020. Accelerating mineral carbonation in ultramafic mine tailings via direct CO_2 reaction and heap leaching with potential for base metal enrichment and recovery. Economic Geology, 115(2), pp.303-323.

Harrison, A.L., Power, I.M., and Dipple, G.M., 2013. Accelerated carbonation of brucite in mine tailings for carbon sequestration. Environmental Science & Technology, 47(1), pp.126-134.

Haug, T.A., Kleiv, R.A., and Munz, I.A., 2010. Investigating dissolution of mechanically activated olivine for carbonation purposes. Applied Geochemistry, 25(10), pp.1547-1563.

Hill, R.J., and Howard, C.J., 1987. Quantitative phase analysis from neutron powder diffraction data using the Rietveld method. Journal of Applied Crystallography, 20(6), pp.467-474.

Huijgen, W.J., Witkamp, G.J., and Comans, R.N., 2006. Mechanisms of aqueous wollastonite carbonation as a possible CO_2 sequestration process. Chemical Engineering Science, 61(13), pp.4242-4251.

International Energy Agency., 2021. World Energy Outlook 2021: Executive Summary. VGB PowerTech, 101. https://www.iea.org/reports/world-energy-outlook-2021/executive-summary. (Accessed 13 March 2023).

IPCC (Intergovernmental Panel on Climate Change)., 2018. Global Warming of 1.5°C. An IPCC Special Report on the impacts of global warming of 1.5°C above preindustrial levels and related global greenhouse gas emission pathways. In: The context of strengthening the global response to the threat of climate change, sustainable development, and efforts to eradicate poverty.https://www.ipcc.ch/site/assets/uploads/sites/2/2019/06/SR15_Full_Report_High_Res.pdf. (Accessed 13 March 2023).

IPCC., 2022. Climate Change 2022: Impacts, Adaptation and Vulnerability. https://report.ipcc.ch/ar6/wg2/IPCC_AR6_WGII_FullReport.pdf. (Accessed 13 March 2023).

Jambor, J.L., Dutrizac, J.E., and Raudsepp, M., 2007. Measured and computed neutralization potentials from static tests of diverse rock types. Environmental Geology, 52, pp.1173-1185.

Khan, S., Wani, O.B., Shoaib, M., Forster, J., Sodhi, R.N., Boucher, D., and Bobicki, E.R., 2021. Mineral carbonation for serpentine mitigation in nickel processing: a step towards industrial carbon capture and storage. Faraday Discussions, 230, pp.172-186.

Kurszlaukis, S., and Barnett, W.P., 2003. Volcanological and Structural Aspects of the Venetia Kimberlite Cluster–a case study of South African kimberlite maar-diatreme volcanoes. South African Journal of Geology, 106(2-3), pp.165-192.

Lacis, A.A., Schmidt, G.A., Rind, D., and Ruedy, R.A., 2010. Atmospheric CO_2: Principal control knob governing Earth's temperature. Science, 330(6002), pp.356-359.

Lackner, K.S., Wendt, C.H., Butt, D.P., Joyce Jr, E.L., and Sharp, D.H., 1995. Carbon dioxide disposal in carbonate minerals. Energy, 20(11), pp.1153-1170.

León-Reina, L., García-Maté, M., Álvarez-Pinazo, G., Santacruz, I., Vallcorba, O., De la Torre, A.G., and Aranda, M.A.G., 2016. Accuracy in Rietveld quantitative phase analysis: a comparative study of strictly monochromatic Mo and Cu radiations. Journal of Applied Crystallography, 49(3), pp.722-735.

Lechat, K., Lemieux, J.M., Molson, J., Beaudoin, G., and Hébert, R., 2016. Field evidence of CO_2 sequestration by mineral carbonation in ultramafic milling wastes, Thetford Mines, Canada. International Journal of Greenhouse Gas Control, 47, pp.110-121.

Margiotta, S., Mongelli, G., Summa, V., Paternoster, M., and Fiore, S., 2012. Trace element distribution and Cr (VI) speciation in Ca-HCO_3 and Mg-HCO_3 spring waters from the northern sector of the Pollino massif, southern Italy. Journal of Geochemical Exploration, 115, pp.1-12.

Mayer, K.U., Frind, E.O., and Blowes, D.W., 2002. Multicomponent reactive transport modeling in variably saturated porous media using a generalized formulation for kinetically controlled reactions. Water Resources Research, 38(9), pp.13-1.

McCutcheon, J., Power, I.M., Harrison, A.L., Dipple, G.M., and Southam, G., 2014. A greenhouse-scale photosynthetic microbial bioreactor for carbon sequestration in magnesium carbonate minerals. Environmental Science & Technology, 48(16), pp.9142-9151.

McCutcheon, J., Dipple, G.M., Wilson, S., and Southam, G., 2015. Production of magnesium-rich solutions by acid leaching of chrysotile: A precursor to field-scale deployment of microbially enabled carbonate mineral precipitation. Chemical Geology, 413, pp.119-131.

McCutcheon, J., Wilson, S., and Southam, G., 2016. Microbially accelerated carbonate mineral precipitation as a strategy for in situ carbon sequestration and rehabilitation of asbestos mine sites. Environmental Science & Technology, 50(3), pp.1419-1427.

McCutcheon, J., Turvey, C.C., Wilson, S., Hamilton, J.L., and Southam, G., 2017. Experimental deployment of microbial mineral carbonation at an asbestos mine: Potential applications to carbon storage and tailings stabilization. Minerals, 7(10), p.191.

Mervine, E.M., Wilson, S., Power, I.M., Dipple, G.M., Turvey, C.C., Hamilton, J.L., Vanderzee, S., Raudsepp, M., Southam, C., Matter, J.M., and Kelemen, P.B., 2018. Potential for offsetting diamond mine carbon emissions through mineral carbonation of processed kimberlite: an assessment of De Beers mine sites in South Africa and Canada. Mineralogy and Petrology, 112, pp.755-765.

Min, Y., and Jun, Y.S., 2018. Wollastonite carbonation in water-bearing supercritical CO_2: Effects of water saturation conditions, temperature, and pressure. Chemical Geology, 483, pp.239-246.

Munz, I.A., Brandvoll, Ø., Haug, T.A., Iden, K., Smeets, R., Kihle, J., and Johansen, H., 2012. Mechanisms and rates of plagioclase carbonation reactions. Geochimica et Cosmochimica Acta, 77, pp.27-51.

NOAA (National Oceanic and Atmospheric Administration), 2023. Global monthly mean CO_2. https://gml.noaa.gov/ccgg/trends/ (Accessed 13 March 2023).

Oskierski, H.C., Dlugogorski, B.Z., and Jacobsen, G., 2013. Sequestration of atmospheric CO_2 in a weathering-derived, serpentinite-hosted magnesite deposit: ^{14}C tracing of carbon sources and age constraints for a refined genetic model. Geochimica et Cosmochimica Acta, 122, pp.226-246.

Park, A.H.A., and Fan, L.S., 2004. CO_2 mineral sequestration: physically activated dissolution of serpentine and pH swing process. Chemical Engineering Science, 59(22-23), pp.5241-5247.

Parkhurst, D.L., and Appelo, C.A.J., 2013. Description of input and examples for PHREEQC version 3—a computer program for speciation, batch-reaction, one-dimensional transport, and inverse geochemical calculations. US geological survey techniques and methods, 6(A43), p.497.

Paulo, C., Power, I.M., Stubbs, A.R., Wang, B., Zeyen, N., and Wilson, S., 2021. Evaluating feedstocks for carbon dioxide removal by enhanced rock weathering and CO_2 mineralization. Applied Geochemistry, 129, p.104955.

Power, I.M., Dipple, G.M., and Southam, G., 2010. Bioleaching of ultramafic tailings by *Acidithiobacillus* spp. for CO_2 sequestration. Environmental Science & Technology, 44(1), pp.456-462.

Power, I.M., Wilson, S., Small, D.P., Dipple, G.M., Wan, W., and Southam, G., 2011. Microbially mediated mineral carbonation: roles of phototrophy and heterotrophy. Environmental Science & Technology, 45(20), pp.9061-9068.

Power, I.M., Wilson, S., and Dipple, G.M., 2013a. Serpentinite carbonation for CO_2 sequestration. Elements, 9(2), pp.115-121.

Power, I.M., Harrison, A.L., Dipple, G.M., Wilson, S., Kelemen, P.B., Hitch, M., and Southam, G., 2013b. Carbon mineralization: from natural analogues to engineered systems. Reviews in Mineralogy and Geochemistry, 77(1), pp.305-360.

Pretorius, W., and Barton Jr, J.M., 2003. Petrology and geochemistry of crustal and upper mantle xenoliths from the Venetia Diamond Mine–evidence for Archean crustal growth and subduction. South African Journal of Geology, 106(2-3), pp.213-230.

Pronost, J., Beaudoin, G., Tremblay, J., Larachi, F., Duchesne, J., Hébert, R., and Constantin, M., 2011. Carbon sequestration kinetic and storage capacity of ultramafic mining waste. Environmental Science & Technology, 45(21), pp.9413-9420.

Rietveld, H.M., 1969. A profile refinement method for nuclear and magnetic structures. Journal of Applied Crystallography, 2(2), pp.65-71.

Rozalen, M., and Huertas, F.J., 2013. Comparative effect of chrysotile leaching in nitric, sulfuric and oxalic acids at room temperature. Chemical Geology, 352, pp.134-142.

Ryan, C.G., 2000. Quantitative trace element imaging using PIXE and the nuclear microprobe. International Journal of Imaging Systems and Technology, 11(4), pp.219-230.

Ryan, C.G., Siddons, D.P., Kirkham, R., Dunn, P.A., Kuczewski, A., Moorhead, G., De Geronimo, G., Paterson, D.J., De Jonge, M.D., Hough, R.M., and Lintern, M.J., 2010, April. The new Maia detector system: methods for high definition trace element imaging of natural material. In AIP Conference Proceedings (Vol. 1221, No. 1, pp. 9-17). American Institute of Physics.

Ryan, C.G., Siddons, D.P., Kirkham, R., Li, Z.Y., De Jonge, M.D., Paterson, D.J., Kuczewski, A., Howard, D.L., Dunn, P.A., Falkenberg, G., and Boesenberg, U., 2014, April. Maia X-ray fluorescence imaging: Capturing detail in complex natural samples. In Journal of Physics: Conference Series (Vol. 499, No. 1, p. 012002). IOP Publishing.

Scarlett, N.V., and Madsen, I.C., 2006. Quantification of phases with partial or no known crystal structures. Powder Diffraction, 21(4), pp.278-284.

Schott, J., Pokrovsky, O.S., and Oelkers, E.H., 2009. The link between mineral dissolution/precipitation kinetics and solution chemistry. Reviews in Mineralogy and Geochemistry, 70(1), pp.207-258.

Sciortino, M., Mungall, J.E., and Muinonen, J., 2015. Generation of high-Ni sulfide and alloy phases during serpentinization of dunite in the Dumont Sill, Quebec. Economic Geology, 110(3), pp.733-761.

Seifritz, W., 1990. CO_2 disposal by means of silicates. Nature, 345, pp.486-486.

Stripp, G.R., Field, M., Schumacher, J.C., Sparks, R.S.J., and Cressey, G., 2006. Post-emplacement serpentinization and related hydrothermal metamorphism in a kimberlite from Venetia, South Africa. Journal of Metamorphic Geology, 24(6), pp.515-534.

Stubbs, A.R., Paulo, C., Power, I.M., Wang, B., Zeyen, N., and Wilson, S., 2022. Direct measurement of CO_2 drawdown in mine wastes and rock powders: Implications for enhanced rock weathering. International Journal of Greenhouse Gas Control, 113, p.103554.

Turvey, C.C., Wilson, S., Hamilton, J.L., and Southam, G., 2017. Field-based accounting of CO_2 sequestration in ultramafic mine wastes using portable X-ray diffraction. American Mineralogist: Journal of Earth and Planetary Materials, 102(6), pp.1302-1310.

Turvey, C.C., Hamilton, J.L., and Wilson, S., 2018. Comparison of Rietveld-compatible structureless fitting analysis methods for accurate quantification of carbon dioxide fixation in ultramafic mine tailings. American Mineralogist, 103(10), pp.1649-1662.

Walters, A.L., Phillips, J.C., Brown, R.J., Field, M., Gernon, T., Stripp, G., and Sparks, R.S.J., 2006. The role of fluidisation in the formation of volcaniclastic kimberlite: grain size observations and experimental investigation. Journal of volcanology and geothermal research, 155(1-2), pp.119-137.

Wang, B., Zeyen, N., Wilson, S., Funk, R., and Turvey, C.C., 2024. Quantifying the potential for mineral carbonation of processed kimberlite with the Rietveld-PONKCS method. American Mineralogist, accepted pending minor revisions as of 27 August 2023.

Wang, F., Dreisinger, D., Jarvis, M., Hitchins, T., and Trytten, L., 2021a. CO_2 mineralization and concurrent utilization for nickel conversion from nickel silicates to nickel sulfides. Chemical Engineering Journal, 406, p.126761.

Wang, F., Dreisinger, D., Jarvis, M., Trytten, L., and Hitchins, T., 2021b. Application and optimization of a quantified kinetic formula to mineral carbonation of natural silicate samples. Minerals Engineering, 161, p.106712.

Wang, F., and Dreisinger, D., 2022. Carbon mineralization with concurrent critical metal recovery from olivine. Proceedings of the National Academy of Sciences, 119(32), p.e2203937119.

Wang, L., Lu, A., Wang, C., Zheng, X., Zhao, D., and Liu, R., 2006. Nano-fibriform production of silica from natural chrysotile. Journal of colloid and interface science, 295(2), pp.436-439.

Wilson, S., Raudsepp, M., and Dipple, G.M., 2006. Verifying and quantifying carbon fixation in minerals from serpentine-rich mine tailings using the Rietveld method with X-ray powder diffraction data. American Mineralogist, 91(8-9), pp.1331-1341.

Wilson, S., Dipple, G.M., Power, I.M., Thom, J.M., Anderson, R.G., Raudsepp, M., Gabites, J.E., and Southam, G., 2009a. Carbon dioxide fixation within mine wastes of ultramafic-hosted ore deposits: Examples from the Clinton Creek and Cassiar chrysotile deposits, Canada. Economic Geology, 104(1), pp.95-112.

Wilson, S., Raudsepp, M., and Dipple, G.M., 2009b. Quantifying carbon fixation in trace minerals from processed kimberlite: A comparative study of quantitative methods using X-ray powder diffraction data with applications to the Diavik Diamond Mine, Northwest Territories, Canada. Applied Geochemistry, 24(12), pp.2312-2331.

Wilson, S., Barker, S.L., Dipple, G.M., and Atudorei, V., 2010. Isotopic disequilibrium during uptake of atmospheric CO_2 into mine process waters: Implications for CO_2 sequestration. Environmental Science & Technology, 44(24), pp.9522-9529.

Wilson, S., Dipple, G.M., Power, I.M., Barker, S.L., Fallon, S.J., and Southam, G., 2011. Subarctic weathering of mineral wastes provides a sink for atmospheric CO_2. Environmental Science & Technology, 45(18), pp.7727-7736.

Wilson, S., Harrison, A.L., Dipple, G.M., Power, I.M., Barker, S.L., Mayer, K.U., Fallon, S.J., Raudsepp, M., and Southam, G., 2014. Offsetting of CO_2 emissions by air capture in mine tailings at the Mount Keith Nickel Mine, Western Australia: Rates, controls and prospects for carbon neutral mining. International Journal of Greenhouse Gas Control, 25, pp.121-140.

Wunsch, A., Navarre-Sitchler, A.K., Moore, J., Ricko, A., and McCray, J.E., 2013. Metal release from dolomites at high partial-pressures of CO_2. Applied Geochemistry, 38, pp.33-47.

Zachara, J.M., Cowan, C.E., and Resch, C.T., 1991. Sorption of divalent metals on calcite. Geochimica et Cosmochimica Acta, 55(6), pp.1549-1562.

Zeyen, N., Wang, B., Wilson, S., Paulo, C., Stubbs, A.R., Power, I.M., Steele-Maclnnis, M., Lanzirotti, A., Newville, M., Paterson, D.J., and Hamilton, J.L., 2022. Cation exchange in smectites as a new approach to mineral carbonation. Frontiers in Climate, 4.

Zhu, B., Wilson, S., Zeyen, N., Raudsepp, M.J., Zolfaghari, A., Wang, B., Rostron, B.J., Snihur, K.N., von Gunten, K., Harrison, A.L., and Alessi, D.S., 2022a. Unlocking the potential of hydraulic fracturing flowback and produced water for CO_2 removal via mineral carbonation. Applied Geochemistry, 142, p.105345.

Zhu, B., Wilson, S., Raudsepp, M.J., Vessey, C.J., Zeyen, N., Safari, S., Snihur, K.N., Wang, B., Riechelmann, S., Paulo, C., and Power, I.M., 2022b. Accelerating mineral carbonation in hydraulic fracturing flowback and produced water using CO_2-rich gas. Applied Geochemistry, 143, p.105380.

Chapter 4

Influence of specific mineralogy on accelerated weathering and carbonation potential of ultramafic rocks and mineral wastes

4.1 Introduction

Global warming has become one of the most pressing environmental issues in the 21st century. Burning of fossil fuels and land use change have led to a substantial increase in the concentration of greenhouse gases (GHG), particularly carbon dioxide (CO_2), in the atmosphere. This increase in CO_2 levels has resulted in a rise in the Earth's average surface temperature, causing severe consequences such as rising sea levels, extreme weather events, loss of biodiversity, and threats to food and water security (IPCC, 2023). Given the detrimental impacts of global warming, there is an urgent need to decrease anthropic CO_2 emissions while implementing strategies to remove CO_2 from the atmosphere (IPCC, 2018). One promising approach to address this challenge is carbon mineralization, also called mineral carbonation, which is a process that involves conversion of CO_2 into stable and environmentally benign carbonate minerals by reaction with silicate and/or hydroxide minerals. Carbon mineralization is a natural process. Ultramafic rocks can weather under acidic conditions, releasing divalent metal cations, typically Mg^{2+} and Ca^{2+}, to react with dissolved CO_3^{2-} ions and precipitate carbonate minerals (*e.g.*, Seifritz, 1990; Lackner et al., 1995; Lackner, 2003). This process offers a long-term and effective solution for CO_2 sequestration and storage, thereby contributing to mitigate global climate change (*e.g.*, Lackner, 2003; Bobicki et al., 2012). Dissolution of rocks is a relatively slow process; as such, there is a need to develop techniques that accelerate weathering and carbon mineralization to make it a viable technology for CO_2 sequestration.

Numerous experimental and field studies have been conducted to investigate the reactivity of Mg- and/or Ca-bearing silicates and hydroxides, including minerals such as brucite [$Mg(OH)_2$] (*e.g.,* Assima et al., 2013; Harrison et al., 2013; Hamilton et al., 2020), portlandite [$Ca(OH)_2$] (*e.g.,* Ruiz-Agudo et al., 2013; Galan et al., 2015; Vance et al., 2015), wollastonite ($CaSiO_3$) (*e.g.,* Huijgen et al., 2006; Min and Jun, 2018), forsterite (Mg_2SiO_4) (*e.g.,* Haug et al., 2010;

Gadikota et al., 2014), serpentine group minerals [$Mg_3Si_2O_5(OH)_4$] (*e.g.,* Park and Fan, 2004; Power et al., 2013a; Hamilton et al., 2018), as well as other minerals such as the plagioclase mineral, anorthite ($CaAl_2Si_2O_8$) (*e.g.,* Munz et al., 2012). In recent years, there has been a growing interest in the study of ultramafic mine tailings as feedstocks for carbon mineralization including nickel mine residues (*e.g.,* Power et al., 2011; Pronost et al., 2011; Wilson et al., 2014), asbestos mine residues (*e.g.,* Wilson et al., 2006, 2009a; Power et al., 2010; McCutcheon et al., 2015, 2016, 2017; Lechat et al., 2016; Turvey et al., 2017, 2018; Hamilton et al., 2018, 2020) and diamond mine residues (*e.g.,* Power et al., 2011; Wilson et al., 2009b, 2011; Mervine et al., 2018; Paulo et al., 2021, 2023; Zeyen et al., 2022; Stubbs et al., 2022). This research interest is primarily due to the large volume of production of ultramafic mine tailings (Bullock et al., 2021), their high specific surface area as a result of ore processing, their reactivity with CO_2 due to the presence of highly reactive Ca and Mg minerals, and the potential to add concurrent benefits during this process, such as enhancing tailings stability or extracting critical metals.

Hamilton et al. (2020) carried out an acid leaching experiment on brucite-bearing chrysotile mine residues, discovering that secondary Fe-(hydr)oxide minerals formed at a pH neutralization front within the acid leaching columns. They observed that transition metals, such as Ni, Mn, Co, and Cr, became progressively concentrated in these secondary Fe-(hydr)oxide minerals in acid-leached chrysotile mine tailings, thereby presenting the potential for the recovery of these valuable metals. In a similar study, Wang et al. (2024, Chapter 3 of this thesis) conducted an acid leaching experiment using processed kimberlite from the Venetia diamond mine. They observed the formation of Fe-(hydr)oxide precipitates predominantly in the leachates and on the walls of the columns treated with acid. However, in their study, the formation of secondary Fe-(hydr)oxide minerals was not found to be associated with other transition metals (*e.g.,* Ni). The reason for this important difference may be due to differences in the mineralogy of these two ultramafic rock types (kimberlite versus brucite-bearing serpentinite).

Here, we assess the influence of mineralogy and mineral assemblages on accelerated weathering and carbon mineralization potential using different ultramafic mine residues or rocks. We conducted acid leaching column experiments on three different ultramafic materials: a processed kimberlite residue sample from the Gahcho Kué diamond mine (NWT, Canada) and two variably serpentinized dunite samples (hereafter referred to as serpentinite) from the Record Ridge project (BC, Canada). These samples were treated with dilute HCl to promote brucite and silicate mineral dissolution within laboratory column reactors. This study hypothesizes that the unique mineralogy of each ultramafic rock type, and each specific ultramafic facies within an ore deposit, will impact the extent to which the rock can be weathered and thus its carbonation potential. The focus of this study is on (1) identifying the specific minerals contributing to the leaching of Ca and Mg and (2) accounting of leached Mg and Ca for carbon sequestration.

4.2 Geological setting and sample collection

4.2.1 Gahcho Kué diamond mine

The Gahcho Kué mine is located in the Northwest Territories (NWT) of Canada, approximately 280 kilometers northeast of Yellowknife (Fig. 4.1) and situated in the southeast Archaean Slave craton (Hetman et al., 2004). The mine consists of four kimberlite pipes, and the age of emplacement of the cluster has been determined to be 538.6 ± 2.5 Ma (Hetman et al., 2004). The pipes in the Gahcho Kué kimberlite cluster were formed by multiple intrusions, with textures ranging from hypabyssal kimberlite (HK) to diatreme-facies tuffisitic kimberlite breccia (TKB). The TKB kimberlite endmember exhibits features such as unaltered country rock xenoliths, pelletal lapilli, serpentinized olivines, and a matrix of microlitic phlogopite and serpentine without carbonate, while the HK kimberlite contains fresh forsterite in a groundmass of monticellite ($CaMgSiO_4$), phlogopite, perovskite, serpentine, and carbonate. A transition from TKB to HK is observed in parts of the four pipes, characterized by a decrease in pelletal lapilli and country rock xenoliths, and increases in groundmass crystallinity, the proportion of fresh olivine, and xenolith digestion (Hetman et al., 2004).

At the Gahcho Kué mine, kimberlite ore is first crushed to reduce the particle size and facilitate further processing. After crushing, the kimberlite particles are further ground to achieve the desired size distribution using high-pressure grinding rolls (HPGR). Processed kimberlite that exhibits grain sizes below 0.8 mm is classified as fine processed kimberlite (FPK). The larger-sized material, ranging from 0.8–8 mm, is identified as coarse processed kimberlite (CPK) and may be retained for potential future re-crushing and processing. The proportion of CPK to FPK generated at the GK mine is 67:33% by mass.

4.2.2 Record Ridge project

The Record Ridge project, located in southern British Columbia, Canada, is an ultramafic magnesium-rich rock deposit (Fig. 4.1). The project is situated within with the Quesnel Terrain of the Intermontane Belt, a geological region characterized by a diverse assemblage of volcanic, sedimentary, and intrusive rocks that are mainly of Mesozoic and Paleozoic age (SRK, 2009). The region is predominantly composed of variably serpentinized peridotite, primarily dunite and wehrlite, which serve as the principal hosts for magnesium, nickel and Platinum Group Elements (PGE) (SRK, 2009). The presence of brucite in these rocks makes them of particular interest for carbon mineralization.

Two samples, one less serpentinized (RRP1) and the other more serpentinized (RRP2), were collected from the Record Ridge deposit in 2020. RRP1 was collected from 49.048030N, 117.875167W at an elevation of 1335 m above sea level (ASL) and RRP2 was collected from 49.041486N, 117.894496W at an elevation of 1458 m ASL.

Figure 4.1 Location of Gahcho Kué mine and Record Ridge project, Canada (modified from Mervine et al., 2018).

4.3 Materials and methods

4.3.1 Sample preparation

The processed kimberlite from the Gahcho Kué mine (GK) was already pulverized and no further processing was done to reduce the grain size. The two serpentinite samples from Record

Ridge (RRP1 and RRP2) were crushed utilizing an automated agate mortar and pestle to produce particle sizes that are equivalent to those of the CPK (0.8–8 mm) and FPK (<0.8 mm) from Gahcho Kué to allow for better comparison of the results between the different materials.

4.3.2 Experimental design

Acid leaching columns were created by filling 60 mL polypropylene syringes with ultramafic material (Fig. 4.2). Each of the ultramafic materials (GK, RRP1, RRP2) was used for both Milli-Q water-treated and acid-treated (0.12 M HCl) columns and a replicate of each column was made for a total of 4 columns of each material and 12 columns in total. Each of the ultramafic materials added to the columns consisted of 67% coarse material (54 g) and 33% fine material (26.5 g) for a total of 80.5 g of material in each column, which filled each column to a depth of 9 cm. The coarse/fine mixture was chosen to optimize dissolution kinetics and flow rate for leachate recovery following the results of Wang et al. (2024,Chapter 3 of this thesis) as well as to mirror the CPK:FPK ratio produced at the Gahcho Kué mine.

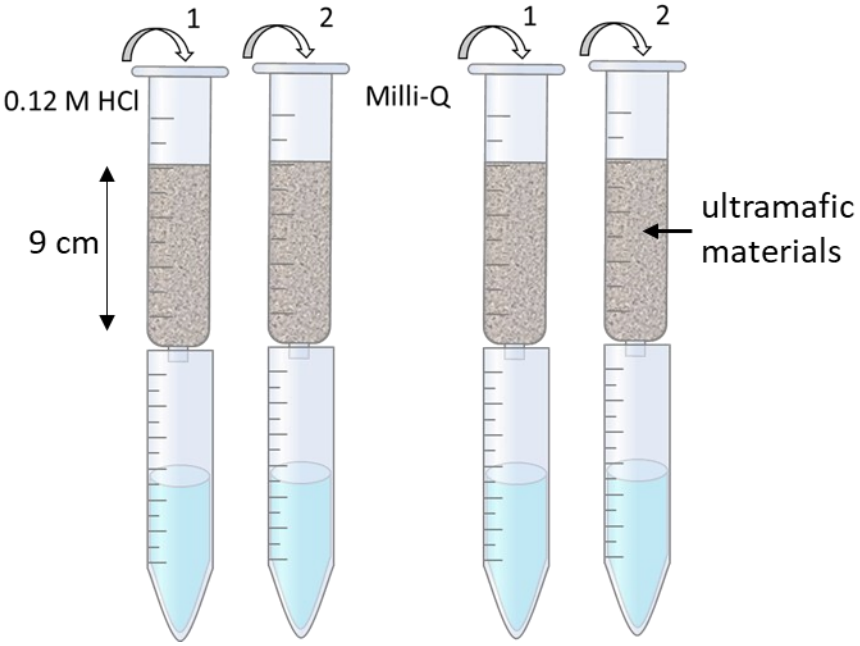

Figure 4.2 Schematic illustration of the column experiment.

Following the method of Chapter 3, a circular piece of nylon fabric mesh with a diameter of 2.67 cm and a pore size of 1 micrometer was positioned at the bottom of each syringe before introducing the mixed tailings into the columns to prevent the escape of fine particles into the leachates from the base of each syringe. Either 16.6 mL of Milli-Q water (18.2 MΩ·cm) or 0.12 M HCl was applied daily, and leachates were collected separately from the bottom of the syringe, in 50 mL tubes, every day for a duration of 28 days. Sampling of leachates was done prior to addition of the next daily dose of water or dilute HCl.

After 28 days of treatment, each column was dried in a fume hood for 60 days. The completeness of drying was monitored by measuring the mass of each column reactor. After this period, one replicate from each of the Milli-Q water-treated columns and the GK and RRP1 columns treated with 0.12 M HCl was divided into three sections: (1) the upper 0—~3 cm of residues within each column, (2) the middle ~3—~6 cm of residues from each column, and (3) the bottom ~6–9 cm of residues. The formation of an orange layer was observed in the RRP2 columns treated with 0.12 M HCl. One of the RRP2 replicate columns was instead separated into five parts: (1) the upper 0—~0.3 cm of residues within the column, (2) the orange layer ~0.3—~1.3 cm of residues from the column (middle1), (3) the middle ~1.3—~4 cm of residues from the column (middle2), (4) the middle ~4—~6.5 cm of residues from the column (middle3), and (5) the bottom ~6.5–9 cm of residues. It should be noted that orange precipitates also sometimes formed in the leachate collected from the bottoms of the RRP2 columns. Leachates were filtered every day after their collection through 0.22 μm polyethersulfone (PES) membranes to collect the orange precipitates on filter membranes. Afterward, any orange precipitates remaining in the leachates were collected using centrifugation (7200 rpm, 5 min) and rinsed three times with Milli-Q water. As replicate columns were conducted during the experiment, one column was used for bulk chemistry and XRD analyses using the sampling methods described above whereas the other column was used for petrographic thin sectioning.

4.3.3 Analytical methods

4.3.3.1 Leachate chemistry

A Thermo Scientific Orion Star A215 pH/Conductivity Meter was used to measure pH, conductivity and temperature of leachates immediately after their collection and before filtration. Cation and anion concentrations of the 0.22 um-filtered leachates were measured for days 2, 4, 6, 8, 12, 16, 20, 24 and 28 following the methods described below.

4.3.3.1.1 Cation analysis by inductively coupled plasma mass spectrometry (ICP-AES)

Dissolved metals, S, and P in leachates were analyzed using a Thermo iCAP6300 Duo inductively coupled plasma-optical emission spectrometer (ICP-OES) at the Natural Resources Analytical Laboratory (NRAL), University of Alberta.

4.3.3.1.2 Anion analysis using the colourimetric method

Concentrations of anions (Cl^-, NO_2^-, NO_3^-, PO_4^{3-} and SO_4^{2-}) as well as NH_4^+ were determined using a Colourimetric Thermo Gallery Plus Beermaster Autoanalyzer at NRAL, University of Alberta.

4.3.3.2 Chemistry and mineralogy of solids

4.3.3.2.1 Bulk elemental chemistry

Bulk elemental chemistry of the initial mixture of processed kimberlite, serpentinite rock samples and the upper, middle, and bottom samples of processed kimberlite and serpentinite rock samples from each column after the experiment, was determined at SGS Mineral Services Geochemical Laboratory in Vancouver, Canada. X-ray fluorescence (XRF) was used to determine the abundances of major element oxides including Al_2O_3, CaO, Cr_2O_3, Fe_2O_3, K_2O, MgO, MnO, Na_2O, P_2O_5, SiO_2, TiO_2 and V_2O_5. The concentrations of minor elements such as Co, Cu, Zn and Ni were determined using inductively coupled plasma atomic emission spectroscopy (ICP-AES). Leco analysis, which employs combustion and measurement of volatiles using Infrared spectroscopy, was used for total S and C abundances.

4.3.3.2.2 Powder X-ray diffraction (XRD)

Solids subsampled from columns and the initial processed kimberlite and serpentinite samples were prepared for analysis using powder X-ray diffraction (XRD). Samples were pulverized using an automated agate mortar followed by 7 minutes of milling in anhydrous ethanol with agate grinding elements in a McCrone Micronizing Mill. Samples were air-dried at room temperature within a fume hood after micronization. As the processed kimberlite samples are rich in smectites (*i.e.*, swelling clays), the upper, middle and bottom processed kimberlite samples from the water-leached and acid-leached columns and one sample of the initial mixture of fine and coarse processed kimberlite were each calcium exchanged in 150 mL of 1 M $CaCl_2$

solution following the method described by Mervine et al. (2018). Samples were then stored in a NaCl slurry box at a relative humidity (RH) of 75% to stabilize the basal (001) spacing of smectites to ~15 Å (after Bish et al., 2003).

XRD patterns were collected using a Bruker D8 Advance X-ray diffractometer equipped with a high-speed energy-dispersive LYNXEYE XE-T detector and a cobalt tube that was operated at 35 kV and 40 mA in the Department of Earth and Atmospheric Sciences, University of Alberta. Data were collected from 3–80° 2θ using a step size of 0.02° 2θ at a rate of 1 s/step. Mineral phase identification was conducted using the DIFFRAC.EVA XRD phase analysis software (Bruker) with reference to the International Center for Diffraction Data Powder Diffraction File 4+ database (ICDD PDF4+). Rietveld refinements (Rietveld, 1969; Hill and Howard, 1987; Bish and Howard, 1988) with XRD data were used to determine mineral abundances using TOPAS 5 (Bruker). Fundamental parameters peak fitting (Cheary and Coelho, 1992) was used for all phases. The method of Partial Or No Known Crystal Structure (PONKCS; Scarlett and Madsen, 2006) was used to model the peak profiles of smectites and lizardite to account for turbostratic stacking disorder as implemented by Mervine et al. (2018) and Wang et al. (2024, Chapter 2 of this thesis). The detection limit of most minerals is generally ~0.1 wt.% for the conditions used to collect XRD data.

4.3.3.2.3 Microfocus X-ray computed tomography

Eight columns were scanned using a Nikon XTH 225 ST industrial CT scanner in the Permafrost Archives Science Laboratory at the University of Alberta. All scans were calibrated to g/cm^3 using an aluminum calibration piece of known density (2.71 g/cm^3). All samples were scanned using the following settings: beam energy 225 kV, beam current 133 μA, exposure 8 fps, gain 30 dB, digital gain 2, effective pixel size 20 μm, 4 frames averaged per projection and the projections optimized. All scans were helical style with the cabinet temperature held steady at 23 °C throughout the scans. Porosity distribution analysis was done using the Dragonfly software package (Comet Technologies Canada).

3.3.2.4 Synchrotron X-ray fluorescence microscopy and X-ray absorption spectroscopy

Trace element distributions were measured in three of the 12 thin sections using X-ray fluorescence microscopy (XFM) at the Australian Synchrotron (ANSTO), Clayton, Australia.

Overview maps were taken with an incident monochromatic X-ray beam of 18.5 keV, focused with Kirkpatrick-Baez mirrors, with 50-µm pixels and a dwell time per pixel of 2.5 ms. Selected regions of interest from the overview maps were then mapped with 3-µm pixels and a 0.15-ms dwell time. Elemental abundance data were collected using a Maia detector (Ryan et al., 2010, 2014), and the full spectrum data were processed using the GeoPIXE software program (Ryan, 2000).

X-ray Absorption Spectroscopy (XAS) analyses were carried out at the XAS Beamline ID-12 at the Australian Synchrotron (ANSTO), Clayton, Australia. For the acquisition of XAS spectra, the photon energy delivered to the sample was calibrated using a nickel metal foil (Kraft et al. 1996). All samples and reference materials were analyzed under a helium environment at room temperature. Spectra were recorded at the Ni-K absorption edge in fluorescence mode using a 100-element HP-Ge detector (Mirion, France). The energy was scanned from 8133 to 8313 eV with a dwell time of 2 seconds per step in 10 eV steps, then the step size was decreased to 0.25 eV over the absorption edge from 8313 to 8383 eV. In the post-edge range, the step size was increased to units of 0.035 $Å^{-1}$, to a maximum of $k = 14$ $Å^{-1}$ (9082 eV) while increasing dwell time linearly from 2 to 8 seconds per step. Fluorescence XAS data were pre-processed using in-house software (Sakura) to sum the spectra collected from each detector element. All XAS data were then processed using ATHENA (freeware) for background subtraction, normalisation, principle component analysis (PCA), and least squares linear combination fitting (LCA) (Ravel and Newville, 2005). E0 was defined as the maximum of the first peak in the derivative. PCA indicates two components can explain 99.997% of the spectral features in the samples. Target transformation analysis indicates the most suitable standards include serpentine, olivine, pentlandite and ferrihydrite. Linear combination fits were performed with combinations of up to three (PCA + 1) of these standards over the XANES range from -20 to +100 eV relative to E0. Individual standard weights were restricted between 0 and 1 while the sum of components was not restricted. A Hamilton test was used to determine whether inclusion of minor fit components significantly improved the fit above a 95% confidence level, (https://www.danielsoper.com/statcalc/calculator.aspx?id=37).

4.3.3.3 Geochemical and reactive transport modeling

The activities of anions and cations as well as saturation indices (SI) of the leachates with respect to different mineral phases were calculated using PHREEQC V3.4 (Parkhurst and Appelo, 2013) and the minteq.v4 database released in 2017. The pCO_2 and pO_2 values used in this study are 4.00×10^{-4} and 0.21 atm, respectively.

The MIN3P reactive transport code (Mayer et al., 2002; Bea et al., 2012) was used to simulate acid leaching experiments and to predict the impacts of mineral dissolution–precipitation processes (Appendix Table A3.1). Hydraulic properties and mineral reactivity parameters were adapted from Bea et al. (2012). Mineralogical abundances used in the model (as volume fractions, Appendix Table A3.2) were based on Rietveld refinement results of the bulk processed kimberlite material used in the column experiments. Calcite ($CaCO_3$), magnetite (Fe_3O_4), forsterite (Mg_2SiO_4), augite [$(Ca,Na)(Mg,Fe,Al,Ti)(Si,Al)_2O_6$], tremolite [$Ca_2Mg_5Si_8O_{22}(OH)_2$], orthoclase ($KAlSi_3O_8$), albite ($NaAlSi_3O_8$), quartz ($SiO_2$), phlogopite [$KMg_3AlSi_3O_{10}(OH)_2$], clinochlore [$Mg_5Al(AlSi_3O_{10})(OH)_8$], talc [$Mg_3Si_4O_{10}(OH)_2$], lizardite (serpentine) [$Mg_3Si_2O_5(OH)_4$], and saponite (smectite) [$M^{m+}_{x/m}Mg_3(Al_xSi_{4-x})O_{10}(OH)_2\cdot nH_2O$] were included with at their initial abundances as measured in the processed kimberlite (Appendix Table A3.2). Lizardite [$Mg_3Si_2O_5(OH)_4$], clinochlore [$Mg_5Al(Si_3Al)O_{10}(OH)_8$], talc [$Mg_3Si_4O_{10}(OH)_2$], tremolite [$Ca_2Mg_5Si_8O_{22}(OH)_2$], forsterite ($Mg_2SiO_4$), brucite [$Mg(OH)_2$] and magnetite ($Fe_3O_4$) were included at their measured initial abundances for modelling of RRP1 and RRP2 columns (Appendix Table A3.3). Chalcedony (SiO_2) and ferrihydrite (approximated as $Fe^{3+}{}_2O_3\cdot0.5H_2O$) were incorporated into the models as possible precipitates within the leachates using an initial volume fraction of 0 (Appendix Table A3.2) because silica and Fe-(hydr)oxides have been observed as common precipitates following acid leaching of ultramafic rocks (Hamilton et al., 2020; Chapter 3). The initial bulk density of the material was set to 1.61 g/cm^3 and porosity at 33.2 % of volume for a 28-day investigation based on Chapter 3. The length of the model column was set to be 9-cm depth and the initial chemical composition of pore water was based on the measured leachate chemistry from the second day of the leaching experiments (Appendix Table A3.4).

4.4 Results

4.4.1 Analytical results

4.4.1.1 Leachate chemistry

Throughout the experimental period, the pH values for the Gahcho Kué (GK) columns consistently remained above 7 (Fig. 4.3a and Appendix Table A3.5). The average pH of leachates collected from Milli-Q water-treated GK experiments varied from an initial value of pH 8.38 to 9.30, while the average pH of leachates from columns treated with 0.12 M HCl varied from 7.33 to 7.82. For the Record Ridge Project 1 (RRP1) samples, the pH of leachates from the columns treated with Milli-Q water was always greater than 8, with average pH values for replicate columns between 8.00 to 8.93 (Fig. 4.3b). However, when treated with 0.12 M HCl, the pH values fell below 2. In the case of the RRP2 samples, the leachate pH values for columns treated with Milli-Q water showed a similar trend to that observed for the RRP1 columns with pH remaining above 9 (Fig. 4.3c). Interestingly, very different pH trends were observed for the replicate RRP2 columns treated with acid. The values of pH in leachates from one RRP2 column treated with 0.12 M HCl decreased from 8.78 to less than 2 and became stable at a value of ~1 on day 16 while pH values in leachates from the replicate RRP2 column treated with acid decreased to 2.68 at day 8 and increased to around 8 again at day 15 and kept constant at ~8 thereafter.

The leachates from all GK, RRP1 and RRP2 columns treated with Milli-Q water consistently exhibited low concentrations of Ca in the range of 0–70 ppm (Fig. 4.3d, e, f). For the columns subjected to acidic treatment, the average Ca concentration in leachates from the Gahcho Kué (GK) columns decreased over time from 1108 ppm at day 2 to 473.1 ppm at day 28. It is noteworthy that the calcium concentration in the leachates from all the Record Ridge (RRP1 and RRP2) columns, irrespective of the treatment administered, remained consistently lower than 110 ppm.

The concentration of Mg in the leachates from all GK, RRP1 and RRP2 columns treated with Milli-Q water was low, in the range of 0–200 ppm (Fig. 4.3g, h, i). The average Mg concentration in leachates from the Gahcho Kué (GK) columns treated with 0.12 M HCl increased from 273.9 ppm on day 2 to 1173 ppm on day 16 after which it stabilized at ~1100 ppm. The average Mg concentration in leachates from the RRP 1 columns treated with 0.12 M HCl increased from 334.6 ppm on day 2 to stabilize at ~1100 ppm from day 16 onwards, while approximately stable from days 16 to 28 there was more variation than seen in the GK columns with a maximum of 1232 ppm on day 16 and a local minimum of 1064 ppm on day 24. The Mg concentration in leachates from one RRP2 column treated with 0.12 M HCl was stable from day 2 until day 12 and then decreased from 1478 ppm on day 12 to 714.2 ppm on day 28. The Mg concentration in leachates from the other RRP2 column treated with acid varied throughout the experiment from ~1300 ppm on days 2–6, before decreasing to ~1100 between days 8–12 and increasing again to ~1500 ppm from days 16–28.

4.4.1.2 Mineralogical changes

4.4.1.2.1 Mineralogy of the initial processed kimberlite and serpentinite rock samples

Based on Rietveld refinement results, clay minerals such as lizardite [$Mg_3Si_2O_5(OH)_4$], smectites, clinochlore [$Mg_5Al(AlSi_3)O_{10}(OH)_8$] and talc [$Mg_3Si_4O_{10}(OH)_2$] and other silicate minerals such as phlogopite [$KMg_3(AlSi_3)O_{10}(OH)_2$], albite ($NaAlSi_3O_8$), orthoclase ($KAlSi_3O_8$), tremolite [$Ca_2Mg_5Si_8O_{22}(OH)_2$], augite [$(Ca,Na)(Mg,Fe,Al,Ti)(Si,Al)_2O_6$], forsterite ($Mg_2SiO_4$), and quartz ($SiO_2$) were the main mineral phases detected in the initial processed kimberlite from Gahcho Kué (Fig. 4.4 and Appendix Table A3.6). The smectite present in Gahcho Kué kimberlites has been characterized as the trioctahedral Mg- and Al-bearing mineral, saponite [$M^{m+}_{x/m}Mg_3(Al_xSi_{4-x})O_{10}(OH)_2 \cdot nH_2O$] (Zeyen et al., 2022). Calcite ($CaCO_3$) and magnetite (Fe_3O_4) were present at 1.4 wt.% and 1.6 wt.%, respectively. No brucite [$Mg(OH)_2$] was detected in the processed kimberlite.

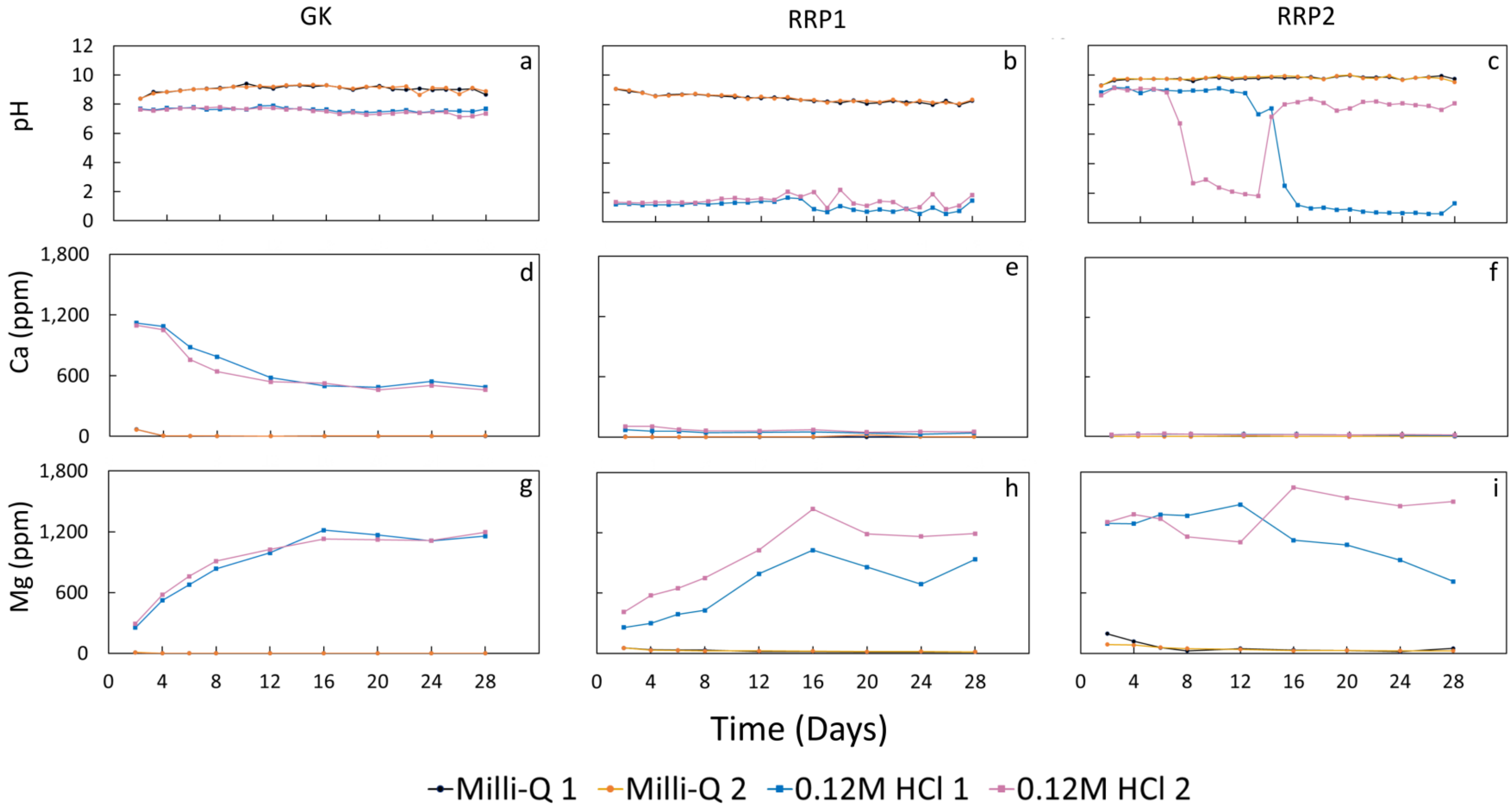

Figure 4.3 Evolution of the pH and Ca and Mg concentrations of daily leachate samples.

The two serpentinite rock samples from Record Ridge had simpler mineral assemblages (Fig. 4.4 and Appendix Table A3.6). Clay minerals such as lizardite [$Mg_3Si_2O_5(OH)_4$], clinochlore [$Mg_5Al(AlSi_3)O_{10}(OH)_8$] and talc [$Mg_3Si_4O_{10}(OH)_2$] and other minerals such as forsterite (Mg_2SiO_4), brucite [$Mg(OH)_2$] and magnetite (Fe_3O_4) were detected in both RRP1 and RRP2 samples. Tremolite [$Ca_2Mg_5Si_8O_{22}(OH)_2$] was only present in RRP1 at a low abundance of 1.5 wt.%. The proportions of forsterite and lizardite in RRP1 and RRP2 are very different: forsterite and lizardite are present in RRP1 at 34.8 wt.% and 33.8 wt.%, respectively, whereas forsterite comprises 8.2 wt.% and lizardite 64.1 wt.% of RRP2. Brucite, which is a product of serpentinization was present at 0.7 wt.% in RRP1 and at 3.5 wt.% in the more serpentinized RRP2. No calcite was detectable in RRP1 or RRP2.

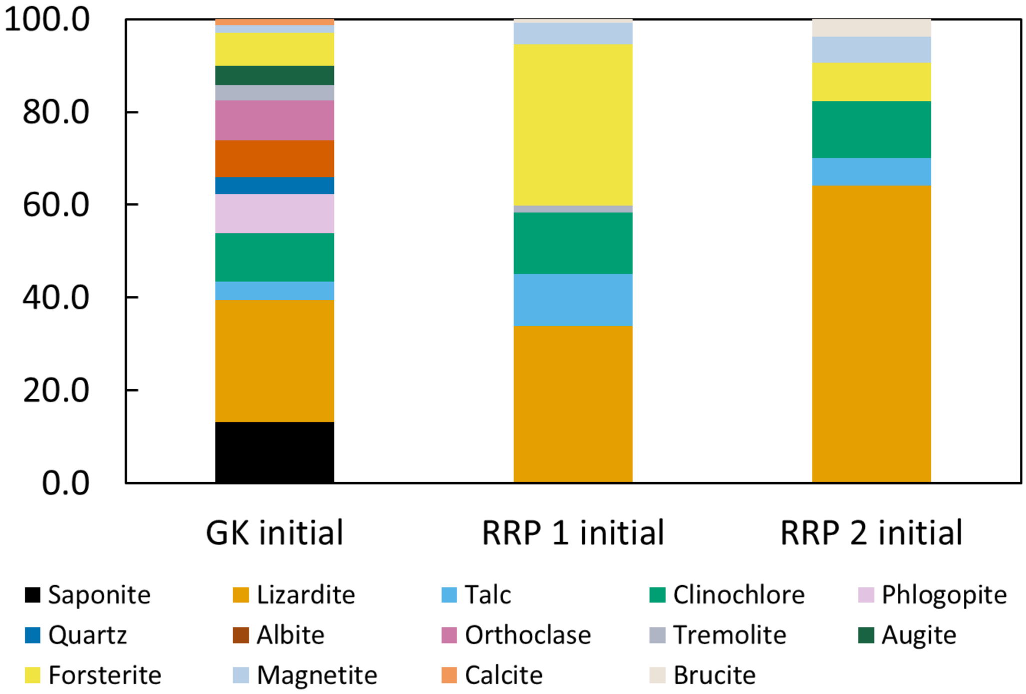

Figure 4.4 Mineralogical compositions from Rietveld refinement of processed kimberlite from Gahcho Kué (GK) and serpentinite rock samples, RRP1 and RRP2, from Record Ridge.

4.4.1.2.2 Mineralogy of the leached processed kimberlite and serpentinite rock samples

Rietveld refinements using XRD data were employed to assess which phases dissolved or precipitated in the column reactors during acid leaching experiments. Rietveld refinement results for most solid residue samples were collected from the tops (0—~3 cm), middles (~3—~6 cm) and bottoms (~6–9 cm) of the leached columns (Fig. 4.5 and Appendix Table A3.6). An exception was made for sampling the RRP2 column treated with 0.12 M HCl; here, Rietveld refinement results are for solid residue samples collected from the top (0–~0.3 cm), middle part 1 (the orange layer, ~0.3–~1.3 cm), middle part 2 (~1.3–~4 cm), middle part 3 (~4–~6.5 cm) and bottom (~6.5–9 cm) of the leached column (Fig. 4.5 and Appendix Table A3.6). There were visibly different horizons in this column suggesting mineralogical differences whereas no such observable differences occurred in the other columns. As such, this column was sampled in a different way.

For the GK column treated with Milli-Q water, no significant change in mineral abundance was discernible across varying depths, with the exception of orthoclase and talc (Fig. 4.5A). The orthoclase content in the GK column treated with Milli-Q water decreased with depth, while the talc content in the middle part was lower. A similar pattern was observed for both RRP1 and RRP2 columns treated with Milli-Q water, wherein there was no noticeable variation in mineral abundance with depth (Fig. 4.5B, C). For the GK column treated with 0.12 M HCl, the calcite content in the bottom part was 1.6 wt.%, similar to the initial calcite content in the processed kimberlite. However, the calcite content in the top and middle parts of the column decreased to 1.0 wt.% and 0.9 wt.%, respectively (Fig. 4.5D and Appendix Table A3.6). In the RRP1 column treated with 0.12 M HCl, the average brucite content was 0.8 wt.%, which is similar to the initial brucite content in the RRP1 sample, implying very limited dissolution of brucite (Fig. 4.5E and Appendix Table A3.6). Contrastingly, the RRP2 column treated with 0.12 M HCl exhibited an average brucite content of 3.1 wt.%, lower than the initial content of brucite of 3.7 wt.% in RRP2 (Fig. 4.5E and Appendix Table A3.6). Interestingly, brucite abundance is greater in the top sample where acid was added.

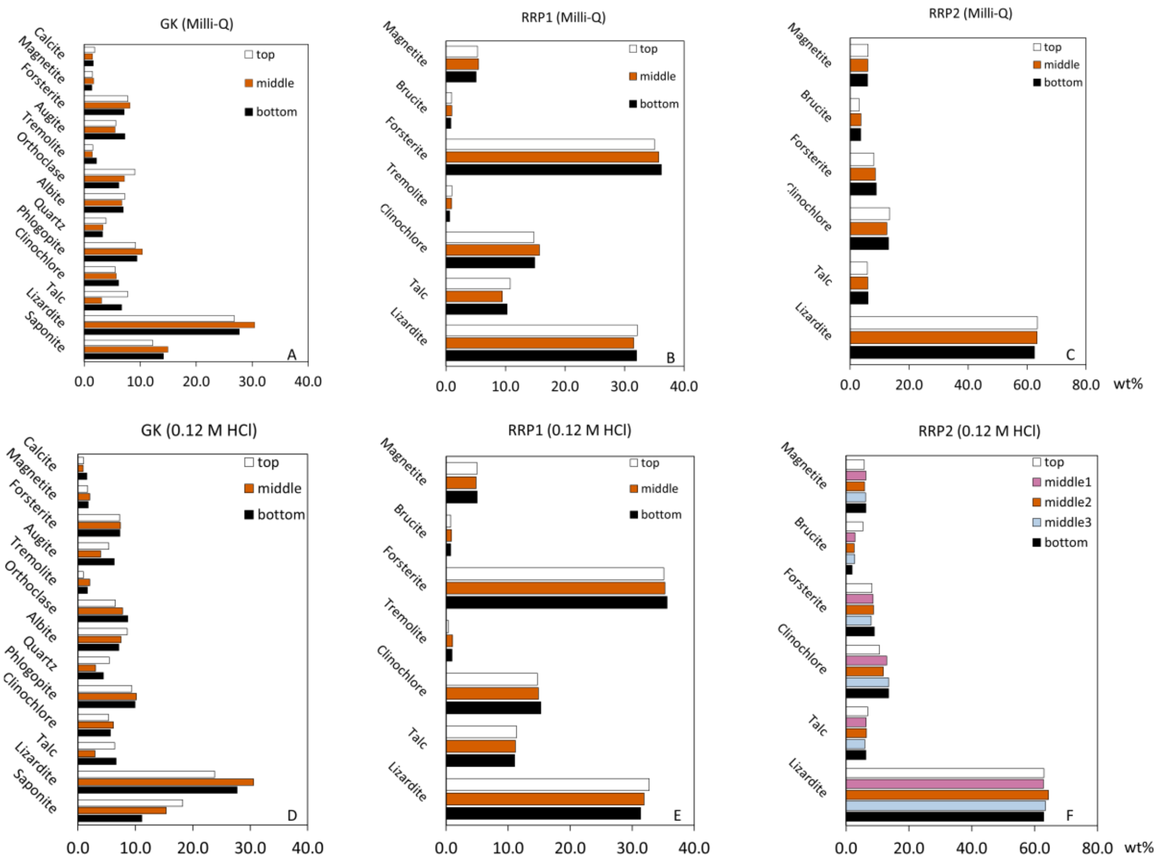

Figure 4.5 Rietveld refinement results at different depths of (A) GK; (B) RRP1; (C) RRP2 columns treated with Milli-Q water and (D) GK; (E) RRP1; (F) RRP2 columns treated with 0.12 M HCl.

4.4.1.3 Porosity distribution

Detailed textural observations of the columns revealed distinct sidewall flow paths in one of the replicate acid-treated RRP2 columns and a noticeable difference in packing density on either side of a defined dashed line (Appendix Fig. A3.1 and A3.2). Microfocus X-ray computed tomography (MicroCT) analysis was used to investigate pore distribution within the columns. The porosities of the two acid treated RRP2 columns are similar in value: 18.31 % and 18.59 %. MicroCT was also used to produce 3D density maps of other columns including (1) GK columns treated with Milli-Q water and 0.12 M HCl and (2) RRP1 columns treated with Milli-Q water and 0.12 M HCl (Appendix Video A3.1). A comparative analysis revealed differential porosity outcomes: GK columns treated with Milli-Q water exhibited a porosity of 15.47 %, which was notably less than the 17.75% observed in GK columns treated with 0.12 M HCl. Similarly, RRP1 columns treated with Milli-Q water demonstrated a porosity of 18.70%, which was lower than the 19.29% porosity recorded for RRP1 columns treated with 0.12 M HCl.

4.4.1.4 Migration of Ni during leaching experiments

Synchrotron-based XAS analyses were conducted on RRP2 column material to characterize the migration of transition metals such as Fe and Ni because an orange rust layer had formed in the acid-treated column (Fig. 4.6). The model compounds utilized in fitting XAS spectra included serpentine, olivine, pentlandite [$(Fe,Ni)_9S_8$], and ferrihydrite. These mineral standards were added or removed from the analysis depending on whether they improved the model fitting. For the initial RRP2 sample, there is no statistically significant improvement in the fit using ferrihydrite than for the fit without ferrihydrite, as such ferrihydrite was removed. The Ni K-edge XAS spectrum of the initial RRP2 material was best fit with a combination of serpentine (41.7 %) and pentlandite (56.7 %). Although no obvious orange rust was observed in the top layer of RRP2 sample treated with 0.12 M HCl after four weeks of treatment, the inclusion of ferrihydrite did improve the fit for the top layer of the column; thus, the Ni *K*-edge XAS spectrum of this top layer was best fit with serpentine (54.3 %), ferrihydrite (23.2 %), and pentlandite (21.6 %). The inclusion of ferrihydrite in the model for the orange layer of the RRP2 sample treated with 0.12 M HCl also improved the fit and is consistent with the visible formation of an oxidized Fe-rich phase in this sample. The hosts for Ni in this layer were also determined to be in serpentine (46.7 %), ferrihydrite (20.5 %), and pentlandite (32.2 %). For the bottom part of the RRP2 sample treated with 0.12 M HCl, the Ni was associated with serpentine (42.2 %) and pentlandite (58.6 %) only, which is consistent with the deportment of Ni in the initial RRP2 sample.

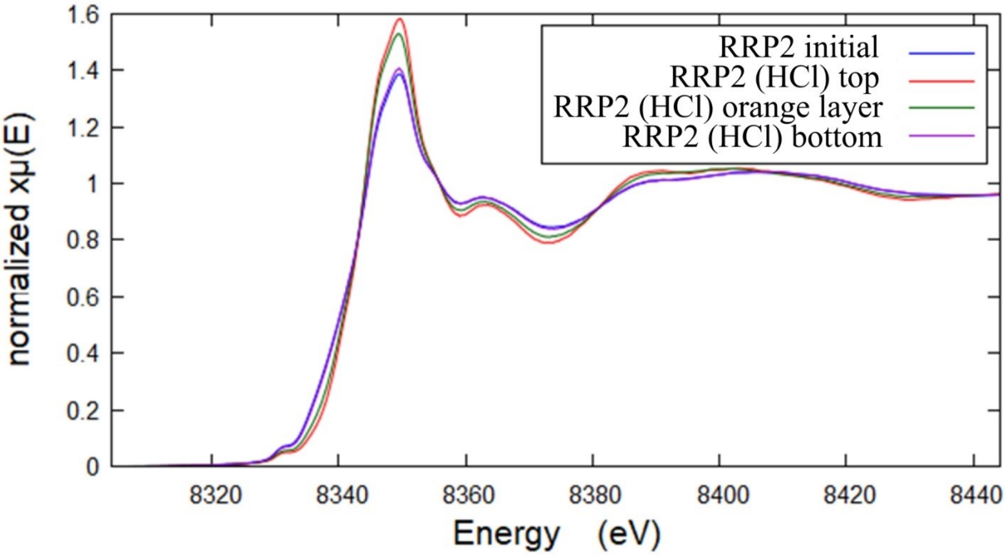

Figure 4.6 XAS analysis at the Ni *K* edge of RRP2 initial sample (blue), top of the acid leached RRP2 column (red), middle 1 part of the acid leached RRP2 column corresponding to the orange layer (green) and bottom of the acid leached RRP2 column (purple).

4.4.2 Geochemical Modelling

Geochemical modelling with PHREEQC was used to determine whether the column leachates were saturated [saturation index (SI) > 0] or undersaturated (SI < 0) with respect to various carbonate minerals, ferrihydrite and amorphous silica. Throughout the entire experimental period, the SI values for all leachates were less than 0 with respect to nesquehonite ($MgCO_3 \cdot 3H_2O$), thus indicating undersaturation (Fig. 4.7A). When observing the leachates from the GK, RRP1, and RRP2 columns treated with Milli-Q water, a similar trend of undersaturation was found with respect to calcite (SI < 0), except in the specific case of the RRP2 column leachate collected on day 2 (Fig. 4.7B). Conversely, the leachates from the GK column treated with 0.12 M HCl showed (super)saturation with regards to calcite. Leachates from the RRP1 column treated with 0.12 M HCl demonstrated undersaturation with respect to calcite, while the replicate 0.12 M HCl RRP2 columns showed initial saturation that shifted to undersaturation from day 12 and day 8, for the first and second RRP2 replicate columns respectively. Furthermore, the GK, RRP1, and RRP2 leachates from columns treated with Milli-Q water were undersaturated with regards to very high magnesium calcite (VHMC, also referred to as protodolomite), with exceptions observed in the RRP2 column on day 2 and day 4 (Fig. 4.7C). In contrast, leachates from the GK column treated with 0.12 M HCl exhibited (super)saturation for

VHMC. Undersaturation with respect to VHMC was observed for RRP1 columns treated with 0.12 M HCl, while the replicate RRP2 columns displayed saturation relative to VHMC, transitioning to undersaturation from day 16 and day 8, for the first and second RRP2 replicate columns respectively.

The concentrations of Fe in the leachates from the GK, RRP1, and RRP2 columns treated with Milli-Q water were below the detection limit, thus the SI values for ferrihydrite ($Fe^{3+}_2O_3\cdot0.5H_2O$) could not be calculated (Fig. 4.7D). However, the leachates from the GK column treated with 0.12 M HCl were supersaturated with respect to ferrihydrite, as was one of the replicate RRP2 columns, except on day 12, with the the replicate RRP2 column leachate becoming undersaturated relative to ferrihydrite from day 16 onward. The leachates from both replicate RRP1 columns treated with 0.12 M HCl remained undersaturated with respect to ferrihydrite throughout the experiment.

Lastly, an examination of the saturation indices for amorphous silica reveals that the leachates collected from the GK columns, regardless of whether they were treated with Milli-Q water or 0.12 M HCl, remained consistently saturated with respect to this phase (Fig. 4.7E). Leachates from the RRP1 column treated with Milli-Q water exhibited undersaturation relative to amorphous silicate, except on day 2, whereas leachates from columns treated with 0.12 M HCl were saturated. In the RRP2 columns treated with Milli-Q water, the leachates were undersaturated with respect to amorphous silica, but the replicate columns treated with 0.12 M HCl alternated from being undersaturated to saturated starting from day 12 and day 8 for the first and second replicates, respectively.

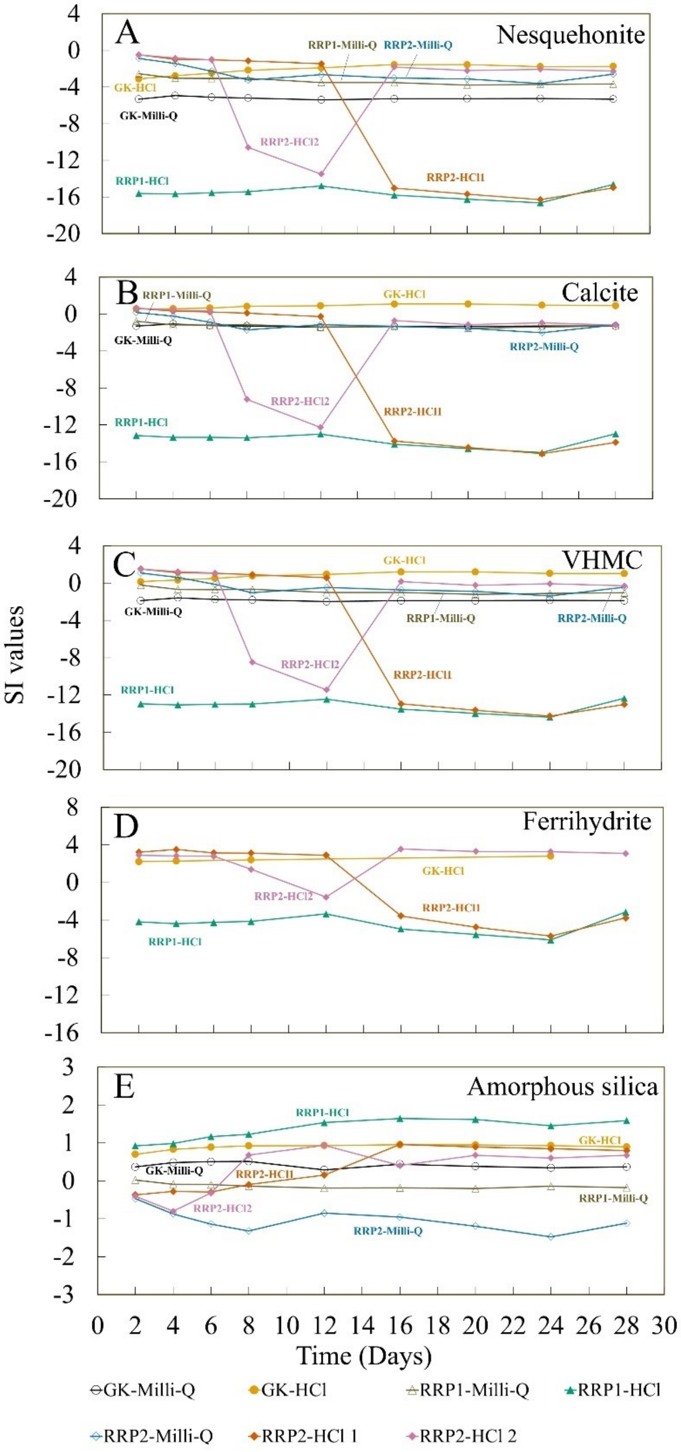

Figure 4.7 Saturation indices of the leachates with respect to different (mineral) phases *versus* time (days) as calculated using PHREEQC (Parkhurst and Appelo, 2013) and the minteq.v4 database released in 2017.

MIN3P reactive transport modelling of the acid-leached columns shows the advancement of acidic conditions downwards through the columns over the course of the experiment (Fig. 4.8). An inspection of the results for all three materials (GK, RRP1 and RRP2) treated with Milli-Q water reveals a consistent pattern wherein modelled pH values remained above 8 (Fig. 4.8A). The modelled pH values for the GK columns treated with 0.12 M HCl decreased to around 2.5 within the first 1.5 cm depth, and then increased to around 7.1 at approximately 6.5 cm, thereafter maintaining stability. Conversely, the modelled pH values for the RRP1 columns treated with 0.12 M HCl remained below 1.5 throughout the entirety of the columns. Modelled pH values for the RRP2 columns treated with 0.12 M HCl were 1.3 at the top, increasing abruptly to ~9 near 4 cm depth. Calcite, which was only detected in GK material, was modelled as being almost entirely dissolved within the first 6.5 cm depth in the GK columns treated with 0.12 M HCl (Fig. 4.8B) but it remained present in the models of columns treated with Milli-Q water at 0.1 vol %, except in the top 0.5 cm of the columns here it was modelled as having been dissolved. Modelling predicted that brucite was completely dissolved throughout the RRP1 columns treated with 0.12 M HCl. In the acid-treated RRP2 columns, the dissolution of brucite was accompanied by an abrupt increase in pH values near 4 cm depth, below which the abundance of brucite increased to its initial value in the RRP2 material (Fig. 4.8C). The MIN3P model indicated the precipitation of ferrihydrite at the base of the acid-leached RRP1 columns without a corresponding pH change, while in the acid-leached GK and RRP2 columns, ferrihydrite formation was coincident with a pH increase at depth (Fig. 4.8D). In the GK columns subjected to acid treatment, ferrihydrite formation was closely associated with the dissolution of sufficient calcite to neutralize the pH, occurring specifically after the pH values increased to around 7. In contrast, within RRP2 columns treated with 0.12 M HCl, ferrihydrite formation was predicted to occur within a narrow zone, ranging from 2 to 4 cm in depth. This localized formation is attributed directly to the dissolution of brucite, leading to pH neutralization. The potential for hydromagnesite precipitation was identified in the RRP1 and RRP2 columns treated with Milli-Q water, specifically ranging from 2 to 5 cm in depth. This aligned well with the modelled dissolution of brucite in these columns. Furthermore, in the RRP2 columns treated with 0.12 M HCl, hydromagnesite was predicted to form in the bottom segment notably beyond 6 cm in depth, following the cessation of brucite dissolution (Fig. 4.8E). Additionally, the precipitation of amorphous silica was predicted from the models for RRP1 and RRP2 columns treated with acid. Particularly in the acid leached RRP2 columns, the formation of amorphous silica was attributed to the neutralization front, further emphasizing the complex interplay between pH and mineral reactivity in the system (Fig. 4.7F).

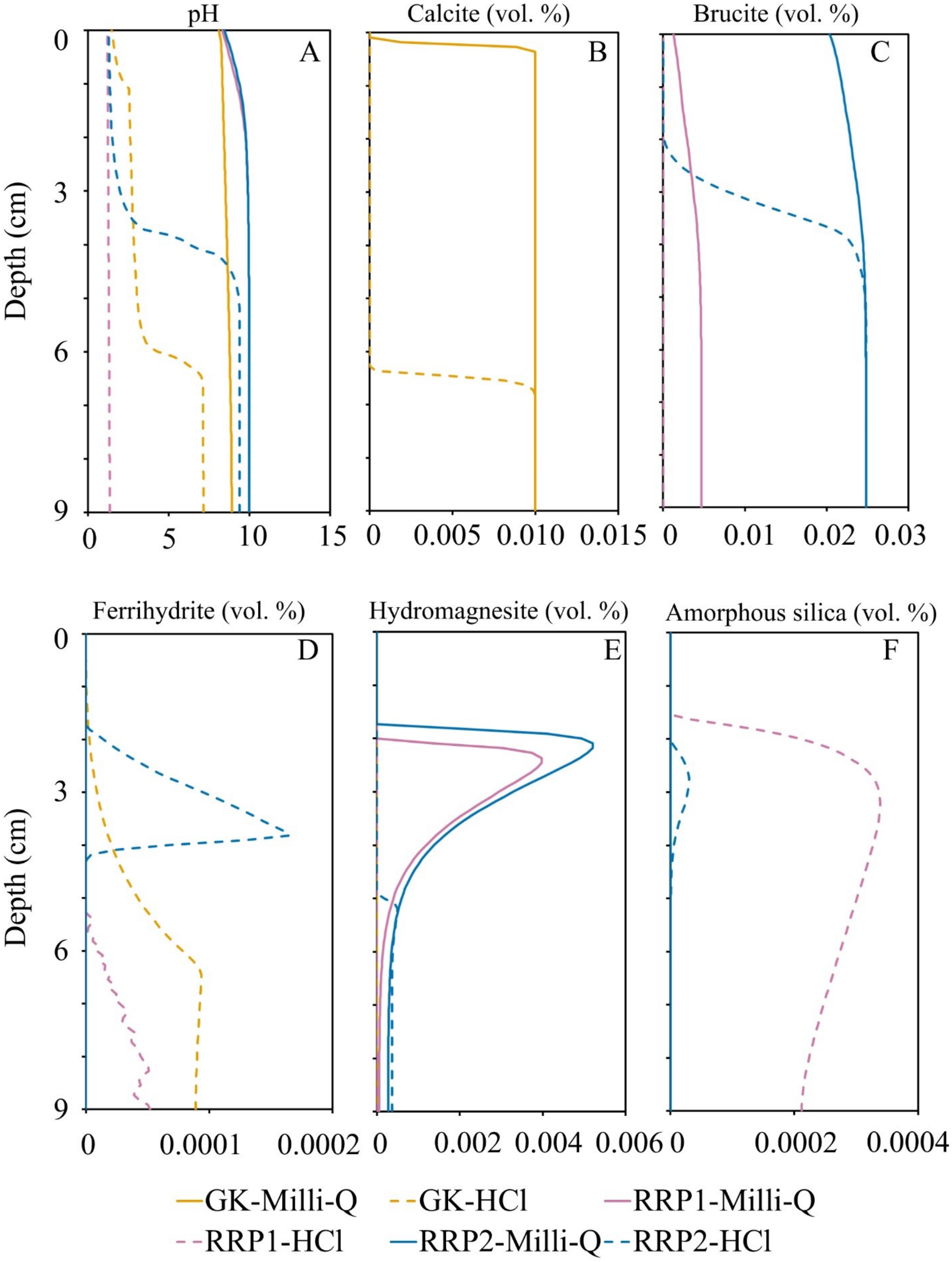

Figure 4.8 MIN3P modeled pH and mineral abundances reported as a volume fraction.

4.5 Discussion

4.5.1 Mineralogical controls on element mobility and solution chemistry

The calcite content of many kimberlites, including that from the Venetia mine (4.2 wt.%; Chapter 3), is significantly higher than what is observed in GK kimberlite. Calcite dissolution was the primary source of Ca during acid-leaching of Venetia kimberlite, clay minerals (*i.e.*, lizardite, smectites, talc, clinochlore) were the main source for Mg, and Fe was sourced mainly from the dissolution of lizardite (Chapter 3). In contrast, the calcite content in the GK processed kimberlite is much lower, at only 1.4 wt.%. Here, the dissolution of calcite, augite, tremolite, and saponite, all played a role in providing Ca. However, silicate minerals including augite, orthoclase, albite, and quartz showed only a limited degree of dissolution in the acid-treated GK columns (Fig. 4.5D). Mg was extracted mainly from the clay minerals (*e.g.,* lizardite, smectites, talc, clinochlore) and forsterite. Fe, similar with the Venetia processed kimberlite, was predominantly sourced from the dissolution of lizardite present within the GK processed kimberlite.

The Ca concentration in the leachates from all the Record Ridge Project (RRP1 and RRP2) columns remained consistently lower than 110 ppm due to the lack of calcite and scarcity of Ca-silicate minerals (*e.g.,* tremolite, present at <1.7 wt.% in RRP1). Based on the Rietveld refinement results (Appendix Table A3.6) and MIN3P modelling (Fig. 4.8C), the preferential dissolution of brucite provided a proportion of the Mg extracted from the acid-leached RRP1 and RRP2 columns. Forsterite and clay minerals (*e.g.,* lizardite, talc, clinochlore) may also act as a source of Mg. Modelling indicates that the greater abundance of brucite in RPP2 accounts for higher pH of leachates from these columns (Fig. 4.8A and C). This observation aligns well with elevated Mg concentrations in the solution when the pH is high in acid-treated RRP2 columns (Fig. 4.3c, i). Fe is predominantly sourced from the dissolution of lizardite present in the RRP1 and RRP2 columns as magnetite is recalcitrant to acid (Appendix Table A3.6). Synchrotron XAS analysis shows Ni is present in the serpentine and pentlandite in the original RRP2 sample and then Ni is released during acid leaching to be incorporated into the ferrihydrite that forms the orange rust layer.

4.5.2 Mass balance for Fe, Ni, Ca and Mg

Using the approach developed in Chapter 3, the mass balance deviations (MBD) of Fe and Ni (Table 4.1) were calculated based on the ICP-AES data (for top, middle and bottom residues, Appendix Table A3.7) and the masses measured for the top, middle and bottom residues sampled from each column reactor after the experiments. Typically, the concentrations of Fe and Ni in the leachates were found to be below the detection limit. Given their low concentrations and sporadic detection in the leachates, the total masses of Fe and Ni present in the leachates were not used in the estimation of the MBD. All samples except for one were sufficiently large to obtain ICP-AES data; the top 0—~0.3 cm of residues within the acid-leached RRP2 column has a mass of 0.4 g, which was insufficient for analysis. Therefore, this sample was omitted from the calculation. The mass balance deviation (MBD) was calculated using Eq. 1 from Chapter 3:

$$\text{MBD}=\frac{M_R-M_O}{M_O}=\frac{M_{top}+M_{middle}+M_{bottom}-M_O}{M_O} \qquad (1)$$

Where M_R is the total mass of a metal in all of the top, middle and bottom residues at the end of the experiment, M_O is the total mass of a metal in the initial residues, M_{top} is the total mass of a metal in the top residues, M_{middle} is the total mass of a metal in the middle residues and M_{bottom} is the total mass of a metal in the bottom residues. A MBD value of 0 % would indicate a perfect mass balance. Deviations away from 0 % indicate either that some fraction of an element is unaccounted for in the system or that the material is highly heterogeneous in composition, which introduces error into the mass balance calculation.

The MBD values for Fe and Ni in the columns treated with Milli-Q water and 0.12 M HCl are detailed in Table 4.1. The Fe MBD values for GK columns are 0.03% and -0.54% for Milli-Q and 0.12 M HCl treatments, respectively. For RRP1 columns, they are 0.45% and -0.13%, and for RRP2 columns, they are -1.16 % and -1.81 %. A negative MBD means that Fe was lost from the columns, which means that all acid-treated columns showed greater extraction of Fe into solution than those treated with Milli-Q water.

Similarly, the MBD values of Ni for GK columns treated with Milli-Q water and 0.12 M HCl are 3.02 % and -4.16 %, respectively. For RRP1 columns, they are 0.62 % (Milli-Q) and -1.54 % (HCl), and for RRP2 columns, they are 0.39 % (Milli-Q) and -3.73 % (HCl). Negative MBD values for acid-treated columns also demonstrate higher Ni extraction in all acid-treated columns compared to those treated with Milli-Q water. No Fe or Ni was added to the any of the column experiments, making positive MBD values impossible; thus, the positive MBD values calculated for the Milli-Q treated columns are an artifact of heterogeneity of the mineral distribution in the initial residues. Functionally, we consider these positive values to mean that there was no measurable loss of Fe or Ni from the Milli-Q treated columns, which is consistent with Fe and Ni concentrations being below detection in leachates from these columns

Table 4.1 The mass balance deviation (MBD) of Fe and Ni based on ICP-AES data, and mass fraction in each column reactor. Positive MBD values correspond to Ni and Fe enrichment in the column and negative value imply depletion in the column.

Sample	Byproduct	Fe (g)	Total Fe (g)	MBD of Fe (%)	Ni (mg)	Total Ni (mg)	MBD of Ni (%)
GK initial	original sample	3.63	3.63	–	80.8	80.8	–
GK (Milli-Q)	top residues	1.36	3.63	0.03	31.86	83.3	3.02
	middle residues	1.08			23.71		
	bottom residues	1.20			27.69		
GK (HCl)	top residues	1.42	3.61	-0.54	28.63	77.5	-4.16
	middle residues	1.03			22.97		
	bottom residues	1.16			25.86		
RRP1 initial	original sample	4.20	4.20	–	164	164	–
RRP1 (Milli-Q)	top residues	1.43	4.22	0.45	55.34	165	0.62
	middle residues	1.49			58.85		
	bottom residues	1.31			50.89		
RRP1 (HCl)	top residues	1.28	4.20	-0.13	47.09	162	-1.54
	middle residues	1.45			56.69		
	bottom residues	1.47			57.75		
RRP2 initial	original sample	4.36	4.36	–	163.25	163	–
RRP2 (Milli-Q)	top residues	1.28	4.30	-1.16	49.36	164	0.39
	middle residues	1.48			57.08		
	bottom residues	1.54			57.45		
RRP2 (HCl)	top residues	–	4.28	-1.81	–	157	-3.73
	middle residues 1	0.91			33.83		
	middle residues 2	0.96			35.87		
	middle residues 3	1.24			45.39		
	bottom residues	1.16			42.08		

The mass balance deviations for Mg and Ca (Table 4.2) were calculated using the compositions of solids and leachate chemistry, as presented in Table 4.2. The M_R for Mg and Ca in Equation (1) represents the total mass of Mg or Ca in the top, middle, and bottom residues and leachates. The Mg and Ca concentrations in leachates were also used to estimate the amount of Mg and Ca extracted (Appendix Table A3.8 and A3.9).

For GK columns, the MBD values of Mg are 1.13 % and -1.20 % for Milli-Q and 0.12 M HCl treatments, respectively. For RRP1 columns, they are -0.41 % and 0.36 %, and for RRP2 columns, they are -1.78 % and -1.45 %. The MBD values of Ca are higher, which is attributed to the relatively low content of Ca in the GK, RRP1, and RRP2 samples and the greater relative error associated with measuring low elemental abundances. The MBD values of Ca are 11.70 % and 18.43 %, respectively, for GK columns treated with Milli-Q water and 0.12 M HCl. For RRP1 columns, they are -22.37 % and -2.29 %, and for RRP2 columns, they are -0.58 % and 36.47 %. These observed MBD values for Ca, especially given there was no addition of Ca, imply a heterogeneity in mineral distribution within the columns. This is further emphasized by the low initial concentrations of Ca in the GK, RRP1, and RRP2 samples. Such variability in mineral content may significantly influence the accuracy of elemental abundance measurements, highlighting the need for careful interpretation of these data.

Table 4.2 The mass balance deviation (MBD) of Mg and Ca based on ICP-AES data, and mass fraction in each column reactor.

Sample	Byproduct	Mg (g)	Total Mg (g)	MBD of Mg (%)	Ca (g)	Total Ca (g)	MBD of Ca (%)
GK initial	original sample	11.1	11.1	–	2.17	2.17	–
GK (Milli-Q)	top residues	4.19	11.2	1.13	0.85	2.43	11.70
	middle residues	3.29			0.77		
	bottom residues	3.71			0.81		
	leachates	0.00			0.01		
GK (HCl)	top residues	4.00	10.9	-1.20	0.76	2.57	18.43
	middle residues	3.04			0.79		
	bottom residues	3.48			0.71		
	leachates	0.40			0.31		
RRP1 initial	original sample	19.67	19.7	–	0.24	0.24	–
RRP1 (Milli-Q)	top residues	6.61	19.6	-0.41	0.05	0.19	-22.37
	middle residues	6.89			0.06		
	bottom residues	6.08			0.07		
	leachates	0.01			0.00		
RRP1 (HCl)	top residues	5.83	19.7	0.36	0.05	0.24	-2.29
	middle residues	6.75			0.08		
	bottom residues	6.81			0.08		
	leachates	0.35			0.03		
RRP2 initial	original sample	19.35	19.4	–	0.08	0.08	–
RRP2 (Milli-Q)	top residues	5.77	19.0	-1.78	0.02	0.08	-0.58
	middle residues	6.59			0.03		
	bottom residues	6.62			0.03		
	leachates	0.02			0.00		
RRP2 (HCl)	top residues	–	19.1	-1.45	–	0.11	36.47
	middle residues 1	3.94			0.02		
	middle residues 2	4.09			0.02		
	middle residues 3	5.39			0.05		
	bottom residues	5.08			0.02		
	leachates	0.57			0.01		

The average values of Mg and Ca concentrations were calculated, and the total concentration and extraction percentage of Mg and Ca in the leachates treated with Milli-Q water and 0.12 M HCl in the GK, RRP1, and RRP2 columns were estimated (Appendix Table A3.8 and A3.9). The extraction percentage was calculated using Equation (2).

$$\text{Total extraction (\%)} = \frac{M_l}{M_O} \times 100 = \frac{Conc \times 27 \times 16.6 \div 10}{M_O} \qquad (2)$$

Where M_l is the total mass (mg) of a metal in leachates, M_O is the total mass (mg) of a metal in the initial residues, *Conc* is the average concentration (ppm) of a metal in leachates from days 2 to days 28. The number 27 refers to the number of days over which the experiment was conducted. The 16.6 represents the volume (in mL) of Milli-Q water or acid that was added daily. The use of the number 10 is a mathematical adjustment to convert our results into units of percent.

All columns from GK, RRP1, and RRP2 treated with Milli-Q water demonstrated a low extraction efficiency of Mg and Ca, not exceeding 1% (Appendix Table A3.8 and A3.9). The leachates from the GK column treated with 0.12 M HCl extracted 14.3 % of the Ca and 3.6 % of the Mg initially present in the processed kimberlite. The leachates from the serpentinite columns treated with 0.12 M HCl contained a low abundance of Ca, which was primarily leached from tremolite, resulting in extraction efficiencies of 11.1 % (RRP1) and 10.8 % (RRP2) (Appendix Table A3.8). A total of 1.8 % and 3.0 % of the Mg was extracted from the RRP1 and RRP2 columns, respectively (Appendix Table A3.9). These results indicate that treatment with 0.12 M HCl enhanced the extraction efficiency of Ca and Mg compared to treatment with Milli-Q water. However, the extraction efficiency remained relatively low, particularly for Mg, suggesting that the acid concentration may need to be increased or that longer residence times should be used for acid treatments to obtain higher extraction efficiencies.

The similarities in the extraction efficiencies of Ca and Mg between the Venetia (Chapter 3) and GK processed kimberlites treated with 0.12 M HCl—14.1% and 3.4% for Venetia, compared to 14.3% and 3.6% for GK, respectively—reveal a complex aspect of their mineralogical composition and its impact on acid leaching performance. Despite differences in the initial mineral content, notably the higher calcite content in Venetia kimberlite (4.2 wt.%) versus the lower content in GK (1.4 wt.%), the resultant extraction ratios for Ca and Mg are strikingly similar. This observation suggests that other factors, such as the presence and solubility of secondary Ca and Mg-bearing minerals (*e.g.,* augite, tremolite, saponite, and potentially other clay minerals), may play compensatory roles in the leaching process, leveling the extraction efficiencies. For the RRP columns treated with 0.12 M HCl, the lower Ca content results in lower extraction efficiencies for Ca, as observed with 11.1% for RRP1 and 10.8% for RRP2. This aligns with the expectation that the absence of significant sources of Ca limits the amount of Ca available for extraction. On the other hand, the higher initial Mg content in these columns compared to Ca, and the presence of highly reactive phases such as brucite, which is known to dissolve readily in acidic conditions, contributes to the Mg extraction process. This is reflected in the Mg extraction efficiencies of 1.8% for RRP1 and 3.0% for RRP2. Despite the higher initial Mg content, the extraction efficiencies remain relatively low compared to kimberlite, indicating that while the presence of brucite and other Mg-bearing minerals such as forsterite and clay minerals (*e.g.,* lizardite, talc, clinochlore) provides a source for Mg, the overall extraction efficiency is influenced by other factors such as mineral solubility, acid concentration, and the specific leaching conditions.

The percentage of calcite dissolved in the GK columns was assessed using Rietveld refinement results (Table 4.3). The initial mixed bulk samples contained 1.4 wt.% calcite, which corresponds to a mass of approximately 1.1 g of calcite in each of the column reactors. The percentage of calcite dissolution is estimated to be 20.5 % in the column reactor treated with 0.12 M HCl. For the column reactor treated with Milli-Q water, the final estimated mass of calcite was 1.3 g (based on refined abundances of 1.8 wt.%, 1.5 wt.% and 1.6 wt.% in the top, middle and bottom of the column, respectively) and thus no calcite dissolution was detected. The positive value for calcite dissolution from the Milli-Q water column is unphysical, suggesting an increase in the amount of calcium, and is instead an artefact of the heterogeneous distribution of calcite in the GK starting material. The proportion of Ca in the leachates obtained from calcite dissolution was also calculated (Appendix Table A3.10). Calcite dissolution is estimated to provide 29.8 % of total Ca in the leachates treated with 0.12 M HCl. Silicate minerals such as tremolite were thus the main source for Ca in leachates.

Table 4.3 Percentage of calcite dissolution for each GK column reactor. The negative value corresponds to calcite enrichment in the column and is an artefact of sample heterogeneity.

Sample	Byproduct	Calcite (%)	Mass (g)	Calcite (g)	Total calcite (g)	Calcite dissolution (%)
Initial residues	original sample	1.4	80.5	1.13	1.13	n/a
GK (Milli-Q)	top residues	1.8	30.2	0.54	1.32	-16.8
	middle residues	1.5	24.0	0.36		
	bottom residues	1.6	26.1	0.42		
GK (HCl)	top residues	1.0	31.5	0.32	0.90	20.5
	middle residues	0.9	22.5	0.20		
	bottom residues	1.5	25.2	0.38		

4.6 Implications

4.6.1 CO_2 offset potential

In 2017, the Gahcho Kué mine processed a total of 0.91 Mt of ore, concurrently emitting 0.084 Mt of CO_2 equivalent (CO_2e) emissions (Mervine et al., 2018). Assuming all Mg^{2+} in GK leachates could precipitate as hydromagnesite, the most stable of the hydrated Mg-carbonate phases, the CO_2 offset potential of leached Mg was calculated and compared with the amount of CO_2 emitted by calcite dissolution (Fig. 4.9, Appendix Table A3.11 and A3.12). Our calculations show that the dissolution of clay minerals (*e.g.,* lizardite, smectites, talc, clinochlore), which provides Mg, could lead to an estimated CO_2 offset potential of 7.8% if the tailings at Gahcho Kué were leached with 0.12 M HCl and the resulting leachate was carbonated as hydromagnesite. Rietveld refinement results showed that calcite dissolution in GK columns accounted for 29.8 % of the Ca that was leached, with silicate minerals such as augite, tremolite, and saponite contributing the remaining calcium in the solution. If HCl leaching were applied at mine scale, the release of CO_2 during dissolution of calcite within the tailings would increase mine emissions by 1.4 %. However, the leached Ca resulting from silicate dissolution was also found to have an estimated CO_2 offset potential of 3.2 % if it was converted to calcite (Appendix Table A3.13). If no effort was made to reprecipitate the dissolved calcite, the net estimated CO_2 offset potential by Mg and Ca leached by silicates dissolution is estimated at 9.6%. Conversely, if the Ca derived from calcite dissolution can be fully recarbonated, the amount of Ca and Mg leached equates to an estimated CO_2 offset potential of 11.0 % of the mine's annual greenhouse gas emissions. If all of the calcite were dissolved and all of the Mg and Ca in silicate minerals were extracted from the GK processed kimberlite using a higher concentration of HCl, or an alternative acid, the maximum CO_2 offset potential by Mg and Ca from silicate dissolution will be 215.6 % and 25.5%. This amounts to a total of 241.1 % relative to the mine's annual emissions, with the maximum CO_2 release from calcite being -6.7 % (Fig. 4.9).

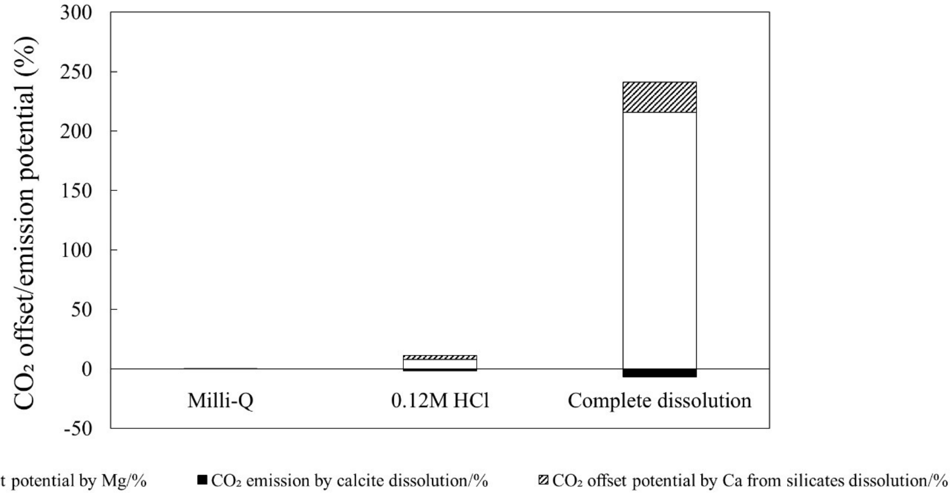

Figure 4.9 CO_2 offset potential of Mg and Ca silicate minerals and CO_2 emissions from calcite at the Gahcho Kué mine.

A total of 4.74 Mt of ore were treated at the Venetia mine in 2016 and the mine emitted 0.21 Mt of CO_2e emissions the same year (Chapter 3). The dissolution of clay minerals provides Mg, accounting for an estimated CO_2 offset potential of 9.8 % for the column reactors treated with 0.12 M HCl at Venetia (Chapter 3). The Ca leached from silicate dissolution could also provide an estimated CO_2 offset potential of 5.5 %. Due to the high content of calcite in Venetia processed kimberlite, calcite dissolution in the columns would correspond to an increase of 10.4 % in annual CO_2 emission, which means CO_2 released by calcite dissolution would largely negate the CO_2 offset potential provided by the silicate minerals unless all the calcium leached from calcite is also recarbonated. If no effort was made to reprecipitate the dissolved calcite, the net estimated CO_2 offset potentials is 4.9 %. If all of the calcite was reprecipitated, dissolution of Mg- and Ca-bearing silicate minerals would sequester 15.3 % of the Venetia mine's annual emissions, with greater offsets attainable using higher concentrations of HCl. Moreover, if all calcite can be dissolved and all Mg in the processed kimberlite can be extracted with a higher concentration of HCl or another acid, the maximum CO_2 offset potential by Mg and Ca from silicate dissolution will be 292.9 % and 72.5 % (365.4 % total) of the mine's annual emissions, while the maximum CO_2 release from calcite would be -41.7 % (Fig. 4.11 in Chapter 3).

Record Ridge is an advanced project, which has yet to be mined, as such it is not possible to make a similar estimate a mine-site CO_2 offset potential. However, the amount of CO_2 that could be sequestered by leaching all of the Mg from 1 kg of ore and precipitating them as hydromagnesite can be calculated for RRP serpentinized dunite samples, GK processed kimberlite, Venetia processed kimberlite (Chapter 3), and the Woodsreef chrysotile residues studied by Hamilton et al. (2020) (Appendix Table A3.14 and Fig. 4.10). For Venetia and GK processed kimberlites, which contain calcite and several Ca-bearing silicate minerals, both the CO_2 offset potential from Ca released by silicate dissolution and the CO_2 emissions due to calcite dissolution were calculated (Appendix Table A3.15, A3.16 and Figure 4.10). Our findings indicate that the carbonation offset potential is 6.3 g/kg for RRP1 columns and 10.3 g/kg for RRP2 columns treated with 0.12 M HCl. For GK columns treated with the same acid concentration, the net offset potential is 8.9 g/kg, with Mg contributing 7.2 g/kg, Ca silicates contributing 3.0 g/kg and with -1.3 g/kg CO_2 released by calcite dissolution. In comparison, Venetia columns treated with 0.12 M HCl offer a lower estimated carbonation offset potential of 2.3 g/kg, with Mg- and Ca-silicates providing 4.4 g/kg and 2.5 g/kg, respectively, and with -4.6 g/kg CO_2 released by calcite dissolution. Increasing the acid concentration to 0.16 M HCl for Venetia columns yields an increased offset potential of 4.3 g/kg, with Mg contributing 7.0 g/kg, Ca from silicate dissolution providing 3.6 g/kg, and with -6.3 g/kg of CO_2 released by calcite dissolution. Hamilton et al. (2020) conducted an acid leaching experiment on completely serpentinized, brucite-bearing chrysotile mine residues from Woodsreef (WR), Australia, using 0.08 M H_2SO_4 (0.16 N). This experiment revealed a significantly higher estimated carbonation offset potential of 29.0 g/kg, attributed to the high serpentine content (over 85 wt.%) and negligible carbonate content in Woodsreef chrysotile mine residues, compared to the variably serpentinized RRP samples. As is shown in Chapter 3, dilute acid leaching holds the greatest potential for serpentine-rich and carbonate-poor mine residues. For carbonate-rich mine residues, dissolution of carbonate minerals during the acid leaching process will decrease the potential offset while requiring recarbonation of Ca leached from calcite, which does not constitute CO_2 sequestration.

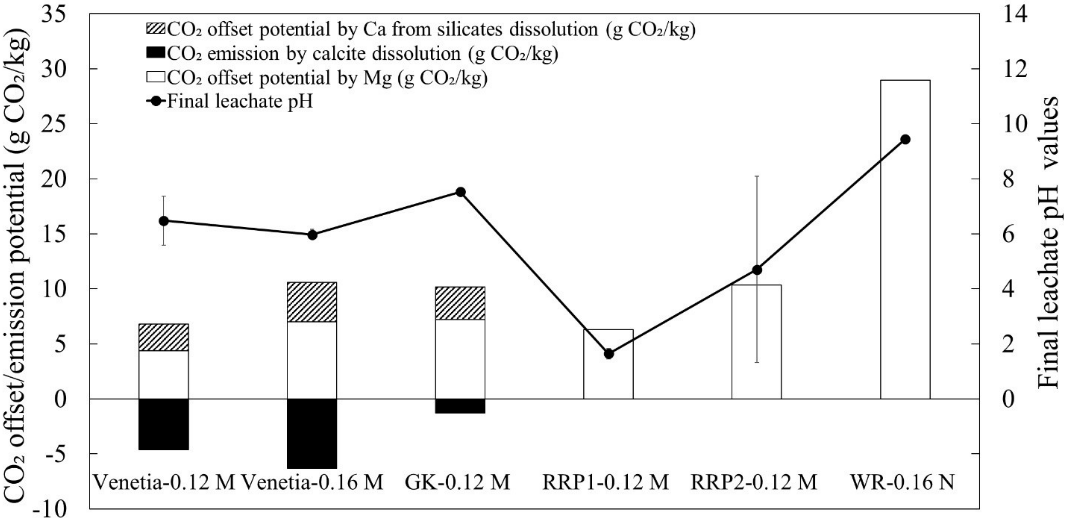

Figure 4.10 CO_2 offset potentials (g CO_2/kg) for Venetia processed kimberlite, GK processed kimberlite, RRP serpentinized dunite samples and fully-serpentinized Woodsreef chrysotile mine residues (WR). Contributions from Mg-silicate and brucite leaching (Mg) and Ca-silicate leaching are calculated separately as are CO_2 emissions from calcite (g CO_2/kg) dissolution where relevant.

4.6.2 Prospects for nickel recovery

Hamilton et al. (2020) found that secondary Fe-(hydr)oxide minerals that formed at a pH neutralization front capturing transition metals, including Ni, Mn, Co, and Cr, within acid-leaching columns of chrysotile mine residues from the Woodsreef mine. Here, Ni was observed in secondary Fe-(hydr)oxides that formed in RRP2 columns treated with 0.12 M HCl. This contrasts with observations for acid-treated processed kimberlite from Venetia and GK as well as RRP1, where, although secondary Fe-(hydr)oxides formed, they did not concentrate Ni or any other transition metals. The absence of transition metals the Fe-(hydr)oxide minerals in these experiments could be attributed to differences in mineralogy between the kimberlite, less serpentinized dunite (RRP1), more serpentinized dunite (RRP2) and the completely serpentinized, brucite-rich rocks from Woodsreef. Jambor et al. (2007) found that different minerals and even specimens of the same mineral species can show a large range of neutralization potentials (NP) values as a function of different particle size distributions, reaction times and/or the temperature of acid digestion. The high serpentine content in Woodsreef chrysotile mine residues (over 85 wt.%) and in more serpentinized RRP2 samples (over 60 wt.%) compared to the less serpentinized RRP1 samples (less than 35 wt.%), and the distinct mineralogy of kimberlite emphasizes the critical role of rock type and mineral reactivity in determining the efficiency of metal recovery and CO_2 sequestration strategies. Serpentinization levels and the availability of brucite, which dissolves quickly and neutralizes acid to raise pH, are the controlling factors in the formation of secondary Fe-(hydr)oxides that can absorb Ni. In highly serpentinized rocks and mine residues (RRP2 and WR), brucite availability encourages a favorable environment for Ni to be absorbed onto Fe-(hydr)oxide surfaces, which requires a specific pH range approximately 6 to 8 (Bigham and Nordstrom, 2000), significantly influencing whether Ni is precipitated as a secondary ore or whether it is released into solution. The deportment of nickel in a solid or a liquid will naturally dictate which recovery strategies can be used for Ni. Conversely, in kimberlite (GK, Venetia) and partially serpentinized dunite (RRP1), the lower neutralization potential of these rocks may require the use alternative processing strategies, such as adjusting the acid concentration, employing different acids to achieve a desirable pH swing for Ni recovery or using chelating agents and reducing conditions to enable concurrent Ni recovery with carbon mineralization as done by Wang et al. (2021) and Wang and Dreisinger (2022).

4.6.3. Impact of physical properties on divalent metal and nickel recovery

Hydrometallurgical processing of ores and mine residues for carbon mineralization and enhanced metal recovery in a manner that is both geotechnically and environmentally sound. Acid heap leaching is used for efficient extraction of valuable metals from low-grade ores with a reduced environmental footprint. This technique involves stacking ore on a leak-proof base and irrigating it with a leaching solution to solubilize the desired metals. Other reduced-footprint hydrometallurgical strategies include *in situ* leaching, which offers the advantage of minimal surface disturbance by injecting the leaching solution directly into the ore body (Sinclair and Thompson, 2015); agitated tank leaching (Mahmoud et al., 2017), known for its controlled processing environment leading to higher recovery rates; and bioleaching (Pradhan et al., 2008), an eco-friendly alternative utilizing microorganisms to facilitate the extraction process. Each method varies in suitability depending on ore type, mineralogy, and environmental impact.

Scaling up to a heap leaching process offers significant benefits, including the potential for cost-effective treatment of low-grade ores and the capacity for processing large volumes of material with relatively low energy consumption. However, this upscaling introduces various risks and challenges that need to be meticulously addressed to ensure the effectiveness and sustainability of the process. Among these challenges are geotechnical failures (Lupo, 2010), which can compromise the structural integrity of the heap leach pad, leading to potential environmental and operational hazards. Hard pan formation (DeSisto et al., 2011), a condition where the leaching solution creates an impermeable layer, can severely limit solution penetration and metal recovery, leading to unreacted zones within the heap where valuable metals such as Ni and Co might remain unextracted. Meanwhile, recovering metals from secondary Fe-(hydr)oxides buried at the base of a pile necessitates a careful design that facilitates the effective infiltration and percolation of the leaching solution to dissolve and transport the target metals for recovery. This includes considerations for heap construction, such as layering, compaction, and the incorporation of systems to distribute the leaching solution evenly, preventing unreacted zones and ensuring comprehensive metal extraction. The reversal of the expected pH trend in the replicate RRP2 columns highlights the considerable influence of spatial heterogeneity, macropore flow, and sidewall flow have on the carbon mineralization potential (Appendix Figure A3.1). Minor physical nuances can lead to profound changes in carbonation potential, which demands thorough investigation because ultramafic rocks have seldom been processed using heap leaching. Additionally, the distinct mineralogy inherent to each type of ultramafic rock, and even among different ultramafic facies within an ore deposit, influences the carbonation potential. This complex synergy between physical and chemical properties highlights the need for an integrated approach to understanding of mineral leaching for coupled mineralization of carbon and enhanced recovery of critical metals.

4.7 Chapter 4 references

Assima, G.P., Larachi, F., Molson, J., and Beaudoin, G., 2014. Impact of temperature and oxygen availability on the dynamics of ambient CO_2 mineral sequestration by nickel mining residues. Chemical Engineering Journal, 240, pp.394-403.

Bigham, J.M., and Nordstrom, D.K., 2000. Iron and aluminum hydroxysulfates from acid sulfate waters. Reviews in mineralogy and geochemistry, 40(1), pp.351-403.

Bish, D.L. and Howard, S.A., 1988. Quantitative phase analysis using the Rietveld method. Journal of Applied Crystallography, 21(2), pp.86-91.

Bish, D.L., Carey, J.W., Vaniman, D.T. and Chipera, S.J., 2003. Stability of hydrous minerals on the martian surface. Icarus, 164(1), pp.96-103.

Cheary, R.W. and Coelho, A., 1992. A fundamental parameters approach to X-ray line-profile fitting. Journal of Applied Crystallography, 25(2), pp.109-121.

DeSisto, S.L., Jamieson, H.E. and Parsons, M.B., 2011. Influence of hardpan layers on arsenic mobility in historical gold mine tailings. Applied Geochemistry, 26(12), pp.2004-2018.

Gadikota, G., Matter, J., Kelemen, P., and Park, A.H.A., 2014. Chemical and morphological changes during olivine carbonation for CO_2 storage in the presence of NaCl and $NaHCO_3$. Physical Chemistry Chemical Physics, 16(10), pp.4679-4693.

Galan, I., Glasser, F.P., Baza, D. and Andrade, C., 2015. Assessment of the protective effect of carbonation on portlandite crystals. Cement and Concrete Research, 74, pp.68-77.

Kraft, S., Stümpel, J., Becker, P. and Kuetgens, U., 1996. High resolution x-ray absorption spectroscopy with absolute energy calibration for the determination of absorption edge energies. Review of scientific instruments, 67(3), pp.681-687.

Hamilton, J.L., Wilson, S., Morgan, B., Harrison, A.L., Turvey, C.C., Paterson, D.J., Dipple, G.M. and Southam, G., 2020. Accelerating mineral carbonation in ultramafic mine tailings via direct CO_2 reaction and heap leaching with potential for base metal enrichment and recovery. Economic Geology, 115(2), pp.303-323.

Hamilton, J.L., Wilson, S., Morgan, B., Turvey, C.C., Paterson, D.J., Jowitt, S.M., McCutcheon, J., and Southam, G., 2018. Fate of transition metals during passive carbonation of ultramafic mine tailings via air capture with potential for metal resource recovery. International Journal of Greenhouse Gas Control, 71, pp.155-167.

Harrison, A.L., Power, I.M., and Dipple, G.M., 2013. Accelerated carbonation of brucite in mine tailings for carbon sequestration. Environmental Science & Technology, 47(1), pp.126-134.

Haug, T.A., Kleiv, R.A., and Munz, I.A., 2010. Investigating dissolution of mechanically activated olivine for carbonation purposes. Applied Geochemistry, 25(10), pp.1547-1563.

Hetman, C.M., Smith, B.S., Paul, J.L. and Winter, F., 2004. Geology of the Gahcho Kué kimberlite pipes, NWT, Canada: root to diatreme magmatic transition zones. Lithos, 76(1-4), pp.51-74.

Hill, R.J. and Howard, C.J., 1987. Quantitative phase analysis from neutron powder diffraction data using the Rietveld method. Journal of Applied Crystallography, 20(6), pp.467-474.

Huijgen, W.J., Witkamp, G.J., and Comans, R.N., 2006. Mechanisms of aqueous wollastonite carbonation as a possible CO_2 sequestration process. Chemical Engineering Science, 61(13), pp.4242-4251.

IPCC, 2023. Climate Change 2023: Synthesis Report. A Report of the Intergovernmental Panel on Climate Change.

Jambor, J.L., Dutrizac, J.E., and Raudsepp, M., 2007. Measured and computed neutralization potentials from static tests of diverse rock types. Environmental Geology, 52, pp.1173-1185.

Lackner, K.S., 2003. A guide to CO_2 sequestration. Science, 300(5626), pp.1677-1678.

Lackner, K.S., Wendt, C.H., Butt, D.P., Joyce Jr, E.L., and Sharp, D.H., 1995. Carbon dioxide disposal in carbonate minerals. Energy, 20(11), pp.1153-1170.

Lechat, K., Lemieux, J.M., Molson, J., Beaudoin, G., and Hébert, R., 2016. Field evidence of CO_2 sequestration by mineral carbonation in ultramafic milling wastes, Thetford Mines, Canada. International Journal of Greenhouse Gas Control, 47, pp.110-121.

Lupo, J.F., 2010. Liner system design for heap leach pads. Geotextiles and Geomembranes, 28(2), pp.163-173.

Mahmoud, A., Cézac, P., Hoadley, A.F., Contamine, F., and d'Hugues, P., 2017. A review of sulfide minerals microbially assisted leaching in stirred tank reactors. International Biodeterioration & Biodegradation, 119, pp.118-146.

McCutcheon, J., Turvey, C.C., Wilson, S., Hamilton, J.L. and Southam, G., 2017. Experimental deployment of microbial mineral carbonation at an asbestos mine: Potential applications to carbon storage and tailings stabilization. Minerals, 7(10), p.191.

McCutcheon, J., Wilson, S. and Southam, G., 2015. Microbially accelerated carbonate mineral precipitation as a strategy for in situ carbon sequestration and rehabilitation of asbestos mine sites. Environmental Science & Technology, 50(3), pp.1419-1427.

McCutcheon, J., Wilson, S., and Southam, G., 2016. Microbially accelerated carbonate mineral precipitation as a strategy for in situ carbon sequestration and rehabilitation of asbestos mine sites. Environmental Science & Technology, 50(3), pp.1419-1427.

Mervine, E.M., Wilson, S.A., Power, I.M., Dipple, G.M., Turvey, C.C., Hamilton, J.L., Vanderzee, S., Raudsepp, M., Southam, C., Matter, J.M. and Kelemen, P.B., 2018. Potential for offsetting diamond mine carbon emissions through mineral carbonation of processed kimberlite: an assessment of De Beers mine sites in South Africa and Canada. Mineralogy and Petrology, 112, pp.755-765.

Min, Y., and Jun, Y.S., 2018. Wollastonite carbonation in water-bearing supercritical CO_2: Effects of water saturation conditions, temperature, and pressure. Chemical Geology, 483, pp.239-246.

Munz, I.A., Brandvoll, Ø., Haug, T.A., Iden, K., Smeets, R., Kihle, J., and Johansen, H., 2012. Mechanisms and rates of plagioclase carbonation reactions. Geochimica et Cosmochimica Acta, 77, pp.27-51.

Park, A.H.A., and Fan, L.S., 2004. CO_2 mineral sequestration: physically activated dissolution of serpentine and pH swing process. Chemical Engineering Science, 59(22-23), pp.5241-5247.

Parkhurst, D.L., and Appelo, C.A.J., 2013. Description of input and examples for PHREEQC version 3—a computer program for speciation, batch-reaction, one-dimensional transport, and inverse geochemical calculations. US geological survey techniques and methods, 6(A43), p.497.

Paulo, C., Power, I.M., Stubbs, A.R., Wang, B., Zeyen, N., and Wilson, S., 2021. Evaluating feedstocks for carbon dioxide removal by enhanced rock weathering and CO_2 mineralization. Applied Geochemistry, 129, p.104955

Paulo, C., Power, I.M., Zeyen, N., Wang, B. and Wilson, S.A., 2023. Geochemical modeling of CO_2 sequestration in ultramafic mine wastes from Australia, Canada, and South Africa: Implications for carbon accounting and monitoring. Applied Geochemistry, 152, p.105630.

Power, I.M., Dipple, G.M. and Southam, G., 2010. Bioleaching of ultramafic tailings by Acidithiobacillus spp. for CO_2 sequestration. Environmental science & technology, 44(1), pp.456-462.

Power, I.M., Wilson, S., and Dipple, G.M., 2013. Serpentinite carbonation for CO_2 sequestration. Elements, 9(2), pp.115-121.

Power, I.M., Wilson, S.A., Small, D.P., Dipple, G.M., Wan, W. and Southam, G., 2011. Microbially mediated mineral carbonation: roles of phototrophy and heterotrophy. Environmental Science & Technology, 45(20), pp.9061-9068.

Pradhan, N., Nathsarma, K.C., Rao, K.S., Sukla, L.B. and Mishra, B.K., 2008. Heap bioleaching of chalcopyrite: A review. Minerals Engineering, 21(5), pp.355-365.

Pronost, J., Beaudoin, G., Tremblay, J., Larachi, F., Duchesne, J., Hébert, R., and Constantin, M., 2011. Carbon sequestration kinetic and storage capacity of ultramafic mining waste. Environmental Science & Technology, 45(21), pp.9413-9420.

Ravel, B. and Newville, M., 2005. ATHENA, ARTEMIS, HEPHAESTUS: data analysis for X-ray absorption spectroscopy using IFEFFIT. Journal of synchrotron radiation, 12(4), pp.537-541.

Rietveld, H.M., 1969. A profile refinement method for nuclear and magnetic structures. Journal of applied Crystallography, 2(2), pp.65-71.

Ruiz-Agudo, E., Kudłacz, K., Putnis, C.V., Putnis, A. and Rodriguez-Navarro, C., 2013. Dissolution and carbonation of portlandite [$Ca(OH)_2$] single crystals. Environmental Science & Technology, 47(19), pp.11342-11349.

Ryan, C.G., 2000. Quantitative trace element imaging using PIXE and the nuclear microprobe. International Journal of Imaging Systems and Technology, 11(4), pp.219-230.

Ryan, C.G., Siddons, D.P., Kirkham, R., Dunn, P.A., Kuczewski, A., Moorhead, G., De Geronimo, G., Paterson, D.J., De Jonge, M.D., Hough, R.M., and Lintern, M.J., 2010, April. The new Maia detector system: methods for high definition trace element imaging of natural material. In AIP Conference Proceedings (Vol. 1221, No. 1, pp. 9-17). American Institute of Physics.

Ryan, C.G., Siddons, D.P., Kirkham, R., Li, Z.Y., De Jonge, M.D., Paterson, D.J., Kuczewski, A., Howard, D.L., Dunn, P.A., Falkenberg, G., and Boesenberg, U., 2014, April. Maia X-ray fluorescence imaging: Capturing detail in complex natural samples. In Journal of Physics: Conference Series (Vol. 499, No. 1, p. 012002). IOP Publishing.

Scarlett, N.V. and Madsen, I.C., 2006. Quantification of phases with partial or no known crystal structures. Powder Diffraction, 21(4), pp.278-284.

Seifritz, W., 1990. CO_2 disposal by means of silicates. Nature, 345, pp.486-486.

Sinclair, L. and Thompson, J., 2015. In situ leaching of copper: Challenges and future prospects. Hydrometallurgy, 157, pp.306-324.

SRK consulting, 2009. NI 43-101 Technical Report on Resources. https://edityr8x9wf.exactdn.com/wp-content/uploads/2022/11/NI.43-101.pdf (Accessed 1 May 2023).

Stubbs, A.R., Paulo, C., Power, I.M., Wang, B., Zeyen, N., and Wilson, S., 2022. Direct measurement of CO_2 drawdown in mine wastes and rock powders: Implications for enhanced rock weathering. International Journal of Greenhouse Gas Control, 113, p.103554.

Turvey, C.C., Hamilton, J.L., and Wilson, S., 2018. Comparison of Rietveld-compatible structureless fitting analysis methods for accurate quantification of carbon dioxide fixation in ultramafic mine tailings. American Mineralogist, 103(10), pp.1649-1662.

Turvey, C.C., Wilson, S., Hamilton, J.L., and Southam, G., 2017. Field-based accounting of CO_2 sequestration in ultramafic mine wastes using portable X-ray diffraction. American Mineralogist: Journal of Earth and Planetary Materials, 102(6), pp.1302-1310.

Vance, K., Falzone, G., Pignatelli, I., Bauchy, M., Balonis, M. and Sant, G., 2015. Direct carbonation of $Ca(OH)_2$ using liquid and supercritical CO_2: implications for carbon-neutral cementation. Industrial & Engineering Chemistry Research, 54(36), pp.8908-8918.

Wang, F., Dreisinger, D., Jarvis, M., Hitchins, T., and Trytten, L., 2021. CO_2 mineralization and concurrent utilization for nickel conversion from nickel silicates to nickel sulfides. Chemical Engineering Journal, 406, p.126761.

Wang, F., and Dreisinger, D., 2022. Carbon mineralization with concurrent critical metal recovery from olivine. Proceedings of the National Academy of Sciences, 119(32), p.e2203937119.

Wilson, S., Dipple, G.M., Power, I.M., Barker, S.L., Fallon, S.J., and Southam, G., 2011. Subarctic weathering of mineral wastes provides a sink for atmospheric CO_2. Environmental Science & Technology, 45(18), pp.7727-7736.

Wilson, S., Dipple, G.M., Power, I.M., Thom, J.M., Anderson, R.G., Raudsepp, M., Gabites, J.E., and Southam, G., 2009a. Carbon dioxide fixation within mine wastes of ultramafic-hosted ore deposits: Examples from the Clinton Creek and Cassiar chrysotile deposits, Canada. Economic Geology, 104(1), pp.95-112.

Wilson, S., Harrison, A.L., Dipple, G.M., Power, I.M., Barker, S.L., Mayer, K.U., Fallon, S.J., Raudsepp, M., and Southam, G., 2014. Offsetting of CO_2 emissions by air capture in mine tailings at the Mount Keith Nickel Mine, Western Australia: Rates, controls and prospects for carbon neutral mining. International Journal of Greenhouse Gas Control, 25, pp.121-140.

Wilson, S., Raudsepp, M., and Dipple, G.M., 2006. Verifying and quantifying carbon fixation in minerals from serpentine-rich mine tailings using the Rietveld method with X-ray powder diffraction data. American Mineralogist, 91(8-9), pp.1331-1341.

Wilson, S., Raudsepp, M., and Dipple, G.M., 2009b. Quantifying carbon fixation in trace minerals from processed kimberlite: A comparative study of quantitative methods using X-ray powder diffraction data with applications to the Diavik Diamond Mine, Northwest Territories, Canada. Applied Geochemistry, 24(12), pp.2312-2331.

Zeyen, N., Wang, B., Wilson, S., Paulo, C., Stubbs, A.R., Power, I.M., Steele-Maclnnis, M., Lanzirotti, A., Newville, M., Paterson, D.J., and Hamilton, J.L., 2022. Cation exchange in smectites as a new approach to mineral carbonation. Frontiers in Climate, 4.

Chapter 5

Microbial CO_2 removal into carbonate sediments using acid leaching and cation exchange leachates from kimberlite mine residues — Results from Project CarbonVault

5.1 Introduction

Human activities, principally through emissions of greenhouse gases (GHG), have caused global average surface temperature to reach ~1.1 °C above pre-industrial levels (IPCC, 2023). Despite a deceleration in the rate of growth, mean annual GHG emissions during 2010–2019 were still higher than in any previous decade (IPCC, 2023). Numerous approaches to decarbonation are being explored to stabilize Earth's climate. Among them, carbon mineralization is considered a promising solution due to its ability to store large amounts of carbon dioxide (CO_2) in a stable and environmentally friendly way (*e.g.*, Seifritz, 1990; Lackner et al., 1995; Lackner, 2003; Power et al., 2013). Carbon mineralization is a process by which atmospheric CO_2 is converted into stable carbonate minerals following dissolution of silicate minerals (Power et al., 2013). To date, two field demonstrations, Wallula in Washington, USA and CarbFix in Iceland, have successfully mineralized CO_2 in geological formations. In the Wallula project, ~60% of the injected CO_2 was sequestered through mineralization within two years (White et al., 2020). The CarbFix project achieved a 95% mineralization rate in its pilot phase and has continued to mineralize over 60% of injected CO_2 in larger-scale industrial operations, demonstrating the feasibility of safe and permanent carbon storage in basalt formations (Matter et al., 2016; Clark et al., 2020).

Traditional carbon capture and storage (CCS) techniques focus on utilizing geological formations for CO_2 storage, generating economic benefits that can partially offset the costs of sequestration (Lackner, 2003). The underground environment's high pressure necessitates merely a chemically reactive rock and the introduction of CO_2 either as a supercritical fluid or in the form of dissolved inorganic carbon. Conversely, the significantly lower partial pressure of CO_2 at the Earth's surface introduces unique challenges to the engineering of carbon mineralization processes (*e.g.* Power et al., 2013). In nature, a variety of microorganisms can accelerate the precipitation of carbonate minerals by altering water chemistry (*e.g.*, Vasconcelos et al., 2006; Perry et al., 2007; Dupraz et al., 2009; Spadafora et al., 2010; Iniesto et al., 2021). During the Precambrian era, photosynthetic microbes began to form stromatolites by microbially-mediated mineralization, which influenced the composition of the atmosphere by taking up CO_2 and generating free oxygen (Kasting and Howard, 2006). Autotrophic and heterotrophic organisms play important roles in microbially-mediated mineral carbonation: heterotrophic organisms increase concentrations of dissolved inorganic carbon (DIC) and produce organic acids that can dissolve silicate minerals while photosynthetic bacteria generate carbonate alkalinity that promotes formation of carbonate minerals (*e.g.*, Dupraz et al., 2009; Power et al., 2011; McCutcheon et al., 2015; Görgen et al., 2021). Microbes can also provide nucleation sites for carbonate precipitation (*e.g.*, Pentecost and Bauld, 1988; Dupraz et al., 2009; Obst et al., 2009a, 2009b; Chagas et al., 2016; Görgen et al., 2021).

Microbially-mediated mineralization has been studied in detail using ultramafic mine tailings (*e.g.*, Power et al., 2010, 2011; McCutcheon et al., 2014, 2015, 2016, 2017). Power et al. (2010) showed that microbially-mediated carbonation process could accelerate dissolution of chrysotile asbestos and McCutcheon et al. (2015, 2017) demonstrated the ability of cyanobacteria to cement asbestiform chrysotile in a way that minimizes windblown dust. Microbially-mediated carbon mineralization has the potential to be integrated into various industrial sectors, such as power generation, cement production, and waste management, including the management of mine tailings. For instance, Power et al.（2011）estimated that redesigning the tailings storage facilities at the Diavik diamond mine to include microbial carbon mineralization with biomass production could reduce the mine's greenhouse gas emissions by 2.5%.

The mining sector is actively investigating the potential of carbon mineralization as a strategy to mitigate its significant, yet challenging to reduce CO_2 emissions. Among the forefront of these explorations is De Beers, which has ambitiously pledged to achieve carbon neutrality across its operations by 2030. This commitment is particularly relevant given the inherent carbon sequestration capabilities of certain mine tailings, including those from diamond, nickel-copper-platinum group element (Ni-Cu-PGE), chromium, and historical asbestos mining operations (*e.g.,* Wilson et al., 2006, 2009a, 2009b, 2010, 2014; Pronost et al., 2011; Bobicki et al., 2012; Lechat et al., 2016; Turvey et al., 2017, 2018; Hamilton et al., 2018, 2020; Mervine et al., 2018).

These tailings are reactive to CO_2 and, thus, present an opportunity to offset emissions through the extraction of magnesium (Mg) and calcium (Ca) from silicate minerals, followed by the accelerated precipitation of carbonate minerals. There are two known ways to extract Mg and Ca from silicate minerals for this purpose: acid leaching, which dissolves minerals, and provides access to the bulk of a rock's carbon mineralization potential (Chapter 3 and 4), and cation exchange (Zeyen et al., 2022), which quickly extracts lesser amounts Mg and Ca from the interlayers of the smectites that are common in kimberlite while avoiding primary carbonate dissolution. Here, we report results from a multi-tonne microbial carbonation pilot using kimberlite (diamond) mine tailings from the Venetia mine, South Africa. The goals of this work are to (1) evaluate the suitability of combining either acid leaching of tailings or a cation exchange method with microbially-mediated carbon mineralization and (2) test the feasibility of implementing this approach to microbial carbonation on a large scale.

5.2 Materials and methods

5.2.1 Sample collection

The geological context of the Venetia kimberlite cluster is described in Chapter 3. Samples of processed kimberlite predominantly composed of the dark volcaniclastic kimberlite (DVK) facies were procured from the Venetia mine during the year 2019. The DVK facies, which is one of the primary kimberlite types present in the Venetia kimberlite cluster, is distinguished by its dark color and its abundant volcaniclastic material, including basaltic lava fragments and volcanic ash (Buse et al., 2011). The production process for both the fine residue deposit (FRD) and the coarse residue deposit (CRD) has been detailed in Chapter 3. For the purposes of the field trials, the CRD sample from the DVK facies was exclusively selected due to its coarser grain size, which facilitates enhanced drainage capabilities when administering treatments involving water, acidic solutions, and aqueous cation exchange processes.

5.2.2 Experimental design

The field trials were conducted using two-step reactors at De Beers Technology (DebTech) in Johannesburg, South Africa. Four leaching reactors consisted of 1-m^3 intermediate bulk containers (IBC), each containing ~850 kg of CRD from the DVK facies. For the first step, treatments of (1) tap water, (2) 0.12 M HCl, (3) 1 M ammonium acetate (NH_4OAc) or (4) 1 M ammonium chloride (NH_4Cl) were applied weekly for six weeks to extract or exchange cations such as Ca^{2+} and Mg^{2+} from the CRD. Each treatment was 200 L. Within the context of the trial, tap water serves as the control treatment, providing a baseline against which the effects of the acid and cation exchange treatments can be assessed. HCl was chosen based on its proven efficacy in dissolving silicate minerals, thereby facilitating the release of metal cations—a process extensively discussed in relation to acid leaching techniques in Chapter 3 and 4. As the mineralogy of these processed kimberlites is dominated by serpentine and (Mg,Ca)-rich smectites, a cation exchange method using less desirable species/cations (*e.g.*, NH_4^+) may liberate Mg^{2+} and Ca^{2+} from the interlayer spaces of smectites during leaching process while avoiding primary carbonate dissolution. Specifically, these species/cations (*e.g.*, NH_4^+) are commonly employed to extract metal cations from smectites in cation exchange capacity (CEC) tests, highlighting their utility in simulating natural geochemical interactions within a controlled experimental setup. After reacting overnight with the kimberlite in IBCs, the solutions generated by each leaching reactor were drained and divided into two equivalent volumes and dispensed into two 1400-L carbonation reactors. One carbonation reactor, referred to as "bio", initially contained dense microbial mats collected from the wall of the open pit of the Venetia mine in September 2019 and cultivated directly in the reactors by monthly BG11 treatment. Details about the composition of the BG11 and volume added are provided in Appendix Table A4.1. By contrast, no microbes were deliberately introduced to the second carbonation reactor, referred to as a control reactor that was initially empty and served as an evaporative control system (Fig. 5.1).

The trials started with the first treatment on Feb 14, 2020 (day 0) and finished on Feb 22, 2021 (day 374). Prior to the initiation of the treatment process, water samples in the four bio carbonation reactors were collected. This preparatory step was conducted at three distinct time points: eight days (day -8), three days (day -3), and half a day (day -0.5) before the commencement of the first treatment. Collection of water (weekly) and biomass (monthly) samples was done starting day 8 with samples collected before the first treatment and thereafter the day before each subsequent treatment during Feb– Mar 2020. After the COVID-19 lockdown in Johannesburg from March to May 2020, weekly monitoring of water pH, temperature, and conductivity was conducted. Water samples were collected on a weekly basis while biological samples were collected monthly. Solid samples were collected at the bottom of each of the eight carbonation containers after four months following the first treatment. Solid samples from various depths within the IBCs were collected during May and June of 2020. Upon the conclusion of the experimental trial, a comprehensive sampling procedure was undertaken to evaluate the outcomes of the treatment processes. From each of the eight reactors involved in the study, a volume of 20 L of solution was collected, along with sediment samples, which were obtained in triplicate. A detailed breakdown of the samples is given in Table 5.1. Processing of samples typically took several months, including sterilization, filtration, centrifugation, drying and milling.

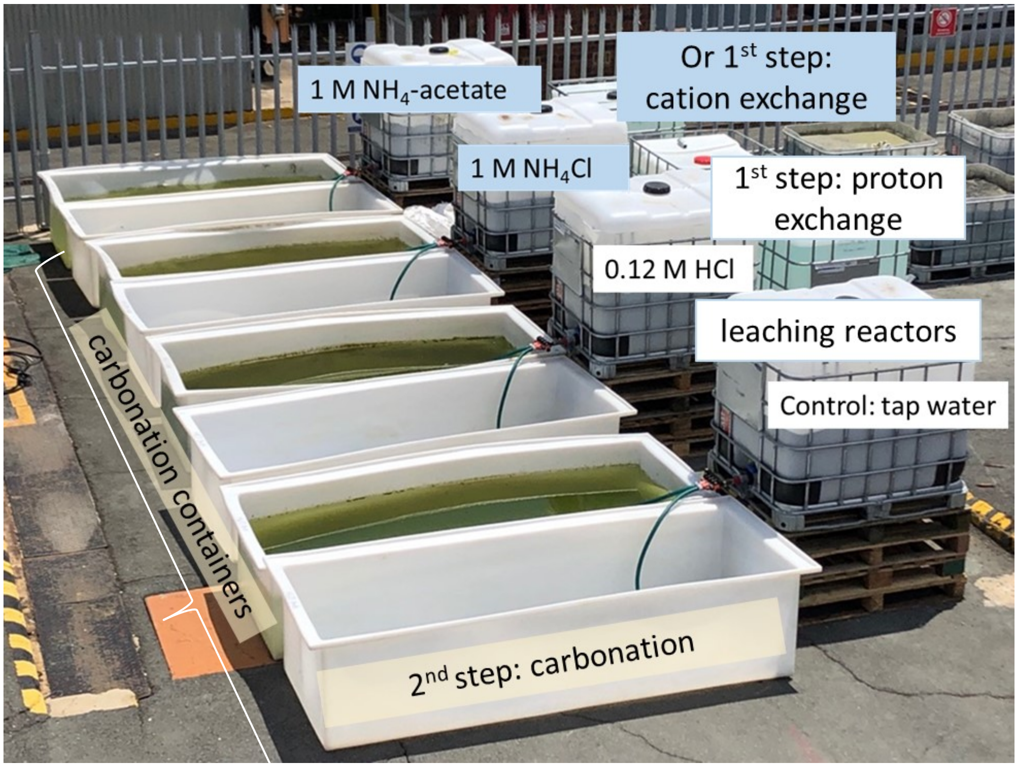

Figure 5.1 DebTech field trials (early February 2020), prior to the first treatment.

Table 5.1 Summary of sampling for DebTech field trials.

Sample type	Date of sampling	Numbers of samples
Water samples from carbonation reactors	▪ ~Weekly Feb 2020 – Feb 2021 ▪ note: no samples were collected from 26 Mar –19 May 2020 owing to the lockdown	▪256 samples (06 Feb 2020 –22 Feb 2021)
Sediments from carbonation reactors	▪ Jun, Oct 2020, Feb 2021, Nov 2022	▪ 54 samples
Biomass from carbonation reactors	▪ ~Monthly Feb 2020 – Mar 2021	▪ 80 samples (Feb 2020–Feb 2021)
Treated CRD from leaching reactors	▪ Deep samples: 28 May 2020 ▪ Surface samples: 18 Jun 2020	▪ 48 samples
Initial DVK CRD	▪ February 2020	▪ 3 samples (triplicate)
Calcite grains picked from the initial DVK CRD	▪ February 2020	▪ 2 samples (duplicates)
Natural biofilm from Venetia and cultured biofilm (collected from one of the carbonation reactors)	▪ September 2019	▪2 samples

5.2.3 Analytical methods

5.2.3.1 RNA sequence analysis

The biofilm collected from the Venetia mine pit in September 2019 was cultivated in bioreactors with a capacity of around 1,400 L until the initiation of the field trials. The natural biofilm sample and the cultured biofilm sample were sampled using sterile tools, and approximately 2 g of material was transferred to a clean tube for DNA extraction. Subsequently, 16S rDNA extraction was performed in a laminar flow cabinet to aseptically recover nucleic acids. DNA was extracted from 50 to 200 mg of the sample, and preliminary bead beating (BioSpec Products #11079101) was carried out using 0.1-mm diameter glass beads on a Powerlyser 24 homogenizer. The samples were then added to a bead tube containing 850 µl of CD1 (Qiagen cat #47016) and mixed using a vortex. The tubes were heated to 65 °C for 10 min and then bead-beaten for 5 min at 2,500 rpm, followed by centrifugation for 1 min at 15,000 *g*. The resulting lysate was transferred to a new collection tube for PCR amplification, with a final elution volume of 50 µl.

Amplification of the extracted DNA was targeted to the V6 to V8 regions of the 16S rRNA gene, using universal primers 926f and 1392r, which were adapted to contain Illumina-specific adapter sequences. The forward primer sequence was 5′-TCGTCGGCAGCGTCAGATGTGTATAAGA GACAGaaactyaaakgaattgacgg-3' and the reverse primer sequence was 5′-GTCTCGTGGG CTCGGGTCTCGTGGGCTCGGAGATGTGTATAAGAGACAG acgggcggtgtgtrc-3'. Libraries were prepared as described by Illumina (#15044223 Rev B), with the exception of using Q5 Hot Start High-Fidelity polymerase and PCR mastermix (New England Biolabs, Ipswich, MA, USA). The resulting PCR amplicons were purified using Agencourt AMPure XP beads (Beckman Coulter, Brea, CA, USA), and the purified DNA was indexed with unique 8-bp barcodes using the Illumina Nextera XT 384 Index Kit A-D (Illumina FC-131-1002) in standard PCR conditions with NEBNext® Ultra™ II Q5® Mastermix. Finally, the indexed amplicons were pooled together in equimolar concentrations and sequenced on a MiSeq Sequencing System (Illumina) using paired-end sequencing with V3 300 bp chemistry, according to the manufacturer's protocol.

5.2.3.2 Leachate chemistry

Conductivity, pH and temperature of solutions in the eight carbonation reactors (before August 11th, 2020) were measured *in situ* using an Orion Star™ A329 pH/ISE/Conductivity/Dissolved Oxygen Portable Multiparameter Meter. The water samples were collected immediately after measurements were taken and filtered using 0.45 µm filters. For water samples collected after August 17, 2020, the conductivity, pH and temperature were measured upon receipt at the University of Alberta. Owing to filtration difficulties at the field site, some of the water samples were filtered at the University of Alberta after their receipt.

5.2.3.2.1 Cation analysis by inductively coupled plasma mass spectrometry (ICP-AES)

Concentrations of dissolved metals, S, and P in leachates were analyzed using a Thermo iCAP6300 Duo inductively coupled plasma-optical emission spectrometer (ICP-OES) at the Natural Resources Analytical Laboratory (NRAL), University of Alberta.

5.2.3.2.2 Other elements

Concentrations of anions (Cl^-, NO_2^-, NO_3^-, PO_4^{3-} and SO_4^{2-}) as well as NH_4^+ were determined using a Colourimetric Thermo Gallery Plus Beermaster Autoanalyzer at NRAL, University of

Alberta. Dissolved organic carbon (DOC), and total nitrogen (TN) were determined at NRAL using a Shimadzu TOC-L CPH Model Total Organic Carbon Analyzer with an ASI-L and TNM-L. Dissolved inorganic carbon (DIC) analyses were performed at Trent University, utilizing a CM5017 CO_2 coulometer.

5.2.3.3 Chemistry and mineralogy of solids

5.2.3.3.1 Bulk elemental chemistry

Bulk elemental chemistry of initial DVK CRD and the processed kimberlite samples from various depths of IBCs was determined at SGS Mineral Services Geochemical Laboratory in Vancouver, Canada. X-ray fluorescence (XRF) was used to determine the abundances of major element oxides including Al_2O_3, CaO, Cr_2O_3, Fe_2O_3, K_2O, MgO, MnO, Na_2O, P_2O_5, SiO_2, TiO_2 and V_2O_5. The concentrations of minor elements such as Co, Cu, Zn and Ni were determined using inductively coupled plasma atomic emission spectroscopy (ICP-AES). Leco analysis was used for total S and C abundances. Total inorganic carbon (TIC) of thick sediments at the bottoms of carbonation reactors was determined using a CO_2 coulometer (CM5017, UIC Inc, USA) at Trent University.

5.2.3.3.2 Powder X-ray diffraction (XRD)

Solid samples from various depths of IBCs and the sediments at the bottom of the carbonation reactors were milled using an automated agate mortar and pestle. This was followed by a 7-minute milling process in anhydrous ethanol, utilizing agate grinding elements in a McCrone Micronizing Mill. Samples were air-dried at room temperature within a fume hood after micronization. Solid samples from IBCs were calcium exchanged in 150 mL of 1 M $CaCl_2$ solution following the method described by Mervine et al. (2018). Samples were then stored in a NaCl slurry box at a relative humidity (RH) of 75% to stabilize the basal (001) spacing of Ca-smectites to ~15 Å (after Bish et al., 2003). An internal standard of 20 wt.% Baikalox Ultrapure Precision α-Al_2O_3 was added to each of the sediment samples collected from the bottoms of the carbonation reactors, followed by a 3-minute micronization step, to quantify smectites alongside organic matter using the method of Wilson et al. (2006).

XRD patterns were collected using a Bruker D8 Advance X-ray diffractometer equipped with a high-speed energy-dispersive LYNXEYE XE-T detector and a cobalt tube that was operated at

35 kV and 40 mA in the Department of Earth and Atmospheric Sciences, University of Alberta. Data were collected from 3–80° 2θ using a step size of 0.02° 2θ at a rate of 1 s/step. Mineral phase identification was conducted using the DIFFRAC.EVA XRD phase analysis software (Bruker) with reference to the International Center for Diffraction Data Powder Diffraction File 4+ database (ICDD PDF4+). Rietveld refinements (Rietveld, 1969; Hill and Howard, 1987; Bish and Howard, 1988) with XRD data were used to determine mineral abundances using TOPAS 5 (Bruker). Fundamental parameters peak fitting (Cheary and Coelho, 1992) was used for all phases. The method of Partial Or No Known Crystal Structure (PONKCS; Scarlett and Madsen, 2006) was used to model the peak profiles of smectites (in IBC samples) and lizardite (in both IBC and carbon reactor samples) to account for turbostratic stacking disorder as implemented by Mervine et al. (2018) and described in detail in Chapter 2.

5.2.3.3.3 Scanning electron microscopy and synchrotron-based scanning transmission X-ray microscopy

Solid samples collected from the bottoms of the carbonation reactors were analyzed using a Zeiss Sigma 300 variable-pressure field-emission scanning electron microscope (VP-FESEM) equipped with secondary electron (SE) and backscattered electron detectors (BSD) in the Department of Earth and Atmospheric Sciences, University of Alberta. Secondary and backscattered electron images were acquired at an accelerating voltage of either 2 kV, 15 kV or 25 kV (variable pressure mode) at a working distance of ~7.6 mm and using a 30 μm aperture. The elemental compositions of mineral phases were determined using energy dispersive X-ray spectrometry (EDXS) with an EDS QUANTAX detector. EDXS data were analyzed using the ESPRIT software package (Bruker).

Selected sediment samples collected from the bottom of the carbonation reactors were analyzed using scanning transmission X-ray microscopy (STXM) at the carbon *K*-edge (C *K*-edge) and the calcium $L_{2,3}$-edge (Ca $L_{2,3}$-edge). Analyses were performed on beamline SM at the Canadian Light Source (CLS), Saskatoon, Canada using a 25 nm zone plate. The samples were prepared by depositing a small amount of an aqueous suspension (1–2 μL) onto a silicon nitride (Si_3N_4) window, which was subsequently allowed to air-dry. Data included images and image stacks, from which X-ray absorption near edge structure (XANES) spectra were produced. The aXis2000 software package was used for image and spectral processing (Hitchcock, 2012).

5.2.3.4 Geochemical modeling

The activities of anions and cations as well as saturation indices (SI) of the leachates with respect to different mineral phases were calculated using PHREEQC V3.4 (Parkhurst and Appelo, 2013) and the minteq.v4 database.

5.3 Results

5.3.1 Analytical results

5.3.1.1 RNA sequence results

The molecular analyses of the natural biofilm collected from the Venetia mine pit in September 2019 highlighted a diverse consortium of bacteria including photosynthetic organisms as well as aerobic and anaerobic heterotrophs. The molecular analyses of the cultured Venetia biofilms revealed that it is feasible to replicate natural biofilms under pilot-scale conditions with similar bacterial biodiversity. Treatment with BG11 and exposure to sunlight stimulated preferential growth of cyanobacteria in the cultured biofilm (Fig. 5.2).

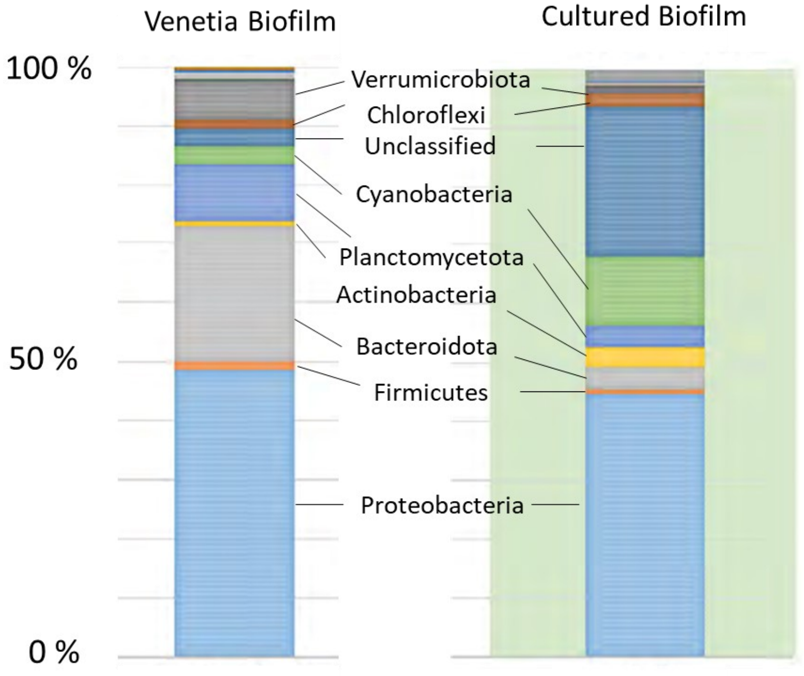

Figure 5.2 Composition of original and cultured microbial communities based on phylum-level 16S rRNA sequencing results.

5.3.1.2 Aqueous geochemistry of the carbonation reactors

Water chemistry data for Feb 2020–Feb 2021, including pH, cations, and DIC, are provided in Appendix Table A4.2. Throughout the year-long experiment, the growth of biomass was observed in all eight carbonation reactors. The visible amount of biomass in the 'bio' reactors, which were inoculated with cultured biofilm from Venetia, was greater compared to that observed in the control (initially empty) reactors. As anticipated, the four control reactors also grew biomass, providing an indication of the potential biomass growth in mine leachates without intentional microbial inoculation.

5.3.1.2.1 Evolution of pH in carbonation reactors

Before day 179, the leachates from all four bio reactors exhibited greater pH values compared to their corresponding control reactors (Fig. 5.3a and Appendix Table A4.2). The pH of the water samples collected from the H_2O control reactor remained 8.10– 9.42 before day 353 and decreased to 7.63 on day 374. Prior to day 179, the pH of the H_2O bio reactor exhibited slight fluctuations, but overall increased to a plateau of approximately 9.6. Thereafter, the pH began to decrease and eventually reached a value of 6.69 on day 374. The pH levels in the HCl control reactor remained stable at around 8 until day 179, after which they remained steady at around 7. The pH of the leachates collected from the HCl bio reactors increased to 10.11 while treatments were being delivered during the first ~6 weeks and remained between values of 8.8 and 9.5 following the lockdown before day 179. Thereafter, the pH values remained between approximately 6.5 and 7.4. The pH measurements for HCl bio reactor that were taken between mid-March and mid-July 2020 (days 32 to 158) showed greater variation than observed in similar laboratory experiments (described in Chapters 3 and 4). The pH of the water samples collected from the NH_4Cl control reactor decreased rapidly from 7.45 to 4.68 on day 4 and remained between 4.4 to 6.5 throughout the remainder of the experiment. The pH of the water samples collected from the NH_4Cl bio reactor decreased from 8.41 before the first treatment to 3.47 on day 374. The pH of the water samples collected from the NH_4OAc control reactor increased from 6.37 on day 4 to 8.06 on day 26 following treatments and then remained stable between values of 6.2 and 6.8. The pH in the NH_4OAc bio reactor increased during treatments to a value of ~9, declined gradually to a value of 6.51 on day 26 following treatments, and then remained between 7.2 to 8.2.

5.3.1.2.2 Evolution of Ca and Mg concentrations in carbonation reactors

Water samples from the H_2O control reactor contained undetectable concentrations (~0 ppm) of Ca and Mg from days 0 to 374 of the experiment (Fig. 5.3b, c and Appendix Table A4.2). Water samples from the H_2O bio reactor exhibited greater concentrations of Mg and Ca with levels not exceeding 170 ppm due to monthly addition of BG11 to feed the microbial community. In contrast, the concentrations of Mg and Ca in leachates from the HCl bio reactor were lower than those in the HCl control reactor. The concentrations of Ca and Mg in leachates from the HCl control carbonation reactor increased over time and reached a maximum of 2272.9 ppm and 585.9 ppm on day 234, respectively, and then decreased after that to 987.8 ppm and 250 ppm on day 374. Four days after the initial treatment, elevated levels of Ca and Mg were measured in the water samples collected from the control NH_4OAc and control NH_4Cl carbonation reactors. The concentrations of Ca and Mg in the water collected from the NH_4OAc control reactor reached up to 8397.4 and 1408.6 ppm, respectively. In the NH_4Cl control reactor, the concentrations of Ca and Mg, again four days after the first treatment, reached 4110.2 and 682.3 ppm, respectively. The concentrations of Ca and Mg in the NH_4OAc and NH_4Cl control reactors abruptly decreased until day 41 and slowly increased again until day 234, followed by a gradual decrease until day 374. This trend of having very high concentrations of Ca and Mg after the first treatment with NH_4OAc or NH_4Cl, with decreasing concentrations after subsequent treatments, was also observed during laboratory column experiments of cation exchange in processed kimberlite (Zeyen et al. in prep). Most of the Ca and Mg was extracted in the first few treatments, with less being extracted in subsequent treatments, thus leading to a dilution of the Ca and Mg concentration over time. Mg and Ca concentrations in the NH_4OAc and NH_4Cl bio reactors were much lower compared to their corresponding control reactors at the beginning of the trials.

5.3.1.2.3 Evolution of DIC concentrations in carbonation reactors

DIC measurements were not conducted on water samples from the H_2O control reactor or the NH_4OAc bio reactor due to the samples not being filtered at DebTech prior to submission for analysis. In the H_2O bio reactor, DIC levels increased from an initial value of 17.97 ppm to 74.97 ppm of $NaHCO_3$ by day 199, stabilizing until day 276, followed by a decline to 49.36 ppm by day 374. The HCl bio reactor experienced an increase in DIC from 36.23 ppm to 92.16 ppm within the first 219 days, before decreasing to 32.91 ppm by the end of the observation period. Throughout the year, the NH_4Cl bio reactor consistently maintained DIC concentrations below 25 ppm. Similarly, the HCl control, NH_4Cl control, and NH_4OAc control reactors had DIC values less than 45 ppm, with an exception of 158.66 ppm on day 0 in the HCl control reactor.

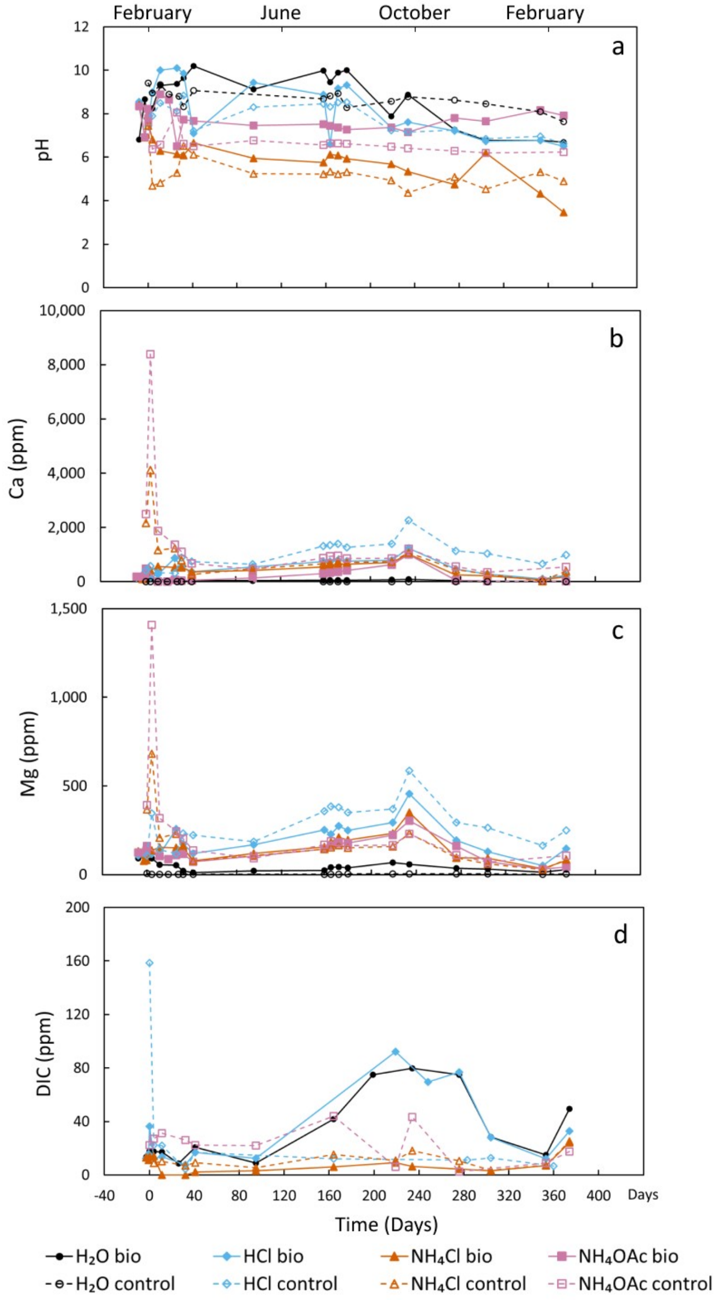

Figure 5.3 Evolution of the aqueous chemistry of the samples collected from the eight carbonation reactors throughout one year.

5.3.1.3 Geochemical and mineralogical changes to solids

5.3.1.3.1 Bulk chemistry and mineralogy of the initial DVK CRD kimberlite

Bulk chemistry results for triplicate samples of the original DVK CRD residue indicate that this material is heterogeneous in composition (Appendix Table A4.3). In particular, the Ca abundance varies from 4.3 to 5.8 wt.%. The total carbon varies from 0.814 to 1.128 wt.% and the abundance of Mg varies from 12.3 to 13.2 wt.% while that of Si varies from 17.1 to 18.1 wt.%. Ni abundances vary from 755 to 866 ppm.

The original DVK CRD showed the same mineral assemblage as the MVK CRD studied in Chapter 3), but with variable abundances as determined using Rietveld refinements (Fig. 5.4 and Appendix Table A4.4). The initial DVK CRD is mainly composed of clay minerals such as lizardite [$Mg_3Si_2O_5(OH)_4$], saponite [$M^{m+}_{x/m}Mg_3(Al_xSi_{4-x})O_{10}(OH)_2 \cdot nH_2O$], clinochlore [$Mg_5Al(AlSi_3)O_{10}(OH)_8$] and talc [$Mg_3Si_4O_{10}(OH)_2$] as well as other silicate minerals such as diopside ($CaMgSi_2O_6$), tremolite [$Ca_2Mg_5Si_8O_{22}(OH)_2$], albite ($NaAlSi_3O_8$), orthoclase ($KAlSi_3O_8$), phlogopite [$KMg_3(AlSi_3)O_{10}(OH)_2$] and quartz ($SiO_2$) as well as calcite ($CaCO_3$), and a small amount of hydroxylapatite [$Ca_5(PO_4)_3(OH)$]. Lizardite was the most abundant mineral phase (26.2 wt.%) followed by saponite (13.6 wt.%), diopside (10.3 wt.%) and phlogopite (9.5 wt.%) in the DVK CRD. The saponite content in DVK CRD (13.6 wt. %) was lower than that in MVK CRD, which had a saponite content of 22.8 wt. %. The DVK CRD contained 7.2 wt. %, which was greater than that observed in MVK-CRD (5.1 wt. %). Grains of calcite present in the CRD were picked and analyzed with XRD and scanning electron microscopy with energy dispersive X-ray spectroscopy (SEM-EDXS) (Fig. 5.5). The EDXS and XRD results show that the carbonate is pure Ca-calcite (Mg-free), with a *d*(104) diffraction peak for calcite at 34.42 °2θ (cobalt).

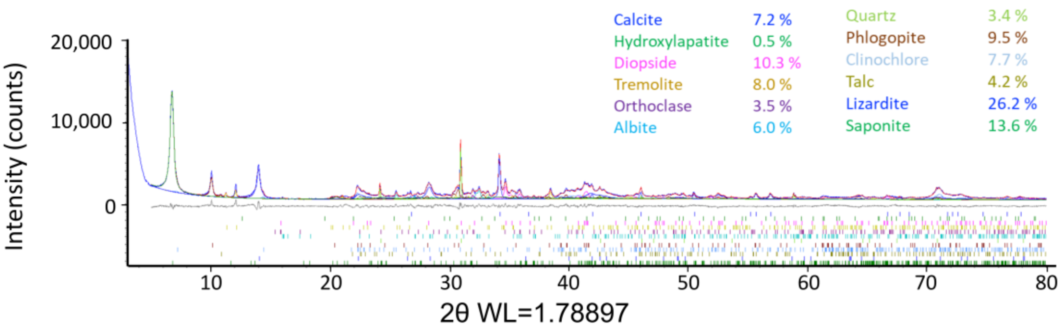

Figure 5.4 Rietveld refinement plot for the initial DVK CRD sample. X-ray diffraction data (blue curve), the modelled fit to the data (red), residual intensity (grey) and fits to individual mineral phases (colors as marked in the legend) are displayed. The positions of Bragg peaks for each phase employed in the model are indicated as short vertical lines beneath the observed and modelled XRD patterns. The R_{wp} of this refinement is 6.7%.

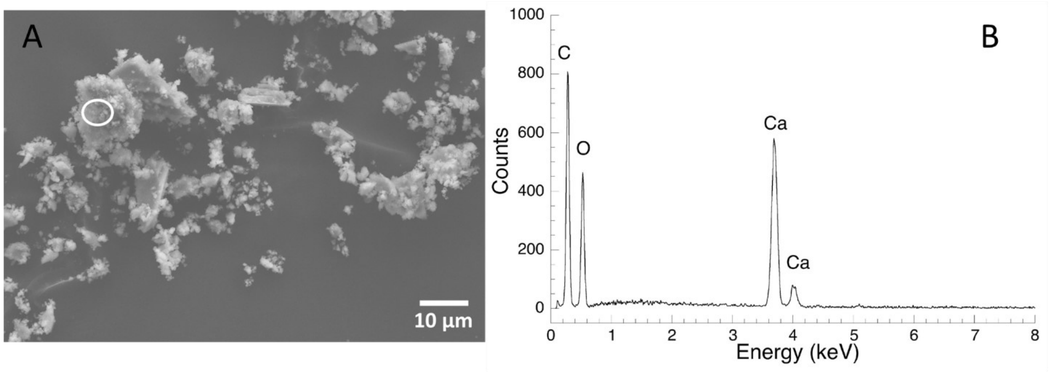

Figure 5.5 SEM micrographs of (A) calcite grains in the original DVK CRD, (B) EDXS data corresponding to the circled area in (A).

5.3.1.3.2 Bulk chemistry and mineralogy of the leached DVK CRD kimberlites

Rietveld refinements using XRD data were employed to assess the mineralogical compositions of solid samples from the leaching reactors (IBCs) treated with different solutions at varying positions and depths (Fig. 5.6 and Appendix Table A4.4). Rietveld refinement results (Appendix Table A4.4) and elemental geochemistry results (Appendix Table A4.3) show that minerals were not homogeneously distributed at different depths or positions (right/left/front/back) within the leaching reactors, which was expected owing to the initial heterogeneity of DVK CRD kimberlite. The same assemblage of 12 minerals was observed at different depths for the H_2O-treated leaching reactor. Lizardite was the most abundant phase in H_2O-leached solid samples

(26.5–39.6 wt.%), followed by saponite varying from 9.2 to 20.9 wt.%. Noticeably, calcite (5.7–8.4 wt.%) was abundant in H_2O-leached solid samples. In the HCl-treated leaching reactors, calcite varied from 2.7 to 8.4 wt.%, with samples from the top of the reactor having the lowest calcite abundances owing to its dissolution. No significant mineralogical changes were observed in the leaching reactors treated with NH_4Cl and NH_4OAc, which is promising as there was no indication of major calcite dissolution as was observed in the HCl-treated leaching reactor.

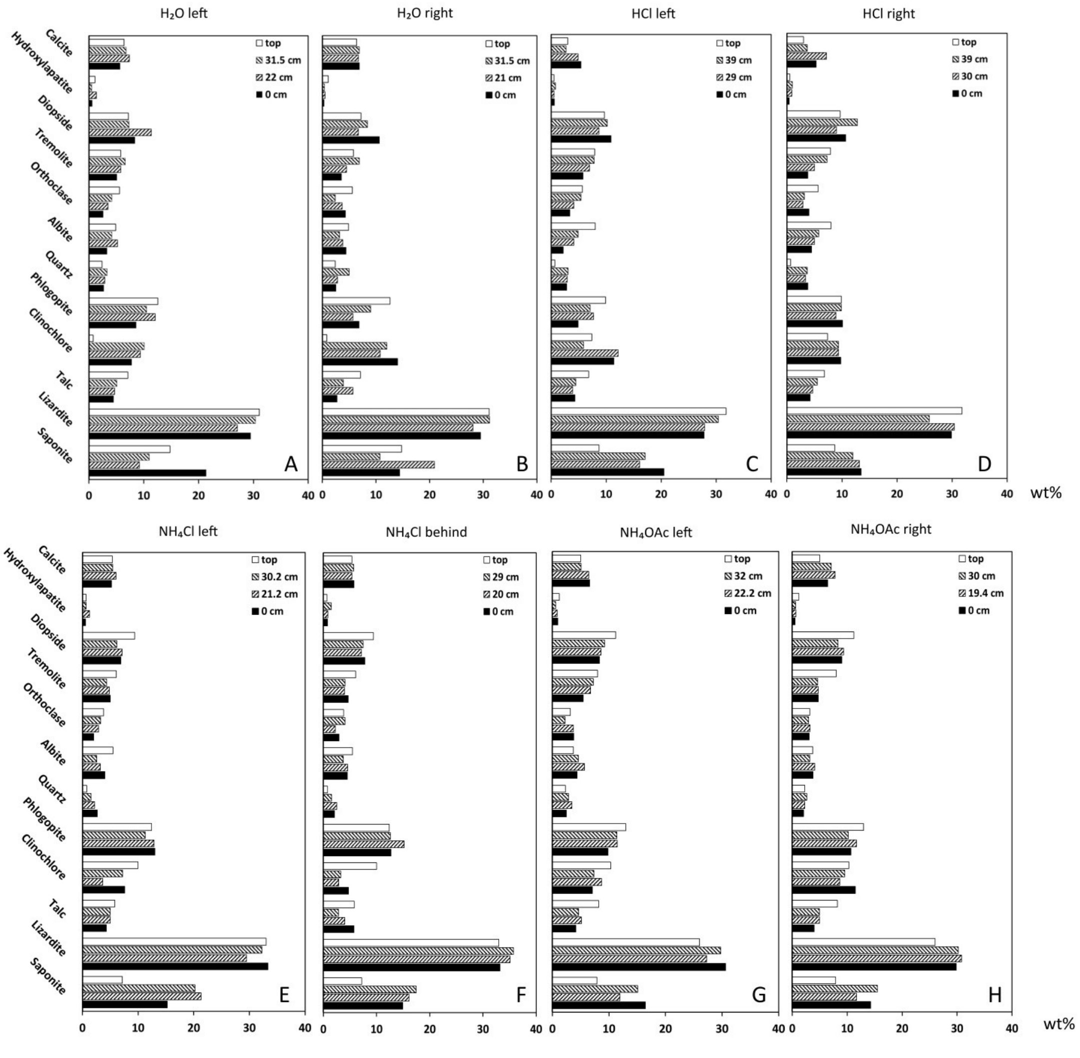

Figure 5.6 Rietveld refinement results of solid samples collected in May and June 2020, following all treatments, at varying positions and depths from the leaching reactors treated with different solutions: (A) H_2O, left; (B) H_2O, right; (C) HCl, left; (D) HCl, right; (E) NH_4Cl, left; (F) NH_4Cl, behind; (G) NH_4OAc, left; (H) NH_4OAc, right.

5.3.1.3.3 Mineralogy of the sediments from the eight carbonation reactors

Thick sediments (over 1 cm deep) were present at the bottoms of the carbonation reactors. The sediments consisted of newly formed mineral phases, kimberlite grains, organic matter and, in the case of the bio reactors, salts used for the nutrient amendment (BG11). XRD analyses of sediments from both H_2O carbonation reactors indicated the presence of minerals that were mainly leached from the DVK CRD (Fig. 5.7a and Appendix Table A4.5). Low Mg-calcite (LMC) in solids from the H_2O control carbonation reactor varied from 4.5 to 6.3 wt.%. By contrast, the sediments in the H_2O bio carbonation reactor contained 1.9 to 7.4 wt. % low Mg-calcite alongside up to 9.0 wt. % of very high Mg-calcite (VHMC, $Mg_{0.5}Ca_{0.5}CO_3$), also called protodolomite or disordered dolomite. In addition, struvite ($NH_4MgPO_4 \cdot 6H_2O$) and bassanite ($CaSO_4 \cdot H_2O$) were present in the H_2O bio carbonation reactor as a result of the addition of BG11. Low Mg-calcite comprised 16.6–24.9 wt.% of the solids from the HCl control carbonation reactor, which was higher than the content observed in the H_2O carbonation reactors. By contrast, solid sediments from the HCl bio carbonation reactor contained various newly-formed carbonate phases, including LMC (2.5–30.0 wt.%), VHMC (2.5–21.4 wt.%), and monohydrocalcite ($CaCO_3 \cdot H_2O$; 0–1.0 wt.%). Bassanite in solids from the HCl bio carbonation reactor varied between 0 to 2.5 wt.%.

Solids collected from the NH_4Cl bio and control carbonation reactors showed a similar mineralogy with the presence of both kimberlite minerals drained during the leaching process and newly formed carbonates including VHMC (9.3–42.1 wt.%) and LMC (0–2.5 wt.%). Meanwhile, solids collected from the NH_4OAc control carbonation reactor contained only fine particles of kimberlite minerals drained from the leaching reactor. Sediments collected from the NH_4OAc bio carbonation reactor were composed of CRD minerals, struvite and three types of newly formed Ca-Mg carbonate minerals: rhombs of VHMC (0–33.1 wt.%), dumbbell-like LMC (7.9–28.3 wt.%) (Fig. 5.8) and high Mg-calcite (5.6–15.3 wt.%).

Synchrotron-based STXM analyses were performed on sediments collected from the carbonation reactors to better characterize the organic matter in these samples (Fig. 5.9). XANES spectra at the C-*K* edge of the sediments showed an intimate association between carbonates and organic polymers. The strong absorption peak at ~290.3 eV (Fig. 5.9b, e) is a characteristic feature exhibited by carbonates (Urquhart and Ade, 2002). The XANES spectrum at the Ca $L_{2,3}$-edge displayed characteristic peaks of calcite at 346.9, 347.4, 348.0, 349.2, 351.3 and 352.5 eV

(Benzerara et al., 2004). The peak at 285.0–285.3 eV is interpreted as a $1s \rightarrow \pi^*$ electronic transition of carbon in aromatic groups (Brandes et al., 2004). The peak at 288.3–288.5 eV is interpreted as a $1 s \rightarrow \pi*$ transition in carboxylic C-functional groups (Brandes et al., 2004). For the sediments collected from the NH_4OAc bio carbonation reactor, bacteria (with peaks at 285.0, 285.4, 288.1 and 288.6 eV) were intimately associated with calcite (Fig. 5.9 d, e, f).

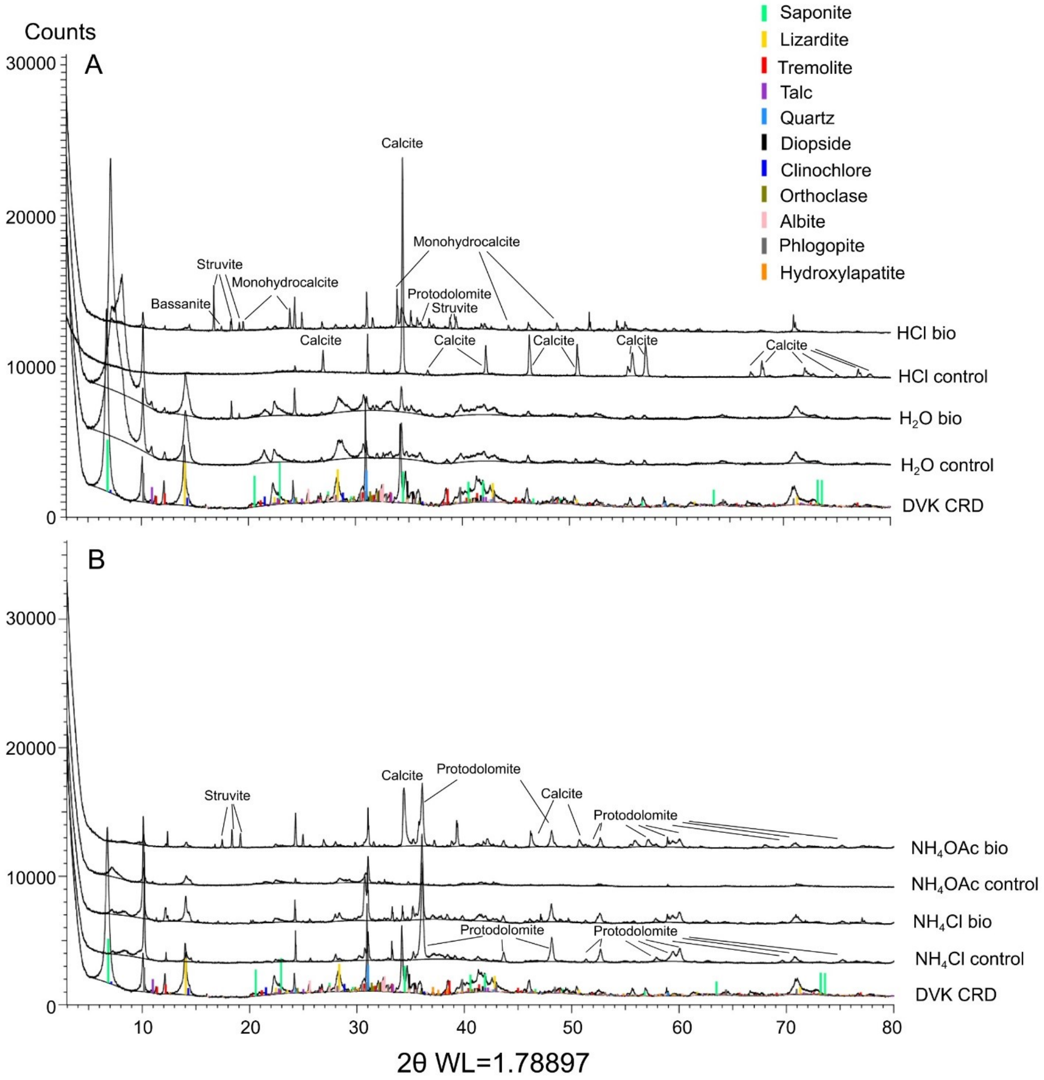

Figure 5.7 Mineralogy of solid samples from carbonation reactors treated with different solutions and sampled on June 2020 (day 115).

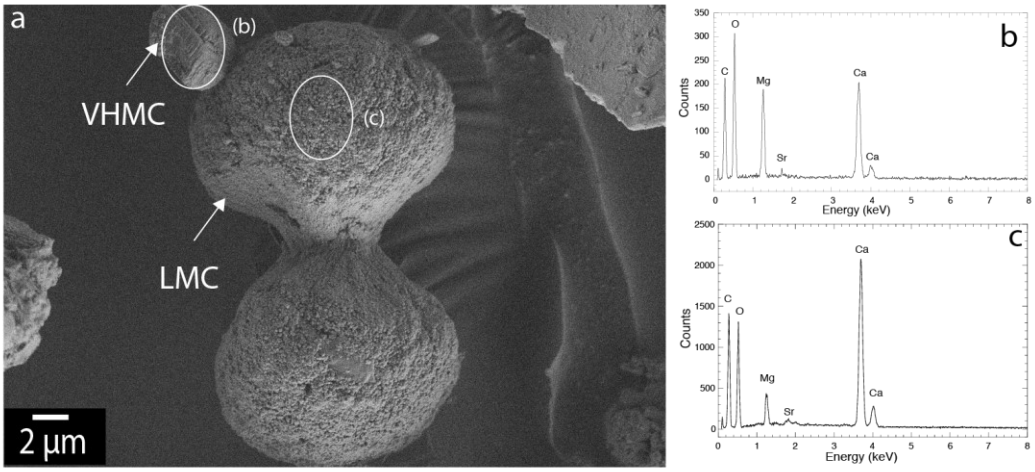

Figure 5.8 Morphology and EDXS analyses of carbonate minerals observed in sediments formed in the NH_4OAc bio carbonation reactor. (a) Secondary electron SEM image of low Mg-calcite (LMC) with a dumbbell shape composed of fibro-radial spherules and a rhomb of very high Mg-calcite (VHMC); (b-c) EDXS data for the areas circled in (a).

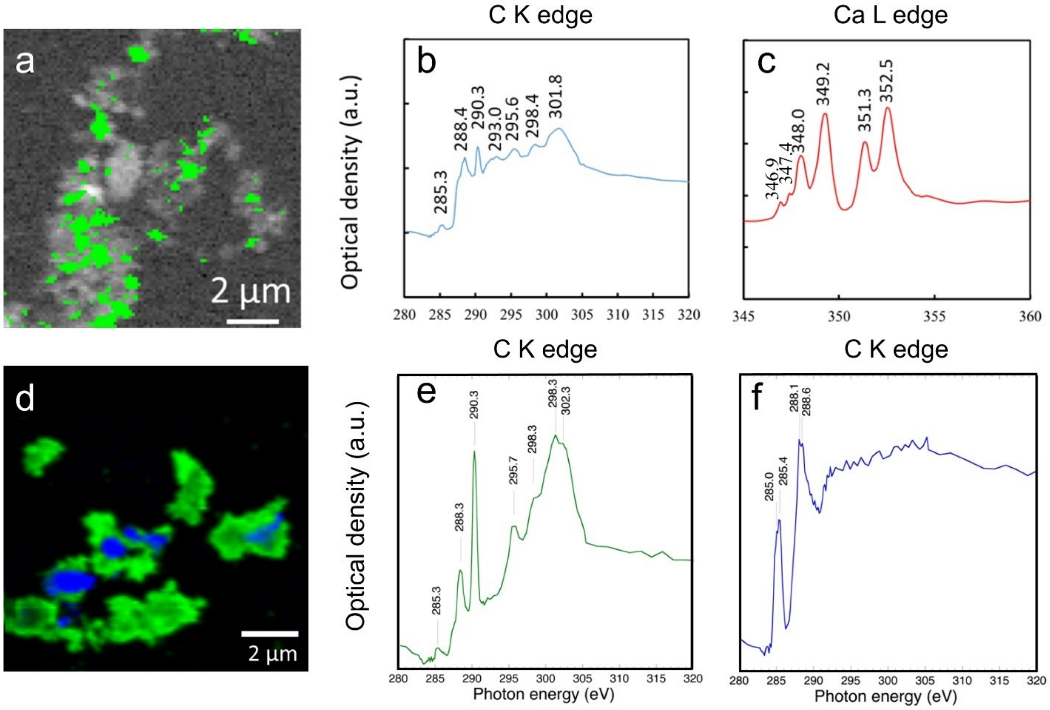

Figure 5.9 STXM analyses of carbonates minerals observed in sediments produced in the HCl control and NH_4OAc bio carbonation reactor. (a) Low Mg-calcite (LMC) in sediments from the HCl control carbonation reactor; (b-c) XANES spectra at the C *K*-edge and Ca $L_{2,3}$-edge,

respectively, corresponding to the green areas in (a); (d) An intimate association between Mg-calcite (green) and bacterial organic polymers (blue) in sediments from the NH_4OAc bio carbonation reactor; (e-f) XANES spectra at the C *K*-edge corresponding to the green and blue areas in (d).

5.3.2 Modelling results

Geochemical modelling was used to determine the saturation states of the leachates in all eight carbonation reactors with respect to various carbonate minerals, amorphous silica, struvite, and gypsum over a six-month period from day -8 to day 179. All leachates collected from the four control reactors were saturated with respect to amorphous silica, with the exception of leachates from the H_2O control reactor on day 19, the HCl control reactor on day 32, and the NH_4Cl control reactor on day 41 (Fig. 5.10a). In contrast, leachates from the H_2O bio reactor consistently showed undersaturation with respect to amorphous silica (Fig. 5.10a). SI values for amorphous silica in leachates from the HCl bio reactor varied between -1.88 and 0.32. Leachates from both the NH_4Cl bio reactor and the NH_4OAc bio reactor were generally saturated with amorphous silica, with the exception of leachates from the NH_4Cl bio reactor on day -3 and day -0.5.

The SI values of leachates from the eight reactors generally showed similar trends for the carbonate minerals, VHMC, monohydrocalcite and calcite (Fig. 5.10b, c, d). Leachates from the four control reactors were typically undersaturated with respect to VHMC and monohydrocalcite, except for the leachate from the HCl control reactor on day 0 (Fig. 5.10b, c). This pattern of undersaturation with VHMC and monohydrocalcite was also observed in the leachates from the H_2O bio reactor, NH_4Cl bio reactor, and NH_4OAc bio reactor, with exceptions for the NH_4OAc bio reactor on day -0.5 and day 11 (Fig. 5.10b, c). Conversely, leachates from the HCl bio reactor exhibited periods of saturation with VHMC from day 11 to day 32 and again from day 171 to 179 (Fig. 5.10b). However, leachates from the HCl bio reactor were always undersaturated with respect to monohydrocalcite (Fig. 5.10c). Leachates from the H_2O control reactor, the NH_4Cl control reactor, and the NH_4OAc control reactor consistently showed undersaturation with respect to calcite (Fig. 5.10d). In contrast, leachates from the HCl control reactor experienced intervals of calcite saturation during days 0 to 4 of the experiment, on day 41, and later from day 158 to 179 (Fig. 5.10d). While leachates from both the NH_4Cl bio and

NH_4OAc bio reactors remained undersaturated with calcite, those from the H_2O bio reactor achieved saturation between days 171 and 179. Additionally, leachates from the HCl bio reactor were saturated with calcite from day 11 to 32, day 95 to 158, and day 171 to 179 (Fig. 5.10d).

All leachates from the eight reactors were undersaturated with respect to struvite and gypsum over the six-month period (Fig. 5.10e, f).

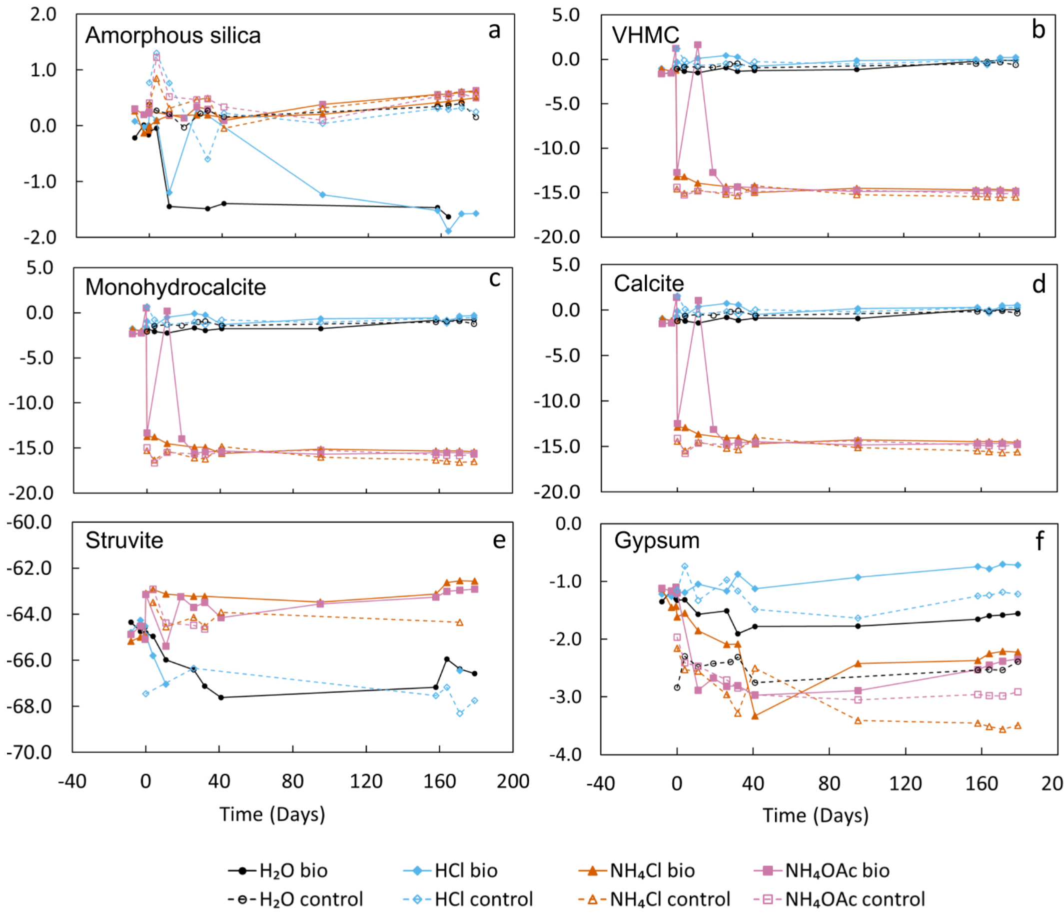

Figure 5.10 Saturation indices of the leachates with respect to different (mineral) phases *versus* time (days) as calculated using PHREEQC (Parkhurst and Appelo, 2013) from the minteq.v4 database released in 2017.

5.4 Discussion

5.4.1 Solution chemistry and microbes determine mineral sinks for CO_2

Mg and Ca concentrations were greater in the control carbonation reactors compared to their respective bio carbonation reactors at the beginning of the experiment, and they remained so over the course of the experiment (Fig. 5.3). The observed dilution effect in the bio carbonation reactors can be partly attributed to the initial filling of the bio reactors with culture media, which contained microbes and nutrients (BG11) in water whereas no water was added to the control carbonation reactors prior to treatments. The precipitation of Ca and Mg carbonate minerals in association with microbes could have led to more removal of Ca and Mg from solution in the bio carbonation reactors, thereby further decreasing Ca and Mg concentrations. It is important to note once again that the control carbonation reactors were eventually colonized by microbes – likely a combination of microbes indigenous to the DebTech site and those from the adjacent bio carbonation reactors. The carbonation reactors were also left uncovered and they received rainfall throughout the year-long experiment. As such, the difference in Mg and Ca concentrations between the bio and control carbonation reactors tends to be smaller and less important from ~41 days after the start of the experiment. Before day 179, the leachates from all four bio reactors exhibited higher pH values compared to their corresponding control reactors (Fig. 5.3a), which can be attributed to the generation of hydroxyl ions (OH^-) by the metabolic activity of photosynthetic microorganisms.

The aqueous Mg/Ca ratio has historically been regarded as a key factor influencing carbonate mineralogy in aqueous environments (*e.g.*, Müller et al., 1972; Berner, 1975; Folk and Land, 1975). Müller et al. (1972) proposed that a Mg/Ca ratio of less than 2 results in the formation of low magnesium calcite, while a ratio greater than 2 leads to the precipitation of aragonite, high magnesium calcite, and dolomite. High Mg/Ca ratios (greater than 39) are associated with the formation of hydromagnesite. The presence of high Mg-calcite (HMC) and monohydrocalcite seems to be more closely correlated with the total concentration of Mg in the water, as these minerals have been observed only in lakes with Mg concentrations exceeding 75 meq/L (Chagas et al., 2016). In this study, Mg/Ca ratios were always lower than 2 in leachates from all four control reactors with exceptions in the leachate from the H_2O control reactor on day 0 and the leachate from the NH_4Cl control reactor on day 353 (Appendix Table A4.2). In contrast, high Mg/Ca ratios (greater than 2) were observed in leachates from the H_2O bio reactor from day 304 to day 374 and also in leachates from the NH_4OAc bio reactor from day 11 to day 41 and day 276 to day 374. This is consistent with the observation of VHMC in solids collected from the NH_4Cl control reactor and the NH_4OAc bio reactor (Fig. 5.7B). The Mg/Ca ratios in leachates from the HCl bio reactor were always lower than 2. This may be attributed to the precipitation of

Ca and Mg carbonate minerals in conjunction with microbes, leading to the change of Mg/Ca ratios.

Gregg et al. (2015) assumed the formation of microbial VHMC may represent the initial phase in a sequence of metastable phases ultimately culminating in the development of stoichiometric, ordered dolomite. Raudsepp et al. (2022) suggested a transformation sequence from 'amorphous to crystalline', proposing that amorphous Ca-Mg carbonates act as precursors to crystalline forms such as Mg-calcite or VHMC. In nature, the presence of high-density carboxyl groups on natural surfaces, including microbial biomass and organic matter, may serve as a mechanism for the formation of ordered dolomite nuclei. Carboxyl groups, present in cell wall biomass and exopolymeric substances, due to their negative charge, facilitate carbonation by binding and dehydrating Mg ions, thereby decreasing the kinetic barrier and promoting carbonate nucleation (Kenward et al., 2013; Roberts et al., 2013; Power et al., 2017). In this study, formation of authigenic carbonate minerals including low Mg-calcite, high Mg-calcite, very high Mg-calcite and monohydrocalcite has been observed in the carbonation reactors. The morphology of carbonates formed through microbially-mediated carbonate precipitation can exhibit smooth rhomb or dumbbell shapes (Dupraz et al., 2009), which align with the very high magnesium calcite (VHMC) and low Mg-calcite observed in solids collected from the NH_4OAc bio carbonation reactor (Fig. 5.8). Results show calcite in Venetia DVK CRD is Mg-free. It is highly pure calcium carbonate, which means that it can be distinguished from newly precipitated carbonate minerals if they have a different composition (Fig. 5.5). The carbonate minerals that developed in the NH_4OAc carbonation reactor contained both magnesium and strontium (Fig. 5.8). As a result, these elements could potentially serve as markers to differentiate newly formed carbonate minerals from the originally present pure calcite in CRD, which contains only calcium.

The mineralogical composition of the thick sediment layers at the bases of carbonation reactors is complex (Fig. 5.7 and Appendix Table A4.4). Based on the Rietveld refinement results and considering the carbon weight percentages in low and high Mg-calcite (~12.00 %), VHMC (13.03 %) and monohydrocalcite (10.17 %), the total inorganic carbon (TIC) content is calculated and subsequently compared with the total inorganic carbon measured via coulometry (Fig. 5.11 and Appendix Table A4.5). A robust positive correlation is observed, with a coefficient of determination (R^2) value of 0.9928, which signifies a high level of agreement between the two analytical methods. Nevertheless, the total inorganic carbon calculated via

Rietveld refinement results is approximately 20% relative lower than the measured TIC values. This underestimation may be attributed to the simultaneous presence of high organic matter content and smectite within the sediment samples. Further investigations are necessary to elucidate the impact of these factors on the accurate quantification of inorganic carbon in carbonation reactor sediments.

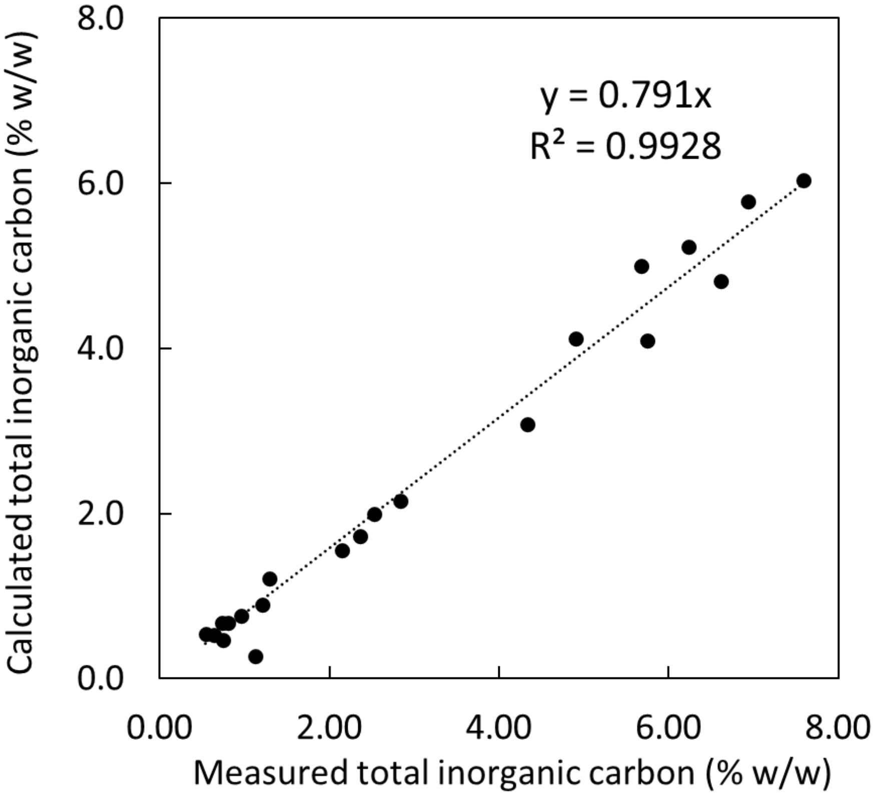

Figure 5.11 The robust positive correlation between the total inorganic carbon (TIC) calculated based on Rietveld refinement results and the total inorganic carbon analytically measured by CO_2 coulometry.

5.4.2 Carbon accounting during heap leaching and microbially-mediated carbonation

Two different methods were used to determine the amount of CO_2 emissions (as a %) that could be offset each year if this heap-leaching and microbially-mediated carbonation pathway were scaled up at the Venitia diamond mine (Fig. 5.12).

The first approach was to determine the amount of carbonate alkalinity stored in the carbonation reactors. A volume of 20 L of solution was collected from each of the eight reactors following the field trial for this purpose. The CO_2 offset was calcluated using the DIC data measured from these large samples and extrapolating those concentrations to the ~3.9 × 10^6 m^3/yr of process water used at Venetia and the 0.21 Mt of CO_2e emissions generated by the mine in 2016 (Paulo et al., 2023) (Fig. 5.12 and Appendix Table A4.6). The resulting CO_2 offset rates for the H_2O control, HCl control, NH_4Cl control, and NH_4OAc control reactors were 0.27%, 0.11%, 0.00%, and 0.01% respectively, while the H_2O bio, HCl bio, NH_4Cl bio, and NH_4OAc bio reactors accounted for rates of 0.56%, 0.14%, 0.04%, and 1.12% respectively, with the NH_4OAc bio reactor achieving the highest CO_2 offset rate among them.

The second approach was to determine the amount of CO_2 converted to solid carbonate minerals. Measurement involved collecting three replicates of solid samples from each carbonation reactor following the field trial, each with a surface area of 15 cm × 15 cm. Given that the total surface area for the interior base of each carbonation reactor was 0.0225 m^2, the amount of CO_2 sequesered in the sediments could be calculated for each reactor using measured TIC data (Appendix Table A4.7). Given that ~850 kg of CRD were used per reactor, and considering the 4.74 Mt of ore processed at Venetia in 2016 (Mervine et al. 2018), the amount of sequestered CO_2 could be extrapolated to determine what the offset would be at mine scale (Fig. 5.12 and Appendix Table A4.7). The CO_2 offsets for the H_2O control, HCl control, NH_4Cl control, and NH_4OAc control reactors were 0.17%, 0.31%, 0.00%, and 0.01% respectively, while the H_2O bio, HCl bio, NH_4Cl bio, and NH_4OAc bio reactors gave offsets of 1.40%, 1.87%, 0.33%, and 0.45% respectively, with the HCl bio reactor showing the highest CO_2 offset. For both methods, all bio reactors provided a greater CO_2 offset compared with the control reactors.

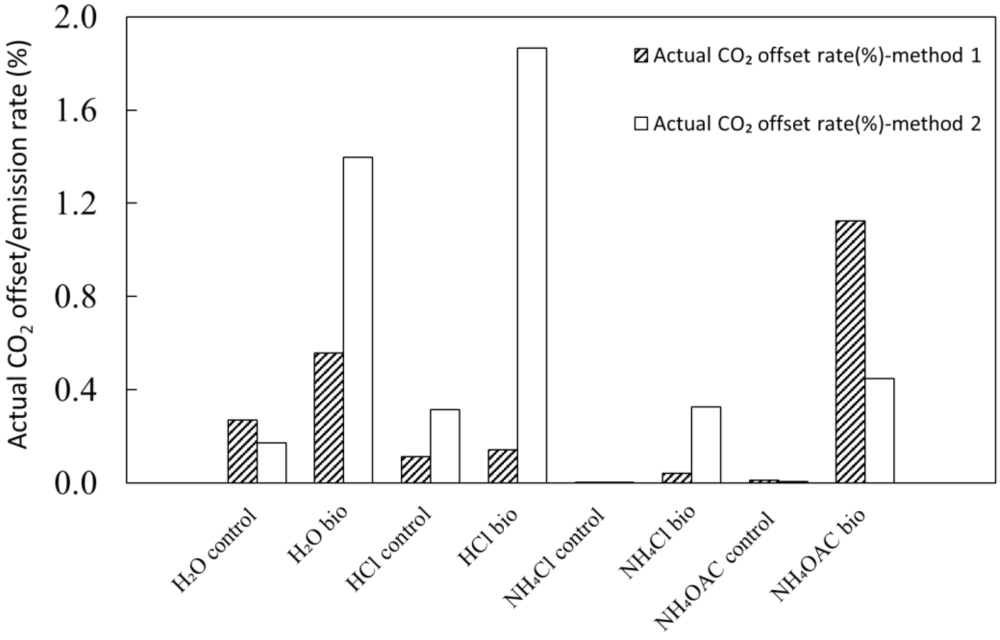

Figure 5.12 Actual CO_2 offset rate (%) calculated based on two different methods at the Venetia mine.

5.4.3 Comparison to offsets from passive carbonation and lessons for implementation

Passive weathering processes of silicate minerals in processed kimberlite at the Diavik diamond mine in Canada contribute to a ~0.2 % offset of the mine's annual emissions (Wilson et al., 2011). In comparison, studies by Stubbs et al. (2022) and Paulo et al. (2023) suggest that passive carbonation at the Venetia mine has the potential to offset CO_2 emissions by ~1.0–1.5%. Analysis of 35 fresh rock drainage (FRD) samples from the Venetia mine revealed an average alkalinity of 129.4 mg/L measured as bicarbonate (HCO_3^-) concentration (Paulo et al., 2023). The formation of carbonate minerals within these carbonation reactors in this study indicates a decrease in the alkalinity, suggesting a more efficient capture of CO_2. The microbially-mediated carbonation method in this study could potentially double the rate of CO_2 sequestration in minerals and water compared to the current rates observed at Venetia.

Mervine et al. (2018) have provided an estimate for the maximum CO_2 sequestration potential at the Venetia Mine, suggesting a theoretical potential of up to 719% increase in sequestration. However, the experiment detailed in Chapter 3 and further investigated in this study indicates a significantly lower actual CO_2 capture capacity. The challenge lies in extracting substantial amounts of Ca and Mg from the processed kimberlite, which proves to be more difficult than initially anticipated. Specifically, the acid-leaching technique, while effective in certain contexts, may not be optimal for kimberlite that is rich in calcite and other carbonate minerals. The initial bulk samples contained 7.2 wt.% calcite. In the HCl-treated leaching reactors, calcite varied from 2.7 to 8.4 wt.%, with samples from the top of the reactor having the lowest calcite abundances owing to its dissolution. CO_2 released by calcite dissolution will largely decrease the CO_2 offset potential of leached Mg. The combination of acid leaching and microbially-mediated carbonation may be best employed for calcite-poor ultramafic mine residues. Meanwhile, the design of this field trial faced certain constraints. Primarily, we were limited to using atmospheric CO_2, with its concentration of ~ 420 ppm, as there was no concentrated CO_2 source available at Venetia. Furthermore, the use of concentrated acids was avoided to prevent any negative impact on the sedimentation behavior of clays and the efficiency of water recovery within the existing processing framework, which could not be altered. Reflecting on the outcomes of the column experiments in Chapter 3 and 4, several adjustments would be considered for future trials to enhance the effectiveness of carbonation processes at a larger scale. Recognizing the unique mineral composition of each ultramafic rock type and even within individual kimberlite facies is crucial, as these characteristics significantly influence the potential for mineral carbonation. This understanding should guide the selection of treatment methods, whether they involve chemically or physically accelerated carbonation. Additionally, experimenting with various types of salts may yield better results for cation exchange, potentially reducing overall costs and improving the efficiency of CO_2 sequestration efforts for ultramafic tailings rich in both smectites and carbonates.

During mining process, the most hard-to-abate greenhouse gas emissions primarily come from mine trucks and similar equipment. As mines move towards electrification, adopt renewable energy sources, and improve energy efficiency, these hard-to-abate emissions become a key focus for achieving environmental goals. Integrating carbon offset strategies, such as those discussed in Chapter 3 , 4 and this research, could significantly contribute to the mining industry's efforts to achieve CO_2 neutrality. To ensure these strategies are both practical and cost-effective, it is essential to apply tools like Techno-Economic Analysis (TEA) and Life Cycle Assessment (LCA). These tools evaluate the feasibility, environmental impact, and economic viability of implementing such carbon offset measures. Through optimization and rigorous assessment using TEA/LCA, the proposed approach has the potential to play a vital role in helping the mining sector meet its commitment to carbon neutrality.

5.5 Conclusions

This study evaluated the suitability of combing acid-heap leaching or cation exchange leaching of kimberlite with microbially-mediated mineralization of atmospheric CO_2 as a means to offset greenhouse gas emissions from the Venetia diamond mine. It tested the feasibility of implementing microbial carbonation on a large scale. We employed two primary methods to evaluate the annual CO_2 offset achievable. Initially, we assessed the carbonate alkalinity stored within carbonation reactors, utilizing samples collected post-trial to estimate offsets against the mine's process water and CO_2e emissions. This analysis revealed that the NH_4OAc bio reactor was the most effective, achieving a CO_2 offset rate of 1.12%. Furthermore, we examined the sequestration of CO_2 into solid carbonate minerals, identifying the HCl bio reactor as yielding the highest offset at 1.87%. Interestingly, all bio-assisted reactors outperformed their control counterparts, highlighting the significant role of microbial mediation in carbon sequestration. Comparing these results with Stubbs et al. (2022) and Paulo et al. (2023), which estimated a passive carbonation potential at Venetia of ~1.0–1.5% CO_2 offset, this microbially-mediated approach suggests the possibility of doubling these rates. To further enhance CO_2 offsets, the very specific mineralogy of each ultramafic rock type and even each kimberlite facies must dictate which treatment pathways should be used for enhanced weathering and carbonation. For ultramafic tailings rich in both smectites and carbonates, exploring different salts for improved cation exchange could offer cost reductions and efficiency improvements, demonstrating a clear path forward for scaling up carbon capture technologies in the mining sector.

5.6 Chapter 5 references

Berner, R.A., 1975. The role of magnesium in the crystal growth of calcite and aragonite from sea water. Geochimica et Cosmochimica Acta, 39(4), pp.489-504.

Bish, D.L. and Howard, S.A., 1988. Quantitative phase analysis using the Rietveld method. Journal of Applied Crystallography, 21(2), pp.86-91.

Bish, D.L., Carey, J.W., Vaniman, D.T. and Chipera, S.J., 2003. Stability of hydrous minerals on the martian surface. Icarus, 164(1), pp.96-103.

Bobicki, E.R., Liu, Q., Xu, Z., and Zeng, H., 2012. Carbon capture and storage using alkaline industrial wastes. Progress in Energy and Combustion Science, 38(2), pp.302-320.

Brandes, J.A., Lee, C., Wakeham, S., Peterson, M., Jacobsen, C., Wirick, S. and Cody, G., 2004. Examining marine particulate organic matter at sub-micron scales using scanning transmission X-ray microscopy and carbon X-ray absorption near edge structure spectroscopy. Marine Chemistry, 92(1-4), pp.107-121.

Buse, B., Sparks, R.S.J., Field, M., Schumacher, J.C., Chisi, K. and Tlhaodi, T., 2011. Geology of the BK9 kimberlite (Damtshaa, Botswana): implications for the formation of dark volcaniclastic kimberlite. Bulletin of Volcanology, 73, pp.1029-1045.

Chagas, A.A., Webb, G.E., Burne, R.V. and Southam, G., 2016. Modern lacustrine microbialites: towards a synthesis of aqueous and carbonate geochemistry and mineralogy. Earth-Science Reviews, 162, pp.338-363.

Cheary, R.W. and Coelho, A., 1992. A fundamental parameters approach to X-ray line-profile fitting. Journal of Applied Crystallography, 25(2), pp.109-121.

Clark, D.E., Oelkers, E.H., Gunnarsson, I., Sigfússon, B., Snæbjörnsdóttir, S.Ó., Aradottir, E.S. and Gíslason, S.R., 2020. CarbFix2: CO_2 and H_2S mineralization during 3.5 years of continuous injection into basaltic rocks at more than 250 °C. Geochimica et Cosmochimica Acta, 279, pp.45-66.

Dupraz, C., Reid, R.P., Braissant, O., Decho, A.W., Norman, R.S. and Visscher, P.T., 2009. Processes of carbonate precipitation in modern microbial mats. Earth-Science Reviews, 96(3), pp.141-162.

Folk, R.L. and Land, L.S., 1975. Mg/Ca ratio and salinity: two controls over crystallization of dolomite. AAPG bulletin, 59(1), pp.60-68.

Görgen, S., Benzerara, K., Skouri-Panet, F., Gugger, M., Chauvat, F. and Cassier-Chauvat, C., 2021. The diversity of molecular mechanisms of carbonate biomineralization by bacteria. Discover Materials, 1, pp.1-20.

Gregg, J.M., Bish, D.L., Kaczmarek, S.E. and Machel, H.G., 2015. Mineralogy, nucleation and growth of dolomite in the laboratory and sedimentary environment: a review. Sedimentology, 62(6), pp.1749-1769.

Hamilton, J.L., Wilson, S., Morgan, B., Turvey, C.C., Paterson, D.J., Jowitt, S.M., McCutcheon, J., and Southam, G., 2018. Fate of transition metals during passive carbonation of ultramafic mine tailings via air capture with potential for metal resource recovery. International Journal of Greenhouse Gas Control, 71, pp.155-167.

Hamilton, J.L., Wilson, S., Morgan, B., Harrison, A.L., Turvey, C.C., Paterson, D.J., Dipple, G.M. and Southam, G., 2020. Accelerating mineral carbonation in ultramafic mine tailings via direct CO_2 reaction and heap leaching with potential for base metal enrichment and recovery. Economic Geology, 115(2), pp.303-323.

Hill, R.J. and Howard, C.J., 1987. Quantitative phase analysis from neutron powder diffraction data using the Rietveld method. Journal of Applied Crystallography, 20(6), pp.467-474.

Hitchcock, A. (2012). aXis 2000 – Analysis of X-ray Images and Spectra. Available online at: http://unicorn.mcmaster.ca/aXis2000.html [Accessed February 16, 2012].

Iniesto, M., Moreira, D., Reboul, G., Deschamps, P., Benzerara, K., Bertolino, P., Saghaï, A., Tavera, R. and López-García, P., 2021. Core microbial communities of lacustrine microbialites sampled along an alkalinity gradient. Environmental Microbiology, 23(1), pp.51-68.

IPCC, 2023. Climate Change 2023: Synthesis Report. A Report of the Intergovernmental Panel on Climate Change. Contribution of Working Groups I, II and III to the Sixth Assessment Report of the Intergovernmental Panel on Climate Change https://www.ipcc.ch/report/ar6/syr/downloads/report/IPCC_AR6_SYR_LongerReport.pdf (Accessed 26 April 2023).

Kasting, J.K., and Howard, M.T., 2006. Atmospheric composition and climate on the early Earth. Philosophical Transactions of the Royal Society B 361, 1733–1742.

Kenward, P.A., Fowle, D.A., Goldstein, R.H., Ueshima, M., González, L.A. and Roberts, J.A., 2013. Ordered low-temperature dolomite mediated by carboxyl-group density of microbial cell walls. AAPG bulletin, 97(11), pp.2113-2125.

Lackner, K.S., Wendt, C.H., Butt, D.P., Joyce Jr, E.L., and Sharp, D.H., 1995. Carbon dioxide disposal in carbonate minerals. Energy, 20(11), pp.1153-1170.

Lackner, K.S., 2003. A guide to CO_2 sequestration. Science, 300(5626), pp.1677-1678.

Lechat, K., Lemieux, J.M., Molson, J., Beaudoin, G., and Hébert, R., 2016. Field evidence of CO_2 sequestration by mineral carbonation in ultramafic milling wastes, Thetford Mines, Canada. International Journal of Greenhouse Gas Control, 47, pp.110-121.

Matter, J.M., Stute, M., Snæbjörnsdottir, S.Ó., Oelkers, E.H., Gislason, S.R., Aradottir, E.S., Sigfusson, B., Gunnarsson, I., Sigurdardottir, H., Gunnlaugsson, E. and Axelsson, G., 2016. Rapid carbon mineralization for permanent disposal of anthropogenic carbon dioxide emissions. Science, 352(6291), pp.1312-1314.

McCutcheon, J., Power, I.M., Harrison, A.L., Dipple, G.M., and Southam, G., 2014. A greenhouse-scale photosynthetic microbial bioreactor for carbon sequestration in magnesium carbonate minerals. Environmental Science & Technology, 48(16), pp.9142-9151.

McCutcheon, J., Wilson, S., and Southam, G., 2015. Microbially accelerated carbonate mineral precipitation as a strategy for in situ carbon sequestration and rehabilitation of asbestos mine sites. Environmental Science & Technology, 50(3), pp.1419-1427.

McCutcheon, J., Turvey, C.C., Wilson, S., Hamilton, J.L. and Southam, G., 2017. Experimental deployment of microbial mineral carbonation at an asbestos mine: Potential applications to carbon storage and tailings stabilization. Minerals, 7(10), p.191.

Mervine, E.M., Wilson, S.A., Power, I.M., Dipple, G.M., Turvey, C.C., Hamilton, J.L., Vanderzee, S., Raudsepp, M., Southam, C., Matter, J.M. and Kelemen, P.B., 2018. Potential for offsetting diamond mine carbon emissions through mineral carbonation of processed kimberlite: an assessment of De Beers mine sites in South Africa and Canada. Mineralogy and Petrology, 112, pp.755-765.

Müller, G., Irion, G. and Förstner, U., 1972. Formation and diagenesis of inorganic Ca-Mg carbonates. Naturwissenschaften, 59(4), pp.158-164.

Obst, M., Dynes, J.J., Lawrence, J.R., Swerhone, G.D., Benzerara, K., Karunakaran, C., Kaznatcheev, K., Tyliszczak, T. and Hitchcock, A.P., 2009a. Precipitation of amorphous

$CaCO_3$ (aragonite-like) by cyanobacteria: a STXM study of the influence of EPS on the nucleation process. Geochimica et Cosmochimica Acta, 73(14), pp.4180-4198.

Obst, M., Wehrli, B. and Dittrich, M., 2009b. $CaCO_3$ nucleation by cyanobacteria: Laboratory evidence for a passive, surface-induced mechanism. Geobiology, 7(3), pp.324-347.

Parkhurst, D.L. and Appelo, C.A.J., 2013. Description of input and examples for PHREEQC version 3—a computer program for speciation, batch-reaction, one-dimensional transport, and inverse geochemical calculations. US geological survey techniques and methods, 6(A43), p.497.

Paulo, C., Power, I.M., Zeyen, N., Wang, B. and Wilson, S., 2023. Geochemical modeling of CO_2 sequestration in ultramafic mine wastes from Australia, Canada, and South Africa: Implications for carbon accounting and monitoring. Applied Geochemistry, 152, p.105630.

Pentecost, A. and Bauld, J., 1988. Nucleation of calcite on the sheaths of cyanobacteria using a simple diffusion cell. Geomicrobiology Journal, 6(2), pp.129-135.

Perry, R.S., Mcloughlin, N., Lynne, B.Y., Sephton, M.A., Oliver, J.D., Perry, C.C., Campbell,K., Engel, M.H., Farmer, J.D., Brasier, M.D., and Staley, J.T., 2007. Defining biominerals and organominerals: direct and indirect indicators of life. Sedimentary Geology 201, 157–179.

Paulo, C., Power, I.M., Zeyen, N., Wang, B. and Wilson, S., 2023. Geochemical modeling of CO_2 sequestration in ultramafic mine wastes from Australia, Canada, and South Africa: Implications for carbon accounting and monitoring. Applied Geochemistry, 152, p.105630.

Power, I.M., Dipple, G.M. and Southam, G., 2010. Bioleaching of ultramafic tailings by Acidithiobacillus spp. for CO_2 sequestration. Environmental Science & Technology, 44(1), pp.456-462.

Power, I.M., Wilson, S.A., Small, D.P., Dipple, G.M., Wan, W. and Southam, G., 2011. Microbially mediated mineral carbonation: roles of phototrophy and heterotrophy. Environmental Science & Technology, 45(20), pp.9061-9068.

Power, I.M., Harrison, A.L., Dipple, G.M., Wilson, S., Kelemen, P.B., Hitch, M., and Southam, G., 2013. Carbon mineralization: from natural analogues to engineered systems. Reviews in Mineralogy and Geochemistry, 77(1), pp.305-360.

Power, I.M., Kenward, P.A., Dipple, G.M. and Raudsepp, M., 2017. Room temperature magnesite precipitation. Crystal Growth & Design, 17(11), pp.5652-5659.

Pronost, J., Beaudoin, G., Tremblay, J., Larachi, F., Duchesne, J., Hébert, R., and Constantin, M., 2011. Carbon sequestration kinetic and storage capacity of ultramafic mining waste. Environmental Science & Technology, 45(21), pp.9413-9420.

Raudsepp, M.J., Wilson, S., Morgan, B., Patel, A., Johnston, S.G., Gagen, E.J. and Fallon, S.J., 2022. Non-classical crystallization of very high magnesium calcite and magnesite in the Coorong Lakes, Australia. Sedimentology, 69(5), pp.2246-2266.

Rietveld, H.M., 1969. A profile refinement method for nuclear and magnetic structures. Journal of applied Crystallography, 2(2), pp.65-71.

Roberts, J.A., Kenward, P.A., Fowle, D.A., Goldstein, R.H., González, L.A. and Moore, D.S., 2013. Surface chemistry allows for abiotic precipitation of dolomite at low temperature. Proceedings of the National Academy of Sciences, 110(36), pp.14540-14545.

Scarlett, N.V. and Madsen, I.C., 2006. Quantification of phases with partial or no known crystal structures. Powder Diffraction, 21(4), pp.278-284.

Seifritz, W., 1990. CO_2 disposal by means of silicates. Nature, 345, pp.486-486.

Spadafora, A., Perri, E., McKenzie, J.A., and Vasconcelos, C., 2010. Microbial biomineralization processes forming modern Ca:Mg carbonate stromatolites. Sedimentology 57 (1), 27–40.

Stubbs, A.R., Paulo, C., Power, I.M., Wang, B., Zeyen, N., and Wilson, S., 2022. Direct measurement of CO_2 drawdown in mine wastes and rock powders: Implications for enhanced rock weathering. International Journal of Greenhouse Gas Control, 113, p.103554.

Turvey, C.C., Wilson, S., Hamilton, J.L., and Southam, G., 2017. Field-based accounting of CO_2 sequestration in ultramafic mine wastes using portable X-ray diffraction. American Mineralogist: Journal of Earth and Planetary Materials, 102(6), pp.1302-1310.

Turvey, C.C., Hamilton, J.L., and Wilson, S., 2018. Comparison of Rietveld-compatible structureless fitting analysis methods for accurate quantification of carbon dioxide fixation in ultramafic mine tailings. American Mineralogist, 103(10), pp.1649-1662.

Urquhart, S.G. and Ade, H., 2002. Trends in the carbonyl core (C 1s, O 1s)$\rightarrow \pi^*$ C= O transition in the near-edge X-ray absorption fine structure spectra of organic molecules. The Journal of Physical Chemistry B, 106(34), pp.8531-8538.

Vasconcelos, C., Warthmann, R., McKenzie, J.A., Visscher, P.T., Bittermann, A.G., and van Lith, Y., 2006. Lithifying microbial mats in Lagoa Vermelha, Brazil: modern Precambrian relics? Sedimentary Geology. 185 (3–4), 175–183.

White, S.K., Spane, F.A., Schaef, H.T., Miller, Q.R., White, M.D., Horner, J.A. and McGrail, B.P., 2020. Quantification of CO_2 mineralization at the Wallula basalt pilot project. Environmental Science & Technology, 54(22), pp.14609-14616.

Wilson, S., Raudsepp, M., and Dipple, G.M., 2006. Verifying and quantifying carbon fixation in minerals from serpentine-rich mine tailings using the Rietveld method with X-ray powder diffraction data. American Mineralogist, 91(8-9), pp.1331-1341.

Wilson, S., Dipple, G.M., Power, I.M., Thom, J.M., Anderson, R.G., Raudsepp, M., Gabites, J.E., and Southam, G., 2009a. Carbon dioxide fixation within mine wastes of ultramafic-hosted ore deposits: Examples from the Clinton Creek and Cassiar chrysotile deposits, Canada. Economic Geology, 104(1), pp.95-112.

Wilson, S., Raudsepp, M., and Dipple, G.M., 2009b. Quantifying carbon fixation in trace minerals from processed kimberlite: A comparative study of quantitative methods using X-ray powder diffraction data with applications to the Diavik Diamond Mine, Northwest Territories, Canada. Applied Geochemistry, 24(12), pp.2312-2331.

Wilson, S., Barker, S.L., Dipple, G.M., and Atudorei, V., 2010. Isotopic disequilibrium during uptake of atmospheric CO_2 into mine process waters: Implications for CO_2 sequestration. Environmental Science & Technology, 44(24), pp.9522-9529.

Wilson, S., Dipple, G.M., Power, I.M., Barker, S.L., Fallon, S.J., and Southam, G., 2011. Subarctic weathering of mineral wastes provides a sink for atmospheric CO_2. Environmental Science & Technology, 45(18), pp.7727-7736.

Wilson, S., Harrison, A.L., Dipple, G.M., Power, I.M., Barker, S.L., Mayer, K.U., Fallon, S.J., Raudsepp, M., and Southam, G., 2014. Offsetting of CO_2 emissions by air capture in mine tailings at the Mount Keith Nickel Mine, Western Australia: Rates, controls and prospects for carbon neutral mining. International Journal of Greenhouse Gas Control, 25, pp.121-140.

Zeyen, N., Wang, B., Wilson, S., Paulo, C., Stubbs, A.R., Power, I.M., Steele-Maclnnis, M., Lanzirotti, A., Newville, M., Paterson, D.J., and Hamilton, J.L., 2022. Cation exchange in smectites as a new approach to mineral carbonation. Frontiers in Climate, 4.

Chapter 6

Conclusions

6.1 Summary of research outcomes

The primary goal of this thesis is to deepen the understanding of mineral carbonation, particularly focusing on the role of specific mineralogies in accelerating weathering processes and the potential for carbon sequestration in kimberlite mine residues. Additionally, this thesis aims to thoroughly investigate the behavior and mobility of transition metals, such as Ni, during enhanced weathering processes using ultramafic mine residues or rocks.

In Chapter 2, the Partial Or No Known Crystal Structure (PONKCS) method was used to model the peak profiles of a smectite and lizardite to account for turbostratic stacking disorder in synthetic samples of processed kimberlite. The results can be very accurate (4.2–14.1 wt.% total bias) using correctly calibrated, instrument-specific PONKCS models. However, even small differences in instrument parameters between two similar XRDs can also lead to inconsistent and less accurate Quantitative Phase Analysis (QPA) results using PONKCS (9.8–32.7 wt.% total bias). Therefore, correct calibration of PONKCS models to a specific XRD instrument is required for accurate QPA and quantification of CO_2 mineralization in clay-rich rocks.

At the Venetia diamond mine (Chapter 3), the acid leaching method could offset 4.2–23.9 % of CO_2 emissions. However, this acid-leaching method may not be suitable for calcite-rich processed kimberlite. The CO_2 sequestration potential of abundant, Mg-rich clay minerals and other Mg- and Ca-bearing silicates in kimberlites can only be accessed by first dissolving pre-existing Ca-carbonate minerals, which releases CO_2. The CO_2 emission potential of pre-existing calcite ranges from 2.1–14.3 %. After acid leaching experiments, most of the transition metals remained in feedstock minerals such as serpentine or oxides. Moreover, the formation of secondary minerals such as iron (hydr)oxides was not associated with other transition metals (*e.g.,* Ni) due to the low pH in leachates. This result was very different from what has been previously documented for serpentinites; therefore, the very specific mineralogy of each ultramafic rock type is a dramatic control on carbonation potential as well as how critical metals might be recovered during CO_2 mineralization. This must dictate which treatment pathways should be used for enhanced weathering and carbonation.

Using materials from the Gahcho Kué diamond mine (Chapter 4), the amount of Mg leached using 0.12 M HCl equates to an estimated CO_2 offset potential of 7.8 % of the mine's annual greenhouse gas emissions. Although the dissolution of calcite within the tailings would effectively increase mine emissions by 1.4 %, the leached calcium resulting from silicate dissolution could offer an estimated CO_2 offset potential of 3.2 %. This leads to an estimated cumulative net CO_2 offset potential to 9.6%. For ore from the Record Ridge project, Mg leaching efficiencies were determined to be 1.8 % and 3.0 % for the RRP1 and RRP2 columns, respectively, using 0.12 M HCl. Despite these results, the overall extraction efficiency remained relatively low, indicating a potential need for optimization of acid concentration or the leaching process for enhanced extraction. Synchrotron XAS coupled with microscopy and XRD analysis revealed the presence of nickel in serpentine and pentlandite in the original RRP2 sample, suggesting its migration into ferrihydrite forming during the acid-leaching process. This finding opens up possibilities for recovering these metals, which were previously challenging to extract from silicate minerals. Significantly, the diverse mineralogy between samples led to varying leachate compositions. Moreover, the unexpected reversal of the pH trend in the replicate RRP2 columns highlighted the substantial impact of spatial heterogeneity, macropore flow, and sidewall flow on mineral carbonation potential, illustrating the complexity of the leaching process in these settings.

In Chapter 5, the microbially-mediated carbonation combining with the acid leaching method and a new cation exchange method was implemented on a large scale using processed kimberlite from the Venetia mine. Calcite (7.2 wt.%) is abundant in the initial processed kimberlite and acts as the main source of Ca in the leachate treated with 0.12 M HCl. In contrast, Mg is extracted mainly from dissolution of phyllosilicate minerals. Very high magnesium calcite (VHMC, also called protodolomite), low-Mg calcite and monohydrocalcite formed in the carbonation reactors as a result of microbially-mediated carbonation following acid leaching process. The sediments in the NH_4OAc carbonation reactors were predominantly composed of low Mg-calcite exhibiting a dumbbell morphology. VHMC also formed in the sediments from the NH_4OAc and NH_4Cl carbonation reactors. Two distinct methods were employed to quantify the CO_2 offset (%) achievable through this microbially-mediated carbonation if it were implemented at scale for the

Venetia mine. The first method involved analyzing 20 L of solution collected from each reactor after the field trial to determine alkalinity storage, considering the processing water volume and CO_2e emissions at the Venetia mine. The CO_2 offsets from alkalinity storage ranged from 0.00% to 1.12%, with the NH_4OAc bio reactor achieving the highest value. The second method involved analyzing solids samples collected from each reactor to determine the magnitude of mineral storage, with the CO_2 offsets ranging from 0.00% to 1.87%, with the the HCl bio reactor achieving the highest value. The bio reactors consistently stored greater amounts of CO_2 as both alkalinity and in minerals compared to the control reactors.

This thesis reveals that the specific mineralogy of each ultramafic rock type critically influences carbonation potential. Different treatment pathways should be used for enhanced weathering and carbonation based on the distinct mineralogy of each rock type. For ultramafic residues rich in both smectites and carbonates, the cation exchange method is suggested as more suitable for mineral carbonation. The acid leaching method holds more promise for serpentine-rich and carbonate-poor residues such as processed kimberlite from the Gahcho Kué diamond mine.

6.2 Suggestions for future research

This thesis highlights the importance of precise calibration of instrument-specific PONKCS models for accurate estimation of kimberlite's carbonation potential using XRD data. The complex mineralogy of kimberlite, often altered and containing variable amounts of gangue carbonate minerals, necessitates a comprehensive quantitative mineralogical approach for distinguishing between CO_2 previously present and that newly trapped in minerals. As a supplement to the Rietveld-PONKCS method, quantitative thermogravimetric analyses (TGA) (Turvey et al., 2022) have been shown to be more accurate and precise for detection of trace amounts of brucite (as low as 0.3 wt.%) in serpentinites. The same TGA method has also been used to rule out the presence of brucite in kimberlite when there is uncertainty about its detection owing to peak overlap with chlorite (Zeyen et al., 2022). The combination of the quantitative mineralogical approach developed in this study and those of Turvey et al. (2022) and Zeyen et al. (2022) could be used with a correction factor for CO_2 stored in gangue minerals (Paulo et al., 2021) and total carbon analysis using a LECO carbon-sulfur analyzer (Turvey et al., 2018) to obtain a more accurate and reliable baseline estimate of carbonation potential at diamond mines.

Although the acid leaching method shows promise for enhancing weathering and mineral carbonation in serpentine-rich and carbonate-poor residues, a detailed Life Cycle Assessment (LCA) and Techno-Economic Analysis (TEA) are needed to optimize the leaching process and to ensure it is carbon negative. Moreover, considering the complex mineralogical composition of processed kimberlites, further research into how different minerals influence rock weathering and their individual roles in carbon sequestration is crucial. Investigating these aspects using distinct pure minerals could provide deeper insights into the complex interactions and efficiencies within the mineral carbonation process, potentially leading to more effective and scalable carbon sequestration strategies.

Exploring the beneficial co-effects of carbon mineralization in mining operations presents a promising research avenue. Recent studies, such as those by Power et al. (2021), have shown that brucite carbonation can serve dual purposes by both sequestering carbon and stabilizing serpentinite mine residues, thereby enhancing dam stability and reducing the risk of failures. Additionally, microbially-mediated carbonation processes, as demonstrated by McCutcheon et al. (2016, 2017), can efficiently dissolve chrysotile while simultaneously cementing these asbestiform fibers, effectively reducing hazardous windblown dust. Concurrent mineral carbonation with enhanced recovery of critical metals, such as Ni and Co, which are needed for production and storage of renewable energy, has the potential to increase global metal production from carbon neutral or carbon negative mines (Hamilton et al., 2020; Khan et al., 2021; Wang and Dreisinger, 2022). Further research is necessary to explore diverse mineral carbonation strategies and their concurrent benefits for both industrial application and environmental conservation.

6.3 Chapter 6 references

Hamilton, J.L., Wilson, S., Morgan, B., Harrison, A.L., Turvey, C.C., Paterson, D.J., Dipple, G.M. and Southam, G., 2020. Accelerating mineral carbonation in ultramafic mine tailings via direct CO_2 reaction and heap leaching with potential for base metal enrichment and recovery. Economic Geology, 115(2), pp.303-323.

Khan, S., Wani, O.B., Shoaib, M., Forster, J., Sodhi, R.N., Boucher, D., and Bobicki, E.R., 2021. Mineral carbonation for serpentine mitigation in nickel processing: a step towards industrial carbon capture and storage. Faraday Discussions, 230, pp.172-186.

McCutcheon, J., Wilson, S., and Southam, G., 2016. Microbially accelerated carbonate mineral precipitation as a strategy for in situ carbon sequestration and rehabilitation of asbestos mine sites. Environmental Science & Technology, 50(3), pp.1419-1427.

McCutcheon, J., Turvey, C.C., Wilson, S., Hamilton, J.L., and Southam, G., 2017. Experimental deployment of microbial mineral carbonation at an asbestos mine: Potential applications to carbon storage and tailings stabilization. Minerals, 7(10), p.191.

Paulo, C., Power, I.M., Stubbs, A.R., Wang, B., Zeyen, N., and Wilson, S., 2021. Evaluating feedstocks for carbon dioxide removal by enhanced rock weathering and CO_2 mineralization. Applied Geochemistry, 129, p.104955.

Power, I.M., Paulo, C., Long, H., Lockhart, J.A., Stubbs, A.R., French, D., and Caldwell, R., 2021. Carbonation, cementation, and stabilization of ultramafic mine tailings. Environmental Science & Technology, 55(14), 10056-10066.

Turvey, C.C., Wilson, S., Hamilton, J.L., Tait, A.W., McCutcheon, J., Beinlich, A., Fallon, S.J., Dipple, G.M., and Southam, G., 2018. Hydrotalcites and hydrated Mg-carbonates as carbon sinks in serpentinite mineral wastes from the Woodsreef chrysotile mine, New South Wales, Australia: controls on carbonate mineralogy and efficiency of CO_2 air capture in mine tailings. International Journal of Greenhouse Gas Control, 79, pp.38-60.

Turvey, C.C., Wynands, E.R., and Dipple, G.M., 2022. A new method for rapid brucite quantification using Thermogravimetric Analysis. Thermochimica Acta, 718, p.179366.

Wang, F., and Dreisinger, D., 2022. Carbon mineralization with concurrent critical metal recovery from olivine. Proceedings of the National Academy of Sciences, 119(32), p.e2203937119.

Zeyen, N., Wang, B., Wilson, S., Paulo, C., Stubbs, A.R., Power, I.M., Steele-Maclnnis, M., Lanzirotti, A., Newville, M., Paterson, D.J., and Hamilton, J.L., 2022. Cation exchange in smectites as a new approach to mineral carbonation. Frontiers in Climate, 4.

Appendices

A1 Appendix to Chapter 2

Appendix Table A1.1 Detailed parameters for each of three XRDs.

XRD	Goniometer radius (mm)	Divergence slit size (mm or °)	Zero error (°)	Primary Soller angle (°)	Secondary Soller angle (°)
XRD A1	200.5	10 mm	-0.02849353	5.0	5.0
XRD B1	250	0.6 mm	-0.01717877	2.5	2.5
XRD B2	250	0.6 mm	-0.01979303	2.5	2.5

Appendix Table A1.2 Refined mineral abundances (wt.%) using PONKCS models calibrated to each of three XRDs.

Sample	wcskim1			wcskim2			wcskim3			wcskim4			wcskim5		
Phase/XRD	A1	B1	B2	A1	B1	B2	A1	B1	B2	A1	B1	B2	A1	B1	B2
Lizardite	61.9	60.3	60.7	53.5	49.4	48.1	38.2	35.1	35.5	20.0	22.9	22.0	21.4	12.9	12.2
bias	2.5	1.0	1.3	4.0	0.0	-1.3	3.6	0.5	0.9	0.2	3.1	2.3	11.5	3.0	2.3
Ca-montmorillonite	9.5	7.7	9.9	14.0	19.2	22.9	33.4	35.8	34.1	48.7	49.7	41.1	58.9	59.3	50.2
bias (wt.%)	0.1	-1.7	0.5	-4.8	0.4	4.2	0.6	3.0	1.3	1.8	2.8	-5.8	2.6	3.0	-6.1
Calcite	4.6	4.5	5.1	5.7	4.3	4.8	4.8	3.8	5.1	5.9	2.9	6.1	3.9	3.3	5.6
bias	-1.0	-1.1	-0.6	0.1	-1.2	-0.8	-0.6	-1.5	-0.3	0.7	-2.3	0.9	-1.2	-1.9	0.5
Quartz	5.4	3.2	5.1	5.6	3.7	4.9	5.4	3.4	5.9	6.0	4.0	7.8	4.9	4.7	9.1
bias	-0.2	-2.4	-0.5	-0.6	-2.6	-1.4	-1.8	-3.8	-1.3	-2.1	-4.1	-0.3	-3.8	-4.0	0.4
Clinochlore	2.8	8.7	3.2	3.9	7.5	5.6	3.8	6.4	5.2	3.0	5.8	6.2	1.8	6.4	6.6
bias	-2.5	3.5	-2.0	-1.4	2.2	0.4	-1.5	1.1	-0.1	-2.3	0.5	0.9	-3.5	1.2	1.4
Phlogopite	5.6	5.6	5.6	5.9	6.3	5.0	4.7	5.9	5.0	4.7	5.9	6.4	1.8	5.5	6.5
bias	0.6	0.6	0.6	0.9	1.3	0.0	-0.3	0.9	0.0	-0.3	0.9	1.4	-3.2	0.5	1.5
Brucite	3.9	5.0	4.1	4.1	4.9	4.1	4.3	4.3	4.2	4.1	3.6	4.2	2.3	3.5	3.9
bias	-0.8	0.2	-0.6	-0.6	0.1	-0.7	-0.5	-0.4	-0.6	-0.7	-1.2	-0.5	-2.5	-1.3	-0.8
Talc	6.2	4.9	6.3	7.2	4.7	4.5	5.4	5.3	5.0	7.6	5.2	6.1	5.1	4.5	5.8
bias	1.5	0.2	1.6	2.5	0.0	-0.2	0.7	0.6	0.3	2.9	0.5	1.4	0.4	-0.3	1.1
Total	100.0	100.0	100.0	100.0	100.0	100.0	100.0	100.0	100.0	100.0	100.0	100.0	100.0	100.0	100.0
R_{wp} (%)	5.6	13.8	11.0	5.7	12.6	8.8	4.3	10.9	7.9	4.8	10.2	8.8	4.9	9.8	9.7
Total absolute bias (wt.%)	9.3	10.7	7.8	14.9	7.9	8.8	9.4	11.8	4.8	11.0	15.4	13.4	28.6	15.1	14.1

R_{wp}: weighted profile R-factor, a function of the least-squares residual (%).

Appendix Table A1.3 Refined mineral abundances (wt.%) using PONKCS models calibrated to XRD B1.

Sample	wcskim1		wcskim2		wcskim3		wcskim4		wcskim5	
Phase	A1	B2	A1	B2	A1	B2	A1	B2	A1	B2
Lizardite	51.6	54.2	45.4	48.2	38.2	35.4	23.7	22.4	34.5	17.8
bias	-7.7	-5.1	-4.1	-1.3	3.6	0.8	3.9	2.6	24.6	7.9
Ca-montmorillonite	1.5	5.9	5.2	16.8	10.9	28.1	18.8	36.7	23.7	41.2
bias (wt.%)	-7.9	-3.5	-13.6	-1.9	-21.9	-4.7	-28.1	-10.2	-32.6	-15.1
Calcite	5.4	4.7	6.6	4.6	5.8	4.4	6.8	6.0	5.4	5.0
bias	-0.3	-1.0	1.0	-0.9	0.4	-1.0	1.6	0.8	0.3	-0.1
Quartz	7.8	5.4	8.3	5.8	9.8	6.8	12.4	8.6	11.5	10.8
bias	2.2	-0.2	2.1	-0.4	2.6	-0.3	4.3	0.5	2.7	2.1
Clinochlore	12.0	11.4	9.3	8.6	13.2	8.9	11.4	7.9	8.4	6.5
bias	6.8	6.1	4.0	3.3	7.9	3.7	6.1	2.6	3.2	1.2
Phlogopite	5.9	5.3	8.5	5.3	5.6	5.8	6.7	6.9	2.7	6.6
bias	0.9	0.3	3.5	0.3	0.6	0.8	1.7	1.9	-2.3	1.6
Brucite	5.5	4.6	5.5	4.5	5.2	4.1	4.8	4.0	4.1	3.7
bias	0.8	-0.1	0.8	-0.2	0.4	-0.6	0.0	-0.7	-0.7	-1.1
Talc	10.3	8.6	11.3	6.2	11.5	6.4	15.6	7.6	9.9	8.4
bias	5.5	3.9	6.6	1.5	6.7	1.7	10.8	2.9	5.2	3.6
Total	100.0	100.0	100.0	100.0	100.0	100.0	100.0	100.0	100.0	100.0
R_{wp} (%)	6.2	12.1	6.0	11.2	6.2	10.4	6.7	10.2	6.2	11.4
Total absolute bias (wt.%)	32.1	20.1	35.6	9.8	44.1	13.6	56.5	22.1	71.6	32.7

Appendix Table A1.4 Carbonation potentials (g CO_2/kg kimberlite) calculated from the known composition of wcskim samples and refinement results using correctly calibrated PONKCS models with XRD B2 data, and incorrectly calibrated PONKCS models (calibrated to XRD B1) with XRD B2 data and XRD A1 data.

Sample	wcskim1				wcskim2				wcskim3				wcskim4				wcskim5			
Units (g/kg)	Actual	Calibrated B2	Uncal B2	Uncal A1	Actual	Calibrated B2	Uncal B2	Uncal A1	Actual	Calibrated B2	Uncal B2	Uncal A1	Actual	Calibrated B2	Uncal B2	Uncal A1	Actual	Calibrated B2	Uncal B2	Uncal A1
Lizardite	593	607	542	516	495	481	482	454	346	355	354	382	198	220	224	237	99	122	178	345
Mg in lizardite	156	160	143	136	130	127	127	119	91	93	93	100	52	58	59	62	26	32	47	91
Hydromagnesite eq (lizardite)	601	614	549	522	501	487	488	459	350	359	359	387	200	223	227	240	100	124	180	349
Carbonation potential of lizardite	*226*	*231*	*207*	*197*	*188*	*183*	*184*	*173*	*132*	*135*	*135*	*145*	*75*	*84*	*85*	*90*	*38*	*47*	*68*	*131*
Brucite	47	41	46	55	47	41	45	55	47	42	41	52	47	42	40	48	47	39	37	41
Mg in Brucite	20	17	19	23	20	17	19	23	20	17	17	22	20	18	17	20	20	16	15	17
Hydromagnesite eq (brucite)	76	66	74	88	76	66	73	89	76	67	66	83	76	68	64	76	76	63	59	65
Carbonation potential of brucite	*29*	*25*	*28*	*33*	*29*	*25*	*27*	*33*	*29*	*25*	*25*	*31*	*29*	*26*	*24*	*29*	*29*	*24*	*22*	*24*
Ca-montmorillonite	94	99	59	15	188	229	168	52	328	341	281	109	469	411	367	188	563	502	412	237
Mg in Ca-montmorillonite	2	2	1	0	3	4	3	1	6	6	5	2	8	7	7	3	10	9	7	4
Hydromagnesite eq (Ca-montmorillonite)	6	7	4	1	13	16	11	4	22	23	19	7	32	28	25	13	38	34	28	16
Carbonation potential of Mg in Ca-montmorillonite	*2*	*3*	*2*	*0*	*5*	*6*	*4*	*1*	*8*	*9*	*7*	*3*	*12*	*11*	*9*	*5*	*14*	*13*	*11*	*6*
Ca in Ca-montmorillonite	1	1	0	0	2	2	1	0	3	3	2	1	4	3	3	2	5	4	3	2
Calcite eq (Ca-montmorillonite)	2	2	1	0	4	5	4	1	7	7	6	2	10	9	8	4	12	11	9	5
Carbonation potential of Ca in Ca-montmorillonite	*1*	*1*	*1*	*0*	*2*	*2*	*2*	*0*	*3*	*3*	*3*	*1*	*4*	*4*	*3*	*2*	*5*	*5*	*4*	*2*
Total carbonation potential	**258**	**259**	**237**	**230**	**224**	**216**	**217**	**208**	**172**	**172**	**170**	**181**	**120**	**124**	**122**	**126**	**86**	**88**	**105**	**164**

Appendix A1.1 Carbonation potentials calculations

The emissions offset potential results are reported in Appendix Table A1.4 and Fig. 2.6. Carbonation potential was calculated using (1) the known composition of the wcskim samples (Table 2.1), (2) Rietveld refinement results (wt.%) utilizing PONKCS models calibrated to XRD B2 (Appendix Table A1.2), which gave the most accurate results, and Rietveld refinement results (wt.%) using PONKCS models calibrated to XRD B1 with data collected on (3) XRD B2 and (4) XRD A1 (Appendix Table A1.3). Ideal stoichiometries were assumed for lizardite [$Mg_3Si_2O_5(OH)_4$] and brucite [$Mg(OH)_2$]. Average values for Mg (1.773 wt.%) and Ca (0.841 wt.%) content in SWy-2 (Mermut and Cano, 2001) were used for montmorillonite. Considering a sample mass of 1 kg, $E\ eq$, the equivalent proportion (in g/kg) of Mg in lizardite, brucite or montmorillonite or Ca in montmorillonite were then calculated using (1).

$$E\ eq = C \times M \qquad (1)$$

Where *C* is weight of lizardite or brucite in g/kg *and M* is the mass fraction (%) of the element in the mineral (e.g., Mg comprises 26.31 % and 41.58 % of the mass of lizardite and brucite, respectively).

Assuming hydromagnesite [$Mg_5(CO_3)_4(OH)_2 \cdot 4H_2O$] forms from Mg released during complete dissolution of lizardite, brucite and montmorillonite and that calcite ($CaCO_3$) forms from Ca during complete cation-exchange reactions and dissolution of montmorillonite in the presence of aqueous carbonate. *Mineral eq*, the equivalent proportion (in g/kg) of either hydromagnesite or calcite that would contain these amounts of Mg and Ca were then calculated using (2).

$$Mineral\ eq = \frac{E\ eq}{M} \qquad (2)$$

Where *M* is the mass fraction (%) of the element in hydromagnesite or calcite (e.g., Mg comprises 25.99 % of hydromagnesite and Ca comprises 40.04 % of calcite).

Last, the carbonation potential ($CO_{2\ eq}$ in g/kg) stored within secondary carbonate minerals (e.g., hydromagnesite and calcite) was calculated in (3) using the mass fraction of CO_2, which we name the storage factor (*SF*), in the mineral (0.3764 for hydromagnesite and 0.4397 for calcite).

$$CO_2\ eq\ = Mineral\ eq\ \times SF \qquad (3)$$

A2 Appendix to Chapter 3

Appendix A2.1 Additional ICP-MS methods

The leachates collected from days 2–8 were filtered through Basix™ 0.22 μm polyethersulfone (PES) membranes immediately after collection. Leachates collected from days 9–28 were filtered on day 28. In addition, four yellow precipitates collected from the walls of columns and five thin yellow crusts (recovered mass << 1 g), both occasionally observed at the tops of the columns, were digested and analyzed with ICP-MS at the Department of Earth and Atmospheric Sciences, University of Alberta. For this last analysis, digestion of approximately 0.05 g of each sample was initiated with 3 mL of 30% H_2O_2 and 3 mL of 70% HNO_3 at room temperature for 1 h and then at 120 °C for 1 h. Afterwards, 1 mL of HF was added and the samples were heated at 175 °C until all liquid evaporated (Wang et al., 2016). The remains were dissolved in 15 mL of 4.5% H_3BO_3 at 120 °C for 1 h. The samples were diluted to 50 mL with 2% HNO_3 and 0.5% HCl prior to analysis. The amounts of yellow precipitates that formed in leachates were too low for digestion.

Mass analyzer settings and measurement modes of the Agilent 8800 Triple Quadrupole ICP-MS/MS are provided in Appendix Table A2.1. Q1 and Q2 are the mass/charge ratios (*m/z*) selected for the first and second mass separation steps. Argon was used as the carrier gas. External calibration was done with elemental mixtures diluted in 2% HNO_3 and 0.5% HCl while internal standardization was done by introducing Internal Standard Mix 2 by Spex CertiPrep in-line using a T connector. Samples were diluted with 2% HNO_3 and 0.5% HCl prior to analysis to adjust the matrix and to be in the external calibration range. Oxygen was introduced into the reaction chamber (10% O_2) for analysis of P, S, Cr and As and a mass shift of m/z 16 was applied in the second mass analyzer to select for monooxygenated cations. The certified shale material ShBOQ-1 by the U.S. Geological Survey (USGS) was used to monitor digestion recovery for the applied method. Average recoveries are shown in the last column of Appendix Table A2.1.

Appendix A2.2 Additional methods for bulk elemental chemistry of solids

X-ray fluorescence (XRF) was used to determine the abundances of major element oxides including Al_2O_3, CaO, Cr_2O_3, Fe_2O_3, K_2O, MgO, MnO, Na_2O, P_2O_5, SiO_2, TiO_2 and V_2O_5. The concentrations of minor elements such as Co, Cu, Zn and Ni were determined using inductively coupled plasma atomic emission spectroscopy (ICP-AES). Leco analysis, which involves combustion of a sample and quantification of volatiles using Infrared spectroscopy, was used for total S and C abundances. In addition, four yellow precipitates collected from the walls of columns and five thin yellow crusts (recovered mass << 1 g), both occasionally observed at the tops of the columns, were digested and analyzed with ICP-MS at the Department of Earth and Atmospheric Sciences, University of Alberta. For this last analysis, digestion of approximately 0.05 g of each sample was initiated with 3 mL of 30% H_2O_2 and 3 mL of 70% HNO_3 at room temperature for 1 h and then at 120 °C for 1 h. Afterwards, 1 mL of HF was added and the samples were heated at 175 °C until all liquid evaporated (Wang et al., 2016). The remains were dissolved in 15 mL of 4.5% H_3BO_3 at 120 °C for 1 h. The samples were diluted to 50 mL with 2% HNO_3 and 0.5% HCl prior to analysis. The amounts of yellow precipitates that formed in leachates were too low for digestion.

Appendix Table A2.1 Tune mode, mass/charge ratios and detection limits for ICP-MS analysis.

Element	Q1	Q2	Tune mode	Background-equivalent concentration (ppb)	ShBOQ-1 average recovery (%)
Li		7	No gas	21.89	89
Na		23	He	507.9	83
Mg		24	He	1.012	97
Al		27	No gas	1.239	108
Si	28	28	H_2	18.09	104
K		39	He	77.33	93
Ti		48	He	2.279×10^{-2}	109
P	31	47	O_2	4.170×10^{-1}	86
S	32	48	O_2	11.90	98
Ca	40	40	H_2	16.99	105
V		51	He	1.335×10^{-1}	98
Mn		55	He	1.514	–
Fe	56	56	H_2	5.960×10^{-1}	98
Co		59	He	1.736×10^{-2}	108
Ni		60	He	2.356×10^{-1}	109
Cu		63	He	3.355	92
Zn		66	He	1.734	68
Cr	52	68	O_2	5.068×10^{-1}	106
Rb		85	He	9.469×10^{-3}	93
Sr		88	He	1.115	116
As	75	91	O_2	1.876×10^{-2}	88
Mo		96	He	1.925×10^{-2}	62
Ba		138	He	8.596×10^{-2}	104
Pb		208	No gas	1.424×10^{-1}	91

Appendix Table A2.2 Parameters used in MIN3P model.

Parameter	Input	Reference
Porosity	0.332	Measured
Hydraulic conductivity K [m s^{-1}]	5.00×10^{-6}	estimated after Stolburg (2005)[1] for all directions
van Genuchten parameter α [m^{-1}]	0.8	Bea et al. (2012)[1]
van Genuchten parameter *n*	1.4	Bea et al. (2012)[1]
Solid density, ρs [kg m^{-3}]	1300	Measured
Gas phase diffusion coefficient [m^2 s^{-1}]	1.65×10^{-5}	Bea et al. (2012)[1]
Aqueous phase diffusion coefficient [m^2 s^{-1}]	1.00×10^{-10}	Bea et al. (2012)[1]
Initial temperature [°C]	22	Measured

[1] These reference values are for compositionally similar mine tailings from the Mount Keith nickel mine.

Appendix Table A2.3 Initial mineral abundances, input surface areas, and dissolution rate laws used in MIN3P model.

Phase	Abundance (mineral vol. fraction) (%)	Mineral density (g/cm^3)	Effective Surface area (m^2/g) [a]	Input surface area (m^2/L bulk)	Dissolution / precipitation reaction
Clinochlore	3.95×10^{-2}	2.65	n/a	74	kinetic (Parkhurst and Appelo, 2013)
Lizardite	1.16×10^{-1}	2.57	0.6	1.9×10^{2}	kinetic (Daval et al., 2013)
Talc	2.87×10^{-2}	2.75	n/a	1.48×10^{-10}	kinetic[b]
Albite	5.71×10^{-2}	2.62	n/a	1.15×10^{-12}	kinetic (Wollast and Chou, 1985)
Diopside	0.05	3.4	0.8	1.48×10^{-10}	kinetic (Siegel and Pfannkuch., 1984)
Orthoclase	3.40×10^{-2}	2.56	n/a	1.15×10^{-12}	kinetic (Schweda et al., 1990)
Calcite	0.02	2.71	0.04	7.4	kinetic (Chou et al., 1989), irreversible dissolution, log K control
Quartz	3.32×10^{-2}	2.62	n/a	1.0×10^{-9}	quasi-equilibrium, reversible
Saponite	1.20×10^{-1}	2.35	n/a	2.47×10^{-6}	kinetic[b]
Tremolite	3.70×10^{-2}	3.05	n/a	2.4×10^{-11}	kinetic[b]
Phlogopite	5.52×10^{-2}	2.8	n/a	3.70×10^{-10}	kinetic[b]
Hydroxylapatite	3.03×10^{-3}	3.19	n/a	7.40×10^{-8}	kinetic[b]
Chalcedony	0.00	2.65	n/a	n/a	quasi-equilibrium, reversible
Ferrihydrite	0.00	3.80	n/a	n/a	quasi-equilibrium, reversible

[a] Effective surface area for calcite is from Bea et al. (2012).

[b] These reference values are based on the MINTEQA2 database.

Appendix Table A2.4 Water chemistry of initial pore water and acidic water collected on day 2 used for leaching.

	Milli-Q	**0.04 M HCl**	**0.08 M HCl**	**0.12 M HCl**	**0.16 M HCl**
Variable	**(M)**	**(M)**	**(M)**	**(M)**	**(M)**
pH[a]	8.97	8.42	8.18	8.42	8.12
Na^+	9.53×10^{-3}	6.41×10^{-2}	1.10×10^{-1}	1.33×10^{-1}	1.66×10^{-1}
K^+	3.85×10^{-3}	6.02×10^{-3}	9.90×10^{-3}	1.22×10^{-2}	1.50×10^{-2}
Mg^{2+}	2.22×10^{-5}	4.00×10^{-4}	1.59×10^{-3}	2.35×10^{-3}	4.17×10^{-3}
Ca^{2+}	3.02×10^{-5}	8.80×10^{-4}	3.02×10^{-3}	4.39×10^{-3}	8.21×10^{-3}
Fe^{2+}	1.00×10^{-20}	1.00×10^{-20}	1.00×10^{-20}	1.00×10^{-20}	1.00×10^{-20}
Fe^{3+}	6.00×10^{-6}	2.00×10^{-2}	4.14×10^{-2}	6.00×10^{-6}	6.00×10^{-6}
Al^{3+}	1.00×10^{-13}	1.00×10^{-13}	1.00×10^{-13}	1.00×10^{-13}	1.00×10^{-13}
H_4SiO_4	1.06×10^{-4}	6.00×10^{-4}	7.21×10^{-4}	5.10×10^{-3}	8.84×10^{-4}
NO_3^-	4.07×10^{-4}	3.07×10^{-4}	2.37×10^{-4}	3.02×10^{-4}	3.13×10^{-4}
PO_4^{3-}	1.00×10^{-13}	1.00×10^{-13}	1.00×10^{-13}	1.00×10^{-13}	1.00×10^{-13}
SO_4^{2-}	1.46×10^{-4}	1.46×10^{-4}	1.02×10^{-3}	1.00×10^{-3}	7.00×10^{-4}
Cl^-	1.75×10^{-3}	4.90×10^{-2}	8.10×10^{-2}	1.57×10^{-1}	2.00×10^{-1}
pCO_2[b]	4.00×10^{-4}	4.00×10^{-4}	4.00×10^{-4}	4.00×10^{-4}	4.00×10^{-4}
pO_2[b]	0.21	0.21	0.21	0.21	0.21

[a] Unitless

[b] Unit = atm

Appendix Table A2.5 Leachate chemistry based on average value of triplicate columns.

Sample name	Day	pH	Alkalinity (mg/L)	Mg/ppm	Ca/ppm	Si/ppm	Ni/ppm	Fe/ppm	Cr/ppm
M0	2	8.88	409.49	0.4458	1.263	11.34	BDL	0.07875	BDL
M0	4	9.13	345.13	7.399	1.322	19.63	0.07813	2.547	0.01167
M0	6	9.41	308.94	1.783	0.7723	13.84	0.01861	0.5942	BDL
M0	8	9.50	277.81	1.493	0.8010	12.51	0.01631	0.5139	BDL
M0	12	9.67	281.62	1.063	0.7662	10.45	0.01161	0.3669	BDL
M0	17	9.71	237.52	0.7607	0.8275	9.757	0.07813	0.2594	BDL
M0	20	9.67	231.88	0.6289	0.8647	9.151	0.01861	0.2104	BDL
M0	24	9.63	229.21	0.3670	1.148	8.185	BDL	0.09935	BDL
M0	28	9.80	211.01	0.1911	0.6546	7.430	BDL	0.04506	BDL
M1	2	8.41	575.78	10.50	32.33	19.74	BDL	1303	BDL
M1	4	8.51	433.25	9.230	26.02	25.92	BDL	1129	BDL
M1	6	8.50	440.88	11.04	26.78	29.59	BDL	998.9	BDL
M1	8	8.48	341.79	23.61	48.36	33.00	BDL	867.4	BDL
M1	12	8.08	224.50	94.48	203.5	36.72	0.05630	480.7	BDL
M1	17	8.24	216.31	155.2	418.1	44.16	0.09717	212.6	BDL
M1	20	8.13	128.59	177.9	481.6	43.53	0.1073	60.35	BDL
M1	24	7.98	166.74	196.0	539.0	40.93	0.1278	13.84	BDL
M1	28	8.02	198.63	213.2	562.2	43.57	0.1547	9.600	BDL
M2	2	8.10	485.73	35.90	106.1	19.54	0.03826	2200	BDL
M2	4	8.14	358.82	62.24	173.0	31.24	0.07086	1737	BDL
M2	6	7.90	320.36	116.3	347.1	38.23	0.1802	1248	BDL
M2	8	7.68	275.27	207.2	621.2	46.36	0.3871	743.4	BDL
M2	12	7.30	229.23	304.9	886.9	51.14	0.7603	194.3	BDL
M2	17	7.75	242.01	356.5	979.0	52.16	1.276	23.05	BDL
M2	20	7.74	168.54	383.2	983.1	49.92	1.338	16.30	BDL
M2	24	7.45	168.26	442.4	899.2	45.22	1.546	12.12	BDL
M2	28	7.45	200.33	521.9	835.7	44.15	1.949	10.91	BDL
M3	2	8.20	505.04	61.84	191.6	135.5	0.3467	BDL	BDL
M3	4	7.78	335.93	145.5	441.1	240.5	1.304	BDL	BDL
M3	6	7.46	230.13	254.0	861.3	284.1	3.612	BDL	BDL
M3	8	7.46	200.27	368.0	1311	298.1	4.974	0.01374	BDL
M3	12	7.26	218.44	463.2	1471	275.5	9.646	0.2985	BDL
M3	17	6.81	248.23	622.5	1443	255.0	21.80	0.1482	BDL
M3	20	6.65	178.57	701.1	1276	219.9	26.17	30.20	BDL
M3	24	6.80	160.18	809.8	1144	204.5	26.30	0.04068	BDL
M3	28	6.48	101.52	863.3	991.4	172.3	27.95	95.51	BDL
M4	2	8.15	455.27	109.5	331.2	25.41	0.1065	BDL	BDL
M4	4	7.64	329.10	298.2	1086	52.37	0.6331	BDL	BDL
M4	6	7.48	241.26	455.2	1650	55.45	1.260	BDL	BDL
M4	8	7.35	194.70	646.7	2333	52.34	2.343	0.03230	BDL
M4	12	7.03	155.67	711.2	1878	50.50	4.605	0.05996	BDL
M4	17	6.50	109.17	1025	1789	35.64	7.167	0.01166	BDL
M4	20	6.53	70.36	1149	1562	29.17	7.376	2.7452	BDL
M4	24	5.94	25.93	1198	1237	24.59	8.115	32.02	BDL
M4	28	5.97	18.14	1301	1164	25.66	7.532	69.62	BDL

Appendix Table A2.6 Rietveld refinement results (wt.%) for the initial processed kimberlites (CRD, FRD and Mmixed) and the leached processed kimberlite columns at different depths.

Sample	Residue position	Calcite	Hydroxylapatite	Diopside	Tremolite	Orthoclase	Albite	Quartz	Phlogopite	Clinochlore	Talc	Lizardite	Saponite	Total wt.%	R_{wp}^{*} (%)
CRD	–	5.1	0.9	9.0	7.6	5.8	8.9	3.9	7.7	2.9	2.3	23.3	22.8	100.0	10.6
FRD	–	4.2	1.1	7.3	3.0	4.5	5.9	4.1	14.4	4.8	2.2	18.5	29.9	100.0	11.1
Mmixed	–	4.2	0.6	11.2	7.0	5.4	9.3	5.4	9.6	6.5	4.9	18.5	17.5	100.0	9.1
Milli-Q-1	top	4.3	0.4	11.9	6.7	5.7	9.0	5.4	9.5	6.4	4.5	18.7	17.7	100.0	9.1
Milli-Q-1	middle	4.7	0.6	12.9	7.5	4.7	9.0	5.5	8.0	7.9	4.8	19.4	15.0	100.0	8.2
Milli-Q-1	bottom	4.6	0.4	11.9	6.8	4.6	7.4	5.2	9.1	9.5	5.0	18.8	16.9	100.0	7.6
0.04 M-1	top	1.8	1.3	11.6	5.6	4.9	9.8	6.0	13.8	6.1	5.2	17.2	16.8	100.0	10.6
0.04 M-1	middle	4.2	0.9	10.4	6.1	5.4	7.9	5.4	11.4	6.6	4.7	20.1	17.0	100.0	9.9
0.04 M-1	bottom	4.8	1.1	10.6	7.3	4.1	9.5	6.4	11.4	5.5	4.3	19.3	15.7	100.0	9.1
0.08 M-1	top	1.4	1.3	11.4	7.5	5.6	8.2	7.3	13.1	6.7	4.9	16.8	15.8	100.0	10.4
0.08 M-1	middle	3.3	0.7	11.2	6.7	4.3	7.8	5.6	10.6	7.2	4.9	18.1	19.7	100.0	9.2
0.08 M-1	bottom	4.5	1.2	10.4	8.5	3.0	7.8	6.0	12.1	6.0	2.6	19.9	18.0	100.0	9.3
0.12 M-1	top	1.3	1.6	11.7	6.3	6.2	9.6	6.1	14.6	6.3	3.9	16.7	15.8	100.0	10.1
0.12 M-1	middle	2.8	1.5	10.7	5.8	4.3	9.2	4.8	12.8	5.8	3.6	20.3	18.5	100.0	9.6
0.12 M-1	bottom	4.8	1.5	9.5	5.1	4.4	8.4	4.3	14.1	6.4	4.7	18.7	18.2	100.0	10.7
0.16 M-1	top	0.8	1.5	10.5	7.0	6.0	12.1	5.7	14.1	6.5	3.5	14.3	18.1	100.0	10.4
0.16 M-1	middle	2.2	1.6	8.3	3.5	4.8	8.1	5.7	14.5	5.8	3.3	19.2	23.1	100.0	11.4
0.16 M-1	bottom	4.4	1.5	9.9	7.4	4.1	6.3	3.0	13.3	7.0	3.7	19.8	19.8	100.0	10.9

*R_{wp}: the weighted pattern index, a function of the least-squares residual.

Appendix Table A2.7 Oxide and elemental abundances for column samples collected at different depths determined using XRF (oxides), ICP-AES (most elements), and Leco analysis (for C).

	Al_2O_3	CaO	Cr_2O_3	Fe_2O_3	K_2O	MgO	Na_2O	SiO_2	TiO_2	MnO	Fe	Ca	Mg	Co	Cu	Ni	Zn	C
UNITS	%	%	%	%	%	%	%	%	%	%	%	%	%	ppm	ppm	ppm	ppm	%
Detection limit	0.01	0.01	0.01	0.01	0.01	0.01	0.01	0.01	0.01	0.01	0.01	0.1	0.01	10	10	10	10	0.005
Mmixed (70 % FRD:30 % CRD)	7.96	7.04	–	8.66	1.93	17.30	1.40	46.35	0.82	0.16	5.77	4.6	8.96	50	51	608	66	0.425
Milli-Q-1-top	7.75	6.55	0.11	8.43	2.04	17.13	1.26	47.12	0.83	0.14	5.59	4.6	10.12	48	53	716	73	0.487
Milli-Q-1-medium	7.70	6.63	0.11	8.10	2.07	17.27	1.34	47.34	0.85	0.14	5.39	4.5	9.95	48	56	669	71	0.495
Milli-Q-1-bottom	7.63	6.54	0.11	8.09	2.04	17.99	1.33	47.00	0.82	0.14	5.46	4.5	10.53	47	56	706	70	0.499
0.04 M-1-top	8.46	4.83	0.11	8.71	1.85	16.80	1.15	48.87	0.85	0.14	5.92	3.4	9.73	39	55	611	75	0.14
0.04 M-1-medium	7.94	6.54	0.11	8.21	1.99	16.90	1.08	46.97	0.82	0.14	5.56	4.6	9.69	42	51	669	74	0.432
0.04 M-1-bottom	7.80	6.96	0.1	8.32	1.92	16.90	1.05	46.82	0.83	0.15	5.54	4.8	9.45	37	51	636	69	0.514
0.08 M-1-top	7.94	4.65	0.11	8.54	1.79	16.66	1.07	49.58	0.85	0.14	5.79	3.3	9.47	34	63	560	73	0.119
0.08 M-1-medium	7.80	6.12	0.11	8.37	1.84	17.56	1.08	47.01	0.84	0.15	5.60	4.2	9.90	43	56	680	85	0.379
0.08 M-1-bottom	7.68	6.86	0.11	7.97	1.92	17.19	1.10	46.73	0.78	0.15	5.39	4.8	9.98	44	53	728	73	0.518
0.12 M-1-top	7.83	4.54	0.11	8.08	1.79	16.55	1.23	49.98	0.86	0.13	5.40	3.1	9.57	37	42	573	69	0.095
0.12 M-1-medium	8.01	5.68	0.11	8.25	1.88	17.10	1.19	47.02	0.78	0.14	5.65	4.0	10.11	48	55	688	72	0.267
0.12 M-1-bottom	7.52	6.66	0.11	8.14	1.93	17.73	1.02	46.02	0.80	0.15	5.54	4.7	10.46	50	58	759	73	0.534
0.16 M-1-top	8.09	4.78	0.11	8.03	1.73	15.4	1.36	50.82	0.87	0.13	5.38	3.3	8.90	40	44	550	62	0.048
0.16 M-1-medium	8.05	4.99	0.11	8.03	1.95	17.68	1.13	48.74	0.80	0.13	5.38	3.4	10.10	45	49	695	65	0.183
0.16 M-1-bottom	7.67	7.04	0.13	8.47	1.81	17.73	1.25	45.44	0.84	0.15	5.87	5.0	10.46	50	55	714	76	0.460

Appendix Table A2.8 ICP-MS data for solids (crusts and initial residues).

	Initial residues	Milli-Q Crust	0.04 M Crust	0.08 M Crust	0.12 M Crust	0.16 M Crust
unit	ppm	ppm	ppm	ppm	ppm	ppm
Li	25.91	23.13	23.71	1312.92	BDL	BDL
Na	10200	8388	5325	9743	4128	3085
Mg	112300	113300	140000	95830	96840	81300
Al	36820	42800	48460	42660	30390	25700
Si	14020	3044	3528	7761	6555	2879
K	15380	17610	15170	14340	12670	9380
Ti	4821	5238	7013	4680	5970	4793
P	1051	1300	423.2	326.5	442.2	350.5
S	679.0	1216	1301	676.3	962.1	682.3
Ca	39680	44950	26710	23760	20500	17460
V	108.5	115.6	136.7	94.57	100.4	82.58
Mn	935.5	921.5	935.3	655.4	663.5	564.1
Fe	54230	57030	69270	44600	46790	38970
Co	51.14	59.11	68.11	39.73	44.21	40.12
Ni	646.9	693.0	772.2	495.5	534.6	465.0
Cu	136.6	22.18	56.20	11.26	BDL	5.677
Zn	43.56	72.89	109.0	94.78	142.7	104.5
Cr	293.1	342.5	426.3	292.9	284.5	229.5
Rb	74.51	86.02	89.14	68.37	65.34	45.09
Sr	316.0	354.4	135.5	139.9	84.46	68.43
As	3.820	2.805	1.901	1.629	1.986	1.654
Mo	10.27	4.275	2.450	1.625	2.213	1.509
Ba	663.4	717.3	767.1	558.4	446.5	406.2
Pb	13.58	31.35	14.06	9.953	4.648	4.371

Appendix Table A2.9 ICP-MS data for yellow precipitates collected from the walls of the columns.

	0.04 M HCl	0.08 M HCl	0.12 M HCl	0.16 M HCl
unit	ppm	ppm	ppm	ppm
Li	27.93	23.54	28.04	17.06
Na	26570	6524	95220	11580
Mg	83830	84200	82740	70260
Al	33500	34960	34860	31440
Si	167900	198600	196400	184300
K	14210	12000	13390	13220
Ti	5213	4513	4932	4403
P	633.6	371.8	681.1	244.5
S	845.6	1342	4188	1607
Ca	18660	16470	17050	15520
V	106.2	106.3	107.2	93.58
Mn	671.8	598.5	602.3	563.0
Fe	51300	48460	45030	39130
Co	41.38	41.40	42.10	39.38
Ni	436.7	465.8	456.7	380.7
Cu	58.88	68.93	76.68	61.36
Zn	102.7	43.49	65.93	50.30
Cr	265.0	296.5	284.8	260.4
Rb	64.17	58.49	65.46	61.62
Sr	120.3	98.15	83.56	91.84
As	2.730	2.379	3.324	4.777
Mo	10.85	7.468	6.449	2.014
Ba	892.4	1407	1045	1790
Pb	6.856	6.248	5.580	4.405

Appendix Table A2.10 Extraction of Mg in each kind of leachate based on ICP-MS data.

	Milli-Q	0.04 M HCl	0.08 M HCl	0.12 M HCl	0.16 M HCl
Day 2 (ppm)	0.4458	10.50	35.90	61.84	109.5
Day 4 (ppm)	7.399	9.230	62.24	145.5	298.2
Day 6 (ppm)	1.783	11.04	116.3	254.0	455.2
Day 8 (ppm)	1.493	23.61	207.2	368.0	646.7
Day 12 (ppm)	1.063	94.48	304.9	463.2	711.2
Day 17 (ppm)	0.7607	155.2	356.5	622.5	1025
Day 20 (ppm)	0.6289	177.9	383.2	701.1	1149
Day 24 (ppm)	0.3670	196.0	442.4	809.8	1198
Day 28 (ppm)	0.1911	213.2	521.9	863.3	1301
Average concentration–days [2, 8)	2.780	13.59	105.4	207.3	377.4
Average concentration–days [8, 17)	1.105	91.09	289.5	484.5	794.3
Average concentration–days [17, 28]	0.4869	185.5	426.0	749.2	1168
Volume of leachate (mL/day)	16.6	16.6	16.6	16.6	16.6
Total Mg in all leachates (μg)	539.0	51930	138600	242300	389000
Total Mg in initial residues (g)	7.21	7.21	7.21	7.21	7.21
Total Mg extraction (%)	0.0	0.7	1.9	3.4	5.4

Appendix Table A2.11 Extraction of Ca in each leachate based on ICP-MS data.

	Milli-Q	0.04 M HCl	0.08 M HCl	0.12 M HCl	0.16 M HCl
Day 2 (ppm)	1.263	32.33	106.1	191.6	331.2
Day 4 (ppm)	1.322	26.02	173.0	441.1	1086
Day 6 (ppm)	0.7723	26.78	347.1	861.3	1650
Day 8 (ppm)	0.8010	48.36	621.2	1311	2333
Day 12 (ppm)	0.7662	203.5	886.9	1471	1878
Day 17 (ppm)	0.8275	418.1	979.0	1443	1789
Day 20 (ppm)	0.8647	481.6	983.1	1276	1562
Day 24 (ppm)	1.148	539.0	899.2	1144	1237
Day 28 (ppm)	0.6546	562.2	835.7	991.4	1164
Average concentration–days [2, 8)	1.039	33.38	311.8	701.2	1350
Average concentration–days [8, 17)	0.7982	223.3	829.0	1408	2000
Average concentration–days [17, 28]	0.8736	500.2	924.2	1214	1438
Volume of leachate (mL/day)	16.6	16.6	16.6	16.6	16.6
Total Ca in all leachates (μg)	396.8	136300	339000	522000	719800
Total Ca in initial residues (g)	3.70	3.70	3.70	3.70	3.70
Total Ca extraction (%)	0.0	3.7	9.2	14.1	19.4

Appendix Table A2.12 CO_2 offset potential of leached Mg based on Venetia mine data from 2016.

Sample	Proportion of total Mg extracted (%)	Mass fraction of Mg in sample (%)	Hydromagnesite equivalent (%)	CO_2 in hydromagnesite (%)	Venetia ore treated (Mt/year)	Maxmium offset potential of Mg (Mt CO_2/year)	Venetia CO_2 emissions (Mt/year)	Proportion of Venetia CO_2 emissions (%)
Initial residues	–	8.96	34.47	12.98	4.74	0.62	0.21	292.9
Milli-Q-leachates	0.01	0.00	0.00	0.00	4.74	4.60E-5	0.21	0.0
0.04 M-leachates	0.72	0.06	0.25	0.09	4.74	4.42E-3	0.21	2.1
0.08 M-leachates	1.92	0.17	0.66	0.25	4.74	1.18E-2	0.21	5.6
0.12 M-leachates	3.36	0.30	1.16	0.44	4.74	2.07E-2	0.21	9.8
0.16 M-leachates	5.39	0.48	1.86	0.70	4.74	3.32E-2	0.21	15.8

Appendix Table A2.13 Predicted CO_2 emissions from calcite dissolution based on Venetia mine data from 2016.

Sample	Proportion of calcite dissolved (%)	Mass fraction of Ca in calcite (%)	Calcite equivalent (%)	CO_2 in calcite (%)	Venetia ore treated (Mt/year)	Calculated emissions from calcite dissolution (Mt CO_2/year)	Venetia CO_2 emissions (Mt/year)	Proportional increase in potential emissions at Venetia if calcite were dissolved (%)
Initial residues	–	1.68	4.20	1.85	4.74	8.75E-2	0.21	41.7
Milli-Q-leachates	–	-0.13	–	–	–	–	0.21	–
0.04 M-leachates	4.95	0.08	0.21	0.09	4.74	4.33E-3	0.21	2.1
0.08 M-leachates	19.52	0.33	0.82	0.36	4.74	1.71E-2	0.21	8.1
0.12 M-leachates	25.07	0.42	1.05	0.46	4.74	2.19E-2	0.21	10.4
0.16 M-leachates	34.22	0.58	1.44	0.63	4.74	3.00E-2	0.21	14.3

Appendix Table A2.14 CO_2 offset potential of leached Ca from silicates dissolution based on Venetia mine data from 2016.

Sample	Mass fraction of Ca in calcite (%)	Mass fraction of Ca in silicates (%)	Proportional increase in potential emissions at Venetia if calcite were dissolved (%)	Proportion of Venetia CO_2 emissions offset potential by Ca from silicate dissolution (%)
Initial residues	1.68	2.92	41.7	72.5
Milli-Q-leachates	–	–	–	–
0.04 M-leachates	50.00	50.00	2.1	2.1
0.08 M-leachates	76.47	23.53	8.1	2.5
0.12 M-leachates	65.38	34.62	10.4	5.5
0.16 M-leachates	63.89	36.11	14.3	8.1

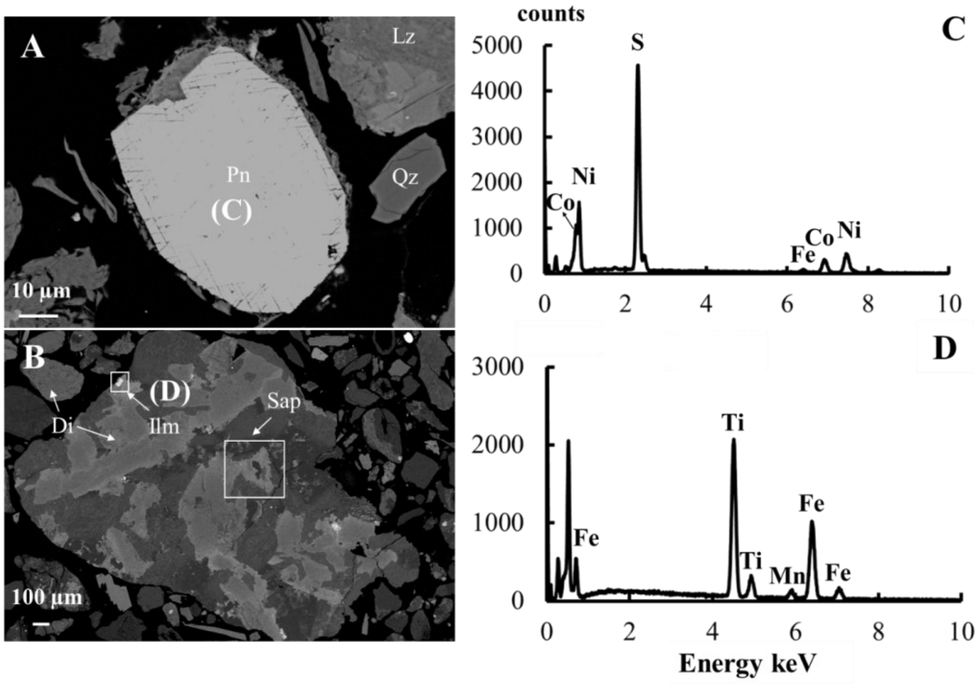

Appendix Figure A2.1 SEM-EDXS results for the large thin section prepared from the Milli-Q-treated column. SEM images taken in backscattered electron mode showing (A) a sulfide grain containing Ni, Co and Fe, likely pentlandite, and (B) a grain of ilmenite associated with diopside and saponite. (C) and (D) show EDXS data corresponding to the pentlandite and ilmenite marked on (A) and (B). Mineral abbreviations: Lz = lizardite, Qz = quartz, Pn = pentlandite, Di = diopside, Ilm = ilmenite, Sap = saponite.

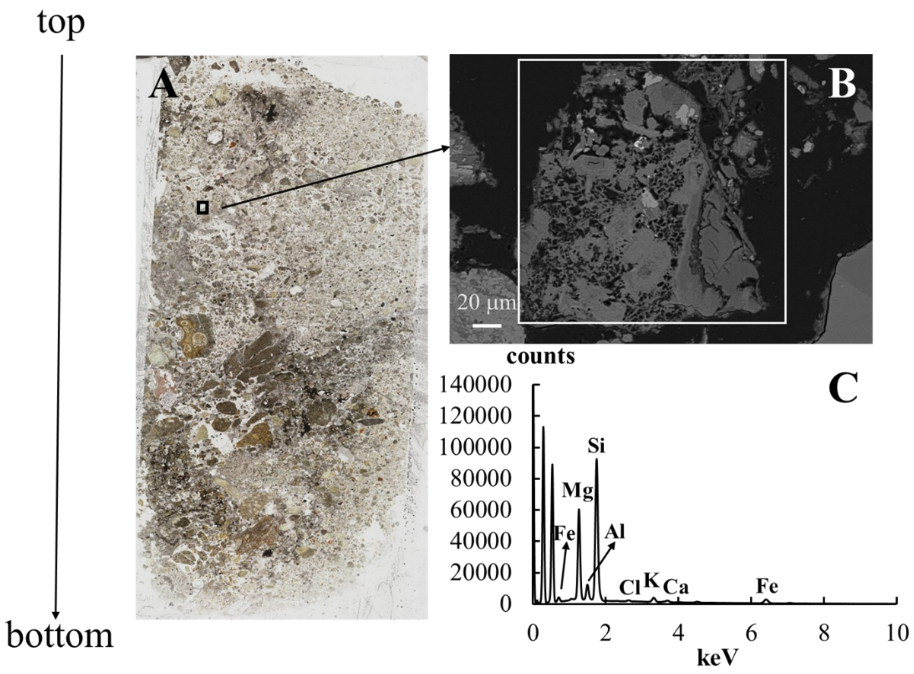

Appendix Figure A2.2 Dissolution of serpentine in the 0.16 M HCl treated column.

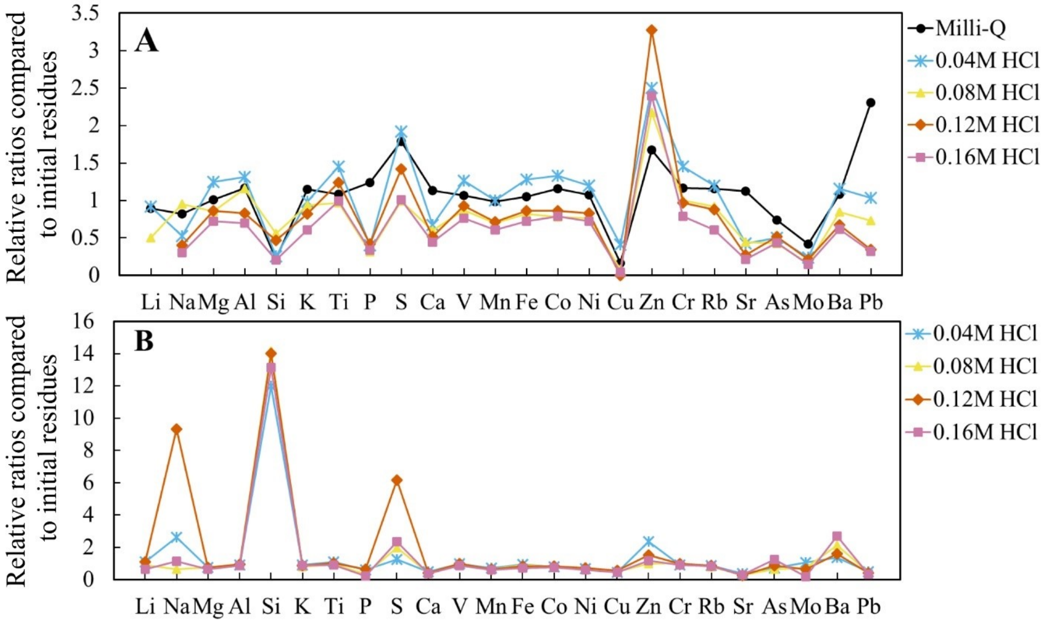

Appendix Figure A2.3 The relative concentrations of elements (A) in crusts, (B) in yellow precipitates collected from the walls of the syringes normalized with initial residues bulk composition.

A3 Appendix to Chapter 4

Appendix Table A3.1 Parameters used in MIN3P model.

Parameter	Input	Reference
Porosity	0.332	Measured
Hydraulic conductivity K [m s^{-1}]	5.00×10^{-6}	estimated after Stolburg (2005)[1] for all directions
α [m^{-1}]	0.8	Bea et al. (2012)[1]
n	1.4	Bea et al. (2012)[1]
Solid density, ρs [kg m^{-3}]	1300	Measured
Gas phase diffusion coefficient [m^2 s^{-1}]	1.65×10^{-5}	Bea et al. (2012)[1]
Aqueous phase diffusion coefficient [m^2 s^{-1}]	1.00×10^{-10}	Bea et al. (2012)[1]
Initial temperature [°C]	22	Measured

[1] These reference values are for compositionally similar mine tailings from the Mount Keith nickel mine.

Appendix Table A3.2 Initial mineral abundances, input surface areas, and dissolution rate laws used in MIN3P model for processed kimberlite from Gahcho Kué.

Phase	**Abundance (mineral vol. fraction) (%)**	**Mineral density (g/cm^3)**	**Effective Surface area (m^2/g) [a]**	**Input surface area (m^2/L bulk)**	**Rate**	**Dissolution / precipitation reaction[b]**
Clinochlore	6.32×10^{-2}	2.65	n/a	74	n/a	kinetic, irreversible dissolution, log K control
Lizardite	1.64×10^{-1}	2.57	0.6	1.9×10^{2}	n/a	kinetic (Daval et al., 2013), irreversible dissolution, log K control
Talc	2.40×10^{-2}	2.75	n/a	1.48×10^{-10}	n/a	kinetic, irreversible dissolution, log K control
Albite	4.79×10^{-2}	2.62	n/a	1.15×10^{-12}	n/a	kinetic, irreversible dissolution, log K control
Augite	0.02	3.4	0.8	1.48×10^{-10}	n/a	kinetic, dissolution or precipitation
Orthoclase	5.41×10^{-2}	2.56	n/a	1.15×10^{-12}	n/a	kinetic, dissolution or precipitation
Forsterite	3.45×10^{-2}	3.27	0.8	1.48×10^{2}	n/a	kinetic (Klein and Hurlbut, 1993), irreversible dissolution, log K control
Calcite	0.01	2.71	0.04	7.4	n/a	kinetic (Chou et al., 1989), irreversible dissolution, log K control
Quartz	2.27×10^{-2}	2.62	n/a	1.0×10^{-9}	n/a	kinetic, dissolution or precipitation
Saponite	9.04×10^{-2}	2.35	n/a	2.47×10^{-6}	n/a	kinetic, dissolution or precipitation
Tremolite	1.74×10^{-2}	3.05	n/a	2.4×10^{-11}	n/a	kinetic, dissolution or precipitation
Phlogopite	4.89×10^{-2}	2.8	n/a	3.70×10^{-10}	n/a	kinetic, dissolution or precipitation
Magnetite	5.00×10^{-3}	5.15	0.0001	3.80×10^{-1}	n/a	kinetic, dissolution or precipitation
Chalcedony	0.00	2.65	n/a	n/a	1.00×10^{-7}	quasi-equilibrium, reversible
Ferrihydrite	0.00	3.80	n/a	n/a	1.00×10^{-9}	quasi-equilibrium, reversible

[a] Effective surface area for calcite is from Bea et al. (2012).

[b] These reference values are based on the MINTEQA2 database.

Appendix Table A3.3 Initial mineral abundances, input surface areas, and dissolution rate laws used in MIN3P model for serpentine rock samples from the Record Ridge Project.

Phase	**Abundance in RRP1 (mineral vol. fraction) (%)**	**Abundance in RRP2 (mineral vol. fraction) (%)**	**Mineral density (g/cm^3)**	**Effective Surface area (m^2/g)** [a]	**Input surface area (m^2/L bulk)**	**Rate**	**Dissolution / precipitation reaction**[b]
Clinochlore	8.02×10^{-2}	7.47×10^{-2}	2.65	n/a	74	n/a	kinetic, irreversible dissolution, log K control
Lizardite	2.12×10^{-1}	4.02×10^{-1}	2.57	0.6	1.9×10^{2}	n/a	kinetic (Daval et al., 2013), irreversible dissolution, log K control
Talc	6.62×10^{-2}	3.45×10^{-2}	2.75	n/a	1.48×10^{-10}	n/a	kinetic, irreversible dissolution, log K control
Brucite	4.72×10^{-3}	2.49×10^{-2}	2.39	0.39	9.24	n/a	kinetic, dissolution or precipitation
Forsterite	1.71×10^{-2}	4.04×10^{-2}	3.27	0.8	1.48×10^{2}	n/a	kinetic (Klein and Hurlbut, 1993), irreversible dissolution, log K control
Tremolite	1.74×10^{-1}	0.00	3.05	n/a	2.4×10^{-11}	n/a	kinetic, dissolution or precipitation
Magnetite	1.47×10^{-2}	1.81×10^{-2}	5.15	0.0001	3.80×10^{-1}	n/a	kinetic, dissolution or precipitation
Chalcedony	0.00	0.00	2.65	n/a	n/a	1.00×10^{-7}	quasi-equilibrium, reversible
Ferrihydrite	0.00	0.00	3.80	n/a	n/a	1.00×10^{-9}	quasi-equilibrium, reversible

[a] Effective surface area for calcite is from Bea et al. (2012).

[b] These reference values are based on the MINTEQA2 database.

Appendix Table A3.4 Water chemistry of initial pore water and acidic water collected on day 2 used for the reactive transport modeling.

	GK-Milli-Q	**GK-HCl**	**RRP1-Milli-Q**	**RRP1-HCl**	**RRP2-Milli-Q**	**RRP2-HCl**
Variable	**(M)**	**(M)**	**(M)**	**(M)**	**(M)**	**(M)**
pH[a]	8.37	7.69	8.89	1.22	9.65	9.16
Na^+	1.00×10^{-2}	2.50×10^{-2}	6.70×10^{-5}	6.70×10^{-5}	9.30×10^{-5}	1.24×10^{-4}
K^+	3.78×10^{-3}	1.09×10^{-2}	2.50×10^{-4}	2.96×10^{-4}	5.90×10^{-5}	1.87×10^{-4}
Mg^{2+}	3.85×10^{-4}	1.05×10^{-2}	2.19×10^{-3}	1.06×10^{-2}	8.05×10^{-3}	5.30×10^{-2}
Ca^{2+}	1.71×10^{-3}	2.8×10^{-2}	7.70×10^{-5}	1.80×10^{-3}	5.70×10^{-5}	4.00×10^{-4}
Fe^{2+}	1.00×10^{-20}	1.00×10^{-20}	1.00×10^{-20}	1.00×10^{-20}	1.00×10^{-20}	1.00×10^{-20}
Fe^{3+}	6.00×10^{-6}	6.00×10^{-6}	6.00×10^{-6}	5.80×10^{-4}	6.00×10^{-6}	1.50×10^{-6}
Al^{3+}	1.00×10^{-17}	1.00×10^{-17}	1.00×10^{-17}	8.50×10^{-5}	1.00×10^{-17}	1.00×10^{-17}
H_4SiO_4	6.68×10^{-4}	1.19×10^{-3}	2.64×10^{-4}	2.00×10^{-3}	8.80×10^{-5}	1.06×10^{-4}
NO_3^-	5.15×10^{-4}	6.00×10^{-4}	9.00×10^{-6}	9.00×10^{-10}	3.50×10^{-5}	3.68×10^{-5}
SO_4^{2-}	3.90×10^{-4}	5.57×10^{-4}	5.40×10^{-5}	1.00×10^{-3}	1.60×10^{-4}	3.80×10^{-4}
Cl^-	1.33×10^{-3}	9.77×10^{-2}	3.64×10^{-4}	9.20×10^{-2}	2.47×10^{-4}	7.6×10^{-2}

[a] Unitless

Appendix Table A3.5 Leachate chemistry of replicate columns.

Sample name	Day	pH (GK)	Mg (GK)	Ca (GK)	pH (RRP1)	Mg (RRP1)	Ca (RRP1)	pH (RRP2)	Mg (RRP2)	Ca (RRP2)
Variable			(ppm)	(ppm)		(ppm)	(ppm)		(ppm)	(ppm)
Milli-Q 1	2	8.37	9.368	68.67	8.89	53.30	3.093	9.65	195.8	2.284
Milli-Q 1	4	8.84	0.949	6.647	8.57	34.52	2.357	9.75	120.5	1.856
Milli-Q 1	6	9.02	0.577	4.082	8.69	32.07	2.275	9.75	57.54	1.368
Milli-Q 1	8	9.12	0.443	3.406	8.63	31.61	2.368	9.60	26.20	0.812
Milli-Q 1	12	9.08	0.341	2.969	8.43	18.46	2.188	9.77	48.34	1.434
Milli-Q 1	16	9.30	0.493	4.028	8.23	19.01	2.658	9.84	33.52	1.548
Milli-Q 1	20	9.25	0.560	4.380	8.06	12.55	2.248	9.98	30.36	1.095
Milli-Q 1	24	8.97	0.576	4.962	8.15	14.46	2.747	9.70	17.42	0.657
Milli-Q 1	28	8.66	0.488	4.875	8.25	15.20	3.421	9.74	49.27	1.222
Milli-Q 2	2	8.39	8.688	66.51	8.96	53.34	2.671	9.73	88.20	1.440
Milli-Q 2	4	8.85	0.928	7.153	8.56	32.13	1.980	9.75	83.77	1.285
Milli-Q 2	6	9.02	0.542	4.298	8.65	30.15	2.180	9.74	59.40	1.096
Milli-Q 2	8	9.06	0.401	3.496	8.64	24.35	2.091	9.74	48.79	1.005
Milli-Q 2	12	9.20	0.338	3.383	8.52	24.21	2.789	9.85	40.11	3.721
Milli-Q 2	16	9.29	0.450	3.935	8.31	21.32	2.782	9.90	28.23	1.595
Milli-Q 2	20	9.17	0.475	4.570	8.23	16.22	21.08	10.02	29.75	0.923
Milli-Q 2	24	9.11	0.504	5.019	8.26	17.79	3.075	9.67	26.01	0.816
Milli-Q 2	28	8.88	0.512	5.923	8.32	14.50	3.194	9.54	26.25	0.812
HCl 1	2	7.69	254.6	1120	1.22	257.0	72.37	9.16	1290	16.12
HCl 1	4	7.73	521.9	1087	1.17	299.9	59.56	8.78	1289	25.44
HCl 1	6	7.78	676.6	881.5	1.18	389.3	58.30	8.98	1380	23.05
HCl 1	8	7.66	835.0	787.5	1.21	427.9	44.73	8.95	1367	22.98
HCl 1	12	7.90	991.8	581.2	1.40	791.1	47.49	8.78	1478	21.11
HCl 1	16	7.63	1215	498.8	0.87	1027	49.35	1.21	1124	20.32
HCl 1	20	7.47	1169	485.2	0.69	857.9	38.85	0.91	1078	17.64
HCl 1	24	7.50	1110	544.2	0.55	687.6	27.90	0.66	926.8	12.58
HCl 1	28	7.68	1157	487.8	1.45	934.9	40.43	1.32	714.2	8.693
HCl 2	2	7.63	293.2	1096	1.30	412.2	106.4	9.13	1304	16.87
HCl 2	4	7.65	577.3	1052	1.33	575.8	105.9	9.08	1381	23.56
HCl 2	6	7.74	760.5	756.8	1.32	647.4	76.60	8.84	1337	27.92
HCl 2	8	7.80	911.1	641.7	1.41	749.4	62.20	2.68	1160	24.70
HCl 2	12	7.73	1026	539.2	1.58	1028	60.98	1.94	1106	17.55
HCl 2	16	7.50	1130	524.7	2.03	1438	72.85	8.18	1648	19.71
HCl 2	20	7.32	1123	460.9	1.09	1188	47.74	7.76	1544	16.37
HCl 2	24	7.45	1113	503.4	1.00	1164	54.03	8.09	1464	18.03
HCl 2	28	7.37	1196	461.0	1.83	1193	51.72	8.09	1508	15.40

Appendix Table A3.6 Rietveld refinement results (wt.%) for the initial processed kimberlites, serpentine rock samples and the leached processed kimberlite and serpentine columns at different depths.

Sample name	**Residue position**	**Calcite**	**Brucite**	**Magnetite**	**Forsterite**	**Augite**	**Tremolite**	**Orthoclase**	**Albite**	**Quartz**	**Phlogopite**	**Clinochlore**	**Talc**	**Lizardite**	**Saponite**	**Total wt.%**	**R_{wp}^* (%)**
GK initial	–	1.4	–	1.6	7.0	4.3	3.3	8.6	7.8	3.7	8.5	10.4	4.1	26.2	13.2	100.0	9.1
GK (Milli-Q)	top	1.8	–	1.5	7.8	5.7	1.5	9.0	7.3	3.9	9.2	5.6	7.8	26.8	12.2	100.0	9.7
GK (Milli-Q)	middle	1.5	–	1.7	8.2	5.5	1.5	7.2	6.7	3.3	10.4	5.7	3.1	30.4	14.9	100.0	10.7
GK (Milli-Q)	bottom	1.6	–	1.4	7.1	7.3	2.2	6.2	7.0	3.3	9.4	6.1	6.7	27.7	14.2	100.0	9.7
GK (HCl)	top	1.0	–	1.7	7.3	5.4	1.0	6.5	8.6	5.5	9.4	5.3	6.4	23.8	18.2	100.0	10.8
GK (HCl)	middle	0.9	–	2.1	7.4	4.0	2.1	7.8	7.5	3.1	10.2	6.2	3.0	30.6	15.3	100.0	11.4
GK (HCl)	bottom	1.5	–	1.8	7.3	6.3	1.7	8.7	7.1	4.4	10.0	5.7	6.7	27.7	11.1	100.0	9.0
RRP1 initial	–	–	0.7	4.7	34.8	–	1.5	–	–	–	–	13.2	11.3	33.8	–	100.0	10.0
RRP1 (Milli-Q)	top	–	1.0	5.3	35.0	–	1.0	–	–	–	–	14.8	10.8	32.1	–	100.0	10.0
RRP1 (Milli-Q)	middle	–	1.0	5.5	35.8	–	1.0	–	–	–	–	15.7	9.5	31.6	–	100.0	10.0
RRP1 (Milli-Q)	bottom	–	0.8	5.1	36.2	–	0.6	–	–	–	–	14.9	10.3	32.0	–	100.0	9.3
RRP1 (HCl)	top	–	0.8	5.0	35.1	–	0.4	–	–	–	–	14.7	11.4	32.7	–	100.0	9.9
RRP1 (HCl)	middle	–	0.9	4.8	35.3	–	1.0	–	–	–	–	14.9	11.2	31.9	–	100.0	9.8
RRP1 (HCl)	bottom	–	0.7	5.0	35.6	–	1.0	–	–	–	–	15.3	11.0	31.4	–	100.0	9.3
RRP2 initial	–	–	3.7	5.8	8.2	–	–	–	–	–	–	12.3	5.9	64.1	–	100.0	10.0
RRP2 (Milli-Q)	top	–	3.1	6.1	8.1	–	–	–	–	–	–	13.4	5.8	63.5	–	100.0	8.8
RRP2 (Milli-Q)	middle	–	3.7	6.0	8.5	–	–	–	–	–	–	12.5	6.0	63.4	–	100.0	8.8
RRP2 (Milli-Q)	bottom	–	3.6	5.9	8.9	–	–	–	–	–	–	13.0	6.0	62.5	–	100.0	8.9
RRP2 (HCl)	top	–	5.4	5.8	8.3	–	–	–	–	–	–	10.6	6.9	63.0	–	100.0	8.6

*R_{wp}: the weighted pattern index, a function of the least-squares residual.

Appendix Table A3.6 (continued) Rietveld refinement results (wt.%) for the initial processed kimberlites, serpentine rock samples and the leached processed kimberlite and serpentine columns at different depths.

Sample name	Residue position	Calcite	Brucite	Magnetite	Forsterite	Augite	Tremolite	Orthoclase	Albite	Quartz	Phlogopite	Clinochlore	Talc	Lizardite	Saponite	Total wt.%	R_{wp}* (%)
RRP2 (HCl)	middle1	–	2.8	6.3	8.6	–	–	–	–	–	–	13.0	6.4	62.8	–	100.0	8.7
RRP2 (HCl)	middle2	–	2.6	5.9	8.8	–	–	–	–	–	–	11.9	6.4	64.4	–	100.0	9.0
RRP2 (HCl)	middle3	–	2.8	6.2	8.0	–	–	–	–	–	–	13.6	6.0	63.5	–	100.0	8.8
RRP2 (HCl)	bottom	–	2.0	6.3	9.0	–	–	–	–	–	–	13.5	6.3	62.9	–	100.0	9.1

*R_{wp}: the weighted pattern index, a function of the least-squares residual.

Appendix Table A3.7 Oxide and elemental abundances for column samples collected at different depths determined using XRF (oxides), ICP-AES (most elements), and combustion analysis (for C and S).

Sample name	Residue position	Al_2O_3	CaO	Cr_2O_3	Fe_2O_3	K_2O	MgO	Na_2O	SiO_2	TiO_2	Ni	Fe	Ca	Mg	C	S
UNITS	–	%	%	%	%	%	%	%	%	%	ppm	%	%	%	%	%
GK initial	–	6.19	4.31	0.17	6.63	2.40	23.64	1.13	46.07	0.55	1004	4.51	2.7	13.74	0.159	0.017
GK (Milli-Q)	top	6.35	4.03	0.16	6.38	2.46	23.19	1.05	46.42	0.52	1055	4.49	2.8	13.86	0.197	0.030
GK (Milli-Q)	middle	6.20	4.60	0.17	6.54	2.33	23.4	1.15	45.69	0.55	988	4.49	3.2	13.72	0.160	0.023
GK (Milli-Q)	bottom	5.72	4.49	0.18	6.71	2.33	24.18	0.97	44.94	0.57	1061	4.59	3.1	14.20	0.177	0.024
GK (HCl)	top	6.34	3.39	0.17	6.55	2.40	21.65	1.05	47.56	0.58	909	4.52	2.4	12.71	0.061	0.029
GK (HCl)	middle	6.54	5.01	0.16	6.55	2.41	22.93	1.11	45.22	0.55	1021	4.58	3.5	13.52	0.109	0.035
GK (HCl)	bottom	6.22	4.03	0.17	6.57	2.38	23.25	1.07	46.07	0.54	1026	4.59	2.8	13.80	0.171	0.031
RRP1 initial	–	1.11	0.35	0.39	7.71	0.03	40.66	0.03	43.13	0.03	2038	5.22	0.3	24.43	0.165	0.103
RRP1 (Milli-Q)	top	1.10	0.24	0.36	7.66	0.03	40.56	0.03	43.18	0.02	2027	5.22	0.2	24.20	0.173	0.097
RRP1 (Milli-Q)	middle	1.10	0.24	0.37	7.68	0.03	40.76	0.04	43.02	0.03	2087	5.28	0.2	24.44	0.135	0.101
RRP1 (Milli-Q)	bottom	1.08	0.28	0.35	7.62	0.03	40.81	0.03	43.24	0.02	2052	5.27	0.3	24.50	0.145	0.101
RRP1 (HCl)	top	1.11	0.17	0.36	7.69	0.03	40.08	0.02	43.60	0.03	1954	5.32	0.2	24.21	0.123	0.100
RRP1 (HCl)	middle	1.07	0.24	0.32	7.63	0.03	40.77	0.03	43.45	0.02	2054	5.25	0.3	24.46	0.139	0.100
RRP1 (HCl)	bottom	1.08	0.21	0.35	7.69	0.03	40.76	0.03	43.29	0.02	2085	5.29	0.3	24.60	0.138	0.102
RRP2 initial	–	0.25	0.07	0.32	7.89	<0.01	40.14	0.02	39.11	<0.01	2028	5.41	0.1	24.04	0.123	0.076
RRP2 (Milli-Q)	top	0.31	0.07	0.49	8.01	<0.01	39.82	0.03	38.68	<0.01	2048	5.32	0.1	23.96	0.190	0.078
RRP2 (Milli-Q)	middle	0.28	0.07	0.46	7.87	<0.01	40.08	0.02	38.96	<0.01	2068	5.38	0.1	23.87	0.132	0.078
RRP2 (Milli-Q)	bottom	0.28	0.07	0.39	7.86	<0.01	40.00	0.02	39.09	<0.01	2074	5.55	0.1	23.91	0.127	0.079
RRP2 (HCl)	top	–	–	–	–	–	–	–	–	–	–	–	–	–	–	–
RRP2 (HCl)	middle1	0.30	0.06	0.48	7.96	<0.01	39.66	0.02	39.33	0.01	2038	5.48	0.1	23.75	0.133	0.082
RRP2 (HCl)	middle2	0.28	0.06	0.46	7.85	<0.01	39.72	0.02	39.32	0.01	2038	5.46	0.1	23.25	0.157	0.082
RRP2 (HCl)	middle3	0.28	0.06	0.36	7.96	<0.01	39.59	0.02	39.41	<0.01	1991	5.45	0.2	23.62	0.118	0.083
RRP2 (HCl)	bottom	0.28	0.04	0.41	8.06	<0.01	38.58	0.02	39.98	<0.01	1939	5.36	0.1	23.39	0.053	0.079

Appendix Table A3.8 Extraction of Ca in each leachate based on average values of ICP-MS data from replicate columns.

	GK (Milli-Q)	GK (HCl)	RRP1 (Milli-Q)	RRP1 (HCl)	RRP2 (Milli-Q)	RRP2 (HCl)
Day 2 (ppm)	67.59	1108	2.882	89.41	1.862	16.49
Day 4 (ppm)	6.900	1070	2.169	82.73	1.571	24.50
Day 6 (ppm)	4.190	819.2	2.228	67.45	1.232	25.48
Day 8 (ppm)	3.451	714.6	2.230	53.46	0.909	23.84
Day 12 (ppm)	3.176	560.2	2.489	54.24	2.578	19.33
Day 16 (ppm)	3.982	511.7	2.720	61.10	1.572	20.01
Day 20 (ppm)	4.475	473.1	11.66	43.30	1.009	17.00
Day 24 (ppm)	4.991	524.0	2.911	40.96	0.737	15.30
Day 28 (ppm)	5.399	474.4	3.308	46.08	1.017	12.05
Average concentration (ppm)	11.57	695.0	3.622	59.86	1.387	19.33
Volume of leachate (mL/day)	16.6	16.6	16.6	16.6	16.6	16.6
Total Ca in all leachates (μg)	5186.8	311500	1623	26828	621.7	8668
Total Ca in initial residues (g)	2.17	2.17	0.24	0.24	0.08	0.08
Total Ca extraction (%)	0.2	14.3	0.7	11.1	0.8	10.8

Appendix Table A3.9 Extraction of Mg in each leachate based on average values of ICP-MS data from replicate columns.

	GK (Milli-Q)	GK (HCl)	RRP1 (Milli-Q)	RRP1 (HCl)	RRP2 (Milli-Q)	RRP2 (HCl)
Day 2 (ppm)	9.028	273.9	53.32	334.6	142.0	1297
Day 4 (ppm)	0.939	549.6	33.33	437.8	102.1	1335
Day 6 (ppm)	0.560	718.5	31.11	518.3	58.47	1359
Day 8 (ppm)	0.422	873.1	27.98	588.6	37.50	1264
Day 12 (ppm)	0.340	1009	21.34	909.4	44.22	1292
Day 16 (ppm)	0.472	1173	20.16	1232	30.88	1386
Day 20 (ppm)	0.518	1147	14.38	1023	30.06	1311
Day 24 (ppm)	0.540	1112	16.12	925.9	21.72	1195
Day 28 (ppm)	0.500	1176	14.85	1064	37.76	1111
Average concentration (ppm)	1.480	892.2	25.84	781.5	56.08	1283
Volume of leachate (mL/day)	16.6	16.6	16.6	16.6	16.6	16.6
Total Mg in all leachates (μg)	663.2	399901	11583	350255	25135	575238
Total Mg in initial residues (g)	11.06	11.06	19.67	19.7	19.35	19.35
Total Mg extraction (%)	0.0	3.6	0.1	1.8	0.1	3.0

Appendix Table A3.10 Proportions of Ca from calcite and silicate dissolution in leachates for each GK column reactor. The negative value corresponds to calcite enrichment in the column.

Sample	Ca from calcite dissolution (mg)	Total Ca in leachates (mg)	Proportion of Ca from calcite dissolution in leachates (%)	Proportion of Ca from silicates dissolution in leachates (%)
GK (Milli-Q)	-77.75	5.19	/	/
GK (HCl)	92.69	311.5	29.8	70.2

Appendix Table A3.11 CO_2 offset potential of leached Mg based on Gahcho Kué mine data from 2017.

Sample	Proportion of total Mg extracted (%)	Mass fraction of Mg in sample (%)	Hydromagnesite equivalent (%)	CO_2 in hydromagnesite (%)	Gahcho Kué ore treated (t/year)	Maxmium offset potential of Mg (t CO_2/year)	Gahcho Kué CO_2 emissions (t/year)	Proportion of Venetia CO_2 emissions (%)
Initial residues	–	13.74	52.87	19.90	910000	181080	84000	215.6
Milli-Q-leachates	0.00	0.00	0.00	0.00	910000	10.86	84000	0.0
HCl-leachates	3.62	0.50	1.91	0.72	910000	6547	84000	7.8

Appendix Table A3.12 Predicted CO_2 emissions from calcite dissolution based on Gahcho Kué mine data from 2017.

Sample	Proportion of calcite dissolved (%)	Mass fraction of Ca in calcite (%)	Calcite equivalent (%)	CO_2 in calcite (%)	Gahcho Kué ore treated (t/year)	Calculated emissions from calcite dissolution (Mt CO_2/year)	Gahcho Kué CO_2 emissions (Mt/year)	Proportional increase in potential emissions at Venetia if calcite were dissolved (%)
Initial residues	–	0.56	1.40	0.62	910000	5602	84000	6.7
Milli-Q-leachates	–	–	–	–	910000	–	84000	–
HCl-leachates	20.54	0.12	0.29	0.13	910000	1151	84000	1.4

Appendix Table A3.13 CO_2 offset potential of leached Ca from silicates dissolution based on Gahcho Kué mine data from 2017.

Sample	Mass fraction of Ca in calcite (%)	Mass fraction of Ca in silicates (%)	Proportional increase in potential emissions at Venetia if calcite were dissolved (%)	Proportion of Venetia CO_2 emissions offset potential by Ca from silicate dissolution (%)
Initial residues	0.56	2.14	6.7	25.5
Milli-Q-leachates	–	–	–	–
HCl-leachates	29.76	70.24	1.4	3.2

Appendix Table A3.14 CO_2 offset potential of leached Mg (g CO_2/kg) for Venetia processed kimberlite, GK processed kimberlite, RRP dunite samples and Woodsreef chrysotile mine tailings (WR).

Sample	Proportion of total Mg extracted (%)	Mass fraction of Mg in sample (%)	Hydromagnesite equivalent (%)	CO_2 in hydromagnesite (%)	ore treated (1 kg)	Offset potential of Mg (g CO_2/kg)
Venetia-0.12 M	3.36	0.30	1.16	0.44	1000	4.4
Venetia-0.16 M	5.39	0.48	1.86	0.70	1000	7.0
GK-0.12 M	3.62	0.50	1.91	0.72	1000	7.2
RRP1-0.12 M	1.78	0.44	1.67	0.63	1000	6.3
RRP2-0.12 M	2.97	0.71	2.75	1.03	1000	10.3
WR-0.16 N	8.40	2.00	7.70	2.90	1000	29.0

Appendix Table A3.15 Predicted CO_2 emissions from calcite dissolution (g CO_2/kg) for Venetia processed kimberlite and GK processed kimberlite.

Sample	Proportion of calcite dissolved (%)	Mass fraction of Ca in calcite (%)	Calcite equivalent (%)	CO_2 in calcite (%)	ore treated (1 kg)	Calculated emissions from calcite dissolution (g CO_2/kg)
Venetia-0.12 M	25.07	0.42	1.05	0.46	1000	4.6
Venetia-0.16 M	34.22	0.58	1.44	0.63	1000	6.3
GK-0.12 M	20.54	0.12	0.29	0.13	1000	1.3

Appendix Table A3.16 CO_2 offset potential of leached Ca from silicates dissolution (g CO_2/kg) for Venetia processed kimberlite and GK processed kimberlite.

Sample	Mass fraction of Ca in calcite (%)	Mass fraction of Ca in silicates (%)	Proportional increase in potential emissions if calcite were dissolved (g CO_2/kg)	Proportion of CO_2 emissions offset potential by Ca from silicate dissolution (g CO_2/kg)
Venetia-0.12 M	65.38	34.62	4.6	2.5
Venetia-0.16 M	63.89	36.11	6.3	3.6
GK-0.12 M	29.76	70.24	1.3	3.0

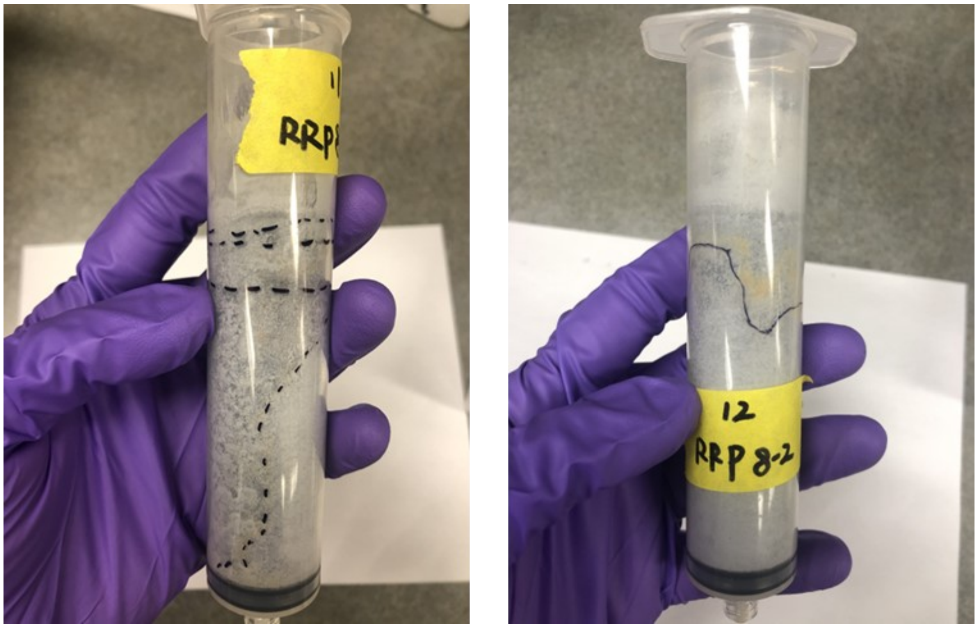

Appendix Figure A3.1 Pictures of replicate acid-leached RRP2 columns. Sidewall flow path was shown in the first column and a noticeable difference in packing material density on either side of a defined dashed line.

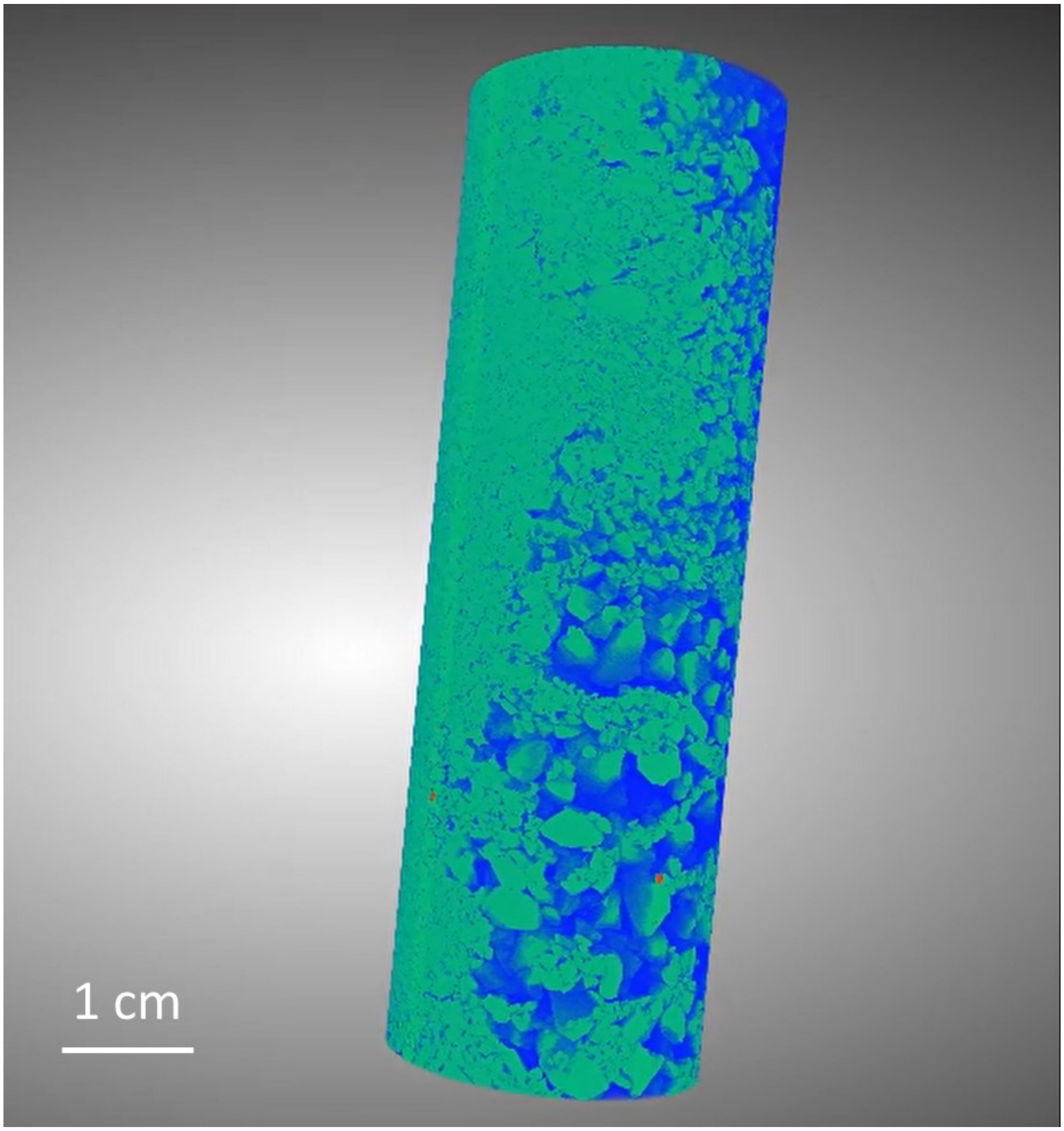

Appendix Figure A3.2 Sidewall flow path shown in the first acid-treated RRP2 column by MicroCT scanning.

Appendix Video A3.1:

https://drive.google.com/drive/folders/19qRW__XZTm4CxTLvjjFYYeDyLmheLalS

Through this technique, various color representations were employed: green symbolizing particle distribution, red signifying dense materials like oxides and sulfides, and blue indicating pore distribution. This analysis confirmed the presence of spatial heterogeneity and indicated where sidewall flow was most likely to occur on one side of the column.

A4 Appendix to Chapter 5

Appendix Table A4.1 Constituents of BG 11 medium used for cultivating microbial mats.

Reagent name	**Concentration (g/L)**
$NaNO_3$	1.5
K_2HPO_4	0.2
$MgSO_4 \cdot 7H_2O$	0.075
$CaCl_2 \cdot 2H_2O$	0.036
Citric acid	0.006
Ferric ammonium citrate	0.006
EDTA (disodium salt)	0.001
Na_2CO_3	0.02
Trace metal mix A5	1.0

Appendix Table A4.2 Aqueous chemistry of the samples collected from the eight carbonation reactors throughout one year. Day 0 corresponds to the first treatment. LOD stands for limit of detection.

Sample name	Day	pH	Na/ppm	K/ppm	Mg/ppm	Ca/ppm	Si/ppm	DIC/ppm	Mg (meq/L)/ Ca (meq/L)
NH_4OAc (BIO)	-8	8.35	327.8	8390.6	124.9	183.9	13.18		1.12
NH_4OAc (BIO)	-3	6.92	306.0	8274.6	123.9	178.5	10.42		1.14
NH_4OAc (BIO)	-0.5	8.23	394.0	8602.7	139.7	216.8	11.34		1.06
NH_4OAc (BIO)	0	7.8	846.2	7868.1	161.9	473.4	11.63		0.56
NH_4OAc (BIO)	11	8.89	1003.2	6788.7	105.7	6.9	12.23		25.35
NH_4OAc (BIO)	19	8.64	736.8	4925.9	87.5	12.4	9.05		11.61
NH_4OAc (BIO)	26	6.51	751.4	4867.2	110.4	67.9	13.26		2.68
NH_4OAc (BIO)	32	7.74	909.5	5857.5	116.6	36.9	12.45		5.21
NH_4OAc (BIO)	41	7.68	428.1	2607.7	72.1	53.9	7.98		2.21
NH_4OAc (BIO)	95	7.47	565.1	3514.1	104.3	130.4	14.35		1.32
NH_4OAc (BIO)	158	7.52	741.5	4646.1	144.3	298.9	20.57		0.80
NH_4OAc (BIO)	164	7.44	776.7	5633.1	162.8	331.5	20.95		0.81
NH_4OAc (BIO)	171	7.37	837.8	5998.8	176.4	374.3	22.35		0.78
NH_4OAc (BIO)	179	7.28	852.6	6360.8	177.5	422.0	23.82		0.69
NH_4OAc (BIO)	219	7.36	979.9	8,982	223.7	633.3	33.13		0.58
NH_4OAc (BIO)	234	7.16	1355.2	11,974	304.7	1,008	46.31		0.50
NH_4OAc (BIO)	276	7.8	748.1	11,263	159.9	61.47	23.68		4.29
NH_4OAc (BIO)	304	7.65	341.6	6,112	72.32	30.80	10.11		3.87
NH_4OAc (BIO)	353	8.17	153.1	2,931	29.78	14.73	4.58		3.33
NH_4OAc (BIO)	374	7.92	235.5	4,218	43.58	23.18	6.16		3.10
NH_4Cl (BIO)	-8	8.41	326.7	8439.4	132.8	184.1	12.12		1.19
NH_4Cl (BIO)	-3	6.9	131.0	5261.3	77.8	110.7	4.97	12.94	1.16
NH_4Cl (BIO)	-0.5	7.94	143.1	5638.9	83.1	110.0	5.64	11.16	1.25
NH_4Cl (BIO)	0	7.61	728.0	5083.7	116.1	373.5	6.27	13.84	0.51
NH_4Cl (BIO)	4	6.81	833.4	5838.2	135.6	416.9	7.85	13.96	0.54
NH_4Cl (BIO)	11	6.3	1025.9	4957.0	155.0	568.1	9.08	<LOD	0.45
NH_4Cl (BIO)	26	6.15	864.0	4166.4	150.9	535.1	8.89		0.46
NH_4Cl (BIO)	32	6.09	858.6	4048.5	151.2	531.1	8.83	<LOD	0.47
NH_4Cl (BIO)	41	6.66	457.4	171.3	76.8	364.8	7.59	2.25	0.35
NH_4Cl (BIO)	95	5.95	569.7	2614.2	118.4	407.9	9.15	3.24	0.48
NH_4Cl (BIO)	158	5.77	768.7	3545.5	156.9	546.5	14.04		0.47
NH_4Cl (BIO)	164	6.13	803.9	4772.0	183.6	593.9	14.35	6.02	0.51

Appendix Table A4.2 (continued) Aqueous chemistry of the samples collected from the eight carbonation reactors throughout one year. Day 0 corresponds to the first treatment. LOD stands for limit of detection.

Sample name	Day	pH	Na/ppm	K/ppm	Mg/ppm	Ca/ppm	Si/ppm	DIC/ppm	Mg (meq/L)/ Ca (meq/L)
NH_4Cl (BIO)	171	6.09	912.3	5325.4	209.9	666.3	15.23		0.52
NH_4Cl (BIO)	179	5.94	861.4	5199.7	195.2	648.2	16.31		0.50
NH_4Cl (BIO)	219	5.68	881.1	7,239	232.6	703.8	21.76	9.28	0.55
NH_4Cl (BIO)	234	5.34	1723.2	14,567	349.4	1,019	33.13	6.43	0.57
NH_4Cl (BIO)	276	4.75	353.4	5,773	94.15	248.3	10.22	4.5	0.63
NH_4Cl (BIO)	304	6.2	281.6	4,987	91.96	221.3	8.88	3.16	0.69
NH_4Cl (BIO)	353	4.33	105.0	1,997	32.94	78.32	3.35	7.02	0.69
NH_4Cl (BIO)	374	3.47	200.0	3,805	79.39	188.1	5.93	24.09	0.70
HCl (BIO)	-8	8.55	295.8	8020.9	106.8	148.7	7.95		1.18
HCl (BIO)	-3	6.91	230.1	7843.5	106.3	149.8	6.29	12.43	1.17
HCl (BIO)	-0.5	7.76	255.7	8272.4	113.4	153.3	6.78	15.62	1.22
HCl (BIO)	0	7.62	519.8	7295.4	106.8	183.6	11.25	36.23	0.96
HCl (BIO)	4	8.99	601.9	8643.7	116.1	168.6	8.23	12.41	1.14
HCl (BIO)	11	10	860.3	7186.7	113.7	273.2	0.42	13.86	0.69
HCl (BIO)	26	10.11	1443.4	425.4	256.4	874.6	13.80		0.48
HCl (BIO)	32	9.85	669.6	4972.8	173.9	551.8	<LOD	7.71	0.52
HCl (BIO)	41	7.09	406.6	2883.7	119.6	372.8	<LOD	16.79	0.53
HCl (BIO)	95	9.44	562.7	3977.7	168.5	545.3	0.39	12.46	0.51
HCl (BIO)	158	8.87	808.2	6776.6	253.2	747.7	0.20		0.56
HCl (BIO)	164	6.61	788.9	5659.7	226.4	742.2	0.09		0.50
HCl (BIO)	171	9.17	873.0	7280.0	274.7	797.2	0.17		0.57
HCl (BIO)	179	9.31	806.1	6960.1	248.8	760.1	0.18		0.54
HCl (BIO)	219	7.36	846.4	9,262	294.9	791.2	0.03	92.16	0.61
HCl (BIO)	234	7.61	1,327	13,794	455.6	1,235	0.40		0.61
HCl (BIO)	276	7.22	555.9	10,342	193.7	467.7	1.60	77.01	0.68
HCl (BIO)	304	6.73	336.3	7,100	129.5	279.6	2.54	28.11	0.76
HCl (BIO)	353	6.78	138.6	3,328	50.58	107.2	1.34	12.22	0.78
HCl (BIO)	374	6.5	316.6	6,925	146.0	242.9	2.22	32.91	0.99
H_2O (BIO)	-8	6.81	173.6	6413.9	93.4	126.4	4.06		1.22
H_2O (BIO)	-3	8.66	305.7	8396.7	122.7	166.4	6.81	13.48	1.22
H_2O (BIO)	-0.5	7.69	186.1	6884.8	99.6	136.5	4.60	15.16	1.20
H_2O (BIO)	0	8.22	210.5	6277.8	85.3	126.7	5.24	17.97	1.11
H_2O (BIO)	4	8.25	242.8	7046.2	91.8	121.2	6.00	17.49	1.25

Appendix Table A4.2 (continued) Aqueous chemistry of the samples collected from the eight carbonation reactors throughout one year. Day 0 corresponds to the first treatment. LOD stands for limit of detection.

Sample name	Day	pH	Na/ppm	K/ppm	Mg/ppm	Ca/ppm	Si/ppm	DIC/ppm	Mg (meq/L)/ Ca (meq/L)
H_2O (BIO)	11	9.29	201.6	4785.4	55.3	72.2	0.24	17.12	1.26
H_2O (BIO)	26	9.37	214.0	4781.1	53.5	73.9	<LOD	8.49	1.19
H_2O (BIO)	32	9.65	104.8	3092.6	20.3	39.9	0.22		0.84
H_2O (BIO)	41	10.2	178.0	2929.8	10.8	42.7	0.28	20.78	0.42
H_2O (BIO)	95	9.13	166.9	3093.8	22.4	46.3	<LOD	8.96	0.80
H_2O (BIO)	158	9.98	252.4	4289.2	23.0	56.5	0.24		0.67
H_2O (BIO)	164	9.45	265.3	5446.5	41.9	62.7	0.16	41.63	1.10
H_2O (BIO)	171	9.89	274.7	5591.2	42.1	61.6	<LOD		1.13
H_2O (BIO)	179	10.01	285.0	6030.6	38.3	62.9	1.10		1.01
H_2O (BIO)	219	7.88	303.7	8,648	68.86	74.85	0.31		1.52
H_2O (BIO)	234	8.87	476.9	12,701	57.21	85.58	0.69	79.6	1.10
H_2O (BIO)	276	7.27	242.3	11,270	36.91	44.61	0.94	75.07	1.36
H_2O (BIO)	304	6.77	126.7	7,388	31.98	25.68	1.00	28.41	2.05
H_2O (BIO)	353	6.78	58.18	3,315	13.27	10.31	0.30	15.02	2.12
H_2O (BIO)	374	6.69	134.8	7,930	28.04	21.41	0.14	49.36	2.16
NH_4OAc (CONTROL)	0	7.66	4383.8	1166.2	391.1	2499.6	13.62	22.4	0.26
NH_4OAc (CONTROL)	4	6.37	15937.2	4356.9	1408.6	8397.4	50.84	27.16	0.28
NH_4OAc (CONTROL)	11	6.58	1575.5	484.7	190.7	1077.3	10.51	31.26	0.29
NH_4OAc (CONTROL)	26	8.06	1841.3	565.9	243.9	1360.5	15.03		0.30
NH_4OAc (CONTROL)	32	6.63	1340.5	389.1	202.4	1099.6	15.64	26.11	0.30
NH_4OAc (CONTROL)	41	6.51	771.1	240.8	137.2	684.8	12.20	22.3	0.33
NH_4OAc (CONTROL)	95	6.78	573.0	178.7	92.3	464.0	7.47	21.99	0.33
NH_4OAc (CONTROL)	158	6.57	990.7	317.1	169.0	874.0	17.64		0.32
NH_4OAc (CONTROL)	164	6.64	1088.4	330.4	189.1	941.7	17.51	43.92	0.33
NH_4OAc (CONTROL)	171	6.64	1084.3	329.3	184.3	964.1	19.05		0.32
NH_4OAc (CONTROL)	179	6.62	945.6	298.9	162.8	850.1	16.91		0.32
NH_4OAc (CONTROL)	219	6.49	981.5	299.10	166.3	864.9	20.90	10.69	0.32
NH_4OAc (CONTROL)	234	6.41	1,354	427.1	230.5	1,210	30.13	18.13	0.31
NH_4OAc (CONTROL)	276	6.29	692.0	229.4	109.4	558.4	15.18	10.37	0.32
NH_4OAc (CONTROL)	304	6.21	415.1	137.6	69.45	347.1	9.38	3.55	0.33
NH_4OAc (CONTROL)	374	6.23	509.3	160.7	108.0	542.9	10.75	25.17	0.33

Appendix Table A4.2 (continued) Aqueous chemistry of the samples collected from the eight carbonation reactors throughout one year. Day 0 corresponds to the first treatment. LOD stands for limit of detection.

Sample name	Day	pH	Na/ppm	K/ppm	Mg/ppm	Ca/ppm	Si/ppm	DIC/ppm	Mg (meq/L)/ Ca (meq/L)
NH_4Cl (CONTROL)	0	7.45	4621.8	1274.5	367.0	2162.5	10.64	13.62	0.28
NH_4Cl (CONTROL)	4	4.68	8750.6	2356.9	682.3	4110.2	21.00	8.86	0.27
NH_4Cl (CONTROL)	11	4.83	2079.7	639.7	208.4	1175.2	9.85	10.24	0.29
NH_4Cl (CONTROL)	26	5.28	1910.5	584.3	229.7	1227.7	12.04		0.31
NH_4Cl (CONTROL)	32	6.53	1049.0	316.4	163.9	799.2	13.01	7.04	0.34
NH_4Cl (CONTROL)	41	6.13	408.2	1901.3	77.8	261.1	5.57	9.23	0.49
NH_4Cl (CONTROL)	95	5.25	560.7	194.2	108.0	487.5	9.77	5.54	0.37
NH_4Cl (CONTROL)	158	5.22	781.1	291.5	145.0	668.1	14.92		0.36
NH_4Cl (CONTROL)	164	5.34	817.0	294.9	154.1	689.7	15.39	15.14	0.37
NH_4Cl (CONTROL)	171	5.23	882.8	333.0	166.7	743.9	15.97		0.37
NH_4Cl (CONTROL)	179	5.32	801.0	276.6	150.1	704.6	16.06		0.35
NH_4Cl (CONTROL)	219	4.93	863.4	290.1	159.0	741.2	20.63	10.69	0.35
NH_4Cl (CONTROL)	234	4.36	1,646	456.0	232.2	1,072	27.53	18.13	0.36
NH_4Cl (CONTROL)	276	5.09	575.7	229.2	95.89	441.3	13.18	10.37	0.36
NH_4Cl (CONTROL)	304	4.54	338.1	124.7	61.18	279.8	7.91	3.55	0.36
NH_4Cl (CONTROL)	353	5.32	134.8	7,930	28.04	21.41	0.14	7.31	2.16
NH_4Cl (CONTROL)	374	4.9	362.7	145.6	84.96	394.0	8.41	25.17	0.36
HCl (CONTROL)	0	7.41	2258.1	458.0	107.2	411.0	39.94	158.66	0.43
HCl (CONTROL)	4	7.91	7626.8	1518.2	344.4	573.6	121.37	22.47	0.99
HCl (CONTROL)	11	8.49	1957.6	400.4	142.3	337.5	38.64	21.99	0.70
HCl (CONTROL)	26	8.11	808.3	6609.0	116.1	323.9	<LOD		0.59
HCl (CONTROL)	32	8.84	1301.6	413.9	231.9	884.5	1.67	4.51	0.43
HCl (CONTROL)	41	7.21	557.2	258.7	221.6	746.8	11.23	16.99	0.49
HCl (CONTROL)	95	8.3	336.5	188.2	185.7	647.5	7.39		0.47
HCl (CONTROL)	158	8.46	673.1	382.4	358.3	1315.3	13.49		0.45
HCl (CONTROL)	164	8.33	716.3	395.3	385.8	1356.2	12.90	11.98	0.47
HCl (CONTROL)	171	8.51	722.8	393.3	379.2	1400.6	13.54		0.45
HCl (CONTROL)	179	8.54	658.7	414.7	349.3	1270.8	11.84		0.45
HCl (CONTROL)	219	7.24	736.4	406.0	370.1	1,401	7.74		0.44
HCl (CONTROL)	234	7.16	1,179	662.3	585.9	2,273	8.01		0.43
HCl (CONTROL)	276	7.26	614.1	348.3	294.7	1,143	6.75		0.43
HCl (CONTROL)	304	6.86	566.5	327.5	263.5	1,033	5.57	12.73	0.42
HCl (CONTROL)	353	6.96	354.9	203.2	164.5	656.0	3.57		0.41
HCl (CONTROL)	374	6.63	397.2	228.6	250.0	987.8	4.54		0.42

Appendix Table A4.2 (continued) Aqueous chemistry of the samples collected from the eight carbonation reactors throughout one year. Day 0 corresponds to the first treatment. LOD stands for limit of detection.

Sample name	Day	pH	Na/ppm	K/ppm	Mg/ppm	Ca/ppm	Si/ppm	DIC/ppm	Mg (meq/L)/ Ca (meq/L)
H_2O (CONTROL)	0	9.42	250.1	54.4	5.6	2.0	16.52		4.64
H_2O (CONTROL)	4	8.95	406.1	64.9	2.2	5.3	13.06		0.69
H_2O (CONTROL)	11	9.33	271.8	46.5	1.3	5.4	11.51		0.41
H_2O (CONTROL)	19	8.9	156.6	63.6	2.0	7.2	6.53		0.45
H_2O (CONTROL)	28	8.81	181.0	38.7	2.0	8.8	11.54		0.38
H_2O (CONTROL)	32	8.33	222.5	45.9	2.0	8.9	13.17		0.38
H_2O (CONTROL)	41	9.07	150.9	31.0	1.2	5.0	10.07		0.39
H_2O (CONTROL)	158	8.68	244.5	83.6	1.9	6.5	15.47		0.47
H_2O (CONTROL)	164	8.82	261.6	53.0	1.9	6.3	16.20		0.50
H_2O (CONTROL)	171	8.94	298.7	72.1	2.0	5.6	17.96		0.59
H_2O (CONTROL)	179	8.29	126.3	29.6	4.6	11.5	9.92		0.66
H_2O (CONTROL)	219	8.57	152.6	43.96	4.899	8.127	6.81		0.99
H_2O (CONTROL)	234	8.78	220.0	57.12	5.065	5.739	10.51		1.46
H_2O (CONTROL)	276	8.62	139.5	40.28	3.509	5.197	9.87		1.11
H_2O (CONTROL)	304	8.45	160.4	47.81	3.944	5.807	11.28		1.12
H_2O (CONTROL)	353	8.1	108.1	30.66	2.169	3.163	6.74		1.13
H_2O (CONTROL)	374	7.63	101.2	28.78	2.727	3.473	5.78		1.29

Appendix Table A4.3 Oxide and elemental abundances for mine residue samples, collected at different depths in the IBC at the end of the experiment, determined using XRF (oxides), ICP-AES (most elements), and combustion analysis (for C). DVK-CRD1, DVK-CRD2 and DVK-CRD3 correspond to the triplicate initial processed kimberlite collected before the experiment.

	Al_2O_3	Cr_2O_3	Fe_2O_3	K_2O	Na_2O	SiO_2	TiO_2	Fe	Ca	Mg	Co	Cu	Ni	Si	C
UNITS	%	%	%	%	%	%	%	%	%	%	ppm	ppm	ppm	%	%
DVK-CRD1	5.45		7.90	1.92	0.98	39.49	0.84	5.32	5.8	12.66	62	42	839	17.1	1.128
DVK-CRD2	5.88		7.98	2.14	0.85	40.89	0.84	5.37	4.4	13.21	61	44	866	18.1	0.698
DVK-CRD3	6.37		8.41	2.01	0.95	40.77	0.94	5.34	4.3	12.25	58	71	755	17.6	0.814
H_2O Top	6.36	0.13	8.33	2.04	0.95	42.01	0.85	5.61	4.5	13.03	57	115	927	19.2	0.896
H_2OF1	6.58	0.14	8.29	2.08	0.96	43.13	0.85	5.29	4.1	12.83	55	53	879	20.1	0.719
H_2OF2	5.53	0.14	7.97	2.00	0.90	40.31	0.91	5.32	5.1	13.4.	57	63	918	18.8	0.662
H_2OF3	6.46	0.12	8.36	2.08	1.06	42.30	0.87	5.67	5.0	12.73	56	56	865	19.1	0.897
H_2OL1	5.96	0.14	8.20	1.97	0.84	41.83	0.91	5.27	4.8	12.87	57	57	913	19.5	0.852
H_2OL2	6.62	0.14	8.18	2.13	1.02	42.49	0.85	5.56	4.8	12.96	54	60	886	19.9	0.850
H_2OL3	6.58	0.12	8.40	2.01	1.07	42.31	0.87	5.64	5.0	13.00	56	63	873	19.2	0.831
H_2OL4	6.38	0.14	8.19	1.93	0.95	41.94	0.8	5.54	4.8	13.15	57	72	897	18.9	0.709
H_2OR1	5.82	0.14	8.24	1.94	0.85	41.92	0.95	5.70	4.5	14.04	62	156	929	19.6	0.804
H_2OR2	5.98	0.13	7.97	1.99	1.00	42.98	0.88	5.32	4.4	13.61	64	55	990	19.9	0.853
H_2OR3	6.81	0.12	8.01	1.98	1.50	42.92	0.94	5.45	5.5	12.49	55	46	831	19.4	0.914
H_2OR4	6.57	0.13	8.04	2.11	1.07	42.15	0.91	5.36	5.2	13.28	54	64	795	18.9	1.023
HCl Top	6.95	0.13	8.32	2.13	0.99	45.78	0.98	5.50	3.2	11.80	50	51	682	21.6	0.218
HClF1	6.09	0.13	7.71	1.89	0.84	41.92	0.80	5.44	5.4	13.48	57	64	910	19.3	0.859
HClF2	6.65	0.14	8.21	2.07	0.89	42.71	0.92	5.44	5.6	12.12	52	74	754	18.2	0.747
HClF3	6.36	0.15	7.71	1.88	0.80	40.88	0.85	5.32	5.5	13.16	56	64	884	19.6	0.895
HClL1	6.60	0.13	8.85	2.01	0.75	44.89	0.99	6.2.	4.2	12.55	55	44	788	20.3	0.285
HClL2	6.66	0.15	8.17	2.00	0.80	42.78	0.85	5.56	4.4	13.19	57	66	828	19.6	0.529

Appendix Table A4.3 (continued) Oxide and elemental abundances for mine residue samples, collected at different depths in the IBC at the end of the experiment, determined using XRF (oxides), ICP-AES (most elements), and combustion analysis (for C). DVK-CRD1, DVK-CRD2 and DVK-CRD3 correspond to the triplicate initial processed kimberlite collected before the experiment.

	Al_2O_3	Cr_2O_3	Fe_2O_3	K_2O	Na_2O	SiO_2	TiO_2	Fe	Ca	Mg	Co	Cu	Ni	Si	C
UNITS	%	%	%	%	%	%	%	%	%	%	ppm	ppm	ppm	%	%
HClL3	6.07	0.15	8.35	2.07	0.71	41.80	0.89	5.57	4.5	13.43	61	69	984	19.7	0.759
HClL4	6.49	0.15	8.29	1.87	0.81	42.08	0.84	5.86	5.0	12.97	59	376	861	19.9	0.684
HClR1	7.63	0.13	8.53	2.02	1.06	44.31	0.89	5.56	4.2	11.98	52	35	818	20.7	0.404
HClR2	6.37	0.13	8.59	1.82	0.75	41.67	0.89	5.64	4.9	12.52	56	102	845	19.2	0.856
HClR3	6.42	0.15	7.77	2.10	0.76	43.37	0.80	5.28	3.8	13.69	60	65	943	19.9	0.622
HClR4	7.26	0.13	8.86	2.12	0.78	43.02	0.86	6.00	4.2	12.32	56	106	846	20.0	0.595
NH_4Cl Top	6.69	0.12	7.61	1.95	0.94	42.25	0.78	5.14	4.9	12.73	57	72	908	18.2	0.584
NH_4ClF1	5.94	0.15	8.40	1.86	0.72	41.37	0.91	5.52	5.0	13.08	59	86	905	19.2	0.871
NH_4ClF2	6.53	0.12	8.21	2.00	0.85	42.60	0.88	5.68	4.8	13.11	57	71	861	20.4	0.777
NH_4ClF3	6.57	0.14	8.36	1.99	0.93	42.34	0.90	5.72	5.6	12.38	53	64	766	20.2	0.755
NH_4ClL1	6.21	0.13	8.21	1.89	0.78	41.13	0.85	5.24	5.6	12.79	55	55	871	19.4	1.012
NH_4ClL2	6.35	0.14	8.16	1.96	0.74	42.02	0.84	5.55	4.9	13.15	55	80	890	20.0	0.801
NH_4ClL3	6.41	0.13	8.4	1.85	0.84	42.22	0.85	5.59	5.0	12.36	55	89	835	19.9	0.843
NH_4ClL4	6.40	0.14	8.38	1.99	0.87	41.93	0.86	5.61	4.4	12.98	57	105	906	19.6	0.807
NH_4ClB1	5.95	0.17	8.00	1.97	0.77	42.18	0.87	5.51	4.6	12.9	60	52	965	19.3	0.832
NH_4ClB2	6.16	0.15	8.09	2.08	0.75	41.73	0.88	5.63	5.0	12.73	58	63	893	18.8	0.834
NH_4ClB3	6.45	0.15	8.18	1.99	0.98	43.07	0.88	5.53	4.7	12.46	57	91	929	19.1	0.693
NH_4ClB4	6.81	0.21	8.54	1.92	0.91	42.35	0.91	5.87	5.2	12.49	58	120	899	20.3	0.72

Appendix Table A4.3 (continued) Oxide and elemental abundances for mine residue samples, collected at different depths in the IBC at the end of the experiment, determined using XRF (oxides), ICP-AES (most elements), and combustion analysis (for C). DVK-CRD1, DVK-CRD2 and DVK-CRD3 correspond to the triplicate initial processed kimberlite collected before the experiment.

	Al_2O_3	Cr_2O_3	Fe_2O_3	K_2O	Na_2O	SiO_2	TiO_2	Fe	Ca	Mg	Co	Cu	Ni	Si	C
UNITS	%	%	%	%	%	%	%	%	%	%	ppm	ppm	ppm	%	%
NH_4OAc Top	6.43	0.13	8.27	2.02	0.94	41.85	0.98	5.61	4.5	12.69	58	65	874	19.2	1.478
NH_4OAcF1	6.38	0.14	8.25	2.01	0.83	42.71	0.85	5.69	4.5	12.85	59	78	956	19.2	0.739
NH_4OAcF2	6.59	0.12	8.03	1.83	0.98	43.11	0.86	5.55	5.2	12.11	57	77	865	19.8	0.953
NH_4OAcF3	6.09	0.14	8.37	1.91	0.92	41.98	0.92	5.84	5.5	12.92	57	55	921	18.5	0.914
NH_4OAcL1	6.82	0.13	8.54	1.96	0.93	43.99	0.85	5.92	4.6	12.14	59	79	827	20.0	0.662
NH_4OAcL2	6.57	0.13	8.34	1.99	0.89	42.92	0.84	5.91	5.3	12.42	54	87	855	19.6	0.837
NH_4OAcL3	6.79	0.14	8.48	2.01	0.85	42.72	0.93	5.95	5.2	12.27	60	105	876	19.5	0.817
NH_4OAcL4	6.10	0.14	8.06	1.90	0.79	41.08	0.82	5.56	5.4	12.33	59	68	899	18.2	0.925
NH_4OAcR1	6.40	0.13	8.14	2.01	0.82	42.12	0.86	5.55	5.6	12.86	61	68	925	18.5	1.04
NH_4OAcR2	5.86	0.17	8.11	1.84	0.72	41.06	0.87	5.61	5.5	12.99	59	72	962	18.6	1.115
NH_4OAcR3	6.27	0.12	8.11	2.07	0.80	41.37	0.86	5.63	5.5	12.63	58	102	904	18.5	1.083
NH_4OAcR4	6.01	0.14	8.33	1.98	0.70	41.16	0.88	5.74	5.2	13.42	60	59	980	18.8	0.94

Appendix Table A4.4 Rietveld refinement results (wt.%) for the initial processed kimberlite (DVK-CRD1) and the leached processed kimberlite collected at different depths in the IBC after the experiment.

Sample	Depth to bottom (cm)	Calcite	Hydroxylapatite	Diopside	Tremolite	Orthoclase	Albite	Quartz	Phlogopite	Clinochlore	Talc	Lizardite	Saponite	Total wt.%	R_{wp}^{*} (%)
DVK-CRD1	–	7.2	0.5	10.3	8.0	3.5	6.0	3.4	9.5	7.7	4.2	26.2	13.6	100.0	6.7
H_2O Top	top	6.4	1.1	7.2	5.8	5.6	4.9	2.4	12.6	0.8	7.1	31.1	14.8	100.0	11.8
H_2OF1	35 cm	6.3	0.9	8.5	8.7	5.7	5.1	3.4	10.6	5.3	6.5	26.5	12.9	100.1	10.5
H_2OF2	23 cm	7.0	1.5	9.1	3.8	1.9	2.7	1.5	11.3	4.5	1.0	39.6	16.2	100.0	9.0
H_2OF3	0 cm	6.7	0.7	8.4	6.3	3.5	3.0	2.1	8.5	4.8	2.3	35.6	18.2	100.0	8.6
H_2OL1	41 cm	7.0	0.5	7.8	5.8	2.8	4.9	2.5	9.2	9.3	4.8	33.0	12.3	100.0	7.5
H_2OL2	31.5 cm	6.8	0.5	7.3	6.6	4.2	4.2	3.3	10.5	10.1	5.1	30.4	11.0	100.0	7.2
H_2OL3	22 cm	7.4	1.4	11.4	5.8	3.5	5.2	2.9	12.1	9.4	4.7	27.1	9.2	100.0	9.9
H_2OL4	0 cm	5.7	0.6	8.4	5.1	2.6	3.3	2.7	8.6	7.8	4.5	29.5	21.4	100.0	8.0
H_2OR1	31.5 cm	6.9	0.4	8.4	6.9	2.4	3.2	5.0	9.0	12.0	3.9	31.2	10.7	100.0	7.4
H_2OR2	21 cm	6.7	0.5	6.7	4.5	3.7	3.8	2.8	5.7	10.8	5.7	28.1	20.9	100.0	8.7
H_2OR3	10 cm	8.4	0.5	7.6	6.2	3.9	7.7	0.4	10.1	6.0	3.3	31.5	14.4	100.0	10.5
H_2OR4	0 cm	6.9	0.3	10.6	3.5	4.3	4.4	2.5	6.8	14.0	2.7	29.5	14.4	100.0	7.5
HCl Top	top	3.0	0.5	9.7	7.9	5.7	8.0	0.7	9.9	7.4	6.8	31.8	8.7	100.0	10.1
HClF1	35 cm	7.2	0.5	8.7	7.2	3.7	3.8	0.2	10.4	11.9	4.1	32.2	10.2	100.0	8.7
HClF2	23.2 cm	6.5	0.7	10.2	5.2	3.7	4.6	0.0	10.5	11.5	5.3	27.7	14.1	100.0	9.2
HClF3	0 cm	8.4	1.1	11.4	7.2	3.5	5.0	3.5	8.1	1.1	10.2	31.8	8.9	100.0	8.5
HClL1	39 cm	2.7	0.8	10.2	7.8	5.4	4.9	3.1	7.1	5.9	4.5	30.4	17.1	100.0	8.0
HClL2	29 cm	4.9	0.5	8.7	7.0	4.1	4.1	2.9	7.7	12.2	3.9	27.9	16.1	100.0	7.6
HClL3	9.5 cm	5.9	0.5	10.0	7.4	4.4	3.1	1.9	6.9	11.2	6.3	26.7	15.7	100.0	7.3
HClL4	0 cm	5.4	0.6	10.9	5.8	3.4	2.2	2.8	4.9	11.4	4.3	27.8	20.5	100.0	7.4
HClR1	39 cm	3.7	1.0	12.8	7.3	3.2	5.8	3.7	9.9	9.4	5.5	25.9	12.0	100.0	8.8

*R_{wp}: the weighted pattern index, a function of the least-squares residual.

Appendix Table A4.4 (continued) Rietveld refinement results (wt.%) for the initial processed kimberlite (DVK-CRD1) and the leached processed kimberlite collected at different depths in the IBC after the experiment.

Sample	Depth to bottom (cm)	Calcite	Hydroxyla patite	Diopside	Tremolite	Orthoclase	Albite	Quartz	Phlogopite	Clinochlore	Talc	Lizardite	Saponite	Total wt.%	R_{wp}* (%)
HClR2	30 cm	7.2	0.9	9.0	5.0	2.9	5.0	3.4	8.9	9.4	4.7	30.4	13.2	100.0	7.8
HClR3	19.6 cm	5.8	0.4	10.3	4.5	4.0	5.7	3.9	7.9	8.7	9.1	26.7	13.1	100.0	7.7
HClR4	0 cm	5.3	0.4	10.7	3.8	4.0	4.5	3.8	10.1	9.8	4.2	29.9	13.5	100.0	7.2
NH_4Cl Top	top	5.4	0.7	9.4	6.1	3.8	5.5	0.8	12.4	10.0	5.8	33.0	7.2	100.0	10.1
NH_4ClF1	35.3 cm	7.1	1.1	6.4	5.4	3.8	3.9	2.1	11.6	3.4	3.9	36.0	15.6	100.0	9.3
NH_4ClF2	21.5 cm	6.7	0.8	7.7	5.0	4.8	3.9	2.7	13.9	4.1	3.3	32.4	14.8	100.0	9.9
NH_4ClF3	0 cm	6.6	1.2	6.9	6.9	5.7	4.2	2.8	13.1	3.5	3.3	33.9	11.9	100.0	10.5
NH_4ClL1	38.8 cm	6.9	1.2	7.3	4.7	3.5	4.2	1.6	11.2	4.1	2.3	33.3	19.6	100.0	10.1
NH_4ClL2	30.2 cm	5.5	0.7	6.2	4.3	3.3	2.6	1.6	11.3	7.2	5.0	32.2	20.2	100.0	9.7
NH_4ClL3	21.2 cm	6.1	1.3	7.1	4.9	2.9	3.2	2.2	12.9	3.7	5.0	29.5	21.3	100.0	10.9
NH_4ClL4	0 cm	5.2	0.6	6.9	5.0	2.1	4.0	2.7	13.0	7.6	4.3	33.4	15.3	100.0	10.0
NH_4ClB1	38.6 cm	6.0	1.4	6.8	3.8	3.0	4.4	2.6	12.7	2.9	2.3	37.5	16.8	100.0	10.0
NH_4ClB2	29 cm	5.7	1.5	7.5	4.1	4.1	3.8	1.6	12.6	3.3	2.8	35.7	17.4	100.0	10.2
NH_4ClB3	20 cm	5.4	0.9	7.2	4.0	2.2	4.6	2.5	15.2	2.9	4.0	35.1	16.1	100.0	11.5
NH_4ClB4	0 cm	5.8	0.8	7.8	4.7	3.0	4.5	2.1	12.7	4.7	5.8	33.2	14.9	100.0	10.2
NH_4OAc Top	top	5.0	1.2	11.2	8.0	3.2	3.7	2.3	13.0	10.3	8.2	26.0	7.9	100.0	7.7
NH_4OAcF1	35 cm	5.8	0.7	8.9	5.0	2.9	5.5	2.7	11.9	11.5	5.5	29.2	10.7	100.0	8.1
NH_4OAcF2	22 cm	6.8	0.5	9.7	6.4	4.0	6.0	2.9	10.3	11.4	5.0	25.8	11.2	100.0	7.2
NH_4OAcF3	0 cm	7.7	0.4	8.3	5.5	3.0	5.9	2.9	10.2	11.5	5.1	27.5	12.2	100.0	6.9
NH_4OAcL1	32 cm	5.1	0.6	9.2	7.2	2.3	4.6	2.8	11.4	7.3	4.6	29.8	15.1	100.0	9.0
NH_4OAcL2	22.2 cm	6.4	0.9	8.6	6.8	3.7	5.7	3.5	11.5	8.7	5.2	27.3	11.9	100.0	7.9
NH_4OAcL3	12 cm	6.3	0.6	9.1	6.8	3.3	5.0	2.6	9.2	9.6	5.1	27.9	14.5	100.0	7.6
NH_4OAcL4	0 cm	6.6	1.0	8.3	5.4	3.8	4.4	2.5	9.8	7.1	4.2	30.6	16.4	100.0	8.5

*R_{wp}: the weighted pattern index, a function of the least-squares residual.

Appendix Table A4.4 (continued) Rietveld refinement results (wt.%) for the initial processed kimberlite (DVK-CRD1) and the leached processed kimberlite collected at different depths in the IBC after the experiment.

Sample	**Depth to bottom (cm)**	**Calcite**	**Hydroxylapatite**	**Diopside**	**Tremolite**	**Orthoclase**	**Albite**	**Quartz**	**Phlogopite**	**Clinochlore**	**Talc**	**Lizardite**	**Saponite**	**Total wt.%**	**R_{wp}* (%)**
NH_4OAcR1	38.8 cm	6.6	0.7	9.9	5.4	3.4	4.2	2.2	10.4	10.7	4.4	29.4	12.8	100.0	7.6
NH_4OAcR2	30 cm	7.1	0.6	8.3	4.6	3.0	3.2	2.7	10.2	9.6	5.0	30.2	15.5	100.0	7.5
NH_4OAcR3	19.4 cm	7.8	0.7	9.4	4.8	3.2	4.1	2.3	11.7	8.7	4.9	30.8	11.7	100.0	7.7
NH_4OAcR4	0 cm	6.5	0.5	9.0	4.8	3.1	3.8	2.1	10.7	11.5	4.0	29.8	14.3	100.0	7.1

*R_{wp}: the weighted pattern index, a function of the least-squares residual.

Appendix Table A4.5 Rietveld refinement results (wt.%), calculated and measured total inorganic carbon (% w/w) for sediment samples collected at the bottom of the 8 different carbonation reactors at different times after the beginning of the experiment.

Sample	Day	Low Mg-calcite	High Mg-calcite	Protodomolite (VHMC)	Monohydrocalcite	Amorphous (organic matter)	Amorphous + smectite	Smectite	lizardite	Clinochlore	Talc	Pyrophyllite	Phlogopite	Tremolite	Quartz	Hydroxylapatite	Orthoclase	Albite	Struvite	Bassanite	Total wt.%	R_{wp}* (%)	calculated % inorganic carbon	measured % inorganic carbon
NH_4OAC Bio	116	25.0	15.1			25.9		18.8	4.6				2.4		1.0				7.2		100.0	10.5	4.8	6.62
NH_4OAC Bio	125	7.9	6.6	33.1			34.4		6.7				2.0	1.3	2.6				5.6		100.0	10.3	6.0	7.59
NH_4OAC Bio	234	9.1	5.6	18.1			38.6		9.9				2.8	1.7	4.3				9.9		100.0	9.6	4.1	4.90
NH_4OAC Bio	367	28.3	15.3			40.0		0.0	3.0				0.5		2.2				10.7		100.0	10.0	5.2	6.24
NH_4Cl Bio	125	2.5		42.1			39.7		6.4				2.2	2.3	4.8						100.0	12.3	5.8	6.93
NH_4Cl Bio	234			9.3			46.2		11.7	1.9	4.0		5.2	4.9	5.2	11.0			0.5		100.0	8.8	1.2	1.29
NH_4Cl Bio	367	0.7		3.3			38.0		7.8				3.1	2.5	6.6	17.1				20.8	100.0	7.8	0.5	0.64
NH_4Cl Control	116	2.2		36.3			37.6		12.0				2.0	3.5	5.0				1.4		100.0	12.6	5.0	5.68
NH_4Cl Control	367						61.1		4.8	3.0	3.4	3.4	1.4	0.3	17.5		1.6	3.5			100.0	7.1	0.0	
HCl Bio	116	9.4		7.2	0.8		65.6		3.1				1.4	1.6	3.2				6.4	1.4	100.0	8.3	2.2	2.84
HCl Bio	125	2.5		21.4			49.1		10.8				3.8	4.9	5.1					2.5	100.0	11.3	3.1	4.33
HCl Bio	234	10.7		2.5	1.0		71.4		3.0				1.3	1.1	2.8				5.5	0.6	100.0		1.7	2.36
HCl Bio	367	30.0		3.8			41.4		14.0				1.8	3.0	3.3				2.8		100.0	12.1	4.1	5.75
HCl Control	116	24.9					70.5		2.8				0.2		1.6						100.0	7.3	3.0	
HCl Control	234	21.0					64.1		4.1			3.7	0.4		6.7						100.0	7.5	2.5	
HCl Control	367	16.6					41.1		37.1				0.3		4.9						100.0	7.0	2.0	2.53
H_2O Bio	116	3.2		0.6			55.1		17.8		9.9		10.0	1.4	1.8				0.3		100.0	8.4	0.5	0.74
H_2O Bio	125	3.2		9.0			49.4		16.2		8.9		8.7	1.9	2.2				0.2	0.3	100.0	8.1	1.6	2.15
H_2O Bio	234	1.9		0.3			63.7		11.1		10.1		3.6	1.6	2.2				5.2	0.2	100.0	9.7	0.3	1.12
H_2O Bio	367	7.4					48.5		10.8	3.2	7.4		6.7	3.4	1.3	0.1	3.6	2.7	4.7		100.0	6.4	0.9	1.21
H_2O Control	116	4.5					43.0		18.5	7.8	9.2		9.0	1.7	1.0	0.0	1.7	3.6			100.0	7.3	0.5	0.54
H_2O Control	125	6.3					46.0		20.1	1.9	7.1		10.5	1.8	0.7	0.0	3.9	1.7			100.0	7.5	0.8	0.96
H_2O Control	234	5.6					39.0		17.7	14.4	6.9		9.1	1.1	1.5	0.0	3.2	1.5			100.0	6.9	0.7	0.74
H_2O Control	367	5.6					41.9		17.6	13.2	7.3		7.2	0.7	2.7	0.0	2.9	0.8			100.0	6.9	0.7	0.81

*R_{wp}: the weighted pattern index, a function of the least-squares residual.

Appendix Table A4.6 Actual CO_2 offset rate based on the final solutions (20 L) collected from the eight carbonation reactors and Venetia mine data from 2016.

Sample	DIC (mg/L)	Venetia processing water treated (Mm^3/year)	Permanent TIC captured (t/year)	Permanent CO_2 captured (t/year)	Venetia CO_2 emissions (Mt/year)	Actual offset (%)
H_2O Control	39.53	3.9	154.17	565.34	0.21	0.27
H_2O Bio	81.90	3.9	319.41	1171.29	0.21	0.56
HCl Control	16.28	3.9	63.49	232.83	0.21	0.11
HCl Bio	20.92	3.9	81.59	299.19	0.21	0.14
NH_4Cl Control	0.26	3.9	0.99	3.65	0.21	0.00
NH_4Cl Bio	6.22	3.9	24.26	88.97	0.21	0.04
NH_4OAc Control	1.81	3.9	7.07	25.91	0.21	0.01
NH_4OAc Bio	164.90	3.9	643.11	2358.31	0.21	1.12

Appendix Table A4.7 Actual CO_2 offset rate based on solids collected from the eight carbonation reactors and Venetia mine data from 2016.

Sample	TIC (%)	Mass fraction of CO_2 in sample (%)	Sample mass (g)	Mass of CO_2 captured (g/m^2)	Average mass of CO_2 captured in each reactor (g/m^2)	Total mass of CO_2 captured in each reactor (g)	Mass of CO_2 captured (g/ton CRD)	Venetia ore treated (Mt/year)	Mass of CO_2 captured using the ore treated (t/year)	Venetia CO_2 emissions (Mt/year)	Actual offset (%)
H_2O Control 1	0.45	1.65	28.1	20.59	28.56	17.75	76.56	4.74	362.88	0.21	0.17
H_2O Control 2	0.60	2.20	31.0	30.29							
H_2O Control 3	0.58	2.12	37.0	34.81							
H_2O Bio 1	1.36	4.98	42.2	93.36	230.66	143.31	618.28	4.74	2930.64	0.21	1.40
H_2O Bio 2	3.29	12.07	75.2	403.34							
H_2O Bio 3	2.19	8.03	54.7	195.28							
HCl Control 1	1.82	6.66	9.8	29.00	52.01	32.31	139.41	4.74	660.79	0.21	0.31
HCl Control 2	2.24	8.23	18.9	69.09							
HCl Control 3	1.63	5.98	21.8	57.93							
HCl Bio 1	3.45	12.64	49.9	280.29	308.48	191.66	826.87	4.74	3919.35	0.21	1.87
HCl Bio 2	4.17	15.30	43.8	297.84							
HCl Bio 3	3.17	11.61	67.3	347.31							
NH_4Cl Control 1	0.01	0.04	10.9	0.17	0.10	0.06	0.26	4.74	1.23	0.21	0.00
NH_4Cl Control 2	0.01	0.04	7.3	0.12							
NH_4Cl Control 3	0.00	0.00	12.5	0.00							
NH_4Cl Bio 1	0.17	0.64	23.1	6.58	53.78	33.41	144.14	4.74	683.25	0.21	0.33
NH_4Cl Bio 2	2.84	10.41	32.7	151.29							
NH_4Cl Bio 3	0.10	0.36	21.6	3.46							
NH_4OAc Control 1	0.07	0.25	13.6	1.52	0.99	0.61	2.65	4.74	12.56	0.21	0.01
NH_4OAc Control 2	0.04	0.13	22.3	1.34							
NH_4OAc Control 3	0.01	0.03	10.0	0.11							
NH_4OAc Bio 1	1.84	6.74	4.6	13.78	74.08	46.03	198.56	4.74	941.18	0.21	0.45
NH_4OAc Bio 2	2.18	8.01	20.6	73.35							
NH_4OAc Bio 3	3.56	13.05	23.3	135.09							